Theoretical and Numerical Calculations for the Dynamics of Colloidal Suspensions of Molecular Particles in flowing solution inside Mesopores

Ali Atwi

▶ To cite this version:

Ali Atwi. Theoretical and Numerical Calculations for the Dynamics of Colloidal Suspensions of Molecular Particles in flowing solution inside Mesopores. Materials Science [cond-mat.mtrl-sci]. Université du Maine; Lebanese University, 2012. English. NNT : . tel-00699779

HAL Id: tel-00699779

https://theses.hal.science/tel-00699779

Submitted on 21 May 2012

Thèse de Doctorat présentée
à l'Université du Maine et l'Université Libanaise
Pour l'obtention du grade de

Docteur en PHYSIQUE

Theoretical and Numerical Calculations for the Dynamics of Colloidal Suspensions of Molecular Particles in flowing solution inside Mesopores

Présentée par
Ali ATWI

Soutenue le 02 Mai 2012 devant le jury composé de :

Loic AUVRAY
DR CNRS Université Paris Diderot - Paris 7 France   *(Rapporteur)*

Wim J BRIELS
Pr University of Twente, the Netherlands   *(Rapporteur)*

Antoine KHATER
Pr Université du Maine Le Mans, France   *(Directeur de Thèse)*

Abbas HIJAZI
Pr Université Libanaise, Hadadth-Beyrouth, Liban   *(Directeur de Thèse)*

Lazhar BENYAHIA
Pr Université du Maine Le Mans, France   *(Examinateur)*

Fouad AL-Haj HASSAN
Pr Université Libanaise, Hadadth-Beyrouth, Liban   *(Examinateur)*

Laurent JOLY
Dr Université Claude Bernard Lyon1, France   *(Examinateur)*

Acknowledgements

A simple "thank you" would never be sufficient to express my great feelings of gratitude to my PhD thesis supervisor professor *Antoine KHATER*. Thank you for offering this valuable chance to perform my PhD studies under your precious supervision. I would like to thank you for your advice, time, and counsel, your support and valuable guidance, your stimulating discussions, zeal for scientific problems, and for many insightful comments during my research period, thank you for your efforts, scientific instructions that you provided me with in order to well achieve my Thesis. It has been a great pleasure to work with you and under your supervision.

I am also grateful to thank Professor *Abbas HIJAZI*, for your diligent assistance to initiate me to research work during 2006-07 at the Lebanese university which was the start to me, and later on during my thesis work as my PhD supervisor at the Lebanese university, I would like to thank him for his advice and counsel, It has been a great pleasure to work with you and under your supervision. I would never forget the scientific discussion that we had, and his support and encouragement during these period. I would like to thank you for your guidance, time, and support.

I would like to express my gratitude to the *Agence Universitaire de la Francophonie (AUF) for the* scholarship, and to the *Ecole Doctorale des Sciences et de Technologie (EDST)* de l'Université Libanaise for financial help.

I would like to thank my committee members, Professors *Wim BRIELS* and *Lazhar BENYAHIA*, for accepting to be members of my PhD committee at the Graduate School at the Université du Maine, and reading my annual reports.

I would like to thank all the members of the Jury DR CNRS *Loic AUVRAY*, Professor *Wim J BRIELS,* Professor *Lazhar BENYAHIA*, Professor *Fouad AL-Haj HASSAN*, and *Dr Laurent JOLY* , for their attendance and for the fruitful discussion we had.

To greatest father, mother, and sisters, I dedicate this work

Abstract

The dynamics and mobility of macromolecular particles in colloidal suspensions in fluids flowing inside mesopores, and the diffusive collisions and possible adsorption of theses particle at the solid boundaries of the pores, is a subject of fundamental physical and biological interest. The analysis of these effects is necessary to understand a variety of complex phenomena, and towards technical applications which involve the flow of such colloidal suspensions.

The purpose of this thesis is to develop a comprehensive model analysis in a three-dimensional spatial frame for the dynamics of molecular particles in dilute colloidal suspensions in solutions flowing inside pores of variable width, using numerical simulations. The approach by simulations is necessary because it is extremely complex to use analytical tools at present to deal with the problem of diffusive collisions of the particles at the solid pore boundaries. The algorithms which we have developed and the corresponding simulations are sufficiently general and refined to be directly applied to the study of the dynamics of a wide variety of polymer and biological particles in dilute solutions under diverse physical and applicable hydrodynamic conditions inside pores.

The thesis contains a general introduction in Chapter I, and contains the conclusions and perspectives for future work in Chapter VI. The intermediate four chapters present the bulk of the research results carried out toward this thesis.

In Chapter II, simulations are carried out, in a two-dimensional spatial frame, to analyze the dynamics of dilute colloidal suspensions of molecular particles inside pores, subject to hydrodynamic forces, Brownian motion and diffusive collisions at the rough pore boundaries. A theoretical model is developed and intensively analyzed for the treatment of the mechanical restitution of the particles due to collisions at the boundaries. In particular we are able to calculate the Probability Distribution Functions (PDF) for the spatial positions and for the orientations of rigid rod-like particles in colloidal suspensions in Poiseuille flow inside the pores. The results are calculated for a variety of pore channel widths referenced to the size of a rod-like particle. These simulations are general in the sense that they are developed for confining and open pore channels, with rough boundaries at the nano scale, and are presented for different segments in the space of the pores and the depletion layer next to the solid boundary, and for a range of several orders of magnitude of the rotational Peclet number. We show that rough surface boundaries induce characteristic PDF properties quite different from those for ideally flat boundaries. The simulations yield also the nematic order parameter for

the colloidal suspensions. In particular, the model calculations are applied for carbon nanotubes in an aqueous DNA solutions flowing inside pores of different sizes. Our calculated results for the nematic order parameter for particles of known lengths permit in principle, when coupled to birefringence and dichroism experimental results, precise estimates for the pore widths of these systems.

We develop in Chapter III the algorithms and simulations necessary to analyze the dynamics of the particles in a three-dimensional spatial frame. In particular we study in this case an open channel pore for which we calculate the PDF distributions in the bulk and in the depletion layer next to a solid boundary. We develop a theoretical model based in this case on the equations of Jeffrey for the dynamics of solid particles in fluids and the molecular dynamics by mechanical restitution for the diffusive collisions of the particles at the solid boundaries. Simulations are carried out to calculate the *equilibrium* PDF distributions for ellipsoidal molecular particles in suspension in a fluid under hydrodynamic flow. The simulation results for the PDF distributions for the spatial positions and the orientations of ellipsoidal particles are calculated for the bulk liquid and in the depletion layers next to an atomically flat solid surface boundary. They are calculated over several orders of magnitude of the rotational Peclet number, and for variable aspect ratios characteristic of the ellipsoidal particles under study. They demonstrate the importance and significance of modeling in a three-dimensional spatial frame as compared to the simulation results based in the Boeder approach over a two-dimensional spatial frame. In particular we are able to produce a complete topography for the PDF distributions segmented as a hierarchy in the depletion layer, covering a complete range of orientations in 3D space. The simulations permit to calculate, for the colloidal suspension, the nematic order parameter over its tensorial representation, for a variety of forms of ellipsoidal particles selected to correspond to real polymer particles. Our results for the nematic order parameter which may be calculated locally inside the space of the depletion layer are innovating and represent a new input as regards these systems.

We derive in Chapter IV the algorithms for the dynamics of a special class of molecular particles, namely rigid rod-like particles, for which the aspect ratio is much greater than unity. This type of molecular particle is of particular interest, it is often found in nature, as the TMV tobacco virus, and may also be produced synthetically for a wide range of technological exploitation, such as the carbon nanotubes. The simulations to calculate the PDF distributions and the nematic order parameters are carried out for two types of solid boundaries, the ideal atomically flat and the rough surface boundaries. To accomplish this we have investigated in this chapter in particular the influence of the roughness on the choice of the hydrodynamic boundary conditions.

The mechanisms leading to the adhesion of particles of nano sizes in the depletion layer under what would be *non-equilibrium* conditions, due to the conflicting influence of the mechanical diffusive collisions and the attractive Hamaker forces at the boundaries, are of major interest. We have hence investigated in Chapter V a theoretical model to calculate the restitution coefficient from basic physical principles. The objective is to quantify the energy balance during the process of a diffusive collision of a nano particle under the influence of the repulsive forces due to the Pauli principle via mechanical bounce on one hand, and the attractive Hamaker forces acting on the nano particle on the other. This is done by developing a model, based on the JKR and Hertz theories, to account for the energy losses during collisions, and for the energy gains due to the Hamaker interactions. Adhesion becomes an outcome if the energy balance permits this. Our theoretical model is developed by proposing a special analytic approach based on the Hamaker potential. We derive from the theoretical analysis a characteristic nonlinear equation for the restitution coefficient, and analyze its properties which determine under given physical conditions the outcome for adhesion or not.

The conclusions and the perspective are presented in Chapter VI. Indeed, the main scope of this thesis aims at investigating the equilibrium dynamics of biological and macromolecular particles of nano dimensions, in colloidal suspensions in fluids inside pore systems, for a wide range of particle forms, for ideally flat and rough surface pore boundaries on the scale of the particles, and under a realistic range of physical conditions (system temperature, solution viscosity, Peclet number, pore width, particle length, particle form and aspect ratio, …). The simulation results such as for the nematic order parameter may also be compared with experimental data whenever these are available. One of the major perspectives of this work is to use our theoretical model for the adhesion and corresponding mobility under non-equilibrium conditions to produce numerical simulations for the adhesion profiles, for different species of particles flowing in colloidal suspensions through pore networks. Such profiles should lead to technical applications as regards the filtering capacities by pore networks for diverse species of biological and macromolecular particles.

Table of Contents

Chapter I

General introduction

"*[decorative script text]*"

Understanding the complex dynamics of macromolecular and nano particles in colloidal suspensions in flowing liquids is necessary to be able to understand natural effects and industrial applications in the domain of nano-fluidics. This understanding is also necessary to solve technical and scientific problems in a variety of domains such as public health (atmospheric pollution, mobility of blood cells,..), sedimentation in waterways (estuaries, deltas,..), and industrial products and applications (cosmetics, inks and paints, waste matter treatment, the processing of fiber composites,..). The dynamics of *dilute* colloidal suspensions of rigid macromolecular and nano particles is the main focus of the present work.

1.1 Basic objectives for modelling the dynamics of colloidal particles in flowing liquids

The dynamics of particles in colloidal suspensions in fluids flowing inside pores, and the diffusive collisions and possible adsorption (sticking) of these particles at the solid boundaries of the pores, is a subject of fundamental physical and biological interest. The study and analysis of these effects is necessary towards technical applications which involve the flow of such colloidal suspensions.

There is a great amount of research work which has investigated the dynamics of colloidal particles suspended in a flowing solution at different scales (Stover and Cohen 1990; Iso, Cohen et al. 1996; Moses, Advani et al. 2001; Pozrikidis 2005; Altenbach. H 2007; Satoh 2008; Jayageeth, Sharma et al. 2009; San, eacute et al. 2009; Atwi, Khater et al. 2010; Choi and Kim 2010; Mueller, Llewellin et al. 2010). This is motivated by the biological and engineering applications which involve the flow of a suspension of particles in the fluid (GOLDSMITH 1972; CARO, PEDLEY et al. 1978)

(Crochet, Dupret et al. 1994; Osswald and Tseng 1994); (Nitsche and Roy 1996; Adams and Fraden 1998; Butler and Shaqfeh 2002; Sepehr, Ausias et al. 2004; Subramanian and Koch 2005; Carlsson, Lundell et al. 2007; Tang and Advani 2007; Rose, Hoffman et al. 2009; Zhang, Donev et al. 2009; Park, Metzger et al. 2010);

Previous research work using experimental and numerical simulations to study the dynamics of suspensions of colloidal particles has concentrated on the study of colloidal suspensions of microscopic fibers and their applications, justifiably neglecting their Brownian motion in this case. Also, since fibers present an industrial interest mostly in the bulk, the question of the interactions of such fibers with boundary conditions at the inner surfaces of a container is not of special importance. If and when this question is addressed, the assumption has been often to assume an ideally flat surface. Furthermore, when numerical simulations are available, it is often observed that algorithm conditions at the surface boundary for diffusive collisions are difficult to clarify and in some cases are simply incorrect.

In this thesis we are interested in the study of the dynamics of *dilute* colloidal suspensions of macromolecular particles and nano particles flowing inside submicroscopic pores. The frame of reference for our study, with particle lengths from 20 nm to 800 nm, implies a scale much smaller than the microscopic. Under these nano fluidic conditions the dynamics of the colloidal particles is subject to a variety of effects, notably the hydrodynamic forces in the flow, the stochastic Brownian motion and the diffusive collisions at the pore boundaries. Since analytical methods are unavailable at present to deal with the problem of the collisions of these particles at the pore solid boundaries, an approach by numerical simulations is necessary.

Our objective consequently is to develop appropriate numerical simulations for the dynamics of colloidal particles in confining pores. Contrary to previous work, we shall investigate to that end the joint influence of all three types of forces, namely hydrodynamic, thermal Brownian, and due to diffusive collisions. Furthermore we shall study the consequences of realistic *rough* inner pore surface boundaries, on the considered scale, towards the equilibrium dynamics of the particles, by developing appropriate algorithms for such rough surfaces. To do so, the conditions at the surface boundary for diffusive collisions are also clarified with the use of the notion of mechanical restitution, which presents a closed measure, to develop unambiguous algorithms for the molecular dynamics of the diffusive collisions, and hence unambiguous numerical simulations.

This thesis aims to develop a novel model analysis by numerical simulations for the equilibrium dynamics of dilute colloidal suspensions of particles in the *two-* and *three-dimensional spatial frame*, for a wide variety of polymer and nano particles in dilute colloidal suspensions in solutions flowing inside sub-microscopic pores of variable widths, and under diverse physical and applicable hydrodynamic conditions.

We consider explicitly the hydrodynamic and Brownian interactions at rough surface boundaries, where the roughness is characterized at an appropriate scale to be commensurable with the dimensions of the pores. We calculate in particular the probability distribution functions (PDF) for the positions of the centres of mass and for the orientations of these particles, and equally the resultant nematic order tensors, throughout the space inside the pore channels, from their confining rough surface boundaries to the bulk limit in the median of open pores.

Since the notion of Newtonian restitution is of significant interest to our calculations, we have developed a theoretical model to quantify this effect in terms of the diverse energy components (kinetic, potential, deformation and adhesive), that contribute to the determination of the energy loss in a collision. In this manner we have derived nonlinear identities for the restitution coefficient for different forms of macromolecular and nano particles, which serve to calculate the restitution coefficient under a wide range of material and physical conditions for the collision of a given particle form. The purpose is to be able to calculate the sticking probability and consequent mobility of a given particle form during its passage through a pore, under the *non-equilibrium conditions* of the flow.

It is recognised that 2D profile analysis of surfaces has been widely carried out in science and engineering, and has been widely used in industry and academic research for more than half a century. Recently (Wehbi, Clerc et al. 1986; Davis, P.J. et al. 1988; Stout, Sullivan et al. 1991; You and Ehmann 1991; Boudreau and Raja 1992; Stout and Blunt 2000; Zhong and Lu 2002; Fischer, Karius et al. 2008; Sakarya, Leloglu et al. 2008; Uchidate, Yanagi et al. 2011) have emphasised the importance of 3D surface topography in science and engineering applications, this importance arises partially as a result of the realisation within both industry and academia that all surfaces interact in three, instead of two, dimensions. In some cases 2D parameters are insufficient to give a comprehensive description and hence unable to meet the needs of a wide variety of applications. In addition, vast growth in modern computing power

and numerical analysis and processing capabilities has also served as an important motivation for the wide acceptance and adoption of the 3D approach to surface topography analysis.

In this work the sub-microscopic pores is modelled as two infinite solid plates which confine the flow along a Cartesian direction parallel to the plates in two and three spatial frame. Specific algorithms are developed for this purpose based on (Boeder 1932) approach for two dimensional spatial frame Chapter 2 and Jeffrey equations (Jeffery 1922) for three dimensional spatial frame Chapter 3 and Chapter 4.

Brownian motion, schematically presented in Fig1.1, is a phenomenon where small colloidal particles suspended in a fluid tend to move in relatively random or *stochastic* paths. The effect was discovered by Robert Brown in 1827, and is called Brownian motion after him. There are two possible Brownian movements for the colloidal particles, translational and rotational diffusion (Annexe I).
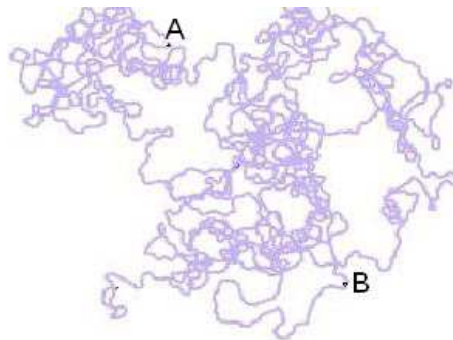
Fig1.1 Brownian motion: a small colloidal particle moves from point A to B in random steps due to the thermal impacts of the liquid molecules surrounding it.

Our simulations consider the hydrodynamic flow to be consistently laminar. The subject of turbulent flow is hence neglected in our work. The laminar flow is assumed to be horizontal, steady state, incompressible and isothermal. The velocity, pressure, and viscosity at each point in the fluid remain constant independent of time. The dimensionless Reynolds number is an important parameter and depends on a number of factors, in particular the average velocity, the characteristic linear dimension, (travelled length of the fluid), density and viscosity of the fluid flow Reynolds numbers of less than 2100 are generally considered to be of a laminar type. Despite the fact that hydrodynamic flow will carry the colloidal suspension in the direction of the flow, we assume the system to be ergodic under equilibrium dynamics, from one cross section of the pore to another, and our calculations are hence independent of the lateral position.

1.2 Model elements for rough surface boundaries of pores

Pores have huge surface areas, providing a vast number of sites where sorption processes can occur. These materials have been recently intensively studied owing to their potential for practical applications, as in catalysis, adsorption, separation, sensing, medical usage, ecology, and nanotechnology (Raman, Anderson et al. 1996; Sayari 1996; Corma 1997; Moller and Bein 1998; Ciesla and Schüth 1999; Ying, Mehnert et al. 1999; Stein, Melde et al. 2000; Sanchez, Soler-Illia et al. 2001; Davis 2002; Vinu, Murugesan et al. 2003; Okabe, Fukushima et al. 2004; Taguchi and Schüth 2005; Vinu, Hossain et al. 2005). Colloidal suspensions of macromolecular and nano particles may be allowed to transit by these pores under hydrodynamic flow. The question then arises as to their interactions with the inner surface boundaries of pores.

The collision of colloidal particles with the surface boundaries of pores is relevant to practical applications. Examples are the nano-particle collection after they are synthesized in chemical reactors or emitted from mobile/stationary combustion sources, micro-contamination control in semiconductor processes, and worker protection in industrial hygiene. These aspects and others motivate the present study.

The physics of surfaces and interfaces is a vast domain in condensed matter physics. From a sub microscopic view point, one can propose dividing surfaces into two major categories: ideal or *atomically flat surfaces*, and *uneven surfaces*.

Atomically flat surfaces are an idealized concept. Even if nano-areas may be prepared initially as atomically flat, such surfaces cannot survive for lengthy periods. The fatigue is the general tendency for material surfaces to lose their order at all scales, and well prepared surfaces will suffer in time different forms of fatigue, presenting an increasing surface disorder. Corrosion is another process by which surfaces, especially metal surfaces, lose their order. Fig 1.2 for example presents an optical mage of atmospheric corrosion. Fabricated surfaces are also never perfect.

Uneven surfaces are hence evidently more realistic. Furthermore, uneven surfaces may be divided into basically two broad classes or types of surfaces, namely *uneven but periodic* and *random rough*.

Since the machining processes have invariably certain technical limits, regardless of the quality and attention in their use, surface irregularities and roughness are

unavoidable on some scale. The uneven but periodic surfaces are usually machine made. During the process of carving a surface (metal, hoses, etc.) some seeds of dust, or other substance, fall under the machine blade, and this produces a periodic damage to the surface while it is applied to make the surface. In Fig 1.3 is a representative example. Though imperfect these surfaces can be important for a variety of applications (Chang, Heilmann et al. 2003; Vass, Osvay et al. 2006).
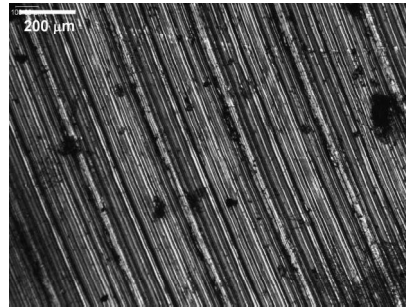
Fig1.2 Optical image of atmospheric corrosion sample (Ni–Cu–Pd) (Liang, Sowards et al. 2010)
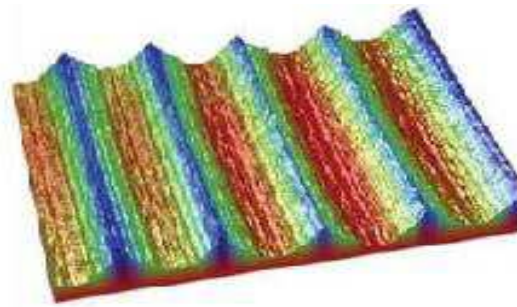
Fig 1.3 periodic uneven surface

The class of uneven yet periodic surfaces does not have a particular incidence on the research work proposed in this thesis. In contrast, the class of random rough surfaces, is of particular interest is. This stems from the fact that the interior surface boundaries of pores are unlikely to be machine prepared, and as a consequence would probably a random nano rough quality (Reiss, Schneider et al. 1990; Zhao, Yang et al. 1996; Pignataro, Bonis et al. 2000; Angelsky, Maksimyak et al. 2006), as compared to the pores diameters and on the scale of the length of colloidal particles (20 nm to 800 nm) of interest in the present work.

It is our objective to model random rough surfaces as an integral component of our algorithms, which we shall use to simulate the dynamics of diffusive collisions for macromolecular and nano particles at the surface boundaries of pores in which the colloidal suspensions flow.

The most common model for randomly rough surfaces is the Gaussian representation which treats the random rough surface as a Gaussian distribution of heights and step levels of the surface topography. The Gaussian distribution is characterized by two parameters, the average height and the variance. For an isotropic Gaussian surface, these parameters are statistically the same along the two directions of the surface. (Chen and Huang 2004) simulated such roughness, as in Fig1.4 (left), measured on the nano scale using AFM microscopy, with a numerical model for the tip. The results are represented by a Gaussian distribution of nano-metric heights as in Fig1.4 (right).
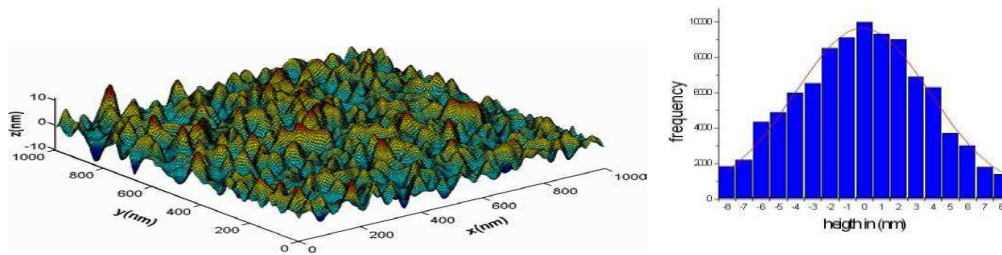
Fig 1.4 Gaussian surface topography and histogram of heights distribution (Chen and Huang 2004)

1.3 Macromolecular particles and their forms

The geometry of the macromolecules is complex and takes several forms and shapes. To facilitate the study of the macromolecules, research scientists have modeled the macromolecules particles by basic and simple geometric shapes: spheres, discs, rods, ellipsoidal, and rod- like particles, and others compound shapes.

Compared to suspensions of spherical particles, suspensions of rigid rod-like and ellipsoidal particles, exhibit a much larger range of behavior since the orientation of these particles makes its configuration more likely to be affected by flow fields than that of a spherical particle. The colloidal suspensions of rod-like and ellipsoidal particles are also important in the non-Newtonian fluid effects (shear thinning and thickening), (Larson 1999).

Our thesis will be focused on two types of macromolecules, namely rod-like and ellipsoidal forms for the colloidal particles.

In recent years, much work has been done on the investigation of non spherical nano-particles for pharmaceutical and medical applications. The potential of these nano-particles materials as drug delivery vehicles is considered to be enormous. Many nano-particle with rod and ellipsoidal shapes based drug formulations and diagnostic agents

7

have already been developed, e.g., for the treatment of cancer, pain, and infections (Kawasaki and Player 2005; Farokhzad and Langer 2006). Moreover, (Daum, Tscheka et al. 2012) worked on the effect of shape of nano-particle materials on the body and related physiological mechanisms, they found that non-spherical shapes, such as rods, discs and ellipsoidal particles, clearly shows the firm binding to the target tissue.

Rod and ellipsoidal -like macromolecules, polymers and particles can be found in many areas of common existing and new emerging technologies. Many macromolecules of biological origin have rod-like structure: a short DNA fragment less than 100 base pairs (50nm) (Newman, Swinney et al. 1974; Tirado, Martinez et al. 1984; Wang, Garner et al. 1991; Tinland, Plen et al. 1997), Xantham gum (Davidson 1980) a helical polysaccharide which roughly forms a cylinder, is used to enhance viscosity of many food products. Other types of polysaccharides, peptides, and polynucleotides also form rigid linear structures. Even micro-organisms, such as FD bacteriophages and tobacco mosaic viruses, have rod-like structure (Caspar 1963; Chen, Koopmans et al. 1980; Tracy and Pecora 1992; Cush and Russo 2002) Fig 1.5.
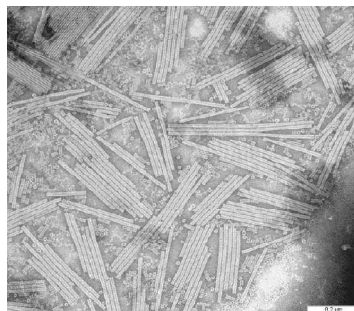
Fig 1.5 an electron micrograph picture of tobacco mosaic virus (TMV) illustrating its rod-like characteristics (Adams, Eby et al. 1989)

Synthetic rigid polymers or nano-tubes are used for improvement of material properties (Adams, Eby et al. 1989) Composites of Kevlar and carbon fiber greatly increase tensile strength and stiffness (Gustin, Joneson et al. 2005), Fig 1.6. In one experiment performed by (Huynh, Dittmer et al. 2002) semiconductor CdSe nano-rods have been cast into a film to make solar cells. By controlling the diameter and length of the nano-rods, as well as the microstructure, (Huynh, Dittmer et al. 2002), were able to improve the performance of the solar cells. A picture of these nano-rods taken by a transmission electron microscope (TEM) is seen in Fig 1.7.

On the other hand, various molecules of natural origin have Ellipsoidal structure: polymethyl methacrylate (PMMA) and polystyrene (PS) (Han, Alsayed et al. 2009). Even some simple micro-organisms have an elongated, ellipsoidal configuration, a

rigid structure actin (Schmidt, Ziemann et al. 1996) and collagen (Oh and Park 1992; Claire and Pecora 1997) Fig 1.8
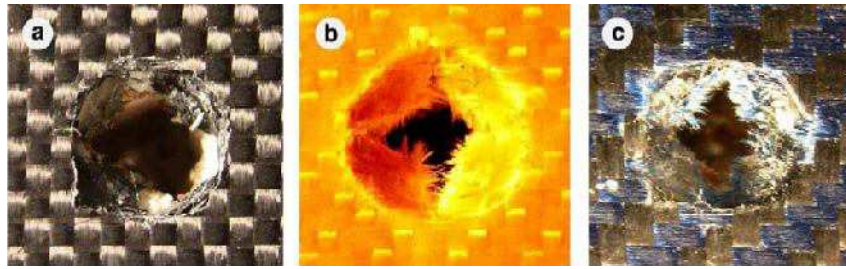
Fig 1.6 Pictures of fabrics made up of carbon fibers (a), Kevlar fibers (b), and a composite of both (c) after they have been subjected to impact and compression testing in the work of (Gustin, Joneson et al. 2005)
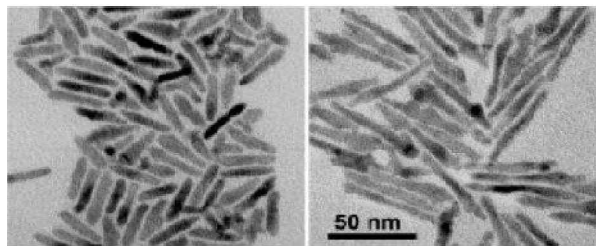
Fig 1.7 Transmission electron microscope images of CdSe nanorods produced in experiments (Huynh, Dittmer et al. 2002) in order to improve the efficiency of hybrid solar cells.

Ellipsoidal particles are important because their colloidal behavior such as Brownian motion, (Grzelczak, Vermant et al. 2010), maximum packing, (Nie, Petukhova et al. 2010) as well as crystal structure (Yang, Kim et al. 2008) can be tuned systematically by changing the aspect ratio of their axes. Moreover, ellipsoidal particles can be an excellent model system in condensed matter physics (Chong and Götze 2002) and drug delivery vehicle design (Gratton, Ropp et al. 2008). Moreover, (Singh, Lele et al. 2009) showed that ellipsoids can be organized into both the translational and orientational order through electric field assembly, leading to new structures that are otherwise unattainable using spherical particles, such ordered structures may have new mechanical properties (Mittal and Furst 2009), Fig 1.9.
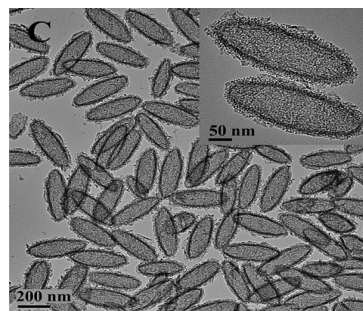
Fig1.8TEM images at low and high (insets) magnifications of ellipsoidal hollow silica particles (Zhao, Lang et al. 2009)

Most theories that treat these macromolecules in dilute solution, considered that the rigid rod-like macromolecule, being a cylinder with surfaces perfectly smooth immersed completely in a continuous hydrodynamics.
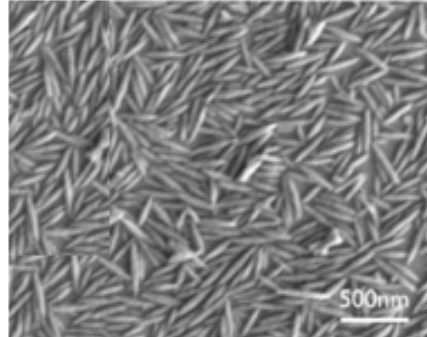
Fig 1.9 A scanning electron microscopy (SEM) image of the titanium dioxide particles; with an aspect ratio of 4.19 (Mittal and Furst 2009).

In this work, rigid rod-like particles are modeled as a long cylinder slender-body Fig 1.10C, this model is popular because distributed resistance along the length(Batchelor 1970; Cox 1970). There have been many similar approaches such as in the works by (Broersma 1960a; Broersma 1960b; Moran 1963; Happel and Brenner 1965).
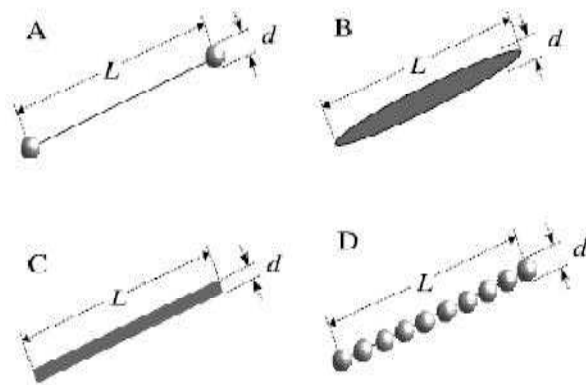
Fig 1.10 Physical models for a rigid rod-like particle: A) rigid-dumbbell, B) prolate Spheroid, C) slender-body, and D) shish-kebab model.

Moreover in this thesis, the ellipsoidal particles are modeled as the prolate spheroid of arbitrary aspect ratio as in Fig 1.10B. Note that (Kim and Karrila 1991; Claeys and Brady 1993a) show by numerical simulation, the efficiency and accuracy to take prolate spheroids in particular by comparison with other numerical methods for flow.

10

Other models for particles are illustrated in Fig 1.10. The rigid dumbbell model is simple (Fixman 1985a; Fixman 1985b; Bitsanis, Davis et al. 1988; Bitsanis, Davis et al. 1990) but improper distribution of resistance results in different diffusivities compared to other models (Cobb and Butler 2005). The shish-kebab' model by (Doi and Edwards 1986) , which considers the macromolecule as N pearls, or spheres, of d diameter, N=L/d, that composes the macromolecule tip to tip asin Fig1.10D.

1.4. Adhesion between solid bodies

Adhesion has been studied intensively over the past 40 years. The problem of determining the adhesion between solid bodies in contact is important for understanding friction, wear, the agglomeration and dispersion of colloidal particles, and many other phenomena (R.G. Horn, Israelachvili et al. 1987) As a complex, multifaceted phenomenon, adhesion involves factors such as surface chemistry, thermodynamics, polymer chemistry and physics, hydrodynamics, and contact mechanics (G.Y. Choi, Zurawsky et al. 1999).

(Mittal 1975) dealt with the term adhesion by dividing it into three categories: (i) basic or fundamental adhesion, (ii) thermodynamic or reversible adhesion, and (iii) experimental or practical adhesion. Basic or fundamental adhesion is defined as the summation of all interfacial intermolecular interactions, such as ionic, covalent, metallic, hydrogen bonding and van der Waals forces, between the contacting materials. Thermodynamic or reversible adhesion signifies the change in Gibbs (or Helmholz) free energy per unit area when an interface is formed (or separated). The practical adhesion (experimental) signifies the force or the work required to remove or detach a solid from another. The measured practical adhesion is strongly influenced by many factors, such as the surface chemistry, mechanical properties and surface roughness, etc.. . This value can also be significantly different when different adhesion measurement techniques, parameters of technique and measuring conditions are used (Mittal 1975).

The adhesiveness of nano-particles on pores depends on the loss of the center-of-mass energy of the incident particles due to the collision. The energy loss mechanisms include the transfer of incident kinetic energy into different new modes such as heat energy, elastic deformation, particle rotation, and others. The significance of these mechanisms is thought to depend on parameters, such as the incident energy, particle-surface interaction, and elastic properties of particle and surface. Several models have been proposed to explain energy loss mechanisms upon the collision (Bitter 1963;

Rogers and Reed 1984; Reed 1989; Wall, John et al. 1989; Tsai, Pui et al. 1990; Wall, John et al. 1990; Xu and Willeke 1993; Andres 1995).

The fundamentals of molecular attraction potentials and the mechanics of adhesion are treated for example by (Krupp 1967), by (Israelachvili and Tabor 1973), (Maugis 1999) and (Kendall 2001). The basic models for elastic behavior were derived by (Hertz 1882) and for constant adhesion by (Johnson, Kendall et al. 1971), and by (B.V. Derjaguin, Muller et al. 1975).

In this work we develop a new model to quantify the energy balance during the process of a diffusive collision of macromolecular and nano particles under the influence of the repulsive and attractive Hamaker forces acting on them in the vicinity of the rough solid surface boundary. This is done by developing a model to account for the energy gains due to the attractive Hamaker interactions and energy losses in the collision. These theories will be presented in detail in Chapter V.

1.6 Overview for the present work

In Chapter 2, simulations will be carry out, in a two-dimensional spatial frame, to analyze the dynamics of dilute colloidal suspensions of molecular particles inside pores, subject to hydrodynamic forces, Brownian motion and diffusive collisions at the rough pore boundaries. A theoretical model is developed and intensively analyzed for the treatment of the mechanical restitution of the particles due to collisions at the boundaries. In particular we are able to calculate the Probability Distribution Functions (PDF) for the spatial positions and for the orientations of rigid rod-like particles in colloidal suspensions in Poiseuille flow inside the pores. The simulations yield also the nematic order parameter for the colloidal suspensions.

We will develop in Chapter 3 the algorithms and simulations necessary to analyze the dynamics of the particles in a three-dimensional spatial frame. In particular we will study in this case an open channel pore for which we calculate the PDF distributions in the bulk and in the depletion layer next to a solid boundary. We will develop a theoretical model based in this case on the equations of Jeffrey for the dynamics of solid particles in fluids and the molecular dynamics by mechanical restitution for the diffusive collisions of the particles at the solid boundaries. Simulations are carried out to calculate the *equilibrium* PDF distributions for ellipsoidal molecular particles in suspension in a fluid under hydrodynamic flow. The simulations will permit us to

calculate, for the colloidal suspension, the nematic order parameter over its tensorial representation, for a variety of forms of ellipsoidal particles selected to correspond to real polymer particles.

We will derive in Chapter 4 the algorithms for the dynamics of a special class of molecular particles, namely rigid rod-like particles, for which the aspect ratio is much greater than unity. This type of molecular particle is of particular interest, it is often found in nature, as the TMV tobacco virus, and may also be produced synthetically for a wide range of technological exploitation, such as the carbon nano-tubes. The simulations to calculate the PDF distributions and the nematic order parameters will carry out for two types of solid boundaries, the ideal atomically flat and the rough surface boundaries. To accomplish this we have investigated in this chapter in particular the influence of the roughness on the choice of the hydrodynamic boundary conditions.

The mechanisms leading to the adhesion of particles of nano sizes in the depletion layer under what would be non-equilibrium conditions, due to the conflicting influence of the mechanical diffusive collisions and the attractive Hamaker forces at the boundaries, are of major interest. We have will investigate in Chapter 5 for a theoretical model to calculate the restitution coefficient from basic physical principles. The objective of this chapter is to quantify the energy balance during the process of a diffusive collision of a nano particle under the influence of the repulsive forces due to the Pauli principle, and the attractive Hamaker forces acting on the nano particle on the other. This will done by developing a model, based on the JKR and Hertz theories, to account for the energy losses during collisions, and for the energy gains due to the Hamaker interactions.

The conclusions and the perspective will be presented in Chapter 6.

References

Adams, M. and S. Fraden (1998). "Phase Behavior of Mixtures of Rods (Tobacco Mosaic Virus) and Spheres (Polyethylene Oxide, Bovine Serum Albumin)." Biophysical Journal **74**(1): 669-677.

Adams, W. W., R. K. Eby, et al. (1989). The Materials Science and Engineering of Rigid-Rod Polymers, Pittsburgh, PA: Materials Research Society: Pittsburgh.

Adams, W. W., R. K. Eby, et al. (1989). The Materials Science and Engineering of Rigid-Rod Polymers Pittsburgh, PA, Materials Research Society symposia proceedings.

Altenbach. H, N. K., Pylypenko. S, Renner. B (2007). "Influence of rotary inertia on the fiber dynamics in homogeneous creeping flows." ZAMM - Journal of Applied Mathematics and Mechanics / Zeitschrift für Angewandte Mathematik und Mechanik **87**(2): 81-93.

Andres, R. P. (1995). "Inelastic Energy Transfer in Particle/surface Collisions." Aerosol Sci. Technol **23**: 40-50.

Angelsky, O. V., A. P. Maksimyak, et al. (2006). "Optical correlation diagnostics of rough surfaceswith large surface inhomogeneities." Opt. Express **14**(16): 7299.

Atwi, A., A. Khater, et al. (2010). "Three-dimensional Monte Carlo simulations of the dynamics of macromolecular particles in solutions flowing in mesopores." Central European Journal of Chemistry **8**(5): 1009.

B.V. Derjaguin, V. M. Muller, et al. (1975). "Effect of contact deformations on the adhesion of particles." Journal of Colloid and Interface Science **53**(2): 314.

Batchelor, G. K. (1970). "Slender-body theory for particles of arbitrary cross-section in Stokes flow." *J. Fluid Mech.* **44**: 419- 440.

Bitsanis, I., H. T. Davis, et al. (1988). "Brownian dynamics of nondilute solutions of rodlike polymers. 1. Low concentrations." Macromolecules **21**: 2824-2835.

Bitsanis, I., H. T. Davis, et al. (1990). "Brownian dynamics of nondilute solutions of rodlike polymers. 2. High concentrations." Macromolecules **23**: 1157-1165.

Bitter, J. G. A. (1963). "A Study of Erosion Phenomena." Wear **6**: 5-21.

Boeder, P. (1932). "Über Strömungsdoppelbrechung." Zeitschrift für Physik A Hadrons and Nuclei **75**(3): 258.

Boudreau, B. D. and J. Raja (1992). "Analysis of lay characteristics of three-dimensional surface maps." International Journal of Machine Tools and Manufacture **32**(1-2): 171-177.

Broersma, S. (1960a). "Rotational difiusion constant of a cylindrical particle." J. Chem. Phys **32**: 1626.

Broersma, S. (1960b). "Viscous force constant for a closed cylinder." J. Chem. Phys. **32**: 1632.

Butler, J. E. and E. S. G. Shaqfeh (2002). "Dynamic simulations of the inhomogeneous sedimentation of rigid fibres. ." J. Fluid Mech **468**: 205{237.

Carlsson, A., F. Lundell, et al. (2007). "Fiber Orientation Control Related to Papermaking." Journal

of Fluids Engineering
J. Fluids Eng. **129**(4): 457-465.

CARO, C. G., T. J. PEDLEY, et al. (1978). The Mechanics of the Circulation, Oxford University Press.

Caspar, D. L. D. (1963). "Assembly and stability of the tobacco mosaic virus particle." Adv. Protein Chem. **18**: 37-121.

Chang, C.-H., R. K. Heilmann, et al. (2003). Fabrication of sawtooth diffraction gratings using nanoimprint lithography, AVS.

Chen, F. C., G. Koopmans, et al. (1980). "Dimensions of xf virus from its rotational and translational diffusion coeffcients." Biochemistry **19**: 1373-1376.

Chen, Y. and W. Huang (2004). "Numerical simulation of the geometrical factors affecting surface roughness measurements by AFM." Measurement Science and Technology **15**(10): 2005.

Choi, C. R. and C. N. Kim (2010). "Direct numerical simulations of the dynamics of particles with arbitrary shapes in shear flows." Journal of Hydrodynamics, Ser. B **22**(4): 456-465.

Chong, S. H. and W. Götze (2002). "Idealized glass transitions for a system of dumbbell molecules." Physical Review E **65**(4): 041503.

Ciesla, U. and F. Schüth (1999). "Ordered mesoporous materials." Microporous and Mesoporous Materials **27**(2-3): 131-149.

Claeys, I. L. and J. F. Brady (1993a). "Suspensions of prolate spheroids in Stokes Flow. Part 1. Dynamics of a finite number of particles in an unbounded fluid." J. Fluid Mech **251** 411-442.

Claire, K. and R. Pecora (1997). "Translational and rotational dynamics of collagen in dilute solution." J. Phys. Chem. B **101**: 746-753.

Cobb, P. D. and J. E. Butler (2005). "Simulations of concentrated suspensions of rigid Fibers: Relationship between short-time difiusivities and the long-Time rotational difiusion." J. Chem. Phys **123**: 054908.

Corma, A. (1997). "From Microporous to Mesoporous Molecular Sieve Materials and Their Use in Catalysis." Chemical Reviews **97**(6): 2373-2420.

Cox, R. G. (1970). "The motion of long slender bodies in a viscous fluid. Part 1. General theory." J. Fluid Mech **44** 791-810.

Crochet, M. J., F. Dupret, et al. (1994). 11- Injection moulding , (Flow and Rheology in Polymer Composites Manufacturing), Elsevier

Cush, R. C. and P. S. Russo (2002). "Self-Diffusion of a rodlike virus in the isotropic phase." Macromolecules **35**: 8659-8662.

Daum, N., C. Tscheka, et al. (2012). "Novel approaches for drug delivery systems in nanomedicine: effects of particle design and shape." Wiley Interdisciplinary Reviews: Nanomedicine and Nanobiotechnology **4**(1): 52-65.

Davidson, R. L. (1980). Handbook of Water-Soluble Gums and Resins, McGraw-Hill.

Davis, E. J., S. P.J., et al. (1988). "The application of 3-D topography to engine bore surfaces,." Surf. Topography **1**(2): 229-251.

Davis, M. E. (2002). "Ordered porous materials for emerging applications." Nature **417**(6891): 813-821.

Doi, M. and S. F. Edwards (1986). "The Theory of Polymer Dynamics.
." Oxford University Press,.

Farokhzad, O. C. and R. Langer (2006). "Nanomedicine: Developing smarter therapeutic and diagnostic modalities." Advanced Drug Delivery Reviews **58**(14): 1456-1459.

Fischer, C., V. Karius, et al. (2008). "Relationship between Micrometer to Submicrometer Surface Roughness and Topography Variations of Natural Iron Oxides and Trace Element Concentrations." Langmuir **24**(7): 3250-3266.

Fixman, M. (1985a). "Dynamics of semidilute polymer rods - An alternative to cages." Phys. Rev. Lett. **55** 2429-2432.

Fixman, M. (1985b). "Entanglements of semidilute polymer rods." Phys. Rev. Lett. **54**: 337-339.

G.Y. Choi, W. Zurawsky, et al. (1999). "Molecular Weight Effects in Adhesion." Langmuir **15**: 8447.

GOLDSMITH, H. L. (1972). The flow of model particles and blood cells and its relation to thrombogenesis, Progress in Hemostasis and Thrombosis.

Gratton, S. E. A., P. A. Ropp, et al. (2008). "The effect of particle design on cellular internalization pathways." Proceedings of the National Academy of Sciences **105**(33): 11613-11618.

Grzelczak, M., J. Vermant, et al. (2010). "Directed Self-Assembly of Nanoparticles." ACS Nano **4**(7): 3591-3605.

Gustin, J., A. Joneson, et al. (2005). "Low velocity impact of combination Kevlar/carbon fiber sandwich composites.
." Comp. Struct **69**: 396-406.

Han, Y., A. Alsayed, et al. (2009). "Quasi-two-dimensional diffusion of single ellipsoids: Aspect ratio and confinement effects." Physical Review E **80**(1): 011403.

Happel, J. and H. Brenner (1965). Low Reynolds Number Hydrodynamics., Prentice-Hall.

Hertz, H. (1882). "Über die Berührung fester elastischer Körper. ." Journal für die Reine und Angewandte Mathematik **92**: 156.

Huynh, W. U., J. J. Dittmer, et al. (2002). "Hybrid nanorod-polymer solar cells."." Science **295**: 2425-2427.

Iso, Y., C. Cohen, et al. (1996). "Orientation in simple shear flow of semi-dilute fiber suspensions 2. Highly elastic fluids." Journal of Non-Newtonian Fluid Mechanics **62**(2-3): 135-153.

Israelachvili, J. N. and D. Tabor (1973). "Van der Waals Forces: Theory and Experiment." Progress in Surface and Membrane Science **7**: 1-55.

Jayageeth, C., V. I. Sharma, et al. (2009). "Dynamics of short fiber suspensions in bounded shear flow." International Journal of Multiphase Flow **35**(3): 261-269.

Jeffery, G. B. (1922). "The Motion of Ellipsoidal Particles Immersed in a Viscous Fluid." Proceedings of the Royal Society of London. Series A **102**(715): 161-179.

Johnson, K. L., K. Kendall, et al. (1971). "Surface Energy and the Contact of Elastic Solids." Proceedings of Royal Society **A324**: 301.

Kawasaki, E. S. and A. Player (2005). "Nanotechnology, nanomedicine, and the development of new, effective therapies for cancer." Nanomedicine: Nanotechnology, Biology and Medicine **1**(2): 101-109.

Kendall, K. (2001). Molecular Adhesion and its Application. Kluwer Academic Publishers New York.

Kim, S. and S. J. Karrila (1991). "Microhydrodynamics: Principles and selected applications." Butterworth-Heinemann.

Krupp, H. (1967). Advances in Colloid Interface Sci **1**: 111.

Larson, R. G. (1999). The Structure and Rheology of Complex Fluids., Oxford University Press.

Liang, D., J. W. Sowards, et al. (2010). "A corrosion study of nickel–copper and nickel–copper–palladium welding filler metals." Materials and Corrosion **61**(11): 909-919.

Maugis, D. (1999). Contact, Adhesion and Rupture of Elastic Solids. Springer, Berlin.

Mittal, K. L. (1975). "Adhesion Measurement of Thin Films." ElectroComponent Science and Technology **3**(1): 21-42.

Mittal, M. and E. M. Furst (2009). "Electric Field-Directed Convective Assembly of Ellipsoidal Colloidal Particles to Create Optically and Mechanically Anisotropic Thin Films." Advanced Functional Materials **19**(20): 3271-3278.

Moller, K. and T. Bein (1998). "Inclusion Chemistry in Periodic Mesoporous Hosts." Chemistry of Materials **10**(10): 2950-2963.

Moran, J. P. (1963). "Line source distributions and slender-body theory." J. Fluid Mech. **17**: 285-304.

Moses, K. B., S. G. Advani, et al. (2001). "Investigation of fiber motion near solid boundaries in simple shear flow." Rheologica Acta **40**(3): 296-306.

Mueller, S., E. W. Llewellin, et al. (2010). "The rheology of suspensions of solid particles." Proceedings of the Royal Society A: Mathematical, Physical and Engineering Science **466**(2116): 1201-1228.

Newman, J., H. L. Swinney, et al. (1974). "Hydrodynamic properties and molecular weight of fd bacteriophage DNA ." Biochemistry **13**: 4832- 4838.

Nie, Z., A. Petukhova, et al. (2010). "Properties and emerging applications of self-assembled structures made from inorganic nanoparticles." Nat Nano **5**(1): 15-25.

Nitsche, J. and P. Roy (1996). "Shear-induced alignment of nonspherical Brownian particles near walls." AIChE Journal **42**(10): 2729-2742.

Oh, Y. R. and O. O. Park (1992). "Transient flow birefringence of calf skin collagen solutions." J. Chem. Eng. Japan **25**: 243-249.

Okabe, A., T. Fukushima, et al. (2004). "Tetrafluoroborate Salts as Site-Selective Promoters for Sol−Gel Synthesis of Mesoporous Silica." Journal of the American Chemical Society **126**(29): 9013-9016.

Osswald, T. A. and S.-C. Tseng (1994). 10- Compression moulding (Flow and Rheology in Polymer Composites Manufacturing), Elsevier.

Park, J., B. Metzger, et al. (2010). "A cloud of rigid fibres sedimenting in a viscous fluid." Journal of Fluid Mechanics **648**: 351-362.

Pignataro, B., A. D. Bonis, et al. (2000). The role of micro- and nanomorphology of rough silver surfaces of different nature in surface enhanced Raman scattering effect: A combined study of scanning force microscopy and low-frequency Raman modes, AIP.

Pozrikidis, C. (2005). "Orbiting motion of a freely suspended spheroid near a plane wall." Journal of Fluid Mechanics **541**: 105-114.

R.G. Horn, J. N. Israelachvili, et al. (1987). "Measurement of the Deformation and Adhesion of Solids in Contact." J. Colloid Interface Sci **115**: 480-492.

Raman, N. K., M. T. Anderson, et al. (1996). "Template-Based Approaches to the Preparation of Amorphous, Nanoporous Silicas." Chemistry of Materials **8**(8): 1682-1701.

Reed, J. (1989). The Adhesion of Small Particles to a Surface. In Particles on Surfaces 2: Detection, Adhesion and Removal, Plenum, New York.

Reiss, G., F. Schneider, et al. (1990). "Scanning tunneling microscopy on rough surfaces: Deconvolution of constant current images " J. Appl. Phys. Lett **57**(9): 867.

Rogers, L. N. and J. Reed (1984). "The Adhesion of Particles Undergoing an Elastic-plastic Impact with a Surface." J. Phys. D **17**: 677-689.

Rose, K., B. Hoffman, et al. (2009). "Hydrodynamic interactions in metal rodlike-particle suspensions due to induced charge electroosmosis." Physical Review E **79**(1): 011402.

Sakarya, U., U. M. Leloglu, et al. (2008). "Three-dimensional surface reconstruction for cartridge cases using photometric stereo." Forensic Science International **175**(2-3): 209-217.

San, eacute, et al. (2009). "Hydrodynamics of confined colloidal fluids in two dimensions." Physical Review E **79**(5): 051402.

Sanchez, C., G. J. d. A. A. Soler-Illia, et al. (2001). "Designed Hybrid Organic−Inorganic Nanocomposites from Functional Nanobuilding Blocks." Chemistry of Materials **13**(10): 3061-3083.

Satoh, A. (2008). "Three-dimensional Monte Carlo simulations of internal aggregate structures in a colloidal dispersion composed of rod-like particles with magnetic moment normal to the particle axis." Journal of Colloid and Interface Science **318**(1): 68-81.

Sayari, A. (1996). "Catalysis by Crystalline Mesoporous Molecular Sieves." Chemistry of Materials **8**(8): 1840-1852.

Schmidt, F. G., F. Ziemann, et al. (1996). "Shear field mapping in actin networks by using magnetic tweezers." Euro. Biophys. J. Biophys. Lett **24**: 348-353.

Sepehr, M., G. Ausias, et al. (2004). "Rheological properties of short fiber filled polypropylene in

transient shear flow." Journal of Non-Newtonian Fluid Mechanics **123**(1): 19-32.

Singh, J. P., P. P. Lele, et al. (2009). "One- and two-dimensional assembly of colloidal ellipsoids in ac electric fields." Physical Review E **79**(5): 050401.

Stein, A., B. J. Melde, et al. (2000). "Hybrid Inorganic–Organic Mesoporous Silicates—Nanoscopic Reactors Coming of Age." Advanced Materials **12**(19): 1403-1419.

Stout, K. J. and L. Blunt (2000). Three Dimensional Surface Topography published by Penton press an imprint of Kogan Page Ltd London.

Stout, K. J., P. J. Sullivan, et al. (1991). Analysis of 3-D surface topography questionnaire. 1st EC Workshop on 3-D Surface Measurement and Characterization.

Stover, C. A. and C. Cohen (1990). "The motion of rodlike particles in the pressure-driven flow between two flat plates." Rheologica Acta **29**(3): 192-203.

Subramanian, G. and D. Koch (2005). "Inertial effects on fibre motion in simple shear flow." Journal of Fluid Mechanics **535**: 383-414.

Taguchi, A. and F. Schüth (2005). "Ordered mesoporous materials in catalysis." Microporous and Mesoporous Materials **77**(1): 1-45.

Tang, W. and S. Advani (2007). Nonequilibrium molecular dynamics simulation to describe the rotation of rigid, low aspect ratio carbon nanotubes in simple shear flow, AIP.

Tinland, B., A. Plen, et al. (1997). "Persistence length of single-strandedDNA " Macromolecules **30**: 5763- 5765.

Tirado, M. M., C. L. Martinez, et al. (1984). "Comparison of theories for the translational and rotational diffusion-coeffcients of rod-like macromolecules-application to short DNA fragments." " J. Chem. Phys. **81**: 2047-2052.

Tracy, M. A. and R. Pecora (1992). "Dynamics of rigid and semirigid rodlike polymers." Ann. Rev. Phys. Chem **43**: 525-557.

Tsai, C. J., D. Y. H. Pui, et al. (1990). "Capture and Rebound of Small Particles upon Impact with Solid Surfaces." Aerosol Sci. Technol **12**: 497-507.

Uchidate, M., K. Yanagi, et al. (2011). "Generation of 3D random topography datasets with periodic boundaries for surface metrology algorithms and measurement standards." Wear **271**(3-4): 565-570.

Vass, C., K. a. Osvay, et al. (2006). "Fabrication of 150 nm period grating in fused silica by two-beam interferometric laser induced backside wet etching method." Opt Exp **14**(18): 8354-8359.

Vinu, A., K. Z. Hossain, et al. (2005). "Recent Advances in Functionalization of Mesoporous Silica." Journal of Nanoscience and Nanotechnology **5**(3): 347-371.

Vinu, A., V. Murugesan, et al. (2003). "Pore Size Engineering and Mechanical Stability of the Cubic Mesoporous Molecular Sieve SBA-1." Chemistry of Materials **15**(6): 1385-1393.

Wall, S., W. John, et al. (1989). Application of Impact adhesion Theory to Particle Kinetic Energy Loss Measurements. In Particles on Surfaces 2: Detection, Adhesion and Removal Plenum, New York. pp. 19-34, .

Wall, S., W. John, et al. (1990). "Measurements of Kinetic Energy Loss for Particles Impacting Surfaces." Aerosol Sci. Technol **12**: 926-946.

Wang, L., M. M. Garner, et al. (1991). "Self-diffusion and cooperative difusion of a rodlike DNA fragment."." Macromolecules **24**: 2368-2376.

Wehbi, D., A. Clerc, et al. (1986). "Three-dimensional quantification of wear tracks on amorphous NiB coatings." Wear **107**(2): 263-278.

Xu, M. and K. Willeke (1993). "Right-angle Impaction and Rebound of Particles." J. Aerosol Sci **24**: 19-30.

Yang, S.-M., S.-H. Kim, et al. (2008). "Synthesis and assembly of structured colloidal particles." Journal of Materials Chemistry **18**(19).

Ying, J. Y., C. P. Mehnert, et al. (1999). "Synthesis and Applications of Supramolecular-Templated Mesoporous Materials." Angewandte Chemie International Edition **38**(1-2): 56-77.

You, S. J. and K. F. Ehmann (1991). "Computer synthesis of three-dimensional surfaces,." Wear **145**: 29-42.

Zhang, Y., A. Donev, et al. (2009). "Tethered DNA dynamics in shear flow,." J. Chem. Phys **130**(23): 13.

Zhao, W., M. Lang, et al. (2009). "Fabrication of uniform hollow mesoporous silica spheres and ellipsoids of tunable size through a facile hard-templating route." Journal of Materials Chemistry **19**(18).

Zhao, Y. P., H.-N. Yang, et al. (1996). "Extraction of real-space correlation function of a rough surface by light scattering using diode array detectors " J. Appl. Phys. Lett **68**(22): 3063.

Zhong, Z. W. and Y. G. Lu (2002). "3D Characterization of super-smooth surfaces of diamond turned OFHC copper mirrors." Materials and Manufacturing Processes **17**(2): 269-280.

Chapter 2

Simulations for the dynamics and nematic order of dilute colloidal suspensions of rod-like particles flowing in 2D-spatial frames of open and confining pores with rough solid boundaries

Abstract: Simulations have been carried out to analyze the dynamics of dilute colloidal suspensions of macromolecular particles in solutions flowing in pores, subject to hydrodynamic forces, Brownian motion and stochastic collisions at rough pore boundaries in a two-dimensional spatial frame. A theoretical model is developed and intensively analyzed for the treatment of the mechanical restitution of the particles due to dynamic collisions at these boundaries. In particular we are able to calculate the Probability Distribution Functions (PDF) for the spatial positions and the orientations of rod-like particles for Poiseuille flow inside the pores. The results are presented for different widths of pore channels referenced to the size of a rod-like particle. These simulations are general in the sense that they are developed for confining and open pore channels, rough at the nano scale, and are valid throughout the space of the pores and in the boundary depletion layers, over several orders of magnitude of the rotational Peclet number. We show that rough surface boundaries induce characteristic PDF properties that are quite different from those for ideally flat ones. The simulations also permit calculating the nematic order parameters for colloidal suspensions; the model calculation is applied for dilute colloidal suspensions of carbon nanotubes 750 nm long in an aqueous single-stranded DNA solution flowing inside pores of different sizes. Our calculated nematic order results for dilute suspensions of particles of known lengths flowing inside porous systems should indicate, when coupled to birefringence and dichroism experimental results, the possibility to estimate the pore widths for these systems.

2.1 Introduction

The dynamics of macromolecules particles in dilute colloidal suspensions in liquid solutions flowing near solid boundary surfaces or inside confined geometries such as pores of variable submicron sizes are long-standing research topics that continue to pose many outstanding questions. Aside from their importance for traditional applications such as lubrication, adhesion, polymer processing, and oil recovery, the topic of the flow of such particle suspensions in porous media, has recently taken on renewed importance with the emergence of the micro-fluidic approach to chemical and biological analyses, particle synthesis, and reaction engineering. To cite just one specific example, we note that the emerging technologies for single-molecule analysis of DNA in micron and nanometer scale devices (Andersen 1999; Chou, Austin et al. 2000; Lim, Dimalanta et al. 2001; Tegenfeldt, Prinz et al. 2004) have fueled substantial interest in the structure and dynamics of confined solutions of DNA (Chopra and Larson 2002; Jendrejack, Schwartz et al. 2004).

Experimental tools, such as the surface forces apparatus and light scattering dichroism (Fry, Langhorst et al. 2006), permit to investigating the confinement effects from the submicron scale down to the nano scale. Indeed the refinements in fabrication technology allow the construction of nano-fluidic devices with dimensions in the sub-100-nm regime.

The diffusion of particles near a surface boundary is determined experimentally by optical microscopy (Banerjee and Kihm 2005; Carbajal-Tinoco, Lopez-Fernandez et al. 2007), total internal reflection microscopy (Bevan and Prieve 2000; Huang and Breuer 2007) and evanescent wave dynamic light scattering (EWDLS) (Holmqvist, Dhont et al. 2006; Holmqvist, Dhont et al. 2007).

There is a certain amount of research work which has investigated the dynamics of dilute colloidal particles suspended in a flowing solution at different scales, using analytical theory and especially numerical simulations. It has been shown that the dynamics of suspended rigid molecular rod-like particles can differ remarkably in a confined domain from that in the unbounded solution (Hijazi and Khater 2001; Khater, Hijazi et al. 2003) owing to the stochastic dynamic collisions of the particles at the confining solid surface boundaries.

More recent numerical simulations and theoretical analysis confirm that rigid polymers and Brownian rods within strong shearing flows migrate away from bounding walls due to hydrodynamic interactions (Sintillan, Shaqfeh et al. 2006; Park, Bricker et al. 2007). This result is consistent with experiments on semi-rigid xanthan molecules in pressure-driven flow, which indicate the migration away from a wall (Ausserré, Edwards et al. 1991), and give

evidence for the depletion layers in flowing solutions. Models for rigid polymers have focused on steric exclusion with the walls (De Pablo, Öttinger et al. 1992; Schiek and Shaqfeh 1995). While neglecting surface boundary hydrodynamic interactions, these studies were reasonably successful at explaining experimental observations, including the thickening of the depletion in strong flows, which may be a result of more frequent collisions with the boundaries, owing to an increased rate of molecular tumbling. Further, previous research work has mostly considered the surface boundaries to be ideally smooth.

Previous research work has mostly considered the boundary surfaces to be ideally smooth. In the present work these boundary surfaces will be considered as rough at an appropriate scale commensurable with the dimensions of the pores. In particular a Gaussian profile of heights is considered, in any given direction in the 2D solid surface, without loss of generality since the simulation algorithm can be applied for other profiles. The dynamic effects due to the stochastic Brownian and causal hydrodynamic forces acting on the particles, as well as those due to the diffusive *mechanical* collisions of the particles with the solid boundary rough Gaussian surface are integrated in the simulations. An algorithm is developed for this purpose based on the Boeder Differential equation (Boeder 1932) for the dynamics of macromolecular rod like particles in bulk fluids, and on the mechanism of the restitution of the particles from the diffusive collisions at the solid boundaries.

The present Chapter is focused on the study of the equilibrium dynamics of dilute colloidal suspensions of rod-like molecular particles flowing inside mesopores, and the extent to which the diffusive collisions on the rough surface boundaries of the pores may be important to their equilibrium dynamics. In the present work we consider hence explicitly the hydrodynamic and Brownian interactions at rough surface boundaries, where the roughness at any appropriate scale is commensurable with the dimensions of the pores. We calculate hence the probability distribution functions (PDF) for the positions of the centres of mass and orientations of these particles in flowing solutions inside mesopore channels throughout the space of the solution from the confining rough boundaries to the bulk limit. We also determine the nematic order parameter for the colloidal suspensions in this space over several orders of magnitude of the Peclet number which characterizes the hydrodynamic conditions.

Since there are no analytical methods available to calculate the PDF functions for the pores due to the difficulty of modelling of the diffusive collisions at the solid boundaries, it is necessary to develop other means for this problem. Our approach is to create appropriate numerical simulations under the conditions of laminar flow. To fix the range of physical dimensions, the pore systems are considered to have diameters in the range of 10^1 to 10^3 nm, but the simulations are otherwise quite general.

The two forces which act on the particles inside the pore system are the hydrodynamic force stemming from shear flow, and another of thermodynamic origin giving rise to Brownian motion. The dynamic effects due to the stochastic Brownian and the hydrodynamic forces, and due to the collisions of the particles at the solid surface boundaries, are modelled by appropriate simulation algorithms. These are developed in the present work in a 2D Cartesian reference, based on the Boeder equation (Boeder 1932) for the dynamics of rod-like particles in fluids, and on the restitution mechanism for the diffusive collisions of the particles at the solid boundaries. In particular a Gaussian distribution of terrace heights with reference to an atomically flat surface is considered for the solid 1D boundary without any loss of generality since the simulation algorithm can be applied for other roughness profiles.

This chapter is focused on the determination of the probability distributions for the positions and the orientations of macromolecular rod-like particles inside mesopores channels in flowing fluid solutions with rough surface boundaries, the two forces that acts on the macromolecular rod like particles inside the pores systems are the hydrodynamic force stemming from shear flow and the other thermal originating from Brownian rotational diffusion.

This Chapter is as follows in section 2.2; we present a general introduction to the problem and to the dynamics of molecular rod-like particles in colloidal suspensions liquid bulk molecular under Brownian and hydrodynamic motion. Section 2.3 presents the developed algorithm for diffusive collisions at rough surface boundaries of pores. 2.4 presents simulation results for the spatial and orientation distributions under a variety of hydrodynamic and Brownian conditions, and particularly for low and high hydrodynamic flow conditions in the confining channel while in section.2.5 presents the simulation results in the open channel. The Nematic order calculation presented in Section 2.6. The conclusions are presented in section 2.7.

2.2 Colloidal particle model dynamics in bulk liquids

The dynamics and orientations of colloidal macromolecular particles in suspension in dilute concentrations in the bulk of a flowing liquid are determined by two competing forces, the first stemming from hydrodynamic shear, and the second, of thermal origin, from Brownian diffusion. (Boeder 1932) is the first to have studied this problem from the theoretical point of view, for rod-like macromolecular particles. Boeder derived initially, without the use of formalisms such as the Langevin equation and the Fokker-Planck equation, (Bird, Curtiss et al. 1987; Gardiner 1990; De Pablo, Öttinger et al. 1992), an ordinary differential equation that governs the probability distribution $P = P(\theta)$ of finding a particle in a two dimensional (2D) flow with an orientation θ with respect to the direction of the flow

$$\frac{d^2}{d\theta^2} P + \frac{d}{d\theta} [\alpha \sin^2(\theta) P] = 0 \qquad (1)$$

The Peclet number α for the flow in Eq.1 is a dimensionless ratio that characterises the relative strengths of hydrodynamic and Brownian effects

$$\alpha = \gamma'/D_{\text{rot}} \qquad (2)$$

γ' is the flow shear rate, $\gamma' = \partial v_x / \partial y$, where the velocity v_x along the x axis may vary in value along the y axis. The shear rate is hence a measure of the velocity profile perpendicular to the flow direction, and it is constant for a laminar flow as in Fig II.1. The rotational Brownian diffusion coefficient for the rod, D_{rot}, is sufficient to describe the equilibrium dynamics in the bulk solution far from solid boundary surfaces. Throughout this study α is considered to be outside the turbulence regime. The positive and negative angles correspond respectively to backward and forward orientations.
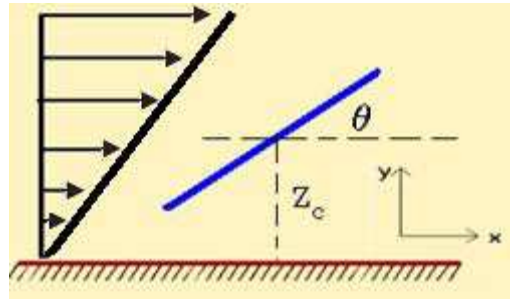
Fig II.1 Schematic representation of the linear or Couette laminar hydrodynamic flow, that shows the shear flow and a rod-like particle of length L of orientation θ with respect to the flow direction.

The shear rate of the hydrodynamic flow, organized in an experiment, provides consequently a rotational couple acting about the center of mass of the rod-like particle. In contrast the Brownian diffusion is thermodynamic and is uncontrolled mechanically. D_{rot} has been calculated, (Broersma 1960a; Broersma 1960b), and may be expressed by the relation.

$$D_{\text{rot}} = \frac{3k_B T}{\pi \eta L^3} [\ln(L/d) - 0.8]. \qquad (3)$$

k_B is the Boltzmann constant, T the temperature of the system, L and d are respectively the length and diameter of the macromolecule, $L \gg d$, and η is the viscosity of the flowing liquid. Different colloidal particles in their solvents have hence quite different D_{rot} as a function of their size and of the temperature, (Tanford 1961; Berne and Pecora 1976). For *dilute solutions*, for which

$$n \, d \, L^2 << 1 \qquad n \, L^3 < 1 \qquad\qquad\qquad (4)$$

n being the particle density, the assumption of non-interacting particles is quite valid.

As has been pointed out, (Boeder 1932) a solution in closed form cannot be obtained for Eq.1 Boeder gave a series of solutions valid for only small values of α. Some improvements have also been made to remove restrictions on the cross-sectional areas of such macromolecules, and to be able to consider their rotational diffusion in three dimensions, (Peterlin 1938; Doi and Edwards 1986), where these efforts have been associated to small values α.

The analytical solutions for the Boeder differential equation in the bulk has been obtained recently for a wide range of α, (Khater, Tannous et al. 2000). In this work special analytical as well as numerical methods are developed in order to calculate accurately the PDF P(θ) distributions in the bulk liquid for arbitrary values of the Peclet flow α.

It is difficult, however, to extend this analytical approach to calculate the PDF distributions in the neighbourhood of solid boundaries and inside pores owing to the difficulty to account analytically for the contributions of the stochastic diffusive collisions of the particles at the boundaries. The consequent approach has hence been to develop appropriate numerical simulations for the neighbourhood of solid boundary surfaces which are adapted from those in the bulk. The simulations are tested to be in agreement with the analytical solutions of the Boeder differential equation, (Hijazi and Khater 2001) for arbitrary values of the rotational Peclet numbers α. This is a necessary requirement for the numerical simulations in the neighbourhood of solid boundary surfaces, as in Fig II.2.
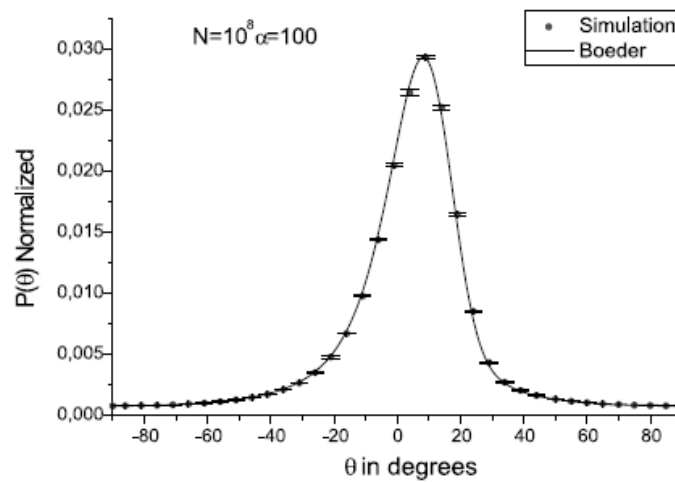

Fig II.2 Calculated PDF orientation distributions for macromolecular rod-like particles in a hydrodynamic flow, for a high Peclet flow α=100. The solution of the Boeder differential equation (continuous curve) is compared to the Monte Carlo simulation (black dots with error bars), for the same α, after (Khater, Tannous et al. 2000).

The numerical simulations for the PDF distributions which we construct in the present work for the equilibrium dynamics are determined by the Brownian and hydrodynamic forces at all points in the space of the pores, and by additional dynamics due to the stochastic diffusive collisions at and in the neighbourhood of the solid surface boundary. The calculated PDF distribution in equilibrium dynamics determines the statistical probability that a particle is in an accessible state, for all possible accessible states. The PDF distributions are presented systematically as normalized with respect to unity. The particles are considered to be in dilute colloidal suspensions, and we neglect particle–particle interactions.

In the simulations using the Boeder equations, the hydrodynamic force tends to align the macromolecular rod-like particles in the direction of the shear flow with an average angular speed ω. This is first given by (Boeder 1932) as

$$\omega = \gamma' sin^2(\theta) \tag{5}$$

θ is taken as positive or negative in the trigonometric sense, where θ = 0, parallel to the flow direction which is parallel to the boundary walls as in Fig II.1. To simulate the hydrodynamic effects in a time interval Δt between two successive simulation events, labelled s and s +1, we compute $\Delta\theta_{hyd}$ (s +1; s), the hydrodynamic rotation about the centre of mass of the particles, using the following algorithm

$$\Delta\theta_{hyd}(s + 1; s) = \theta(t_{s+1}) - \theta(t_s) = \gamma' sin^2(\theta)\Delta t \tag{6}$$

For linear laminar hydrodynamic flow, this rotation $\Delta\theta_{hyd}$ is effectively a negative increment since the rods always follow the direction of the hydrodynamic flow.

In contrast the Brownian dynamical effects create a diffusive rotational motion of the particles. The selection of random $\Delta\theta_{rot}$ simulation events is done to avoid cumulative errors in time, encountered in the algorithm of reference, (Press, Teukolsky et al. 1992). In this procedure the simulation time interval Δt is related to an effective variable for the Brownian rotation diffusion by the following equation

$$\Delta\theta_{rot}^2 = 2D_{rot}\,\Delta t \tag{7}$$

The random variable $\Delta\theta_{rot}(s$ +1; s) can then be simplified in the algorithm to

$$\Delta\theta_{rot}(s+1;s) = \pm\Delta\theta_{rot} \qquad (8)$$

The rotations $-\Delta\theta_{rot}$ and $+\Delta\theta_{rot}$ are respectively clockwise and anticlockwise, and conform to the required symmetry. Other symmetric generating random functions may be used but we find that the square function is quite adequate.

The simulation time interval Δt may be eliminated from the algorithm, with Eq.6 and 7 to yield the random variable $\Delta\theta_{hyd}$ towards the hydrodynamic algorithm

$$\Delta\theta_{hyd} = \alpha\sin(\theta)\left[\Delta\theta_{rot}^2 \big/ 2\right] \qquad (9)$$

In a numerical simulation the choice of a value for $\Delta\theta_{rot}$ is dictated by technical criteria that aim to establish efficient simulation runs and negligible scatter. This choice determines effectively a simulation time interval Δt which is inversely proportional to the diffusion coefficient from Eq.7. For the purpose of the present simulations, we typically take $\Delta\theta_{rot} \sim$ 0.003 radians for a wide range of the Peclet number α. This value for $\Delta\theta_{rot}$ may however be varied for different experimental conditions and different Peclet numbers.

2.3 Simulation algorithms for pore channels

In this section, the simulation algorithms are constructed to yield the joint distributions PDF, $P(\theta, \zeta)$, as a function of θ and of the normalised distance $\zeta = z_c / L$, where z_c defined as the real space distance of the centre of mass of the macromolecular rod like particles from a given boundary surface, (Hijazi and Khater 2001). It is expected that the distributions $P(\theta, \zeta)$, vary inside a depletion solution layer near the solid surface boundary distinctively from their behaviour in the bulk of the solution. This is due to the importance of diffusive collisions of the extremities of the macromolecular particles at the surface boundaries for the equilibrium dynamics of the system of the non interacting macromolecular particles.

The simulations are quite general for pores and rod-like particles provided the prepared algorithms are valid under the selected physical conditions. Typically, we consider the size of pore channels to be in the range of $\sim$ 10 nm to $\sim$ 1000 nm. The word pores is used often to characterize pores of diameters of $\sim$ 10 nm to $\sim$ 100 nm. The choice of given species of colloidal particles in liquids flowing inside a given pore channel, dictates the nature of the problem and whether there is confinement or not.

2.3.1 Simulations algorithm for particle dynamics at a solid surface boundary

The detailed nature of a diffusive collisions between the extremity of a macromolecular particle and real uneven solid surfaces at the atomic scale, is quite complex and varies with the topography of the surface (Khater 1989), and also with the nature of the macromolecular particles. To develop the appropriate simulation algorithm at the solid boundary we introduce a simplifying working assumption based on two coefficients of nano-mechanical restitution, *e* and *é*. These denote the restitution of the macromolecules away from the solid surface due to a diffusive collision, for respectively the Brownian and hydrodynamic collisions.

If the translation diffusive motion is neglected in the bulk owing to translation invariance, this is not the case near a solid surface. The mechanism for molecular dynamics restitution owing to Brownian translation collisions at a solid surface is now schematically presented following (Hijazi and Khater 2001), in Fig II.3. Two limiting situations are considered. Let N denote the event just before collision, and N+1 the event after collision. Note furthermore that E_L and E_R denote the two classically identifiable extremities of the rod-like particles. The upper array in Fig II.3 details one of the limiting situations, namely that when a rod-like particle touches the surface after N and stays in this touching configuration for N+1, until the next simulation event. This upper array corresponds to $e = 0$ for the algorithm Brownian restitution coefficient. The lower array, in contrast, details the second limiting situation, namely that when a particle touches the surface after the N event due to a Brownian translation, and comes back to its initial configuration for N+1, then awaits the next simulation event. This lower array corresponds to $e = 1$ for the algorithm Brownian restitution coefficient.
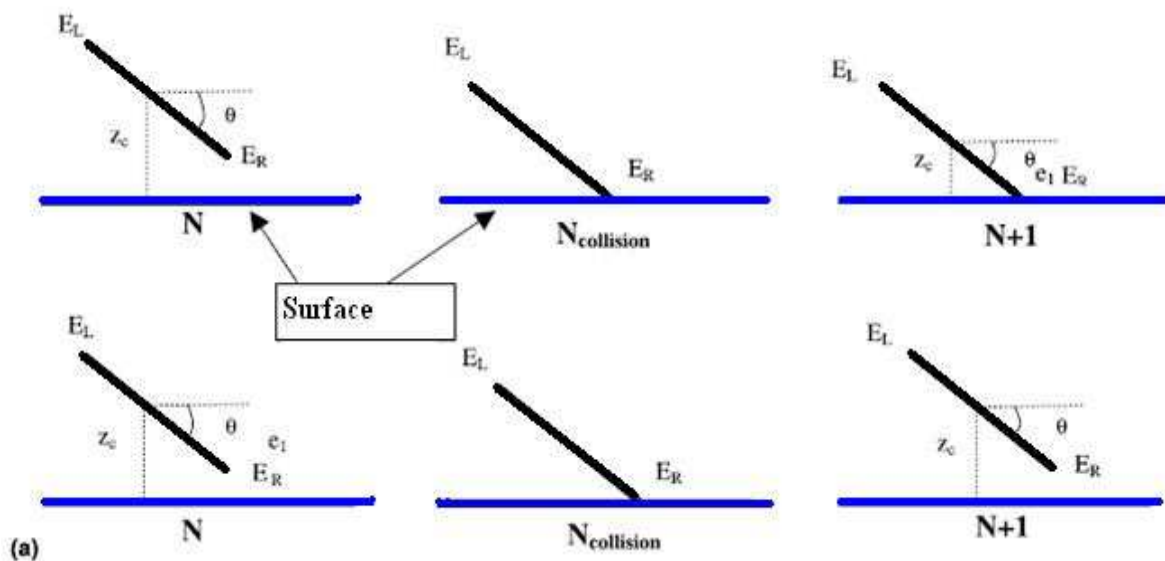

Fig II.3 Schematic representation of the restitution mechanism for a rod like particle – surface collision due to Brownian translations near a solid surface

The component of the algorithm for Brownian rotation may also be given for this restitution near the surface. Since Brownian movements whether of a translation or rotational nature are intrinsically similar, we use the same coefficient, e, to construct the algorithms for both cases. The uniform distribution interval $e \in [0,1]$ accounts consequently in this description for all possible outcomes following a Brownian collision, for all surfaces and macromolecules.

The nano-mechanical restitution is also exploited to describe the algorithm for the molecular dynamics of collisions caused by the hydrodynamic flow near a solid surface. This type of collision is characterized in terms of a different restitution coefficient, $\acute{e}$.

The mechanism for this restitution in the neighbourhood of the surface is schematically presented in Fig II.4. As previously, two limiting situations are considered for the collision of the extremity of the rod-like particle with a solid surface under hydrodynamic flow. The upper array in Fig II.4 details one of the limiting situations, namely that when a macromolecular particle touches the surface after the N event, it slides and stays in this sliding configuration for N+1, until the next event. This upper array corresponds to a value of $\acute{e} = 0$.
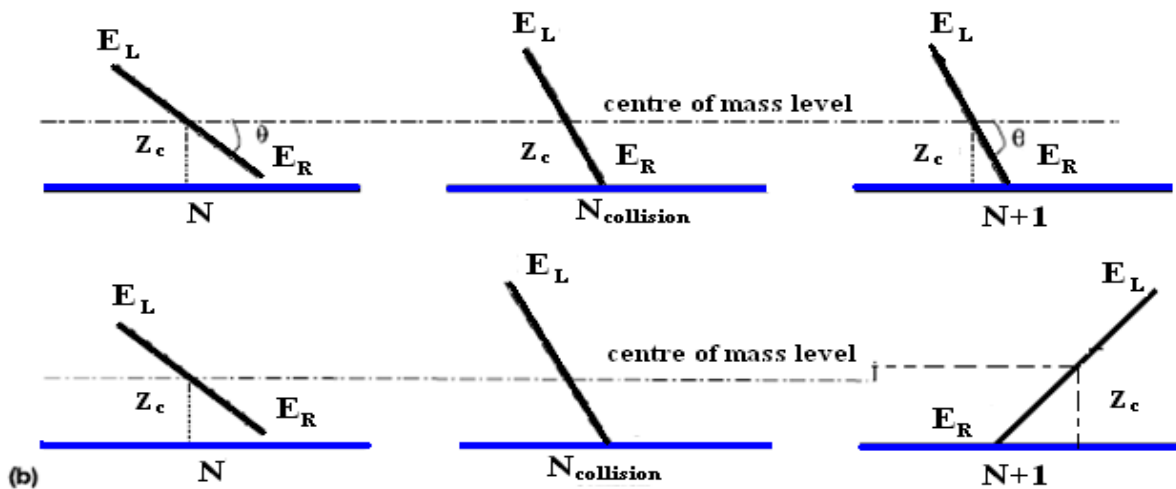
Fig II.4 Schematic representation of the restitution mechanism for a macromolecule–surface collision due to hydrodynamic rotations near a solid surface

The lower array details the other limiting situation namely that when a particle touches the surface after N, at any approach angle, and turns in the flow about its pivot extremity at the surface. The lower array in Fig II.4 corresponds hence to $\acute{e} = 1$ for hydrodynamic restitution. In theory the rotation should take the rod-like particle into $\pi/2$ until the N+1 event, and then awaits the next simulation event. However, recent optical experiments that access the hydrodynamic collisions of microscopic rod like particles, (Hijazi, Ben Yahia et al. 2003), show that a rod-like particles may rotate about their pivot beyond this to a total angle of $3\pi/4$.

We shall hence use this experimentally observed value systematically in this work. The uniform distribution interval $\acute{e} \in [0,1]$ in this model accounts consequently for all possible outcomes following a hydrodynamic collision, for all surfaces and macromolecules.

2.3.2 Box-Muller method to generate the algorithm for Gaussian rough surfaces

In the present work we are concerned with confined pore channels with rough boundary surfaces at an appropriate scale with respect to the size of the colloidal particles. The flow is considered in a 2D reference framework in real space, spanned by the *xy*-plane as in Fig II.5.

In this section an algorithm to simulate rough boundary surfaces is developed which is general, which leads to the algorithm for an atomically flat surface as a limiting case. The uneven solid surfaces may be classified into different types, depending on the scale and type of surface Chapter 1. We shall, however, in this work select a Gaussian rough surface as an appropriate approximation for many solid surfaces. This does not limit the generality of the numerical simulations which indeed may be carried out for any solid surface profile.

A Gaussian representation for the topography of a rough surface may be defined with reference to the Gaussian function, with two parameters, the average height of the terraces that statistically make up the roughness at a given scale, and their variance. For an isotropic Gaussian surface, these parameters are considered as *statistically* the same along any direction in the plane of the solid surface.
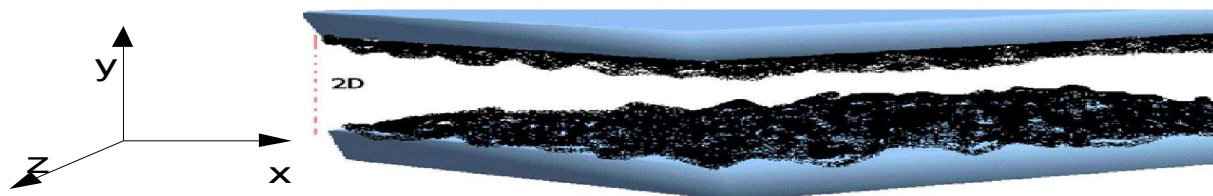
Fig II.5 Confining pore channel presenting a Gaussian rough boundary surfaces. 2*D* is the maximum available distance between the two uneven surfaces.

Generating normal random numbers is an old and important problem for statistical analysis. Several algorithms are available to generate normal random numbers (Box and Muller 1958), (Marsaglia and Bray 1964), (Neumann 1951), and others. The book of (Johnson, Kotz et al. 1995) provides an extensive list of references for the different algorithms available today.

Among the several available methods, the most popular is the Box-Muller transformation method with the improvement suggested by (Marsaglia and Bray 1964).

Fig II.6 Schematic representation of a cross sectional cut for a rough surface with a statistical distribution for terrace heights.

At the first step we indicate the following well known relation

$$\int_{-\infty}^{\infty} e^{-\frac{x^2}{2}} dx = \sqrt{2\pi} \tag{10}$$

It is easy hence to show that

$$1 = \frac{1}{2\pi} \int_{-\infty}^{\infty} e^{-\frac{x^2+y^2}{2}} dx\, dy \tag{11}$$

In the case that x is distributed on probability measure (or mass probability) $p(x) = \frac{1}{\sqrt{2\pi}} e^{-\frac{x^2}{2}}$, stochastic variable is called Gaussian random variable. The Box-Muller method may be resumed as follows. Providing with the law of large numbers or centre limit theorem, the Gaussian random variable has played an important role and one may make useful hypothesis and test data science. We define a new function as

$$U(R) = \frac{1}{2\pi} \int_{x^2+y^2 \leq R^2} e^{-\frac{x^2+y^2}{2}} dx\, dy \tag{12}$$

This integral interval is in $x^2 + y^2 \leq R^2$. We calculate then

$$U(R) = \frac{1}{2\pi} \int_0^{2\pi} d\theta \int_0^R dr\, r\, e^{-\frac{r^2}{2}},$$

Such that

$$U(R) = 1 - e^{-\frac{R^2}{2}} \tag{13}$$

$U(R)$ is a non-decreasing function which satisfies the following conditions

$$\lim_{R \to 0} U(R) = 0$$
$$\lim_{R \to \infty} U(R) = 1 \tag{14}$$

Moreover, by Eq.13 the integral interval is replaced using $0 \leq r \leq R$ and sine cosine equations. Using $p \in [0, 1]$ and Eq.(12), the variable R of $U(R) = p$ is determined as

$$U(R) = p \rightarrow R = \sqrt{-2\log(1 - p)} \tag{15}$$

In setting $s = 1 - p \in [0, 1]$ and $t \in [0, 1]$, one obtains

$$x = \begin{cases} \sqrt{-2\log(s)} \cos(2\pi t) \\ \sqrt{-2\log(s)} \sin(2\pi t) \end{cases} \tag{16}$$

This analysis yields hence the scheme to generate a Gaussian random variable distributed on $N(0,1)$ using the uniform distribution on $[0, 1]$. This Box-Muller method, furthermore, may be generalized to a stochastic variable $z \sim N(\mu, \sigma^2)$, with the mean μ and the variance σ^2, as either of

$$z = \mu + \sigma\sqrt{-2\log(s)} \cos(2\pi t)$$
$$z = \mu + \sigma\sqrt{-2\log(s)} \sin(2\pi t) \tag{17}$$

2.3.3 Simulation algorithm for particle boundary collisions in pore channels

Our algorithm contains components that simulate the hydrodynamic and Brownian movements in the bulk when the ends of the macromolecular rod like particles do not come into contact with the solid boundaries. The algorithm chooses randomly between hydrodynamic and Brownian events.

It is necessary, however, in this novel situation to develop the algorithm to account for the molecular dynamics of the diffusive collisions when they occur on the two uneven boundary surfaces, as shown schematically in Fig II.7, and to test the sequence of collisions, and their consequences, that follow. Throughout this work the coefficients of the restitution, e and $é$, are randomly chosen over the uniform distribution interval $[0, 1]$, which procedure accounts for all possible mechanical restitutions during the collisions at solid boundaries, due to Brownian rotation and translation, and to hydrodynamics.

It is possible to distinguish different types of possible boundary surface collisions, named henceforth A_i, B_i and C_i, where $i = 1, 2$ correspond, respectively, to the upper and lower uneven solid surface boundaries (with respect to the channel centre Fig II.7). The following cases need to be distinguished to account for all possible events in the modified algorithm.
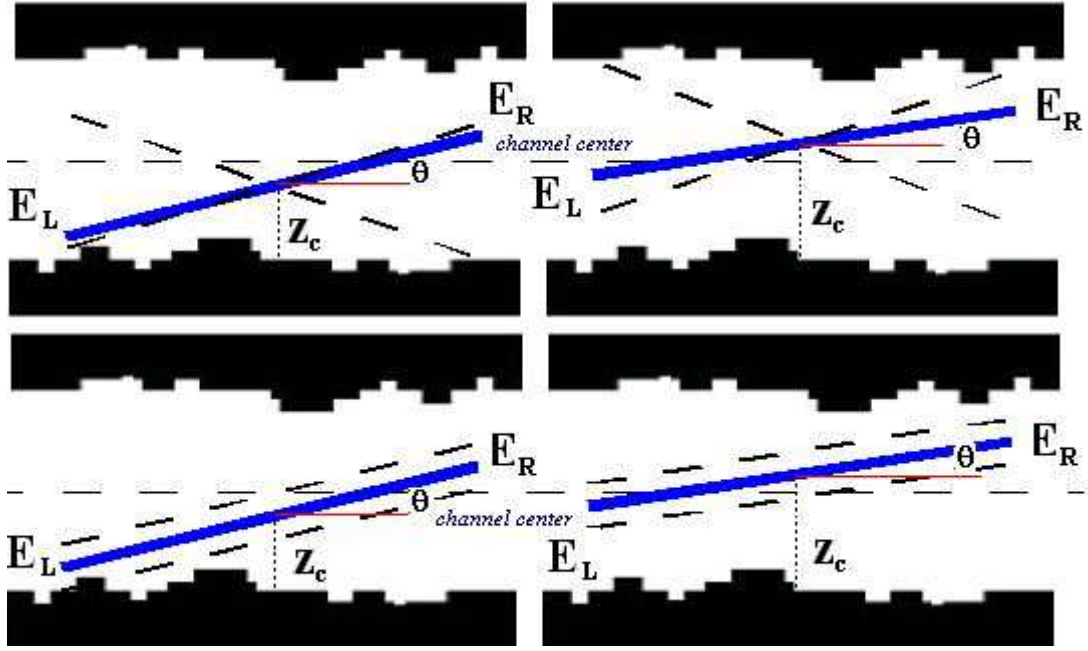
Fig II.7 Schematic representation for a rod-like particle-surface collision on the upper and lower boundary surfaces of a pore channel, due, respectively to hydrodynamic (first row) and Brownian dynamics (second row).

The A1 case corresponds to the situation when the collision is due to hydrodynamic rotation, where $z_c > D$ in the upper half at the event N. The rod-like macromolecular particle in this situation turns about a contact point in the upper boundary surface with a anticlockwise rotation. The algorithm parameters at N+1, after collision, may vary between $z_c(N)$ and z_{max} for the position, and between the contact angle collision and θ_{max} for the orientation. The values z_{max} and θ_{max} correspond to complete contact of the extremities of the rod-like macromolecule with the lower and upper surface boundaries. We introduce in general the term **bgauss(0;1)** which corresponds to a random number generator that has the specific role of modelling appropriately the different accessible terrace heights of the uneven solid boundary surface. The letter **b** corresponds in this case to the maximum height on the scale of the system, encountered in the collisions of the rod-like particles with the surface. We may then write that

$$z_c(N+1) = z_c + \acute{e} \ (z_{max} - z_c)$$
$$\theta(N+1) = \text{Arcsin} \ (2z_c/L) \qquad\qquad (18)$$

The A2 case corresponds to when the collision is due to hydrodynamic rotation for $z_c < D$ in the lower half at the event N. So in this case when we have a hydrodynamic diffusion event brings one of the ends of the rod into collision with the uneven surface. In this case the

algorithm collision is identical to that of $\mathbf{A_1}$ except that the rotation takes place here about a contact point on the lower boundary surface.

The $\mathbf{B_1}$ case corresponds to when the collision is due to Brownian rotation for $z_c > D$ in the upper half at the event N. It follows that in the simple geometrical form we may write the following formulas:

$$\theta_{collision} = |Arcsin\ (2z_c(N) - bgauss(0;1))/L|$$
$$\theta(N+1) = \theta_{collision} + e\ |\theta(N) - \theta_{collision}| \tag{19}$$
$$z_c(N+1) = z_c$$

In this situation the rod-like macromolecule takes up a configuration at N+1 identical to that encountered when colliding with a single boundary surface. For the limit value $e = 0$, the rod stays in contact with the uneven solid surfaces, whereas for the other limit value $e = 1$, the rod goes elastically back to its initial configuration. The orientation $\theta(N+1)$ after collision is calculated with respect to the upper surface boundary. During the Brownian rotation, z_c rests unchanged with respect to the upper and lower surface boundaries, whereas the limits of $\theta(N+1)$ vary between the contact angle θ collision (for $e = 0$) and $\theta(N)$ the orientation before collision (for $e = 1$).

The $\mathbf{B_2}$ case corresponds to when for $z_c < D$ in the lower half at the event N. In this case the algorithm collision is identical to that of $\mathbf{B_1}$ with a rotation that takes place about a contact point on the lower surface boundary.

The C1 case corresponds to when the collision is due to Brownian translation for $z_c > D$ in the upper half at the event N. Then the relation between z_c and $z_{c\ collision}$ of the form:

$$z_{c\ collision} = L/2\ |sin\theta(N)| + bgauss(0;1)$$
$$z_c(N+1) = z_{c\ collison} + e\ [z_c(N) - z_{c\ collision}] \tag{20}$$
$$\theta(N+1) = \theta(N)$$

In this situation the rod-like macromolecule takes up a configuration at N+1 identical to that encountered when the collision is due to Brownian rotation. During the Brownian translation the orientation remains unchanged, whereas the limits of the position after collision vary between $z_{c\ collision}$ (for $e = 0$), and $2D - z_c(N)$ directly (for $e = 1$).

The C2 case corresponds to when the collision is due to Brownian translation for $z_c < D$ in the lower half at the event N. In this case the algorithm collision is identical to that of **C1** except that the translation takes place now about a contact point on the lower surface boundary.

Note that the base reference plane for all uneven surfaces is that for which **b** is equal to zero. The algorithm for the uneven surface presented above yields the *flat surface* algorithm by taking **b** to the limit of zero for all simulation events.

2.3.4 Simulation algorithm for the Poiseuille flow conditions in confining pore channels

The linear or Couette flow is the name given to laminar steady flow between two parallel plates where the bottom plate is stationary, and the top one is moving relative to the other. In contrast the flow between two parallel plates which are both stationary and separated by a fixed distance is called the Poiseuille flow. In this latter case the velocity profile is parabolic. The rotational Peclet number α, identified by (Boeder 1932), is defined in general for the laminar Couette flow. To prepare an algorithm for this reason we need to recalculate the Peclet number α, inside confined channel and under Poiseuille flow, in a way that; first we don't adjust the Boeder differential equation and secondly to keep the analytical work given by (Khater, Tannous et al. 2000) applicable.

The Peclet number α gives uniquely the ratio of the shear differential change for the hydrodynamic flow across the pore channel, in comparison with the Brownian rotational diffusion constant. Increasing α under otherwise constant thermal conditions, and hence constant D_{rot}, implies effectively increasing the flow.

Inside the pore channel of width 2D the flow profile is parabolic (Poiseuille Flow) Fig II.8, under the effect of this profile the rotational Peclet number depends on the positions of the extremities of the rod like particle namely E_L and E_R inside the pores, and we can distinguish three basic locations of the particles:
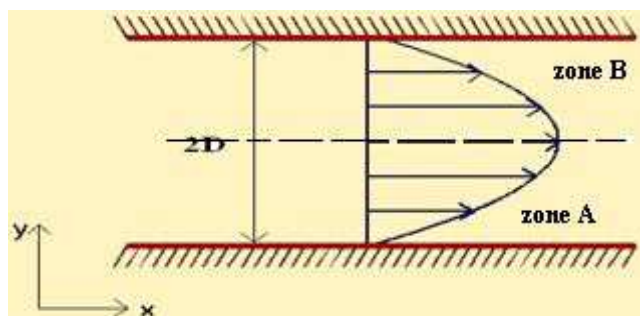
Fig II.8 Poiseuille flow.

1st case: The two extremities E$_L$ and E$_R$ of the macromolecular particle are located *below* the half line or median of the width of the confined channel in zone A as in Fig II.9a.

2nd case: The two extremities E$_L$ and E$_R$ of the macromolecular particle are located *above* the half line of the width of the confined channel in zone B as in Fig II.9b.
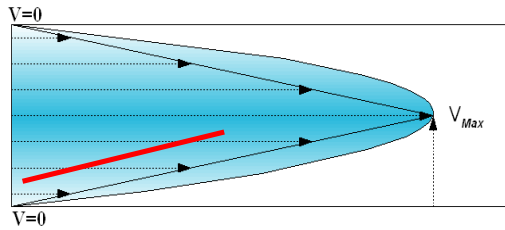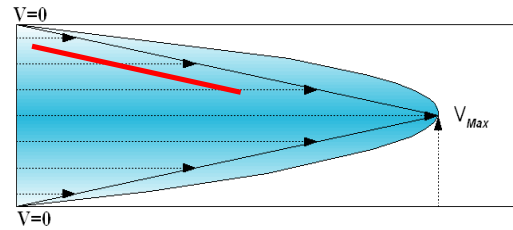
Fig II.9a   Fig II.9b

For both of the above two cases the rotational Peclet number α is that of the bulk flow.

3rd case: The extremities E$_L$ and E$_R$ of the macromolecular do not belong to the same zone as in Fig II.9c. In this case:

- if the particle extremity E$_L$ belongs to zone B, $D < y_{E_L} < 2D$, and hence

$$v_{E_L} = \gamma \cdot (2D - y_{E_L})$$

- the particle extremity E$_R$ belongs to zone A, $0 < y_{E_R} < D$, and hence

$$v_{E_R} = \gamma \cdot y_{E_R} \tag{21}$$
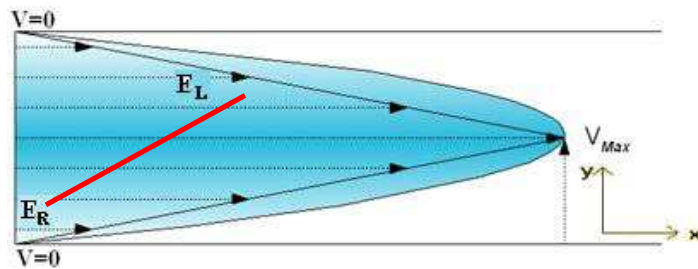
Fig II.9c

Then we calculate a ratio R$_\alpha$

$$R_\alpha = \frac{v_{E_L} - v_{E_R}}{y_{E_L} - y_{E_R}}$$

$$R_\alpha = \frac{v_{E_L} - v_{E_R}}{y_{E_L} - y_{E_R}} = \frac{\gamma \cdot (2D - y_{E_L}) - \gamma \cdot y_{E_R}}{y_{E_L} - y_{E_R}}$$

$$R_\alpha = \gamma \cdot \left[\frac{2D - (y_{E_L} + y_{E_R})}{y_{E_L} - y_{E_R}} \right]$$

$$y_{E_R} = z_c - \frac{L}{2}\sin(\theta)$$

$$y_{E_L} = z_c + \frac{L}{2}\sin(\theta)$$

Where z_c is distance of the centre of mass of the macromolecular rod-like particle from a surface boundary terrace reference level, and θ is its orientation with the flow direction. Therefore

$$R_\alpha = \gamma \cdot \left[\frac{2D - (z_c + \frac{L}{2}\sin(\theta) + z_c - \frac{L}{2}\sin(\theta))}{z_c + \frac{L}{2}\sin(\theta) - z_c + \frac{L}{2}\sin(\theta)} \right] = \gamma \cdot \left[\frac{2D - 2z_c}{L\sin(\theta)} \right] \qquad (22)$$

This yields an effective Peclet flow number α_{eff} for the purpose of the simulations for the pore channels under the third case

$$\alpha_{\text{eff}} = \frac{R_\alpha}{D_{\text{rot}}} = \alpha \left[\frac{2D - 2z_c}{L\sin(\theta)} \right] \qquad (23)$$

Throughout this work, we normalize the width of the pore channel as a function of the particle length L, such that $2D = n\,L$, where 2D is the width of the pore channel as in Fig II.5, and n is a given number.

Consider the surface profile roughness to be modelled in any direction by a statistical distribution $Q(h)$ of terrace heights with a given mean μ and variance σ^2. Also that the maximum terrace level height in the rough boundary is $h_{\text{max}} = 0.1L$ with reference to a base spatial line $h_{\text{min}} = 0$, for both the upper and lower surface boundaries of the pore channel. The average terrace level height is $h_{\text{max}} = 0.05L$. Other characteristic statistical parameters for the terrace height distributions may also be given as a function of the particle length. Throughout this work, we normalize the width of the pore channel as a function of the particle length L, such that $2D = n\,L$, where 2D is the width of the pore channel and n is a given number. The ideal atomically flat surface is retrieved in the numerical simulations by taking $h_{\text{max}} = 0$.

It is useful next to identify the different angles θ_{ij} that may occur when the rod-like particle extremities are in contact with characteristic terrace level heights, $h_{\text{above,i}}$ and $h_{\text{below,j}}$, or the inverse, on the rough upper and lower surface boundaries. We have in general

$$\theta_{ij} = \arcsin \frac{2D - (h_{above,\,i} + h_{below,\,j})}{L} \qquad (24)$$

The simulations follow the behaviour of the macromolecular particles over $N = 10^8$ events per simulation run, which we have found to represent a sufficient number of elementary dynamic events, in the bulk and at the boundaries, for all the Brownian, boundary diffusive, and causal hydrodynamic events, for a simulation run. Our numerical simulations are applied for a wide range of Peclet flow conditions, and for Gaussian rough surfaces characterized in general by b = 0.1L to satisfy the algorithm condition $b \ll L$. The simulation results describe in general the spatial, $P(\zeta)$, and orientation, $P(\theta)$, PDF distributions for respectively the positions of the centres of mass and orientations of the particles, under equilibrium dynamics engendered by bulk hydrodynamic and Brownian dynamics, and the boundary molecular dynamics.

2.4 Simulation results for confining pore channels

The aim in this section is to calculate the relevant spatial and orientation PDF distributions, $P(\zeta)$, and $P(\theta)$, for the dilute suspensions of macromolecular particles in flowing liquids inside pore channels whose widths satisfy the condition

$$2D < L$$

where the mesopore width 2D is smaller than the size L of the macromolecular particles.

Since we are ignorant of the detailed restitution dynamics at the boundaries we chose to investigate the simulation results for prefixed, and for randomly generated hydrodynamic and Brownian restitution coefficients, respectively $é$ and e. The objective is to determine whether the choice of such parameters is biased or not, and to elaborate definite criteria for their use.

2.4.1 PDF simulation results for pore channels for *prefixed* hydrodynamic and Brownian restitution coefficients *é* and *e*

Throughout this section the restitution coefficients e and $é$ are assigned prefixed values for the purpose of the numerical simulations, over the physical range of accessible restitution coefficients, $e \in [0,1]$ and $é \in [0,1]$. Only a selected number of figures are presented to illustrate the results from a much larger number of results.

As we shall see the spatial and orientation PDF distributions, $P(\zeta)$ and $P(\theta)$, for all systems, are symmetric about the median $\zeta_{med} = 0.4$ of the pore channels, which is physically expected.

In Fig II.10, we present the simulation results for the distributions P(ζ) and P(θ), as a function of the normalized positions of their centers of mass, $\zeta = z_c / L$, and their orientation angles θ with respect to the flow direction inside a pore channel of width 2D = 0.8L. These are for low hydrodynamic flow characterized by the Peclet number α = 1, for the Brownian e = 0.5, and hydrodynamic é = 0, 0.5, and 1.

Three spatial PDF distributions $P(\zeta)$ may be clearly distinguished for e = 0.5. The first is a very broad PDF when $e' = 0$, and the other two are extremely peaked for $e' \neq 0$. This illustrates the sensitivity of the PDF distributions to hydrodynamic restitution under the given simulation conditions. When sliding is predominant, $e' = 0$, a broad PDF distribution appears which indicates that the particles are allowed to pass through the channel. The results for non-zero é = 0.5 and 1, bring into perspective the activated role of hydrodynamic collisions, which increase markedly the likelihood of multiple collision scattering of the extremities of the colloidal rod-like particles at the rough surface boundaries, sampling randomly different terrace heights. The hydrodynamic pivoting of the extremities for $e' \neq 0$, give rise to PDF distributions $P(\zeta)$ which peak out, implying that the majority of rod-like particles are blocked with extremities touching the upper and lower surface boundaries, with their centers of mass situated at the median of the pore channel $\zeta_{med} = 0.4$.

Consider next the orientation PDF distributions P(θ) in Fig II.10. In particular the first case for $e' = 0$, corresponds to the complete absence of hydrodynamics effects. A very broad P(θ) PDF distribution appears in this case, centered with a slight maximum at $\theta = 0$. Since $e' = 0$ corresponds to sliding, the broad $P(\theta)$ distribution for this case implies that the rods are aligned mostly in the direction along the median $\zeta_{med} = 0.4$ of the pore channels, and may travel freely down the flow lines for Peclet α = 1. We shall show later in section 2.5 that this is an unlikely event even for this relatively low Peclet flow.
For $e' \neq 0$, the above broad distribution is modified strongly and narrowed down to mostly blocking effect which appear clearly in Fig II.10 for the orientation PDF distributions P(θ). For both é = 0.5 and é = 1 the strong spectral features at $\theta = \pm 44.4°$ correspond effectively to blocking in the clock and anti clock senses at arcsin(0.7) using Eq.(22) for the *average* terrace level heights 0.05 *L*. Note that 0.1 *L* is the *maximum* terrace level height for the Gaussian rough surface on both boundaries, whereas 0.8 *L* is the maximum available distance between the minima terrace heights on the opposing rough boundaries.

When pivoting of the particle extremities dominates for $e' \neq 0$, increasing é will increase the approach to blocking, and consequently the probability of blocked particles in the colloidal

suspension. The value of e = 1 corresponds to a maximum rotation measure of $2\pi/3$, as observed experimentally, (Hijazi, Ben Yahia et al. 2003). Note, however, that a part of the orientation PDF distributions P(θ), which correspond to a significant sub-ensemble of the colloidal macromolecules, indicates nevertheless a certain alignment of particles with the flow, for the relative low Peclet flow α = 1. This implies that these rod-like particles may still pass freely inside the pore channel, which outcome is confirmed by the corresponding spatial PDF distributions $P(\zeta)$, in Fig II.10.
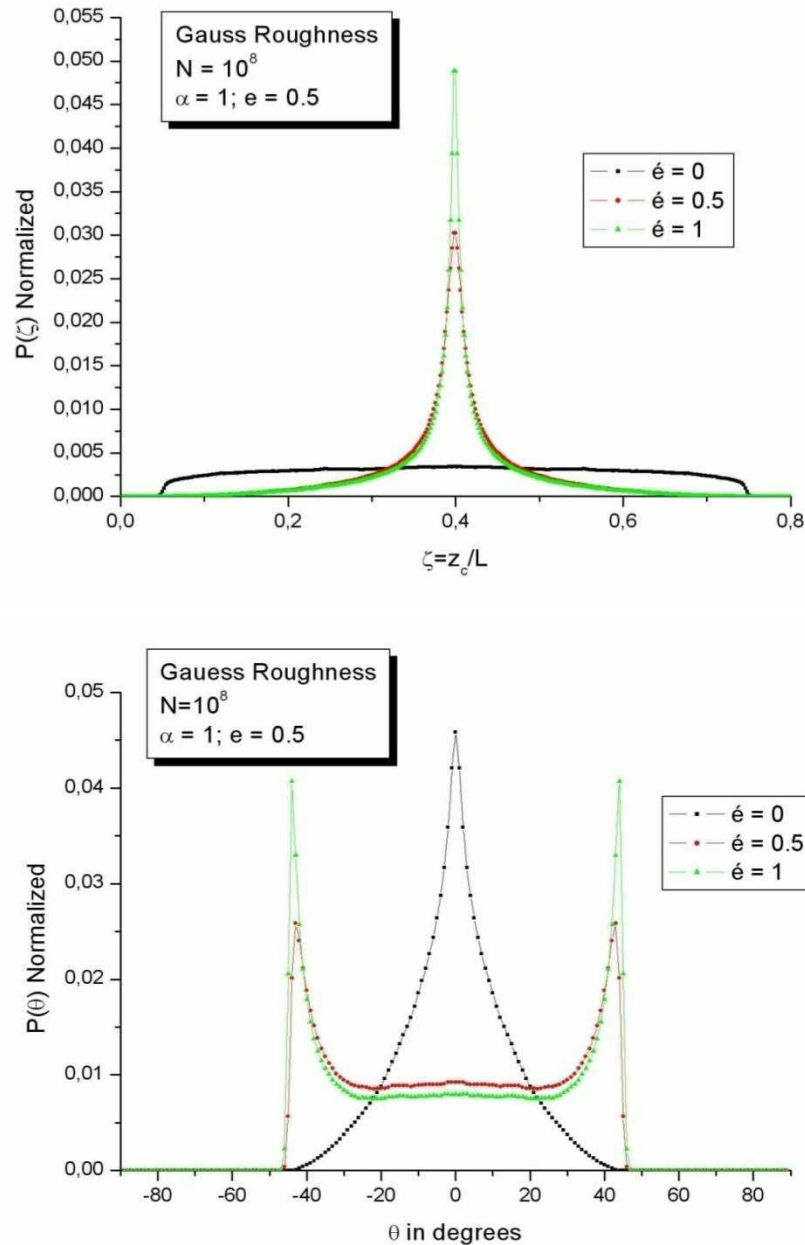
Fig II.10 Simulation results for the normalized spatial, P(ζ), and orientation, P(θ), PDF distributions inside a confining pore channel of width 2D = 0.8L, for low hydrodynamic Peclet flow α = 1, Brownian restitution e = 0.5, and for a range of hydrodynamic restitutions $\acute{e}$.

We have then made simulations for a large number of medium and high Peclet flow in comparison with those for the low Peclet number $\alpha = 1$. In Fig II.11, we present typical simulation results for the spatial, P(ζ), and orientation, P(θ), PDF distributions inside the pore channel of width 2D = 0.8L, for the hydrodynamic flow Peclet $\alpha = 100$. As may be seen by comparing Figs II.10 and II.11, the physical effects observed in Fig II.10 continue to be observed. However, they clearly show, (as other simulation results which are not presented here), that increasing α accentuates the spectral features of the PDF distributions.

In particular, the spatial PDF distributions P(ζ) increase and narrow progressively at $\theta = 0°$ with increasing Peclet flow for $e' \neq 0$. This is a signature of the increasing number of particle blocked with their centre of mass at the median $\zeta_{med} = 0.4$ of the pore channel. The orientation PDF distributions P(θ) confirm this tendency with the spectral features at $\theta = \pm 44.4°$ also increasing and narrowing with increasing Peclet flow for $e' \neq 0$. We conclude that the hydrodynamic flow forces the particles away from the solid boundary surface, with increasing Peclet flow α. This takes place in a configuration where the extremities are blocked at the opposing boundary surfaces and the centers of mass $\zeta = z_c / L$ are symmetrically at the median of the pores. In contrast the simulation results for the case é = 0 remains singular and quite different from all other results for $e' \neq 0$.

Fig II.11 Simulation results for the normalized spatial, P(ζ), and orientation, P(θ), PDF distributions inside a confining pore channel of width 2D = 0.8L, for high hydrodynamic Peclet flow $\alpha = 100$, Brownian restitution $e = 0.5$, and for a range of hydrodynamic restitutions é.

Prefixed e = é

The simulation results for the spatial and orientation PDF distributions, P(ζ) and P(θ), are presented next for a prefixed choice of $e = é = 0.5$, for very small hydrodynamic Peclet flow $\alpha = 0, 0.001,$ and 0.1, in Fig II.12, and for low to high Peclet flow $\alpha = 1, 10, 50, 100$, in Fig II.13, respectively. This deliberate average choice for e and $é$, and the wide choice for the

Peclet flow, are made to test the consequent simulation results in comparison with the previous simulation results in this section.

Fig II.12 Simulation results for the normalized spatial, P(ζ), and rotational, P(θ), PDF distributions inside a confining pore channel of width 2D = 0.8L, for very low Peclet hydrodynamic flow, respectively α = 0, 0.001, 0.1, and for Brownian and hydrodynamic restitutions $e = \acute{e} = 0.5$

For Peclet α = 0 the liquid solution is at rest and the hydrodynamic diffusive surface boundary collisions are absent. The dominant mechanism for the equilibrium dynamics is the Brownian effect in the bulk and at the solid boundary surfaces, which drives the colloidal particles to a broad and homogeneous spatial distribution as may be seen in Fig II.12. The simulation

results for the corresponding orientation PDF distribution, P(θ), which is symmetric, broad based, and centered about the direction of the flow $\theta = 0°$, confirms this. The rods are mostly aligned effectively in the direction of the flow.

Increasing the hydrodynamic flow conditions for example to Peclet $\alpha = 0.001$ and $\alpha = 0.1$, as in Fig II.12, brings into perspective the role of the now activated hydrodynamic diffusive collisions which increase the probability of the scattering for the particles' extremities. This effect exposes the particles' extremities to multiple collisions with the rough boundary surfaces sampling the different terrace heights. The symmetric spatial PDF distributions P(ζ) become increasingly peaked about the median $\zeta_{med} = 0.4$. It is interesting to note, nevertheless, the existence of the symmetric distribution tails for this P(ζ) up to the boundaries at $\zeta = 0$ and 0.8, which indicate significant probabilities of finding particles aligned with the pore channel boundaries at small orientations, their centers of mass lying physically in the neighborhood of the boundaries. This is confirmed by the corresponding PDF distribution P(θ), which is peaked at $\theta = 0°$, but which also presents tails up to the blocking angles at $\pm44.4°$ with distribution tails stretching out to higher angles. Note that the positive and negative angles correspond respectively to backward and forward orientations.

For Peclet flow $\alpha = 0.1$, we note the rise of the spectral features at the characteristic orientations $\theta \simeq \pm44°.4°$ which correspond to blocking angles for the selected pore channel width 2D = 0.8L. The transformation of the spectral features of the results for the orientation PDF distribution P(θ), from $\alpha = 0$ to $\alpha = 0.1$, is clearly illustrated by the inflexion of the spectral features of the intermediate P(θ) for $\alpha = 0.001$. In this latter case the simulation results are intermediate between those for Peclet $\alpha = 0$ and $\alpha = 0.1$, with growing intermediate spectral shoulders at $\theta \simeq \pm37.4°$ which do not correspond to blocking but to the accumulation of the probability distribution at these angles under equilibrium dynamics due to multiple scattering of the particles' extremities.

The simulation results for Peclet flow for increasing $\alpha = 1, 10, 50$, and 100, are presented in Fig II.13. It is clear that the characteristic spectral features of the spatial and orientation PDF distributions, $P(\zeta)$ and $P(\theta)$, are increasingly accentuated with increasing α. The heights of the $P(\zeta)$ distributions at the median $\zeta_{med} = 0.4$, and of the $P(\theta)$ distributions at the characteristic blocking angles, increase with increasing α. In contrast the $P(\theta)$ distributions for accessible orientations outside the blocking angles decrease significantly with increasing α; the laminar hydrodynamic flow at high Peclet α effectively evacuates the macromolecular particles from accessible states to those which correspond to blocking.
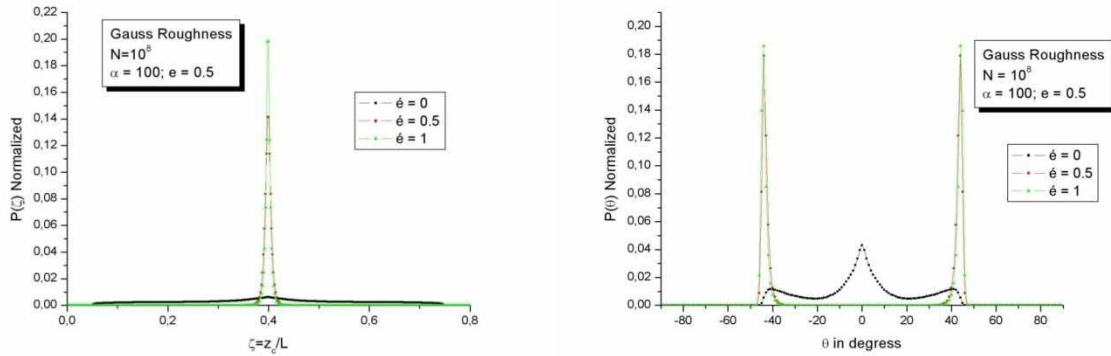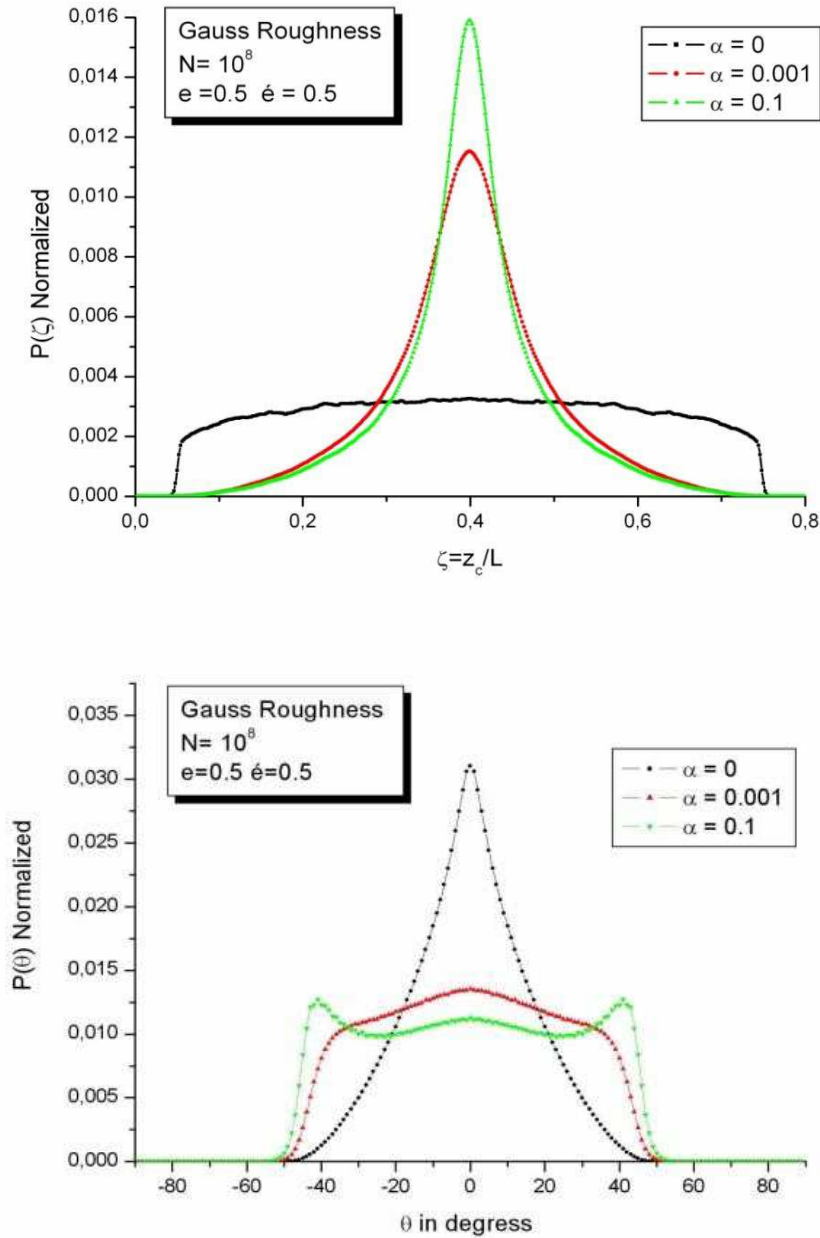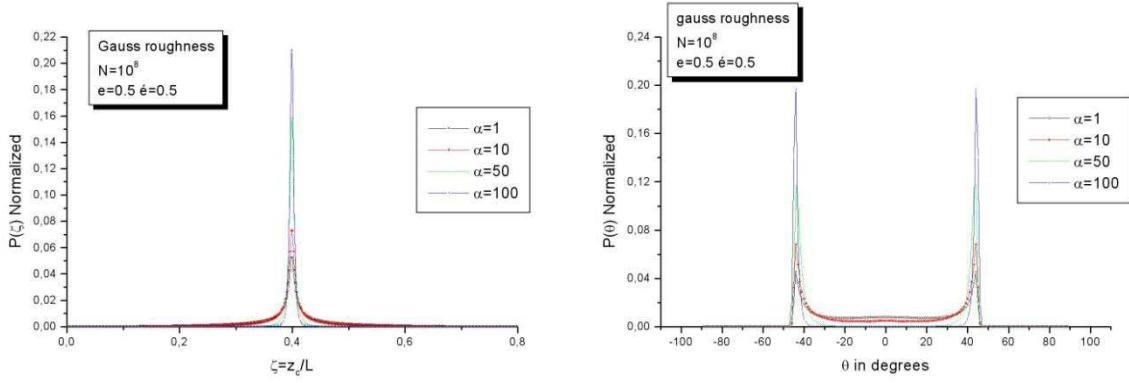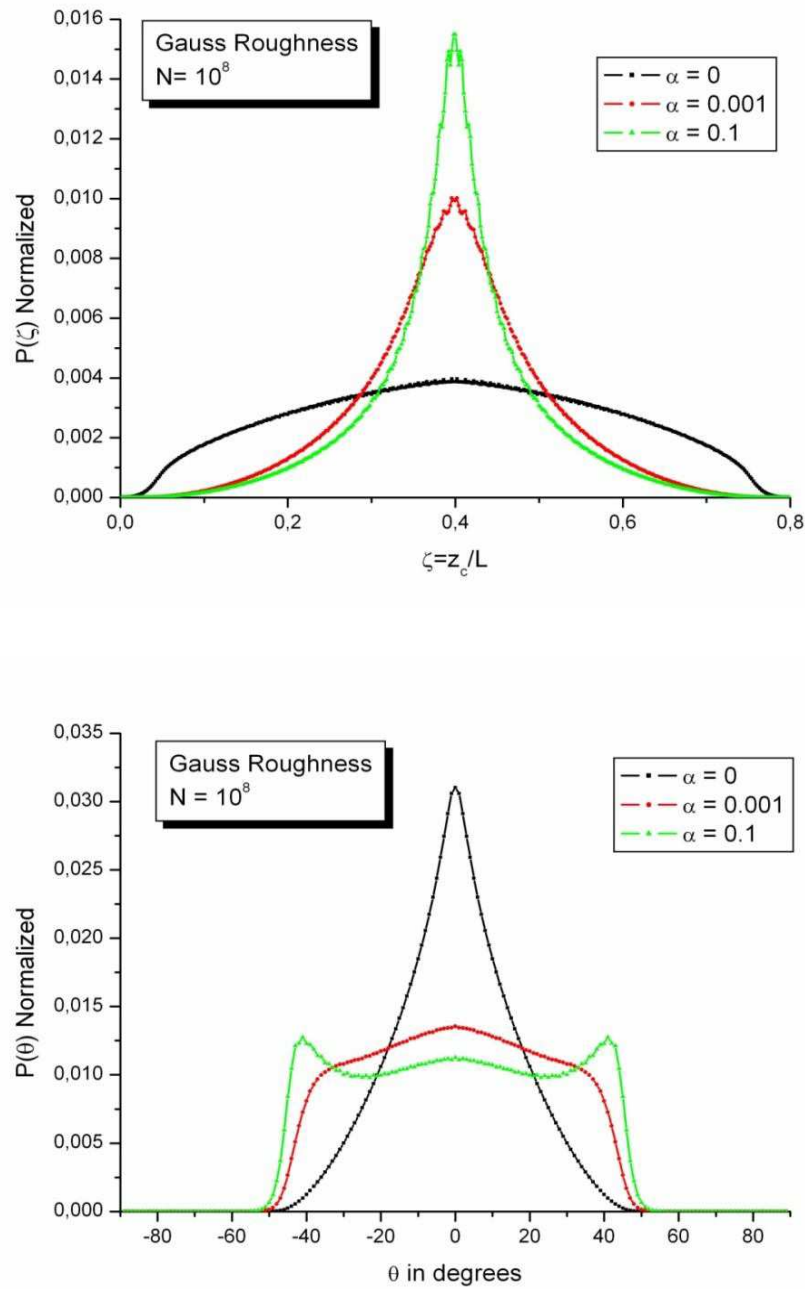
Fig II.13 Simulation results for the normalized spatial, P(ζ), and rotational, P(θ), PDF distributions inside a confining pore channel of width $2D = 0.8L$, for high Peclet hydrodynamic flow, $\alpha = 1$, 10, 50, and 100, and for Brownian and hydrodynamic restitutions $e = \acute{e} = 0.5$

2.4.2 PDF simulation results for pore channels for *randomly generated* hydrodynamic and Brownian restitution coefficients *e* and *é*

In this section the numerical simulations are carried out by treating the hydrodynamic and Brownian restitution coefficients, *e* and *é*, as random variables on the complete uniform distribution [0, 1], to model the molecular dynamics of colloidal particles at the solid boundary surfaces. This choice is justified by the disordered topography of a rough surface which renders unrealistic to propose any fixed value for the restitution coefficients in what are generally random collision events. It is difficult to hazard any specific values for *e* and *é* per collision, and still difficult to propose a theoretical model for the diffusive collision of the particle extremity with the solid surface.

We shall show in this section that the simulation results using the algorithm for randomly generated restitutions per stochastic diffusive collisions differ little in their details from those calculated using prefixed restitution values. Since the differences are not physically significant, this confirms our model choice for the molecular dynamics of the collisions. Furthermore, this novel algorithm accounts appropriately for previous experimental results (Khater, Hijazi et al. 2003) which show that whilst sliding is a possible state, the event is rather statistically rare on the complete uniform distribution [0, 1] for *e*.

In Fig II.14, three spatial PDF distributions, P (ζ), for the centre of mass positions of the rod-like particles, are clearly distinguished for solutions at rest with no hydrodynamic Peclet flow $\alpha = 0$, and for very small hydrodynamic Peclet flow $\alpha = 0.001$ and $\alpha = 0.1$. Also presented in this figure are the three corresponding orientation PDF distributions, P (θ), for the particles.

46

Fig II.14 Simulation results for the normalized spatial, P(ζ), and orientation, P(θ), PDF distribution inside a confining pore channel of width $2D = 0.8L$, for very low Peclet flow $\alpha = 0$, 0.001, 0.10, and randomly generated Brownian and hydrodynamic restitutions.

For Peclet $\alpha = 0$ in Fig II.14 the solution is at rest and the diffusive boundary collisions due to hydrodynamic flow are absent. In this case the dominant mechanism for the equilibrium dynamics is the Brownian effect in the bulk and at the surface boundaries, which drives the colloidal particles into a broad distribution. The calculated spatial PDF distribution P (ζ) is symmetric, about the median $\zeta_{mid} = 0.4$ of the pore channel, with a maximum at $\theta = 0°$. This

spatial PDF compares qualitatively with that in Fig II.12 although some spectral differences are evident. The simulation results for the orientation PDF distributions $P(\theta)$ confirm the character of the $P(\zeta)$. The calculated $P(\theta)$ in Fig II.14 is symmetric about $\theta = 0^0$, with tails ends up to $\theta \simeq \pm 44.4°$. As in Fig II.12 this implies that the rods are mostly aligned in the direction of the flow for Peclet $\alpha = 0$. Again this result illustrates the importance of the random stochastic Brownian movement, in particular for molecular dynamics at the solid boundary surfaces, towards establishing statistically homogeneous distributions for the equilibrium dynamics of the colloidal particles. A similar comparison can be made between the simulation results for Peclet flow $\alpha = 0.001$ and $\alpha = 0.1$, in Fig II.14 and Fig II.12, leading to comparable conclusions. In particular we retrieve the detailed form and magnitude of the spectral features for Peclet $\alpha = 0$ and $\alpha = 0.1$, and those for the intermediate Peclet flow $\alpha = 0.001$, including their spectral shoulders at $\theta \simeq \pm 37.4°$ which do not correspond to blocking but to the accumulation of the probability distribution at these angles due to multiple scattering of the particles' extremities under equilibrium dynamics.

A similar comparison can also be made between the simulation results of Fig II.15 and those in Fig II.13 leading to comparable conclusions, for Peclet flow $\alpha = 1$, 10, and 100. The strong peaks for these Peclet characteristics at the orientations $\theta = \pm 44^°.4^°$ in Fig II.15, as in Fig II.13, are signatures of the blocking effect.

The detailed comparison of the simulation results for the spatial and orientation particle distributions, calculated for randomly generated Brownian and hydrodynamic restitutions, on the one hand, with the simulation results for these same distributions, calculated for prefixed restitutions, on the other hand, where the restitutions model the molecular dynamics during the diffusive collisions of the particles at the solid boundaries, show basic similarities in their spectral features for a wide range of the Peclet flow.

We present in in Fig II.16 the results for the peak heights and widths at half peaks (variance) for the spatial PDF distributions $P(\zeta)$ for Peclet flow $\alpha \in [10^{-3}, 10^{2}]$. It is seen that the widths at half peaks decrease, while the peak heights increase with Peclet α. The remarkable feature of Fig II.16 is that its two graphics represent the simulation results calculated with the algorithms using *prefixed e = é = 0.5* restitutions, and those using *randomly generated* restitutions: there is only a small difference between the two sets of simulation results. The peak heights for prefixed restitutions are slightly greater than those for *randomly generated* restitutions, and the widths are slightly smaller, under normalized distributions.

Fig II.15 Simulation results for the normalized spatial, P(ζ), and orientation, P(θ), PDF distributions inside a confining pore channel of width $2D = 0.8L$, for low to high Peclet flow $\alpha = 1, 10, 100$, and randomly generated Brownian and hydrodynamic restitutions.
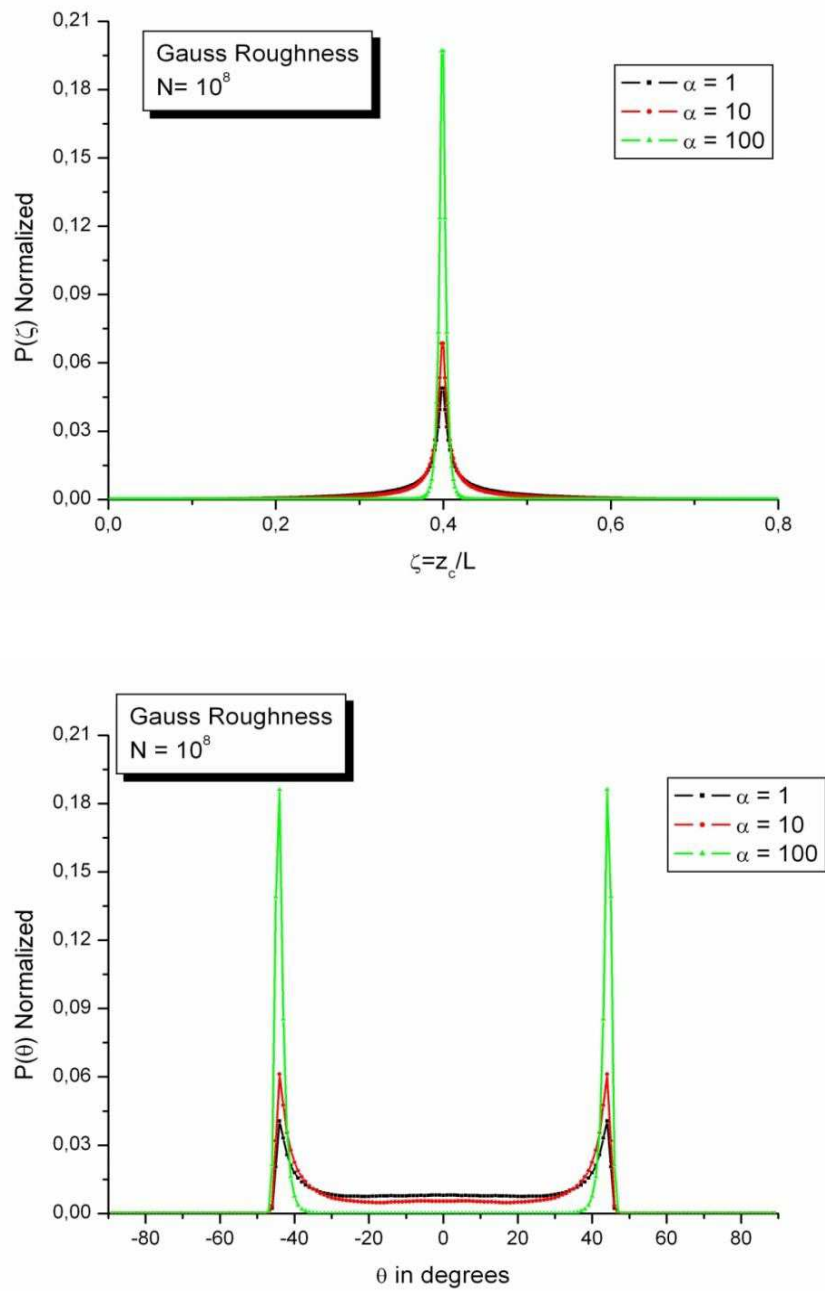
Finally, we present in Fig II.17 for Peclet flow $\alpha = 10$, an example of the difference between simulation results for a rough surface and a flat surface at the same maximal width, namely $2D = 0.8L$. Only the results for the orientation PDF distribution P(θ), are presented. The forms distinguish themselves, notably by the difference in the blocking angles. They are approximately $\theta = \pm 53. 5°$ for the atomically flat surface, and as shown above approximately

$\theta = \pm 44. 4°$ for the Gaussian rough surface. The two corresponding spatial PDF distributions P (ζ), are extremely peaked about the median $\zeta_{med} = 0.4$, though the peak heights and broad bases are not equal.
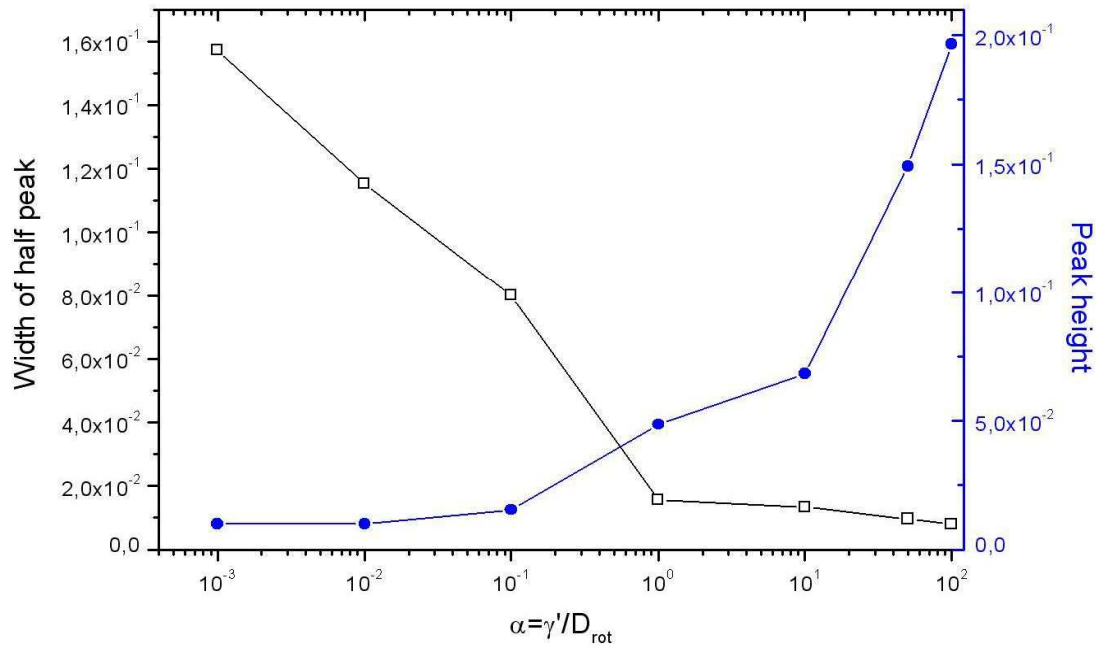
Fig II.16 Peak height and width at half peak (variance) of the spatial PDF distributions P(ζ), as a function Peclet flow α, for randomly generated Brownian and hydrodynamic restitutions. There is no significant difference with the same calculated variables using prefixed Brownian and hydrodynamic restitutions
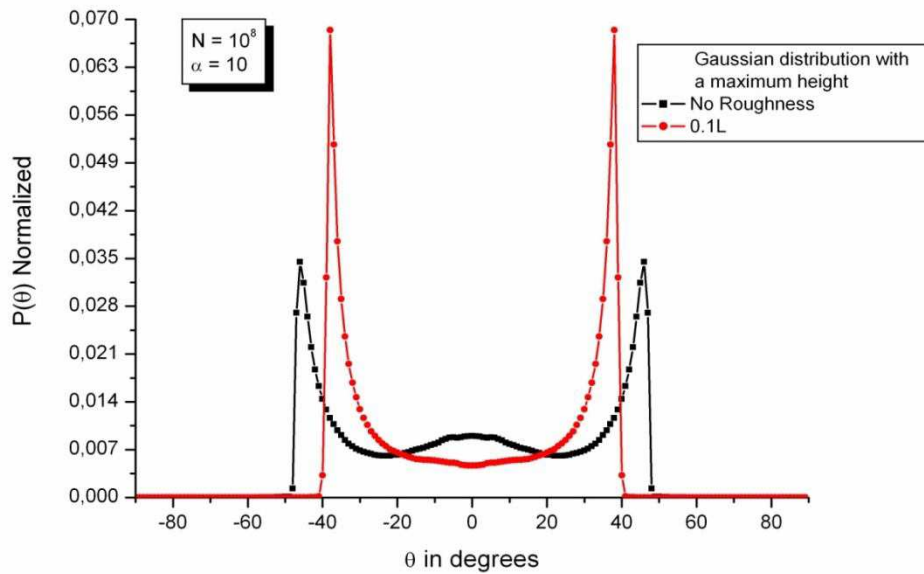
Fig II.17 Simulation results for the normalized spatial PDF, P(θ), inside a channel of width 2D= 0.8 L for Peclet $\alpha = 10$, for two types of boundary surfaces, smooth and Gaussian rough

In conclusion, we have introduced two novel elements into the numerical simulations to calculate the spatial and orientation distributions of dilute solutions of colloidal particles flowing inside pores in equilibrium dynamics under Brownian and hydrodynamic effects:

- In contrast with previous research work, which dealt with only atomically flat boundary surfaces, we have developed algorithms to treat boundary surfaces which are rough on the scale of the dimensions of the pores and the particles, and in particular using the realistic Gaussian model for rough surfaces.
- We have tested a number of algorithms to treat the molecular dynamics of stochastic Brownian and hydrodynamic causal collisions at the solid boundaries, using the notion of nano-mechanical restitution, and found that the most realistic approach is to treat the random collisions as events with randomly generated restitutions.

2.5 Simulation results for open pore channels

The objective of this section is to calculate the PDF distributions for macromolecular rod-like particles in dilute liquid suspensions, flowing inside open pore channels with Gaussian rough boundary surfaces, for which the pore channel width satisfies the condition

$$2D \geq L$$

In particular we consider three different pore widths: 2D = L, 2D = 1.2L, and 2D =1.4L. The simulation results are presented in particular for the orientation PDF distributions, $P(\theta)$, which can be related to experimental measurements of the nematic order parameter of such colloidal suspensions (Fry, Langhorst et al. 2006) (Islam, Rojas et al. 2003), (Zheng, Jagota et al. 2003).

In Fig II.18, Fig II.19 and Fig II.20 are respectively presented the orientation PDF distributions, $P(\theta)$, for the rod-like particles in the pore channels with the above widths. The simulations are carried out using randomly generated restitutions.

In Fig II.18 four orientation PDF distributions, $P(\theta)$, are calculated for the Peclet number α = 0.1, 1, 10, and 100, for a pore channel 2D = L. This choice implies that the rod-like particle can span the maximum possible width between the minima terrace levels on the opposing boundaries of the pore channel. PDF blocking, however, should be activated once the extremities are at an average terrace height on the opposing boundaries, subject to their random collision, where $h_{above,i=av} = h_{below,j=av} = 0.05$ L.

Using Eq. 22 we obtain this onset for blocking at a theoretical θ = arcsin(0.9) ≃ ± 64.2°, which indeed is observed in Fig II.18 for the low Peclet flow α = 0.1 and 1.
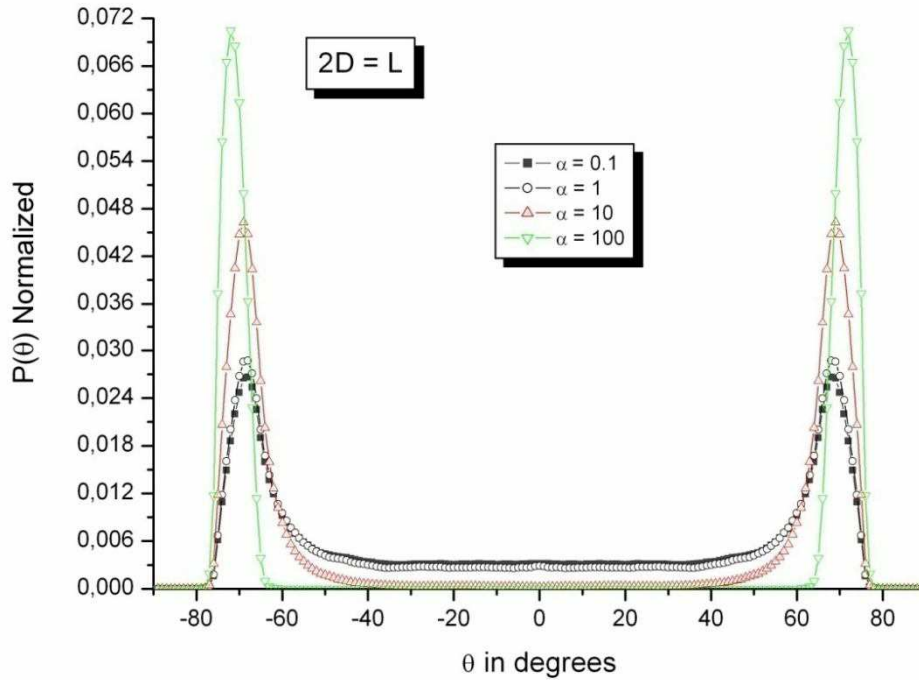
Fig II.18 Simulation results for the normalized orientation PDF, P (θ), inside pore channel of width 2D = 1L, for different hydrodynamics Peclet flow condition

For increasing Peclet flow we expect the blocking angle to increase. The simulations yield a blocking θ ≃ ± 71.8° which corresponds to the configuration where one extremity is at an average terrace level on one boundary and the second extremity is at a minimum terrace level on the other boundary. At higher Peclet numbers tin greater numbers from the neighbourhood of the solid boundaries into blocking configurations.

The existence of finite though small PDF distributions at small angles θ for the relatively small Peclet flow α = 0.1 and 1, indicates that some of the colloidal particles are still aligned in the direction of the flow and pass freely inside the pore channels. These PDF distributions disappear gradually for the higher Peclet flow α = 10 and 100, which is a signature of the evacuation of these particles into other accessible states due to the increasing flow.

In Fig II.90 and Fig II.20 are presented the orientation PDF distributions, P(θ), for the rod-like colloidal particles for a series of Peclet flow α = 0.1, 0.5, 1, 5, 10, 50, and 100, for pore channels with respective widths of 2D = 1.2L and 2D = 1.4L. Note that in both of these two cases the pore width is larger than the length L of the particle beyond the surface roughness.
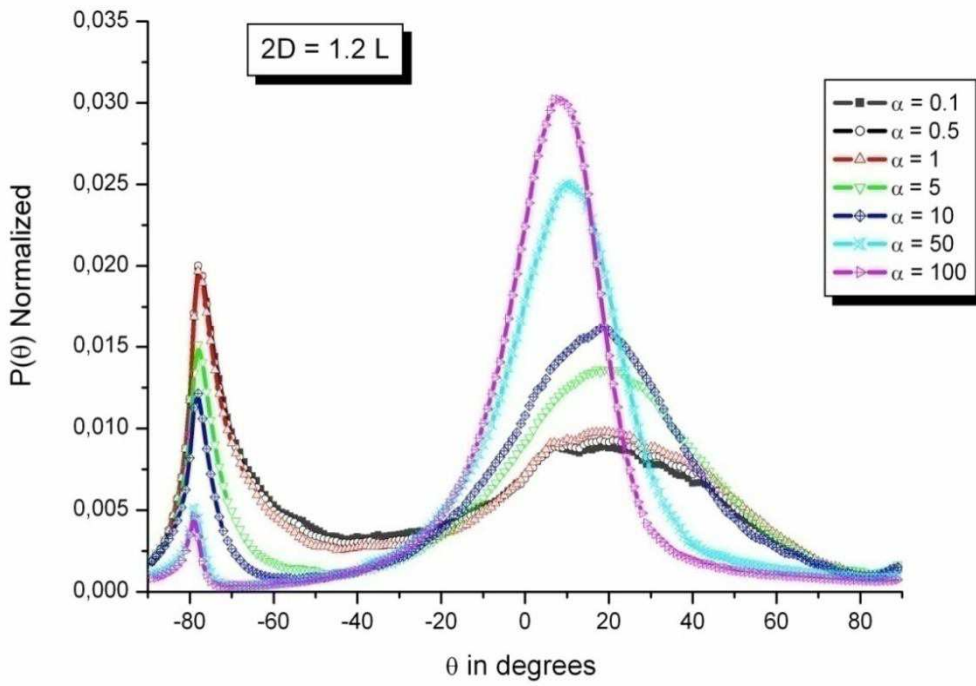
Fig II.19 As in Fig II.18 for pore channel of width 2D = 1.2L
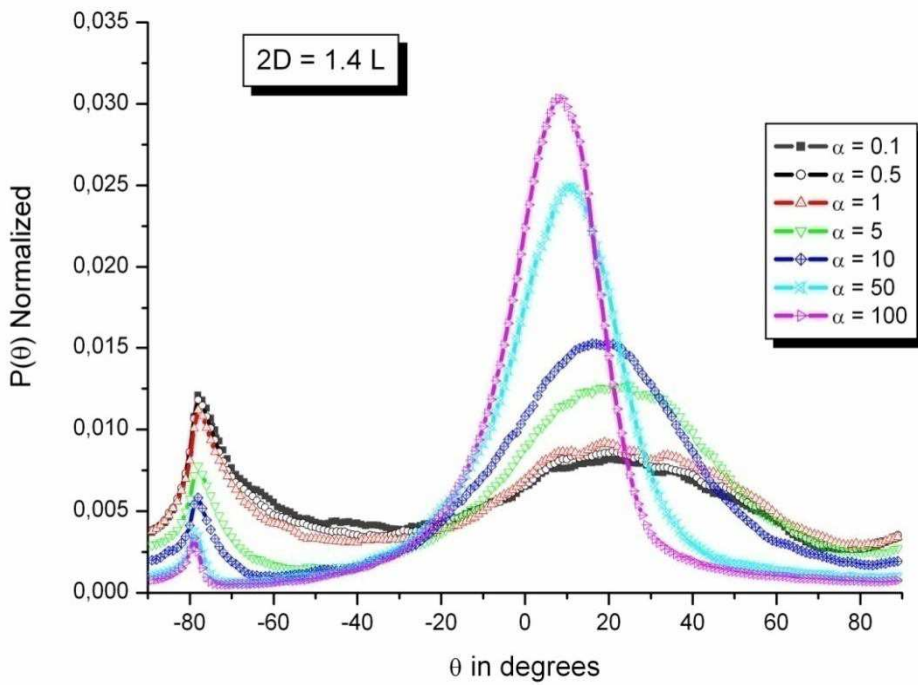
Fig II.20 As in Fig II.18 for pore channel of width 2D = 1.4L

The simulation results yield two major zones with characteristic spectral features, as observed in Fig II.90 and Fig II.20. The first zone on the left shows P(θ) features which are centered about large negative angles in the clockwise sense. The peak heights for the corresponding distributions decrease monotonically whereas their peak angles increase monotonically to larger negative values, with increasing Peclet flow. The second zone on the right shows in contrast P(θ) features which are centered about smaller positive angles in the anti-clockwise sense. The peak heights for the corresponding distributions increase monotonically whereas their peak angles decrease monotonically to the limiting θ = 0°, with increasing Peclet flow.

The P(θ) spectral features under equilibrium dynamics in the right zone for the considered pore channels are comparable to the PDF features usually calculated for *bulk* liquid solutions distant from solid boundaries. They correspond hence to the free movement of the rod-like particles subject to the singular competition between Brownian and hydrodynamics forces. The PDF spectral features under equilibrium dynamics in the left zone for the considered pore channels are in contrast the signatures of the consequences of multiple collisions scattering of the extremities of the colloidal particles at the rough boundaries. Effectively the multiple scattering processes have a tendency to trap the particles in almost perpendicular configurations with respect to the flow direction. The conservation of the total probability unity measure is maintained for any one of the Peclet flow α numbers over the two cited zones as well as other intermediate regions.

The results illustrate the importance of the random stochastic Brownian movement under low hydrodynamic flow conditions, and in particular at the solid boundaries, towards establishing equilibrium dynamics. In contrast increasing the hydrodynamics flow offsets the importance of the stochastic Brownian dynamic events in the bulk and at the solid boundaries.

This result illustrates the importance of the random stochastic Brownian movement under low hydrodynamic flow conditions, and in particular at the solid boundaries, towards establishing statistically random collisions. Increasing the hydrodynamic flow condition will decreases the Brownian movement and collisions with rough surface boundaries at large angle and evacuates the rods on the direction of the flow with small angle.

2.6 Calculation of the nematic order parameter

Rheo-optical methods – at least in the narrow sense of the word – were introduced in the rheological community in the 1950's to determine the constitutive parameters that describe material measurements. The initial aim of the optical methods was the direct measurement of stresses in the material .In the last two decades, the applicability of the rheo-optical

methodology has broadened; it's now regarded as an approach that is used to understand the often complex rheological behavior of a material. Rheo-optical methods have become an established technique in the study of structured fluids. We will concentrate on technique that uses visible light to investigate structural changes during flow. This method is based on changes in the properties of the transmitted light (polarimetry); Polarimetry measures properties of the transmitted light that is affected by phenomena that occur at all length scales present in the material. In this section, the basic principles of the method will be explained. In addition, some case studies will be presented to highlight the ability of this method. The fundamentals of birefringence and dichroism are briefly reviewed. In order to demonstrate the power of the technique,

The relative ordering of colloidal particles in solutions is experimentally accessible by optical experiments (Srinivasarao and Berry 1991; Fry, Langhorst et al. 2006; Prasad and Das 2010). In theory a tensor order parameter S is used to describe the orientation order of colloidal particles. In the 2D frame of the present model the order parameter may be determined as the average of the second order Legendre polynomial

$$S = \; <P_2(\cos\theta)> \; = \; <\frac{3\cos^2\theta - 1}{2}> \tag{25}$$

The $<\dots>$ is a statistical average over the PDF distribution for orientations with respect to the flow direction, θ, and $P_2(\cos\theta)$ the order 2 Legendre Polynomial, for macromolecular rod-like particles

This definition is appropriate, since S = 0 for a randomly isotropic distribution of orientations (unaligned phase), whereas S = 1 corresponds to a perfectly aligned sample. For an arbitrary sample of colloidal molecular particles, one has $S \in [0,1]$. Furthermore, the order parameter can be measured experimentally, notably by optical *birefringence* and *dichroism* techniques. The results for colloidal suspensions in bulk solutions (Tannous 2011), distant from solid boundaries, find for a small rotational Peclet number α, an isotropic distribution characterized by $S \cong 0$, whereas S approaches 1 for perfect alignment under the influence of the increasing Peclet hydrodynamic flow α.

Throughout this section we calculate the order parameter S as a function of the rotational Peclet number α, for different widths of the pore systems that present Gaussian rough surface boundaries. The pore widths are 2D = 0.7 L, 0.8L, 1L, 1.2L, and 1.4L, where L is the length of molecular rod-like particles. The calculated results for S are presented in Fig II.21, using the numerical code established in this work, and h_{max} = 0.05 L for the Gaussian rough surface

boundaries. The results clearly show that the nematic order parameter S, as a function of α, can be grouped in two types.

In Fig II.21 we have clearly three natures of nematic order S as Function of α corresponding to different pores spacious system. The first nature corresponds for a perfectly confined channel system with (2D < L) i.e. (2D = 0.7L and 2D =0.8L) the 2nd one corresponds to the situation where the width of the pores is slightly identical to the length of macromolecular rod like particles (2D = L), and the third nature corresponds to the unrestricted channel i.e. the pores spacious is slightly bigger than the rod particles (2D =1.2L and 2D = 1.4 L).

The first type of the nematic order parameter corresponds to an effectively confining pore of channel width 2D < L (2D = 0.7L and 0.8L). S decreases monotonically in this case with increasing Peclet number α. This is because increasing the hydrodynamic flow causes the evacuation of the particles from states aligned initially for small α with the flow to almost perpendicular orientations due to multiple scattering at the rough boundaries for large α as discussed in section 2.4, and illustrated in particular in Figs II.14 and II.15. Furthermore, it is significant to note that S is greater in amplitude for narrower confining pore channels, for all Peclet numbers α, S being greater for 2D = 0.7L than for 0.8L. This happens because the range for the accessible orientation states narrows down with the decreasing pore width. The pore width 2D = 1.0L may also be placed in this confining group, although the corresponding nematic order parameter presents a particular behavior as may be seen in Fig II.18.

Fig II.21 Variation of the nematic order parameter S as a function of the shear rate for different pore channels

The second type corresponds to open pore channels 2D > L where the pore widths are clearly greater than the length of the particle (2D = 1.2L and 1.4L). The nematic order parameter S for this type increases monotonically and presents common features which are clearly different from those for the confining pore channels. S shows for this case a relatively aligned orientation PDF distribution P(θ), as can be observed for different Peclet flow α from (Figs II.19 and II.20).

The analysis of Fig II.21 implies that it is possible to estimate the widths of pore channels for a considered porous system by direct measurements of the behaviour of its corresponding nematic order parameter, using birefringence and dichroism techniques, (Fry, Langhorst et al. 2006). This would be done using reference species of molecular rod-like particles in colloidal suspension inside the system, and the known physical parameters for the fluid (viscosity) and the particles (length and diameter).

In this section we shall also calculate the nematic order parameter for a particular example of molecular rod-like particles which is discussed in the literature. Optical studies by (Fry, Langhorst et al. 2006) made on colloidal suspensions of carbon nanotubes in polyisobutylene and aqueous single-stranded DNA solutions show that the shear-induced birefringence and dichroism (SABD) Δn′, Δn″ are both proportional to S as defined in Eq.25.
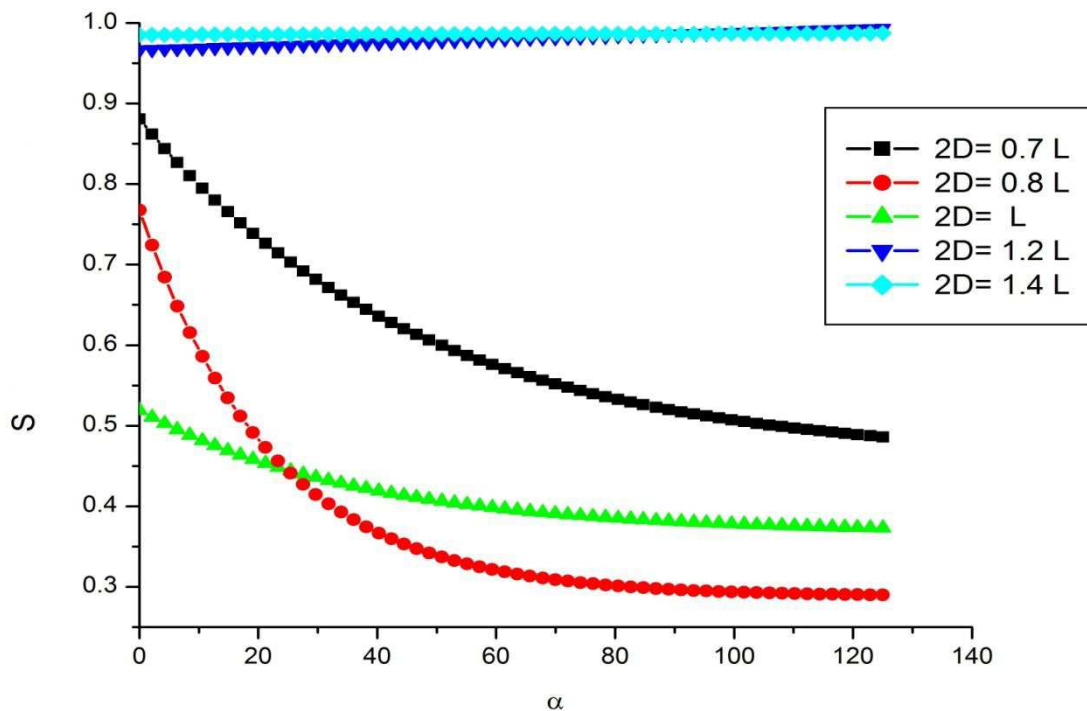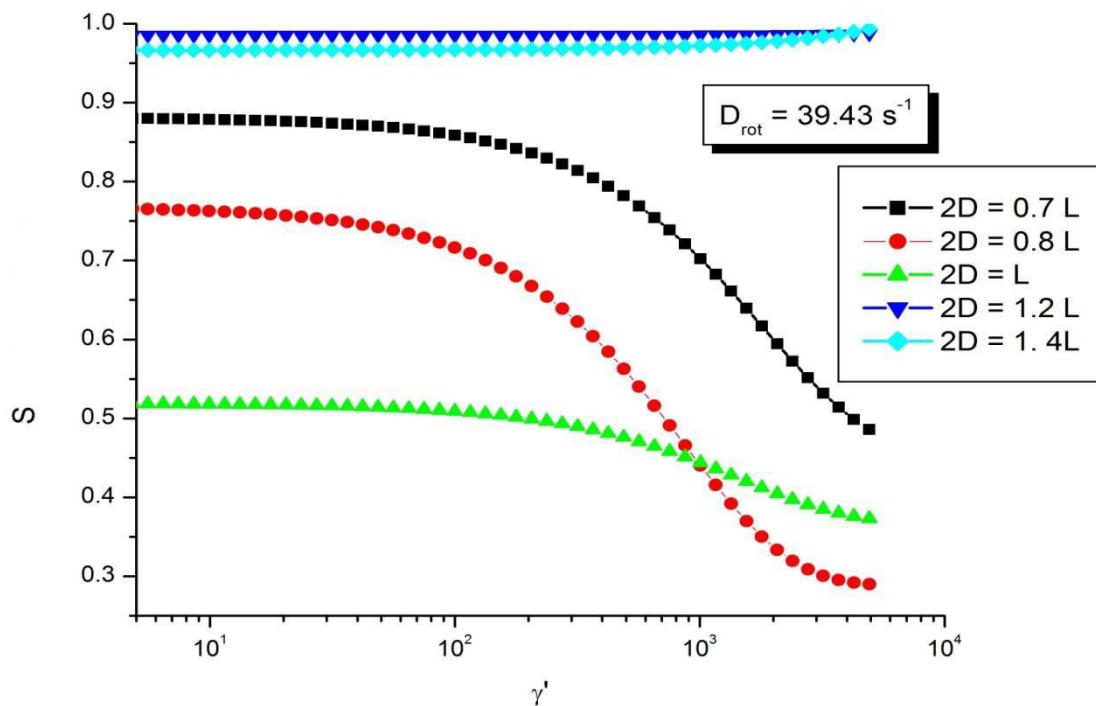

Fig II.22 Variation of the nematic order parameter S as a function of the shear rate for different pore channels

Further, two different fluids with the nanotube suspensions are used in this work, an aqueous ionic surfactant solution (Islam, Rojas et al. 2003), and an aqueous single-stranded DNA solution (Zheng, Jagota et al. 2003). The resulting samples are denoted by S1 and S2, respectively. We will consider the physical parameters of sample S1, and apply our simulation calculations to it. The surfactant suspension S1 has a viscosity $\eta = 9.5 \times 10^{-4}$ Pa.s at room temperature, and the resulting suspension contains individual SWCNTs. Atomic force microscopy AFM, analysis of dried films give a mean nanotube length $L = 750$ nm and mean diameter $d = 13.5$ nm, such that $L/d = 60$. Using Eq.(2) we calculate the rotational diffusion coefficient for these rod-like nanotubes as $D_{rot} = 39.43$ s^{-1}. The nematic order parameter S for different pore widths are presented Fig II.22 as a function of the shear rate variable for the constant rotational diffusion coefficient $D_{rot} = 39.43$ s^{-1} which corresponds to S1.
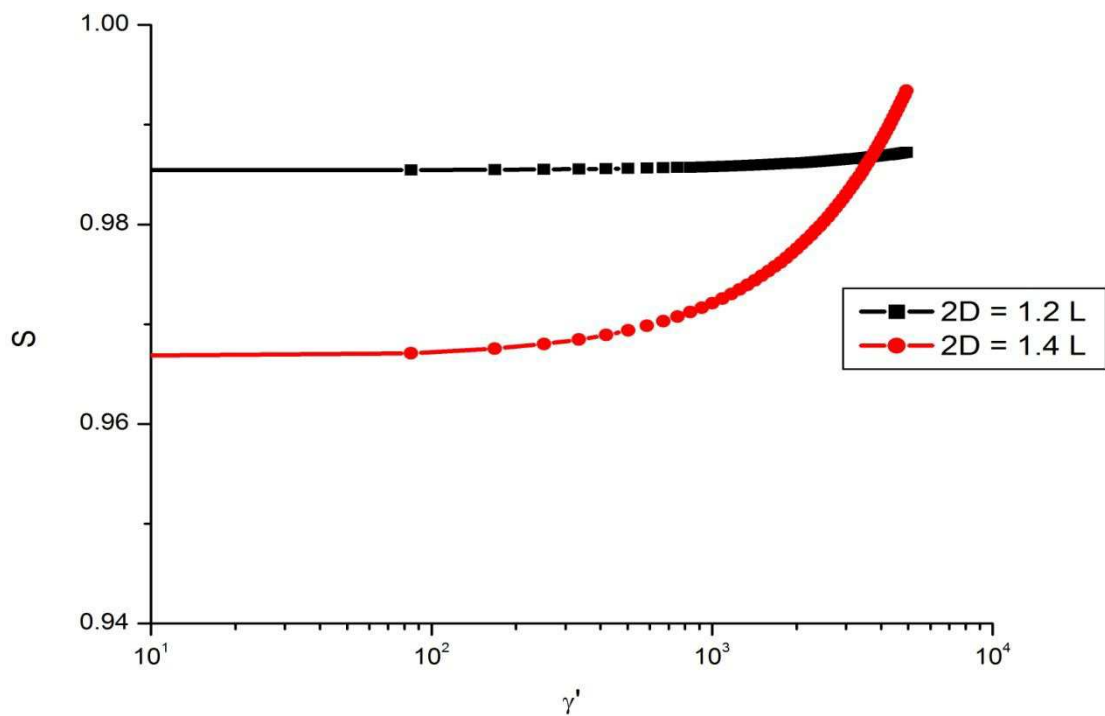
Fig II.22 Details of the nematic order parameter S in Fig II.23 as a function of shear rate for the open pore channels

2.7 Conclusions

We have developed algorithms and carried out numerical simulations to analyze the dynamics of dilute colloidal suspensions of macromolecular particles in solutions flowing inside a porous system. The pores are modeled in a two-dimensional frame of reference with boundaries. The colloidal particles are subject to hydrodynamic forces, Brownian motion and

random collisions at the solid surface boundaries of the pores. To treat the problem realistically we have considered the pores to present rough boundaries at the scale of the length of the particles, and have demonstrated that the assumption of ideally flat surface boundaries is unrealistic. The numerical simulations are carried out to calculate in particular the spatial and orientation statistical PDF distributions of the macromolecular rod-like particles in colloidal suspensions in a solution under equilibrium dynamics in a Poiseuille flow inside the pore channels. The results are presented for different widths of pore channels referenced to the size of a rod-like particle. The simulations are general in the sense that they are developed for confining and open pore channels, and are valid throughout the space of the pores and in the boundary depletion layers, for a wide variety of hydrodynamic flow conditions, at low, intermediate, and high flow, characterised by the rotational Peclet number.

Available experimental work does not access the detailed nature of collisions between Brownian macromolecular rod-like particles and solid surface boundaries, in a confined solution under hydrodynamic Poiseuille flow. However, some experiments, notably birefringence and dichroism can in principle measure the nematic order for dilute colloidal suspensions. Our simulations yield directly the nematic order parameter for colloidal suspensions in the two dimensional frame. It is therefore possible to use the theoretical results for the nematic order parameter together with experimental birefringence and dichroism to estimate the size of pore channels for a given porous system, given a particular reference colloidal suspension of rod-like particles of known length flowing inside the system.

REFERENCES

Andersen, O. S. (1999). "Sequencing and the single channel." J. Biophys 77(6): 2899.

Ausserré, D., J. Edwards, et al. (1991). "Hydrodynamic Thickening of Depletion Layers in Colloidal Solutions." EPL (Europhysics Letters) 14(1): 33.

Banerjee, A. and K. D. Kihm (2005). "Experimental verification of near-wall hindered diffusion for the Brownian motion of nanoparticles using evanescent wave microscopy." Physical Review E 72(4): 042101.

Berne, B. J. and R. Pecora (1976). Dynamic Light Scattering with. Applications to Chemistry, Biology, and Physics. New York, Wiley Interscience.

Bevan, M. A. and D. C. Prieve (2000). "Hindered diffusion of colloidal particles very near to a wall: Revisited." The Journal of Chemical Physics 113(3): 1228-1236.

Bird, R. B., C. F. Curtiss, et al. (1987). Dynamics of Polymeric Liquids, Vol. 2, Kinetic Theory. New York, Wiley.

Boeder, P. (1932). "Über Strömungsdoppelbrechung." Zeitschrift für Physik A Hadrons and Nuclei 75(3): 258.

Box, G. E. P. and M. E. Muller (1958). "A Note on the Generation of Random Normal Deviates." Ann. Math. Statist 29(2): 610.

Broersma, S. (1960a). "Rotational difiusion constant of a cylindrical particle." J. Chem. Phys 32: 1626.

Broersma, S. (1960b). "Viscous force constant for a closed cylinder." J. Chem. Phys. 32: 1632.

Carbajal-Tinoco, M. D., R. Lopez-Fernandez, et al. (2007). "Asymmetry in Colloidal Diffusion near a Rigid Wall." Physical Review Letters 99(13): 138303.

Chopra, M. and R. G. Larson (2002). "Brownian dynamics simulations of isolated polymer molecules in shear flow near adsorbing and nonadsorbing surfaces." J. Rheol 46(4): 831-862.

Chou, C. F., R. Austin, et al. (2000). "Sorting biomolecules with microdevices." Electrophoresis 21(1): 81-90.

De Pablo, J. J., H. C. Öttinger, et al. (1992). "Hydrodynamic changes of the depletion layer of dilute polymer solutions near a wall." AIChE Journal, 38: 273.

Doi, M. and S. F. Edwards (1986). The theory of polymer dynamics. New York, the Clarendon Press, Oxford University Press.

Fry, D., B. Langhorst, et al. (2006). "Rheo-optical studies of carbon nanotube suspensions." J Chem Phys. 124(5): 054703.

Fry, D., B. Langhorst, et al. (2006). "Rheo-optical studies of carbon nanotube suspensions." The Journal of Chemical Physics 124(5): 054703.

Gardiner, C. W. (1990). Handbook of Stochastic Methods, 2nd ed. Berlin, Springer-Verlag.

Hijazi, A., L. Ben Yahia, et al. (2003). "Experimental study of the collision between a rod like macromolecule and a solid surface." European Polymer Journal 39(3): 521.

Hijazi, A. and A. Khater (2001). "Brownian dynamics simulations of rigid rod-like macromolecular particles flowing in bounded channels." Computational Materials Science 22(3-4): 279.

Hijazi, A. and A. Khater (2001). "Simulations of distribution functions for rod-like macromolecules in linear flow near solid surfaces." Computational Materials Science 20(2): 213.

Holmqvist, P., J. K. G. Dhont, et al. (2006). "Anisotropy of Brownian motion caused only by hydrodynamic interaction with a wall." Physical Review E 74(2): 021402.

Holmqvist, P., J. K. G. Dhont, et al. (2007). "Colloidal dynamics near a wall studied by evanescent wave light scattering: Experimental and theoretical improvements and methodological limitations." The Journal of Chemical Physics 126(4): 044707.

Huang, P. and K. S. Breuer (2007). "Direct measurement of anisotropic near-wall hindered diffusion using total internal reflection velocimetry." Physical Review E 76(4): 046307.

Islam, M. F., E. Rojas, et al. (2003). "High Weight Fraction Surfactant Solubilization of Single-Wall Carbon Nanotubes in Water." Nano Letters 3(2): 269.

Jendrejack, R. M., D. C. Schwartz, et al. (2004). "Shear-induced migration in flowing polymer solutions: Simulation of long-chain DNA in microchannels." J. Chem. Phys 120(5): 2513.

Johnson, N., S. Kotz, et al. (1995). Continuous Univariate Distribution Vol. 1. New York, John Wiley and Sons.

Khater, A. (1989). "INTENSITY REFLECTION COEFFICIENTS OF ATOMICALLY IRREGULAR SURFACES IN PHONON SCATTERING." Europhys. Letters 2(7): 539.

Khater, A., A. Hijazi, et al. (2003). "Experimental study of the collision between a rod like macromolecule and a solid surface." European Polymer Journal 39(3): 521.

Khater, A., C. Tannous, et al. (2000). "Exact solutions of the Boeder differential equation for macromolecular orientations in a flowing liquid." Computational Materials Science 18(3-4): 393.

Lim, A., E. Dimalanta, et al. (2001). "Shotgun Optical Maps of the Whole Escherichia coli O157:H7 Genome." Genome Research 11(9): 1584.

Marsaglia, G. and T. A. Bray (1964). "A Convenient Method for Generating Normal Variables." SIAM Review 6(3): 260.

Neumann, J. V. (1951). "Various techniques used in connection with random digits. Monte Carlo methods." National Bureau of Standards Applied Mathematics Series 12: 36.

Park, J., J. M. Bricker, et al. (2007). "Cross-stream migration in dilute solutions of rigid polymers undergoing rectilinear flow near a wall." Physical Review E 76(4): 040801.

Peterlin, A. (1938). "Über die Viskosität von verdÜnnten Lösungen und Suspensionen in Abhängigkeit von der Teilchenform." Zeitschrift für Physik A Hadrons and Nuclei 111(3): 232.

Prasad, A. and M. K. Das (2010). "Optical birefringence studies of a binary mixture with the nematic-smectic A(d)-re-entrant nematic phase sequence." J Phys Condens Matter 22(19): 195106-195106.

Press, W. H., S. A. Teukolsky, et al. (1992). Numerical Recipes in C: The Art of Scientific Computing, Second Edition. New York, Cambridge University Press.

Schiek, R. L. and E. S. G. Shaqfeh (1995). "A nonlocal theory for stress in bound, Brownian suspensions of slender, rigid fibers." J. Fluid Mech. 296: 271.

Sintillan, D., E. G. Shaqfeh, et al. (2006). "Effect of flexibility on the shear-induced migration of short-chain polymers in parabolic channel flow." J. Fluid Mech 557: 297.

Srinivasarao, M. and G. C. Berry (1991). "Rheo-optical studies on aligned nematic solutions of a rodlike polymer." Journal of Rheology 35(3): 379-397.

Tanford, C. H. (1961). Physical Chemistry of Macromolecules. New York, Wiley.

Tannous, C. (2011). "Langevin simulations of rod-shaped object alignment by surface flow." Surface Science 605(9): 923.

Tegenfeldt, J., C. Prinz, et al. (2004). "Micro- and nanofluidics for DNA analysis." Anal Bioanal Chem 378(7): 1678.

Zheng, M., A. Jagota, et al. (2003). "Structure-Based Carbon Nanotube Sorting by Sequence-Dependent DNA Assembly." Science 302(5650): 1545.

Chapter 3

Simulations for the dynamics and nematic order of dilute colloidal suspensions of ellipsoidal-like particles flowing in 3D space in the bulk and near solid boundaries

Abstract: Numerical simulations and algorithms are developed to analyze the dynamics of the ellipsoidal-like particles in a three-dimensional spatial frame. In particular we study in this case of an open channel pore for which we calculate the PDF distributions in the bulk and in the depletion layer next to a solid boundary. We develop a theoretical model based in this case on the equations of Jeffrey for the dynamics of solid particles in fluids and the molecular dynamics by mechanical restitution for the diffusive collisions of the particles at the solid boundaries. Simulations are carried out to calculate the *equilibrium* PDF distributions for ellipsoidal molecular particles in suspension in a fluid under hydrodynamic flow. The simulation results for the PDF distributions for the spatial positions and the orientations of ellipsoidal particles are calculated for the bulk liquid and in the depletion layers next to an atomically flat solid surface boundary. They are calculated over several orders of magnitude of the rotational Peclet number, and for variable aspect ratios characteristic of the ellipsoidal particles under study. They demonstrate the importance and significance of modeling in a three-dimensional spatial frame as compared to the simulation results based in the Boeder approach over a two-dimensional spatial frame. In particular we are able to produce a complete topography for the PDF distributions segmented as a hierarchy in the depletion layer, covering a complete range of orientations in 3D space. The simulations permit to calculate, for the colloidal suspension, the nematic order parameter over its tensorial representation, for a variety of forms of ellipsoidal particles selected to correspond to real polymer particles. Our results for the nematic order parameter which may be calculated locally inside the space of the depletion layer are innovating and represent a new input as regards these systems.

3.1 Introduction

Colloidal suspensions of particles in dilute liquid solutions flowing inside systems of mesopores, are of great importance in industrial processes, such as for example for coatings (Fuji, Fujimori et al. 1998; Bernard P 2002) and catalysis (Jia, Zhu et al. 2003), and in biological processes, such as for example in protein diffusion in membranes (Sokolov, Aranson et al. 2007) and in the circulation of red blood cells and platelets inside the human body.

Colloidal particles have general forms, including the spherical one, and show rich Brownian dynamics. The origin for current models for the study of the dynamics of colloidal non-spherical particles in a shear flow at low Reynolds numbers is historically the approach proposed some time ago (Jeffery 1922). This pioneering research work investigated the rotational behavior of a single ellipsoidal particle in a Newtonian fluid. Jeffery obtained a set of differential equations for the rotation of an ellipsoid, with analytic solutions depending on the initial conditions. This theoretical approach was confirmed experimentally (Trevelyan and Mason 1951), and has been studied and developed since by several groups and researchers, both theoretically and experimentally.

The overall rotation of the colloidal particles in the bulk liquid is referred to as a Jeffery orbit, which will be discussed in detail in section 3.2. In particular (Bretherton 1962) showed that Jeffery's model could be applied to any axis-symmetric particle, provided that an equivalent aspect ratio was introduced. The equivalent aspect ratio was used to estimate the period of rotation for non-interacting particles far away from solid surface boundaries and from other colloidal particles.

The study of the dynamics of spheroids has been carried out by a number of authors. In particular, the numerical simulation of the dynamics for spheroids moving near a solid surface boundary was carried out (Hsu and Ganatos 1994) using Jeffry's equations. The authors concluded that hydrodynamic forces and torque depend strongly on the spheroid orientation and its position relative to a wall boundary; they reported tumbling of spheroids that resulted in motion towards the wall, since the spheroids were turned around the point closest to the wall. Other simulations using Jeffry's equations (Gavze and Shapiro 1997) calculated the hydrodynamic forces on a fiber near a solid wall using a boundary integral equations model. They showed a lift force effect on the fiber due to the presence of the wall boundarey. In addition, they found that the wall retards the fiber motion. Their study confirmed that periodic

rotational motion was occurring in unbounded shear flow, and indicated that fibers close to the wall had longer periods between rotations.

In contrast the experimental study of the fiber motion in a planar Couette shear flow apparatus was investigated (Moses, Advani et al. 2001). These authors introduced an effective shear rate to describe the wall boundary effect and showed a logarithmic decrease of this with increasing distance from the wall. Significantly, the results showed that a fiber centriod situated at a distance larger than its length from the wall verified Jeffery's model. The authors reported that higher aspect ratio fibers rotate faster in the region near the wall than those with lower aspect ratios. Recently new experiments (Holm and Söderberg 2007) demonstrate the influence of shear close to a solid boundary for different planes parallel to the boundary for the fiber orientations with different fiber aspect ratios and concentrations. They show that as the aspect ratio increases the influence of the shear on the fiber orientations decreases for all the parallel planes. We show in this chapter that our recent numerical simulation results confirm this experimentally measured behavior.

In the theoretical research work, cited above, the dynamic effects for colloidal particles due to their stochastic Brownian motion, and their diffusive collisions at the solid wall boundaries, are omitted. It is the purpose of the present work to treat these forces towards a comprehensive analysis of the dynamics of the colloidal particles, in a three-dimensional spatial frame (3D), in the bulk of the flowing fluid as well as near the surrounding solid surface boundaries. To that end we will develop in this chapter appropriate algorithms integrating these random forces, in addition to the effect of the hydrodynamic forces at the heart of Jeffery's equations. Based on these algorithms we then carry out numerical simulations to analyze the dynamics of colloidal particles of general ellipsoidal forms, in dilute suspensions, in the bulk of the flowing liquid solution, and next to ideal atomically flat solid surface boundaries.

Our study is focused on the determination of the PDF distributions, under equilibrium dynamics, for the positions and the orientations of macromolecular ellipsoidal particles. In particular we seek to understand the extent to which the Brownian dynamics and the diffusive collisions at the solid surface boundaries may be important to such equilibrium dynamics.

It is well known that it is intractable to study by the only analytical means the dynamics of the molecular particles in dilute colloidal suspensions near solid surfaces, because of the random nature of the Brownian motion and the equally random nature of diffusive collisions. The only viable alternative is to do this by numerical simulations with appropriate algorithms.

In section 3.2, we present a technical introduction to the problem and to liquid bulk macromolecular dynamics under Brownian and hydrodynamic motion. Section 3.3 presents the developed algorithm for diffusive collisions at the solid surface boundaries of open pore channels. Section 3.4 presents simulation results for the spatial and angular PDF distributions for colloidal suspensions, for a wide range of hydrodynamic conditions and for ellipsoidal particles with variable aspect ratios in bulk solution while section 3.5 near the depletion layer The calculation of the nematic order parameter S in 3D is presented in section 3.6. Cconclusions are presented in section 3.7.

3.2 Colloidal Particle Model Dynamics in 3D-Spatial Frames

Particles moving in a suspension tend to orient themselves in the direction of the shearing which can be quantified by fluid velocity gradients. As the macromolecular particle translates with the fluid, it is assumed that the velocity at that particle centroid is equal to the velocity of the fluid at this position. The macromolecular particle is affected by other particles or walls in close proximity. An ellipsoidal particle in simple shear flow spends most of its time aligned almost parallel to the streamlines but as the concentration of macromolecular particles in the suspension increase, the interaction of the particles with other particles and with the boundary solid surface leads to other induced ordinations. Particle-particle interaction have been the subject of study for many researchers (Folgar and Tucker 1984; Advani and Tucker 1990; Ranganathan and Advani 1991; Férec 2009).

Our present research work deals with dilute suspensions of colloidal particles and hence does not consider the interaction effects between the particles; we focus instead on the particle - solid surface boundary interactions.

The orientations of dilute concentrations of macromolecular particles in the bulk of a flowing fluid have been studied early by Boeder who introduced a differential equation (BDE) in a 2D-spatial frame (Boeder 1932), taking into account the dynamic effects due to the Brownian and hydrodynamic forces acting on the particles. The BDE governs the variations of the probability distribution functions (PDF), P (θ), of the particles as a function of their orientations θ in the bulk with respect to the direction of the shear flow. The BDE depends on the Peclet number $\alpha = \gamma' / D_{rot}$, where γ' is the shear rate of flow and D_{rot} is the rotational diffusion coefficient of the macromolecular particle about its centre of mass. The rotational Peclet number α is the dimensionless ratio that characterises the relative strengths of hydrodynamic and Brownian effects.

In this chapter we generalise the algorithm used previously for the 2D-spatial frame in Chapter 2, to establish an appropriate algorithm for a 3D-spatial frame. This is used to make numerical simulations for the 3D dimensional Cartesian space, in order to calculate the PDF distributions of ellipsoidal macromolecular particles in the bulk liquid solution and in the vicinity of solid surface boundaries.

In particular, the mechanical restitution model at the solid boundaries is generalized to three dimensions, and combined with a fuller implementation of the Jeffery's which govern the motion of ellipsoidal forms of the colloidal particle in an unbounded linear flow field. It is hence thi

s complete version which is used in the present model to calculate the PDF distributions for macromolecular ellipsoidal particles in the neighbourhood of solid surface boundaries.

We consider a simple shear flow acting on an ellipsoidal particle, such that

$$v_x = \dot{\gamma} y \ \ and \ \ v_y = v_z = 0$$

$\dot{\gamma}$ is the hydrodynamic shear rate. The motion of a solid ellipsoid particle, suspended in a simple shear flow, was computed analytically (Jeffery 1922), neglecting the inertia of the fluid and the particle. The ellipsoidal orientation is defined by three angles (θ, φ, ψ),which determine the Cartesian coordinates x, y, z. In contrast, a local coordinate system x', y', z', translates and rotates with the ellipsoidal particle, see Fig III.1. In Jeffery's theory it is assumed that the ellipsoidal center translates with the same linear velocity as that of the particle centriod.
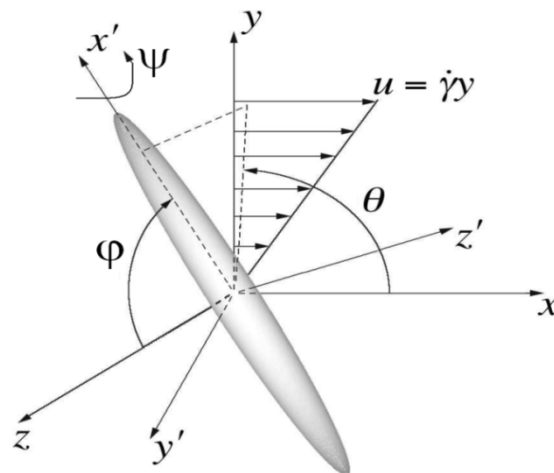
Fig III.1 Coardinate system for ellpsoidal particle centered at the origin

The angles φ and θ are used to define the unit direction of the primary axis and ψ represents the rotational angle about the ellipsoidal particle. The differential equation governing the time evolution of θ and φ are given by

$$\dot{\varphi} = \frac{\dot{\gamma}}{4} \left(\frac{r_e^2 - 1}{r_e^2 + 1}\right) \sin 2\varphi \, \sin 2\theta \qquad (1)$$

$$\dot{\theta} = -\dot{\gamma} \left(\frac{1}{r_e^2 + 1}\right) (r_e^2 \sin^2 \theta + \cos^2\theta) \qquad (2)$$

In these equations, γ' is the shear rate; r_e is the aspect ratio of the ellipsoidal particles, θ is defined as the angle of the particle with respect to flow direction, φ as the vorticity axis; $\varphi = \frac{\pi}{2}$ when the ellipsoidal particle lies in the plane of shear. It can be seen that the angular velocity θ' is maximum when the ellipsoid is perpendicular to the flow direction ($\varphi = \frac{\pi}{2}$) and minimum when it aligned to the flow direction($\theta = 0$).

From Eqts.1 and 2, it is observed that the angular velocities depend linearly on the shear rate, if Eqts.1 and 2 are integrated with respect to time they may be re-written as

$$\theta(t) = \tan^{-1}(r_e \tan \frac{\dot{\gamma} t}{r_e + 1/r_e}) \qquad (3)$$

$$\varphi(t) = \tan^{-1} \frac{Cr_e}{\sqrt{r_e^2 \cos^2 \theta + ^2 \theta}} \qquad (4)$$

While the rotational equation is

$$\psi(t) = \int_0^t \left(\frac{\dot{\gamma}}{2} - \dot{\theta}\right) \cos\varphi \, dt \qquad (5)$$

The constant C characterizes the eccentricity of the orbit executed by the particle, and takes the values between zero and infinity. C = 0 implies that the particle is aligned along the vorticity axis ($\varphi = 0$), while C → ∞ implies that the particle lies in the shear plane $\varphi = \frac{\pi}{2}$, see Fig III.2 for details. The orientation of the ellipsoidal particle can be described completely by the spherical coordinate system. The θ and φ defined in a fixed Cartesian coordinate system, as shown in Fig. III.1, ($-\pi/2 \leq \theta \leq +\pi/2$ and $0 \leq \varphi \leq \pi$), are sufficient because the problem is invariant under the transformation $\varphi \rightarrow \varphi + \pi$.
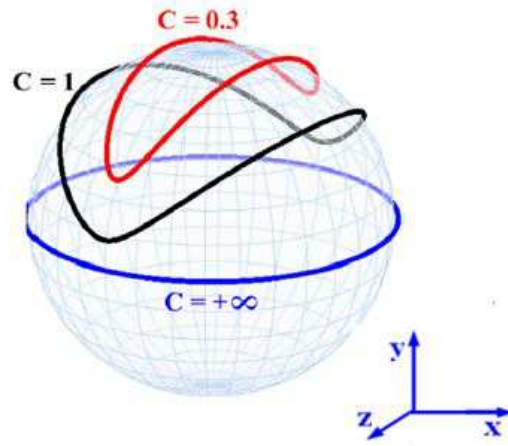
Calculated example of Jeffery's different orbit constants C for $r_e \to \infty$

Note that for large r_e = L/d (L and d are respectively the length and diameter of the macromolecular or nano particle), the ellipsoidal form turns into rod-like particles. This special class of particles is extensively discussed in Chapter 4. For $L \gg d$, i.e. $r_e \gg 1$, Jeffery's equations become

$$\left[\frac{d\theta}{dt}\right] = -\dot{\gamma}\left(\frac{r_e^2}{r_e^2+1}\right)\sin^2\theta - \dot{\gamma}\left(\frac{1}{r_e^2+1}\right)\cos^2\theta \cong -\dot{\gamma}\sin^2\varphi \qquad (6a)$$

$$\left[\frac{d\varphi}{dt}\right] = \frac{\dot{\gamma}}{4}\left(\frac{r_e^2-1}{r_e^2+1}\right)\sin 2\varphi\,\sin 2\theta \cong \frac{\dot{\gamma}}{4}\sin 2\varphi\,\sin 2\theta \qquad (6b)$$

In the simulations using Jeffery's equations, the hydrodynamic force tends to align the ellipsoidal macromolecular particles in the direction of the shear flow, θ is taken as positive or negative in the trigonometric sense, where $\theta = 0$, corresponds to the flow direction parallel to the boundary walls. To simulate the effects of hydrodynamic effects in a time interval Δt between two successive simulation events labelled s and $s +1$, we compute the hydrodynamic rotations about the centre of mass of the particles, $\Delta\theta_{hyd}(s + 1; s)$, and $\Delta\varphi_{rot}(s + 1; s)$, by using the following algorithm

$$\Delta\theta_{hyd}(s+1;s) = \theta(t_{s+1}) - \theta(t_s) = -\dot{\gamma}\left(\frac{1}{r_e^2+1}\right)\left(r_e^2\sin^2\theta\,(t_s) + \cos^2\theta\,(t_s)\right)\Delta t \quad (7a)$$

$$\Delta\varphi_{hyd}(s+1;s) = \varphi(t_{s+1}) - \varphi(t_s) = \dot{\gamma}\left(\frac{r_e^2+1}{r_e^2-1}\right)\frac{\sin 2\theta(t_s)\sin 2\varphi(t_s)}{4}\Delta t \qquad (7b)$$

In contrast the Brownian forces in the bulk liquid solution create a diffusive rotational motion of the particles, for which the rotation variables $\Delta\theta_{rot}(s + 1; s)$ and $\Delta\varphi_{rot}(s + 1; s)$ can then

be assumed in the algorithm as previously for $\Delta\theta_{rot}$ in the form

$$\Delta\varphi_{rot}(s+1;s) = \pm\Delta\varphi_{rot} \tag{8a}$$
$$\Delta\theta_{rot}(s+1;s) = \pm\Delta\theta_{rot} \tag{8b}$$

The Brownian rotations, $\pm\Delta\varphi_{rot}$ and $\pm\Delta\theta_{rot}$, are clock and anticlockwise. In this procedure the simulation time interval Δt is related, as previously stated, to an effective variable for the Brownian rotation diffusion by the following equations

$$\Delta\varphi_{rot}^2 = 2D_{\varphi\,rot}\ \Delta t \tag{9a}$$
$$\Delta\theta_{rot}^2 = 2D_{\theta\,rot}\ \Delta t \tag{9b}$$

For the small Δt simulation time intervals to be unique, at least for hydrodynamic events, they must satisfy

$$\Delta t = \frac{1}{2D_{\theta\,rot}}\ \Delta\theta_{rot}^2 = \frac{1}{2D_{\varphi\,rot}}\ \Delta\varphi_{rot}^2 \tag{10}$$

This leads to the simulation relationship

$$\Delta\theta_{rot}^2 = \frac{2D_{\theta\,rot}}{2D_{\varphi\,rot}}\ \Delta\varphi_{rot}^2 \equiv r_{\theta,\varphi}\ \Delta\varphi_{rot}^2 \tag{11}$$

There are two ways to treat $r_{\theta,\varphi}$ in the numerical simulations, as follows

$$r_{\theta,\varphi} = \frac{D_{\theta\,rot}}{D_{\varphi\,rot}} = 1 \tag{12a}$$
$$r_{\theta,\varphi} = (\sin\varphi)^{-2} \tag{12b}$$

Eq.12a is based on the assumption of independent and random Brownian simulation events, where the ellipsoidal symmetry cuts the same diffusion coefficient in whatever angular displacement it makes. See for details Annex AII. This underestimates somewhat the physical relation of $\Delta\theta_{rot}$ and $\Delta\varphi_{rot}$ for hydrodynamic events, which can be derived directly as in Eq.12b. However, Eq.12b would overestimate this relationship in the global simulation since random Brownian events may be viewed as disconnected. Eqs.12a and 12b yield respectively

$$\Delta\theta_{rot}(s+1;s) = \pm\Delta\theta_{rot} \tag{13a}$$
$$\Delta\varphi_{rot}(s+1;s) = \pm\sin\varphi\ \Delta\theta_{rot} \tag{13b}$$

We have used both Eq.13a and Eq.13b to run our overall simulations, for a variety of hydrodynamic conditions and for a wide range of aspect ratios. The results do not differ in any significant manner, (see Annex AII). It is noticeable however that we gain on the calculation time when simplifying the simulation conditions, by considering $r_{\theta,\varphi} = 1$.

The time interval Δt can be now eliminated from the hydrodynamic algorithm using Eq.12a, so that equations Eq.7a and 7b become

$$\Delta\theta_{hyd}\,(s+1;s) = -\gamma^{'}\left(\frac{1}{r_e^2+1}\right)\left(r_e^2 sin^2\theta + cos^2\theta\right)\frac{\Delta\theta_{rot}^2}{2D_{\theta\,rot}} \tag{14a}$$

$$\Delta\varphi_{hyd}(s+1;s) = \gamma^{'}\left(\frac{r_e^2+1}{r_e^2-1}\right)\frac{sin2\theta\,sin2\varphi}{4}\frac{\Delta\theta_{rot}^2}{2D_{\theta\,rot}} \tag{14b}$$

Using Eq.2 in Chapter 2, the above equations become

$$\Delta\theta_{hyd} = -\alpha\frac{1}{r_e^2+1}\left(r_e^2 sin\square\theta + cos^2\theta\right)\frac{\Delta\theta_{rot}^2}{2} \tag{15a}$$

$$\Delta\varphi_{hyd} = \alpha\frac{(r_e^2+1)}{8(r_e^2-1)}\left(sin\,2\theta\sin 2\varphi\right)\Delta\theta_{rot}^2. \tag{15b}$$

In a numerical simulation the choice of a value for $\Delta\theta_{rot}$ is dictated by technical criteria towards establishing efficient simulation runs and negligible scatter. This choice determines effectively a simulation time interval Δt which is inversely proportional to the diffusion coefficient from Eq.10 in this chapter. For the purpose of the present simulations we typically take $\Delta\theta_{rot} \sim 0.003$ radians, for a wide range of the Peclet number α. This value for $\Delta\theta_{rot}$ may however be varied for different experimental conditions and different Peclet numbers.

3.3 Colloidal Particle Algorithms in 3D-Spatial Frames for open Pore Channels

In this section, we present the model for the numerical simulations for the dynamics and PDF distributions of ellipsoidal colloidal particles in open channels. The mesopore system is hence modelled b two infinite solid plates which confine the fluid flow along a Cartesian direction in the x-y plane parallel to the plates, but which are sufficiently apart to model an open channel as in FigIII.4. The separation D between the plates along the y axis is considered mesoscopic in its dimensions and greater than the length L of the ellipsoidal particle, $D \gg L$. The particles have the liberty to move dynamically in the flow, in translational and rotational movements, in all directions in the 3D space, under the combined

influence of the Brownian and the hydrodynamic forces, and of the diffusive collisions at the solid surface boundary.
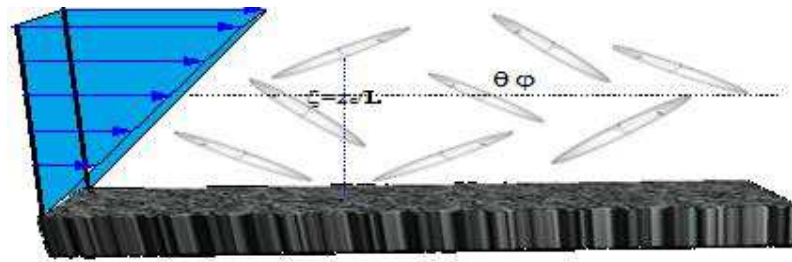

Fig III.4 Schematic representaion of the ellpsiodal macromolecular particles in the depeltion layer next to the solid surface boundary of one of the two plates which confine the hydrodynamic flow of the fluid

The notion of restitution is next developed to build up an algorithm for the diffusive collisions of the macromolecular particles with surface boundaries in a 3D-spatial frame. The joint PDF distributions for the macromolecular particles, namely $P(\theta, \varphi)$, are calculated as a function of angular ordinations θ and φ, and $P(\zeta)$ as a function of the normalized distance of their center of mass ζ measured from a reference plane at the boundary surface.

The detailed nature of a diffusive collision between a macromolecular particle and a given solid surface, is quite complex and varies with the topography of the surface (Khater 1989), it would also vary with the form and nature of the macromolecular specie. To develop an appropriate simulation algorithm at the solid boundaries, we characterize the dynamics of the collision using the same coefficients of mechanical restitution, namely e and $é$, introduced in Chapter 2. The algorithm however is modified to generalize to 3D space.

Our algorithm contains components that simulate both the hydrodynamic and the Brownian movements in the bulk when the extremities of the ellipsoidal macromolecular particles do not come into contact with the solid boundaries. The algorithm chooses randomly between hydrodynamic and Brownian events. It is necessary, however, in this novel situation to develop the algorithm to account for the collisions when they occur at the boundary surfaces, to test the sequence of collisions that follow and their consequences.

Different types of possible collisions may be distinguished, labelled here as **A**, **B**, **C**, and **D**, to account for all possible events in the modified algorithm. Furthermore, the boundary surface is considered as atomically flat for the purpose of our simulations in this chapter.

Case A: corresponds to the situation when a random translation diffusion event brings the particle extremities into contact with the surface because of the collision. We may then write

$$z_{\,collision} = \frac{L}{2}|\sin\theta(N)\,\sin\varphi(N)| \tag{16}$$

It is then possible to write the algorithm for a Brownian diffusion translation between the N and N+ 1 events, as

$$z_c(N+1) = z_{collision} + e\,[\,z_c(N) - z_{collision}\,] \tag{17}$$

For a given macromolecular species and given topography of a prepared surface, (Khater 1989) the collision due to the random diffusive processes may be consequently characterized by a given *e* restitution coefficient as in Eq.17. The event following the arrival of the particle into *N+1* moves the particles into other configurations. A comparable algorithm may be given for a collision arising due to the rotation diffusion around a solid angle determined from the angles θ and φ, since these processes are considered intrinsically similar.

Case B: The Brownian rotation diffusion about an angle θ leaves constant the position of the centre of mass between the *N* and *N+1* events, so that $z_c(N) = z_c(N+1)$. One of the extremities of the particle however may go into collision with the solid surface boundary. It follows for this case that that the angle of collision can be written as

$$\theta_{collision} = \sin^{-1}\left[\frac{z_c(N)}{|\sin\varphi(N)|*\frac{L}{2}}\right] \tag{18a}$$

The Brownian rotation algorithm between N and N+ 1 event, due to collisions, becomes then

$$\theta(N+1) = \theta_{collision} + e\,[\,\theta(N) - \theta_{collision}\,] \tag{18b}$$

Case C: corresponds to the Brownian rotation about the angle φ that brings one of the particle extremities into collision with the solid surface boundary. In this situation we have a similar algorithm as for the random Brownian θ rotation, namely

$$\varphi_{collision} = \sin^{-1}\left[\frac{z_c(N)}{\sin\theta(N)*\frac{L}{2}}\right] \tag{19a}$$

$$\varphi(N+1) = \varphi_{collision} + e\,[\,\varphi(N) - \varphi_{collision}\,] \tag{19b}$$

The similarity of the sets of Eqs.18 and Eqs.19, for the Brownian events, is coherent with the choice of Eq.12a and Eq.13a for the Brownian algorithms.

Case **D**: corresponds to the situation when the collision is due to hydrodynamic rotations in the vicinity of the solid surface boundary. The particle in this situation, between the successive N and N+ 1 event, turns about the contact point determined by the collision in-between, into a solid angle described by the coordinate angles θ and φ

$$\varphi(N + 1) = \varphi(N) + e'[\frac{\pi}{2} - \varphi(N)] \qquad (20a)$$

$$\theta(N + 1) = \theta(N) + e'[\frac{\pi}{4} - \theta(N)] \qquad (20b)$$

$$z_c(N + 1) = \frac{L}{2} [|\sin\theta(N + 1) \sin\varphi(N + 1)|] \qquad (20c)$$

The restitution coefficient *é* characteristic of hydrodynamic events, is treated separately from that for Brownian events, *e*, although both will be treated as random variables, in the interval [0, 1], for the purpose of our simulations.

In our simulations the dynamics for the possible collision events of the macromolecular ellipsoidal particles, as in cases **A**, **B**, **C** and **D**, are introduced through a special algorithm code. This allows us to follow the behaviour of the macromolecular particle over $N = 10^8$ elementary events due to stochastic Brownian and causal hydrodynamic movements for a single simulation run.

3.4 Simulation Results for Ellipsoidal Forms of Colloidal Particles in Bulk solution

The simulation results are presented in bulk and for the depletion layer over the interval $0 \leq \zeta = z/L \leq 0.5$ next to the solid surface boundary for different ellipsoidal particles with different aspect ratio r_e. As stated the simulations are carried out for an *atomically flat* surface boundary at $\zeta = 0$, which is used as the reference plane corresponding to the lowest material levels that a particle extremity can touch in diffusive collisions.

There are difficulties to create polymer particles with controlled ellipsoidal shapes with a required aspect ratio. A large and documented literature of research results however shows an extended range of different families of ellipsoidal shaped colloidal particles from industrial and natural production (Champion, Katare et al. 2007; Park, Saffari et al. 2010). Such particles can be found at the microscopic scale, as well as at the scales nano scale (as pointed

out in Chapter 1). The simulations may be run indifferently for both types of particles. Furthermore, (Han, Alsayed et al. 2009) used video-microscopy measurements to calculate the diffusion under different confinement conditions for polymethyl methacrylate (PMMA) and polystyrene (PS) ellipsoidal particles, which present microscopic features. For these latter particles the collected images are reproduced in Fig III.5 showing different aspect ratios, r_e, which renders them hence useful as a reference for our numerical simulations.
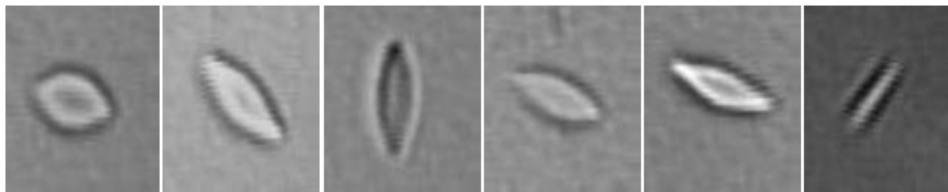
Fig III.5 Microscopic images of six ellipsoidal particles as a function of aspect ratio r_e , increasing from left to right (Han, Alsayed et al. 2009), as 2, 2.85, 2.92, 3.3, 3.55, and 8

In particular we will consider simulating for particles in bulk solutions, distant from the surface boundary, with the following aspect ratios: r_e = 1.02, 1.2 and 2. The last aspect ratio corresponds to the first of the above series, which is interesting in itself in case of potential experimental results. The first and second, however, are outside the above series, but correspond to the interesting case of nearly spherical particles.

We shall also consider the simulations for particles in the depletion layer in the vicinity of the surface boundary, for ellipsoidal particles with aspects ratios: r_e = 2, 2.85 and 3.55.

3.4.1 PDF Simulation results for ellipsoidal forms of colloidal particles in bulk solution

FigIII.6a, b and c, FigIII.7a, b and c and FigIII.8a, b and c, present the angular normalized PDF distributions, P (θ, φ), as a ***3D contour fill surface***, over the plane (θ, φ), for ellipsoidal macromolecular particle in the bulk solution, for different Peclet numbers α. The results correspond to gradually increasing the Peclet number from a relatively low value, as in FigIII.6a, b and c, to a medium value in FigIII.7a, b and c, and then to a high value in FigIII.8a, b and c. This is done in each case for the aspect ratios: r_e = 1.02, 1.2, and 2 which correspond in each group respectively to a, b and c. The angles θ and φ represent the orientation angle for the ellipsoidal particles in the 3D-spatial frame. Note that we use a color scheme in these figures, where ***red*** corresponds to the highest probability for the PDF distributions, and ***black*** to the lowest. Note also that their absolute numerical values need not necessarily have the same value from one set of figures to another.

In general, the simulation results, valid for the open interval

$$\varphi =] \, 0°, \, 180° \, [$$

indicate that for low flow conditions with a typically low Peclet number $\alpha = 1$, the Brownian effect is dominant for the particles in comparison with the hydrodynamic motion. For relatively medium and high flow, which correspond to typically medium and high Peclet numbers $\alpha = 10$ and 100, respectively, the influence of Brownian motion is less important compared to that due to the hydrodynamic motion. For the higher Peclet flow the macromolecular particle orients increasingly in the direction of the flow under the dynamic equilibrium conditions. Moreover, and regardless of the value of the aspect ratio value, the PDF probability around $\theta = 0$ and $\varphi = \pi/2$ increases with increasing α.

FigIII.6a, 6b and 6c, present the simulation results for the normalized PDF distributions of the colloidal particles in the bulk solution, under the conditions of dynamic equilibrium, as a function of a fixed small Peclet number, $\alpha = 1$, with increasing aspect ratios $r_e = 1.02, \, 1.2$ and 2. The *nearly* spherical particles for aspect ratio $r_e = 1.02$, yield the results presented in FigIII.6a. These indicate, as expected, a relatively uniform distribution in the (θ, φ) plane, with already some perceptible symmetry about the $\varphi = \pi/2$ direction. We find this symmetry for all the results of the numerical simulations since the Brownian motion dictates this. To understand FigIII.6a it is important to recall that a particle with spherical symmetry, for which the aspect ratio is strictly $r_e = 1$, has no preferential axis with respect to the flow direction or with respect to the vorticity axes. For such a perfect symmetry we expect that the PDF would be perfectly uniform in the (θ, φ) plane. FigIII.6b shows next the normalized PDF distributions for the greater $r_e = 1.2$ aspect ratio. In this case the PDF distribution is visibly different from that for $r_e = 1.02$, for which the colloidal suspension acquires an orientation tendency, with a distribution that presents particle concentrations (***orange colour***) in the limited domain $\theta = [-20°, 80°]$ for all φ. This tendency to concentrate in a small partial domain is accentuated for the larger $r_e = 2$ aspect ratio, as can be observed in FigIII.6c, where the colloidal suspension tends to regroup in significant concentrations in the narrower solid angle window $\{ \, \theta \approx [10°, \, 40°] \, , \varphi \approx [30°, \, 150°] \, \}$.

We have also carried out numerical simulations for colloidal particles in the bulk with aspect ratios $r_e = 1.2$ and 2, for the range of Peclet numbers, $\alpha = 1, \, 10$, and 100, as above for $r_e = 1.02$. The results are presented in the column figures of FigIII.7 and FigIII.8 respectively. It is then possible to compare the PDF simulation results in another sense by comparing them at a fixed aspect ratio for a series of Peclet numbers. FigIII.7a and FigIII.8a give the normalized PDF distributions for colloidal particles in the bulk solution, with aspect ratio $r_e = 1.02$, for $\alpha = 10$ and 100, and these are compared accordingly with the results in FigIII.6a.

Simulation results for the bulk at low Peclet number α for different aspect ratios
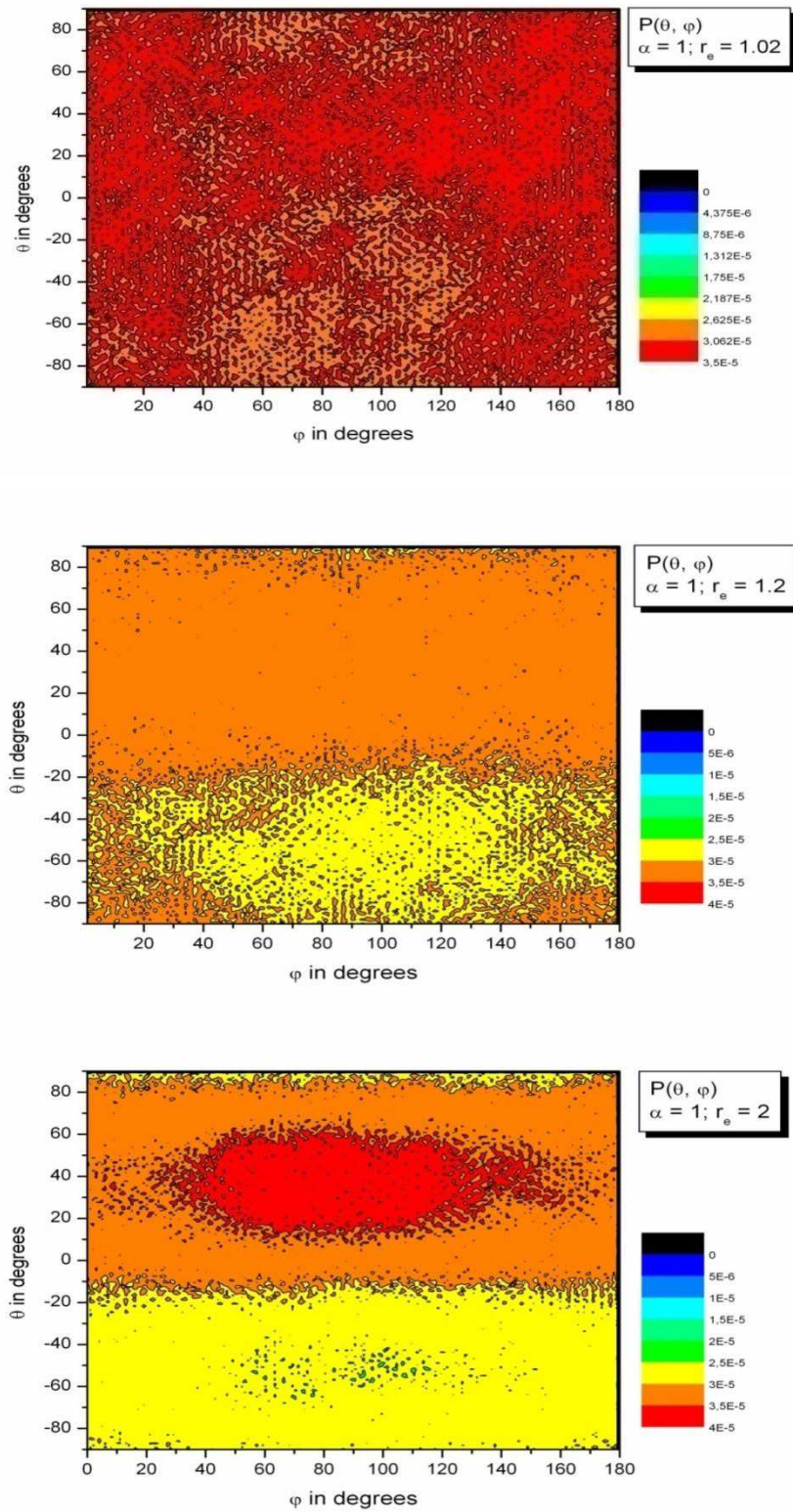
FigIII.6 Simulation results for normalized angular PDF, P (θ, φ), in the bulk at law Peclet number $\alpha = 1$ a): $r_e = 1.02$; (b): $r_e = 1.2$; (c): $r_e = 2$

Simulation results for the bulk at medium Peclet number α for different aspect ratios
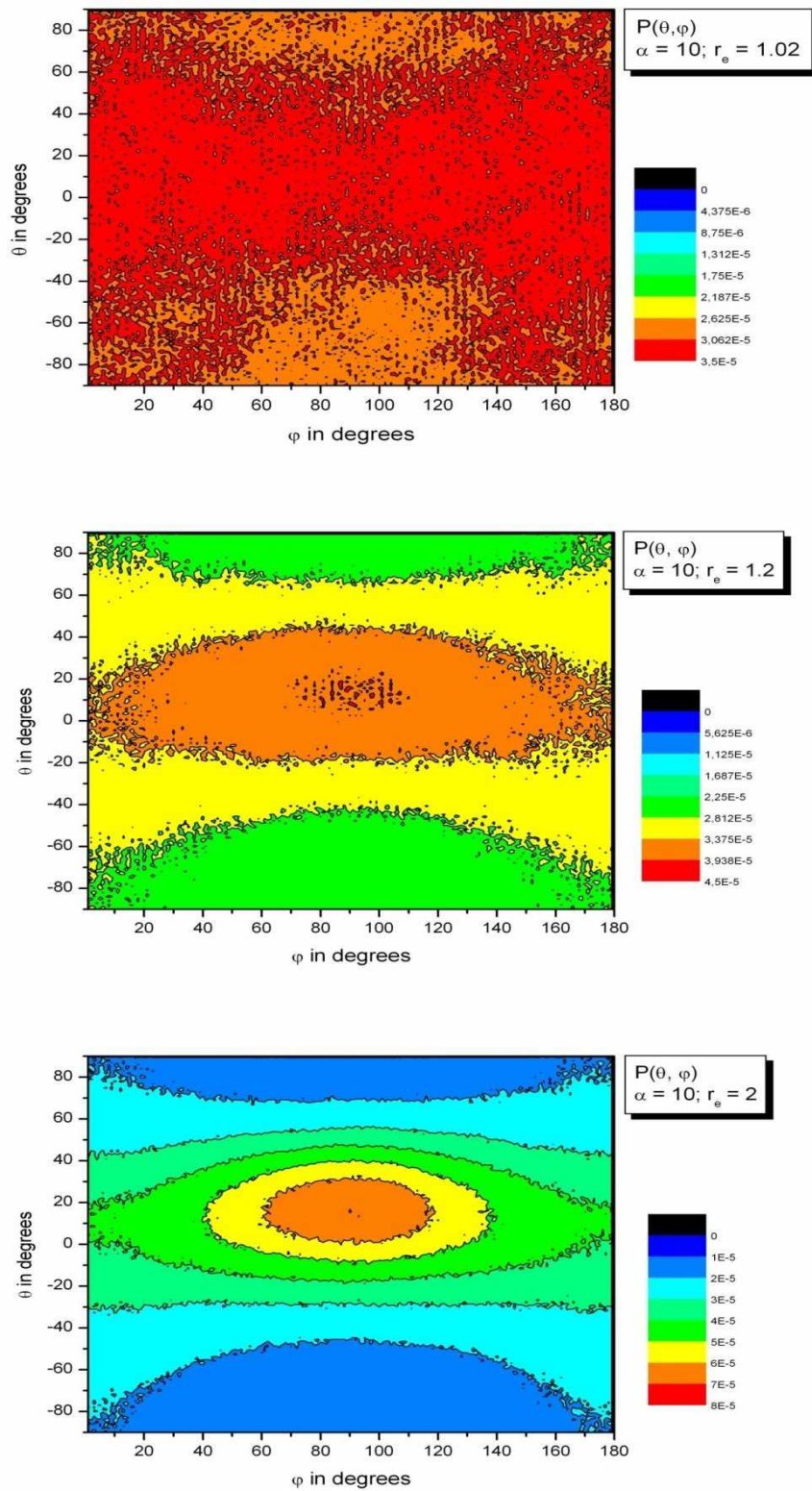
FigIII.7 Simulation results for normalized angular PDF, P (θ, φ), in the bulk at medium Peclet number α = 10 a): r_e = 1.02; (b): r_e = 1.2; (c): r_e = 2

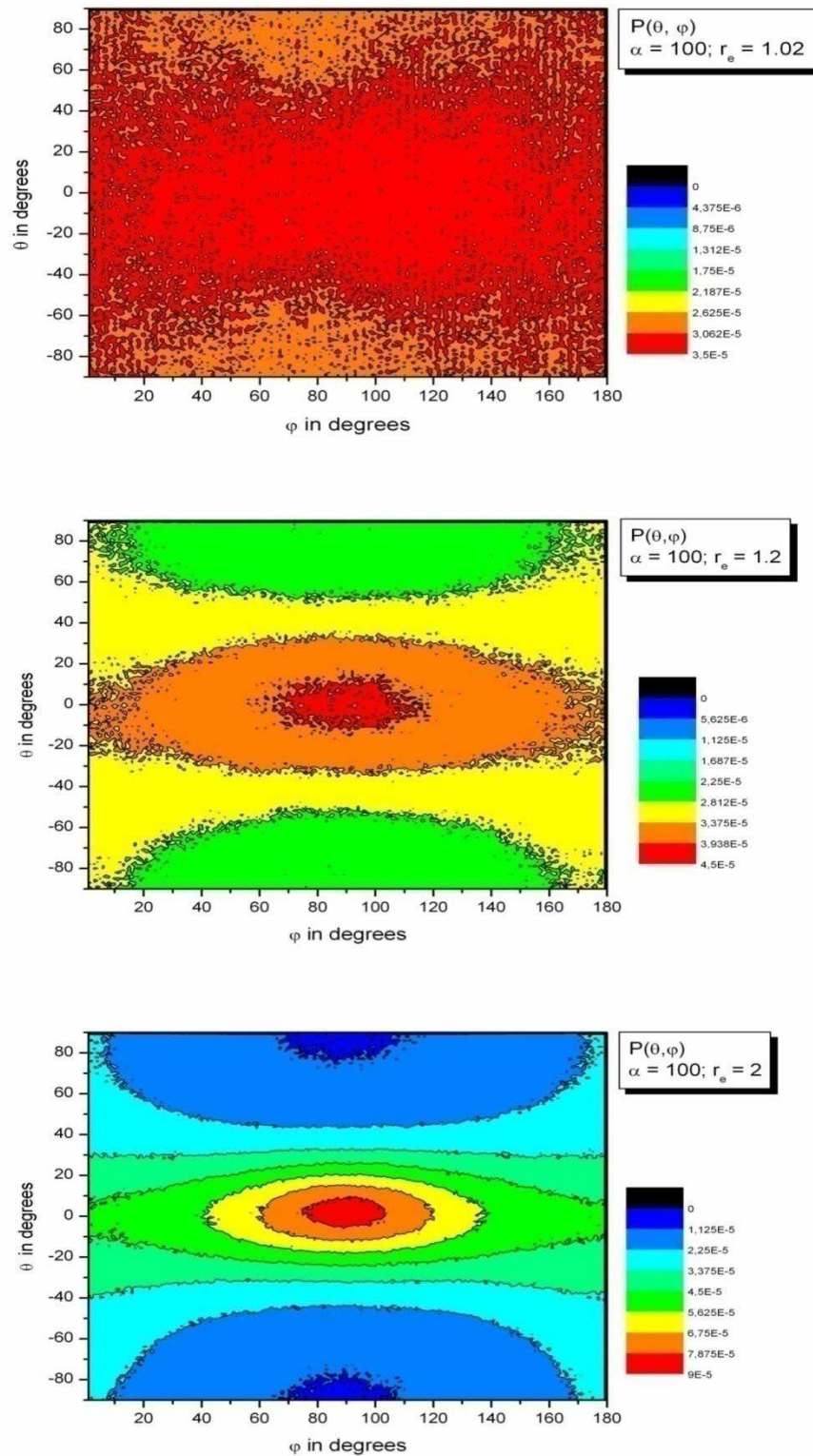**Simulation results for the bulk at high Peclet number α for different aspect ratios**

FigIII.8 Simulation results for normalized angular PDF, P (θ, φ), in the bulk at high Peclet number α = 100 a): r_e = 1.02; (b): r_e = 1.2; (c): r_e = 2

Comparing the PDF results of FigIII.6a, FigIII.7a and FigIII.8a, it is evident that increasing the Peclet number α for the fixed aspect ratio, r_e = 1.02, does not change the overall aspect of the normalized PDF distributions. Increasing the strength of the hydrodynamics flow increases, however, the concentration of the particles in the direction of flow and reduces the importance of the contribution of the Brownian motion.

Comparison of FigIII.6b, FigIII.7b, and FigIII.8b, shows next the simulation results for colloidal suspensions with aspect ratio r_e = 1.2, for the increasing Peclet number, α = 1, 10, and 100. It is again observed that increasing the flow will accentuate the PDF distributions into smaller windows in the (θ, φ) plane. In contrast with the calculated effects at small α, the results for medium and high hydrodynamic flow conditions show that the colloidal particles tend to regroup in significant concentrations, under the conditions of dynamic equilibrium, in the narrow solid angle window of { $\theta \approx [-10°, 10°]$, $\varphi \approx [60°, 120°]$ } for α = 10 as in FigIII.7b, and still narrower solid angle window { $\theta \approx [-10°, 10°]$, $\varphi \approx [70°, 110°]$ } for α = 100 in FigIII.8b. The simulation results results in FigIII.6c, FigIII.7c and FigIII.8c present the same tendency for the larger aspect ratio r_e = 2, presenting even narrower windows.

3.5 PDF Simulation results for ellipsoidal particles in the depletion layer

The simulation results for the normalized PDF distributions are presented for the colloidal particles with aspect ratios r_e = 1.02, 2 and 3.55, over the **depletion layer $0 \leq \zeta \leq 0.5$**, where ζ = z/L defines the particle centre of mass with respect to the adjacent *atomically flat* solid surface boundary. To analyze the results for the depletion layer, we divide it into two regions: **region I ($0 \leq \zeta < 0.2$)** and **region II ($0.2 < \zeta \leq 0.5$)**. These regions have typically nano-metric of thicknesses, for a variety of particles, region I being adjacent to the boundary.

3.5.1 PDF Simulation results in region I ($0 < \zeta \leq 0.2$) of the depletion layer under different hydrodynamic flow conditions

For aspect ratio 2.85, and 3.55

FigIII.9a, b and c show results for the normalized PDF distributions P(θ , φ), presented as a **3D contour fill surface**, with different Peclet numbers α which correspond to typically low, medium and high hydrodynamics flow conditions, for ellipsoidal particles with a small aspect ratio r_e = 2.85 in 3D space. The PDF distributions are observed to be presents significant probabilities for the orientation states in the solid angle window {$\theta \approx [-2°, 2°]$, $\varphi \approx [75°,$

105°] } for α = 1 as in FigIII.9a, the window { θ ≈ [−4°, 4°] , φ ≈ [70°, 110°] } for α = 10 as in FigIII.9b, and still narrower solid angle window { θ ≈ [−10°, 10°] , φ ≈ [80°, 100°] } for α = 100 as in FigIII.9c.

The calculated normalized PDF distributions for aspect ratio r_e = 3.55 are presented in FigIII.10a, b and c. They show significant probabilities in the narrow solid angle window θ ≈ [−1°, 1°] , φ ≈ [75°, 105°] } for α = 1 as in FigIII.10a, the window { θ ≈ [−2°, 2°] , φ ≈ [75°, 105°] } for α = 10 as in FigIII.10b, and still narrower solid angle window { θ ≈ [−2°, 4°] , φ ≈ [80°, 100°] } for α = 100 as in FigIII.10c.

The figures FigIII.10a, b and c, for aspect ratio r_e = 3.55 in 3D, are quite similar to this for aspect ratio r_e = 2.85.

The common features of the normalized PDF distributions for the two different aspect ratios, and for the various hydrodynamic flow conditions, going from low to high Peclet numbers, can be understood in terms of the influence of the solid surface boundary on the equilibrium dynamics of the colloidal particle suspensions. In particular, the extended and approximately equal bases for these distributions, φ ≈ [70°, 110°], running along φ, indicates that the ellipsoidal particles rotate in approximately the same set of families of closed orbits around the vorticity axis φ, regardless of the aspect ratio, and of the Peclet number α, especially for low and medium flow conditions.

However, the influence of the form of the ellipsoidal particles is detectable, it may be observed in the gradual changes of the PDF distributions from FigIII.9c to FigIII.10c, at the relatively high Peclet number α = 100. These changes are naturally related to the influence of the form of the particle, when they are increasingly evacuated by the diffusive collisions from region I of the depletion layer.

The influence of the form of the ellipsoidal particle is further seen from the comparison of FigIII.9c, and FigIII.10c under high flow conditions

As one increases the aspect ratio, it is seen in Fig III. 9c and FigIII.10c that the discontinuities disappear gradually, and that the normalized PDF distributions revert to the more general aspect observed in the other figures.
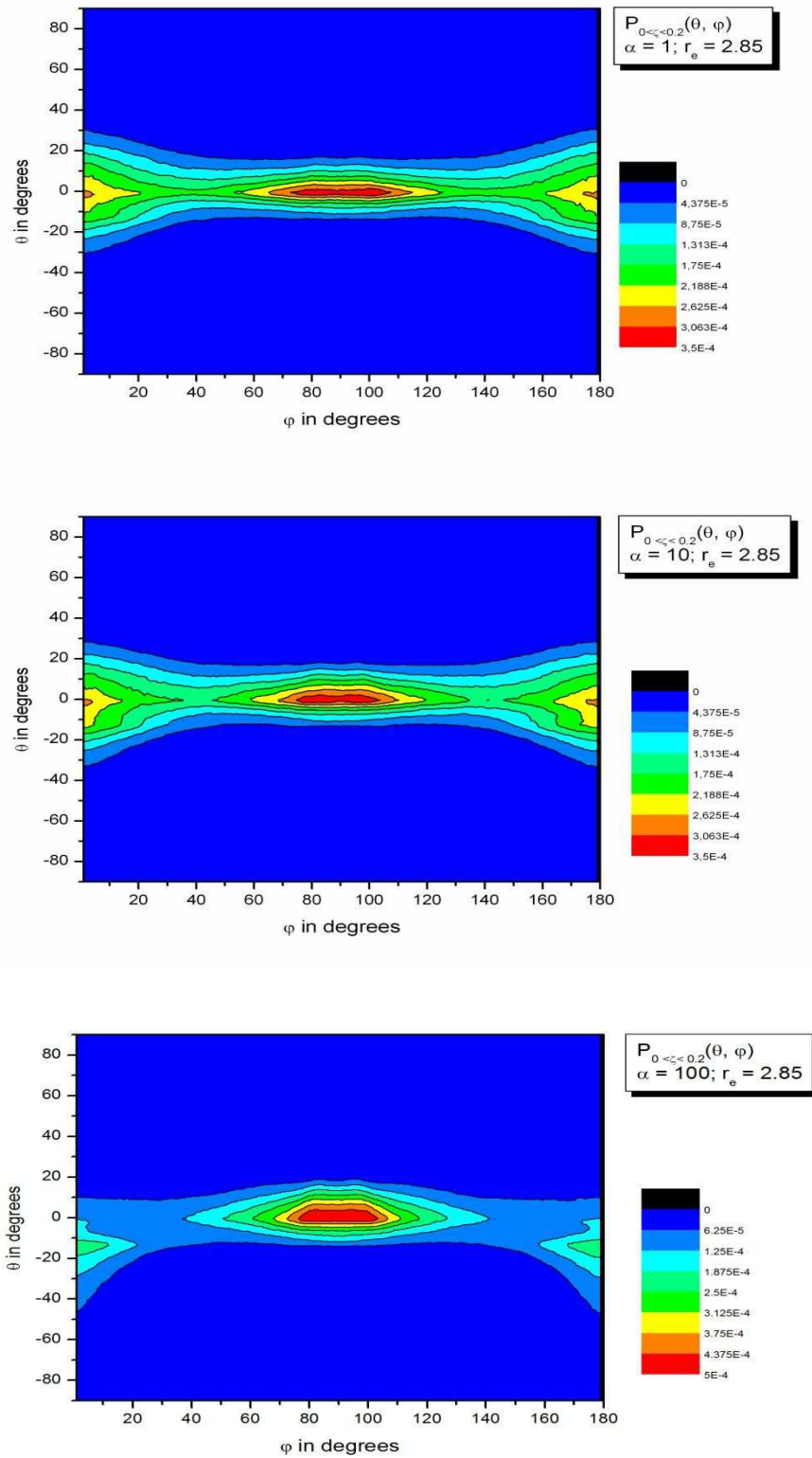
FigIII.9 Simulation results for normalized angular PDF, P (θ, φ), in the 1st region of the depletion layer with aspect ratio r_e = 2.85 with Peclet number a): α = 1; (b): α = 10; (c): α = 100 presented as 3D contour fill surface
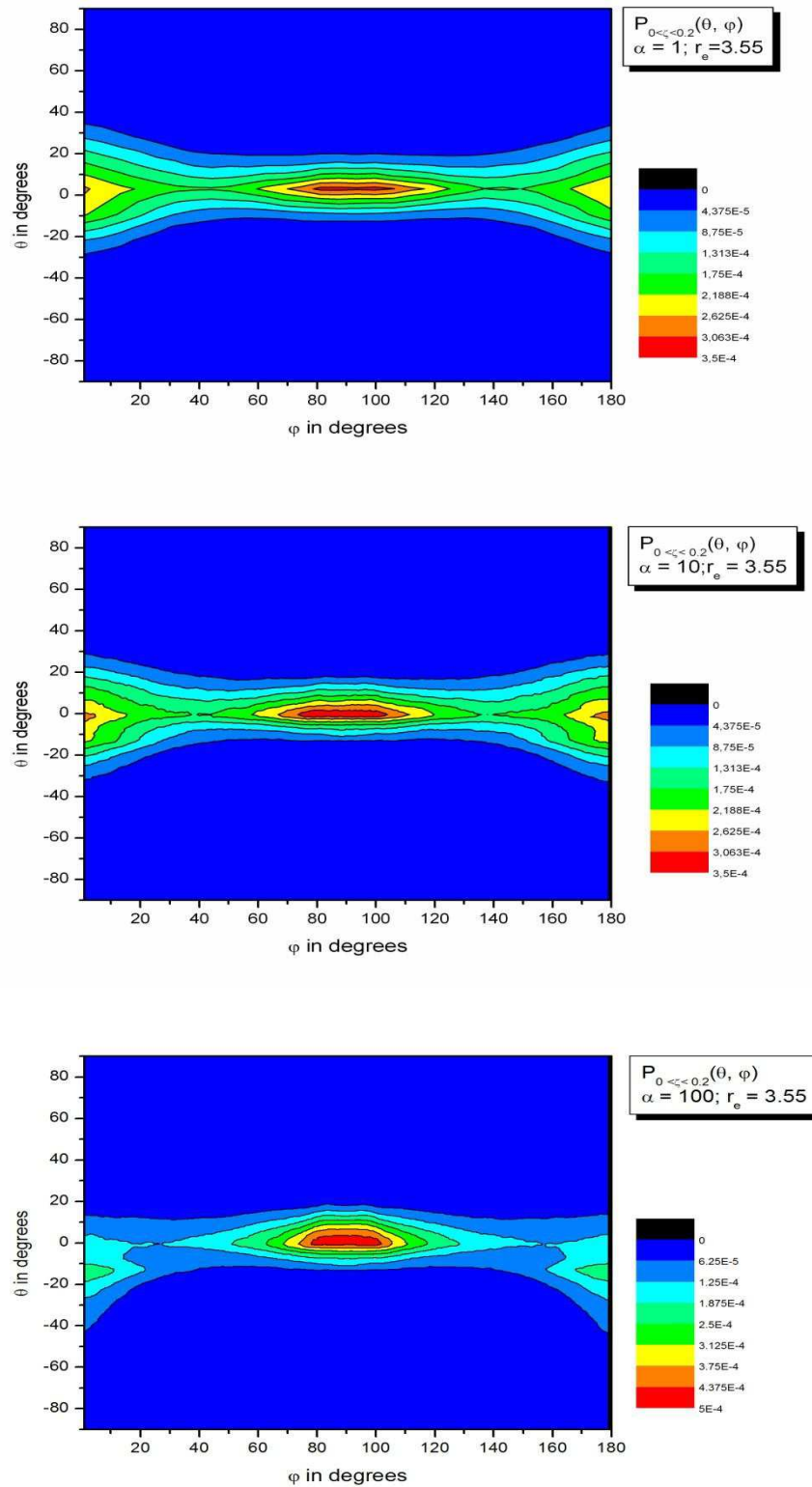
FigIII.10 Simulation results for normalized angular PDF, P (θ, φ), in the 1st region of the depletion layer with aspect ratio r_e = 3.55 with Peclet number a): α = 1; (b): α = 10; (c): α = 100 presented as 3D contour fill surface

3.5.2 PDF Simulation results in region II (0.2 < ζ ≤ 0.5), of the depletion layer under different hydrodynamic flow conditions

For aspect ratio 2, and 3.55

This section presents the results for the normalized PDF distributions P (θ, φ) in region II (0.2 < ζ ≤ 0.5) of the depletion layer, near an *atomically flat* solid surface boundary, for low to high Peclet numbers α, as in the previous section. This is undertaken for different ellipsoidal particle aspect ratios r_e = 2 and 3.55 in the 3D-spatial frame. We shall see that the normalized PDF distributions in region II are quite different from those in region I. The results are presented as the **3D contour fill surface**, and also as the **3D map surface**. The simulation results indicate that the phase space (θ, φ) available to the particles in region II broadens out compared to that in region I. In region II there is effectively a much wider range of solid angles accessible for the dynamics of the particles. The major differences for the PDF distributions in regions I and II arise hence primarily due to a reshuffle of the contributions of the three principal forces acting on the particles, namely Brownian, hydrodynamic and due to diffusive collisions at the surface boundary. Together these forces determine for each region its *characteristic* equilibrium dynamics, and the PDF distributions constitute consequently the basic signatures of these equilibrium dynamics.

In region II, the common features of the normalized PDF distributions shown below for the low hydrodynamic flow conditions, α = 1, for the two aspect ratios, can be understood in terms of the predominating influence of the random Brownian motion and random collisions over that due to the hydrodynamic shear flow. The broad base of the distributions, for all three aspect ratios, indicates that the ellipsoidal particles rotate in a wide set of closed orbits around the vorticity axis under the combined influence of the three forces.

At medium flow conditions α = 10, the normalized PDF distributions start to vary in an important manner with the choice of the aspect ratio r_e = 2 and r_e = 3.55. This is a direct consequence of the rising influence in region II of the hydrodynamic flow coupled to the elongated form of the particles.

The influence of the form of the ellipsoidal particles, for aspect ratio r_e = 2, and 3.55 is detectable under high flow conditions as is visible in FigIII.11c, FigIII.12c, FigIII.14a and FigIII.14b. This influence may be observed in the gradual changes of the PDF distributions from FigIII.14a to FigIII.14b. These changes are naturally related to the influence of the elongated form of the particle, under the diffusive collisions, when they are increasingly

evacuated by these collisions under the hydrodynamic shear flow from region II towards the bulk.
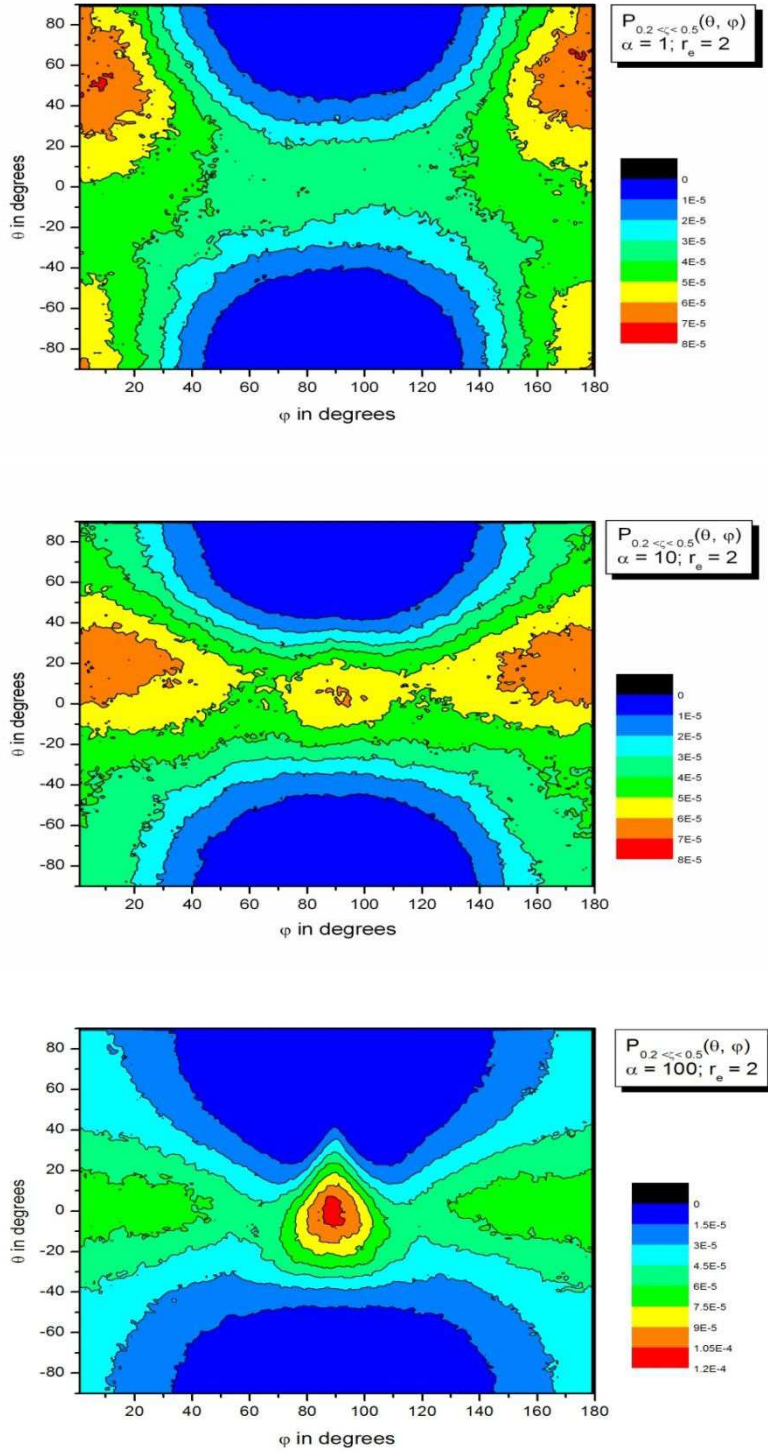
FigIII.11 Simulation results for normalized angular PDF, P (θ, φ), in the 2nd region of the depletion layer with aspect ratio $r_e = 2$ with Peclet number a): $\alpha = 1$; (b): $\alpha = 10$; (c): $\alpha = 100$ presented as 3D contour fill surface
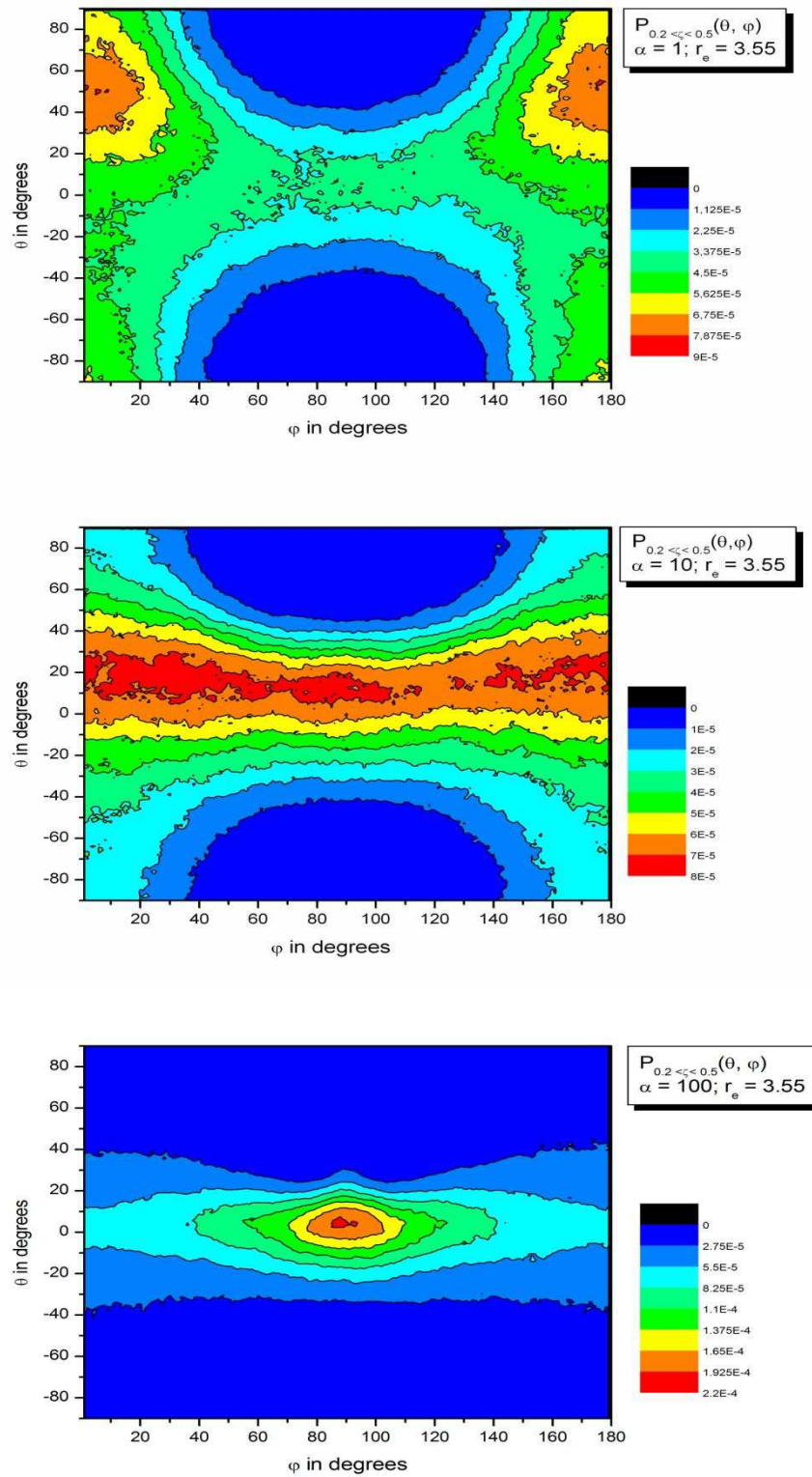
FigIII.12 Simulation results for normalized angular PDF, P (θ, φ), in the 2nd region of the depletion layer with aspect ratio r_e = 3.55 with Peclet number a): α = 1; (b): α = 10; (c): α = 100 presented as 3D contour fill surface
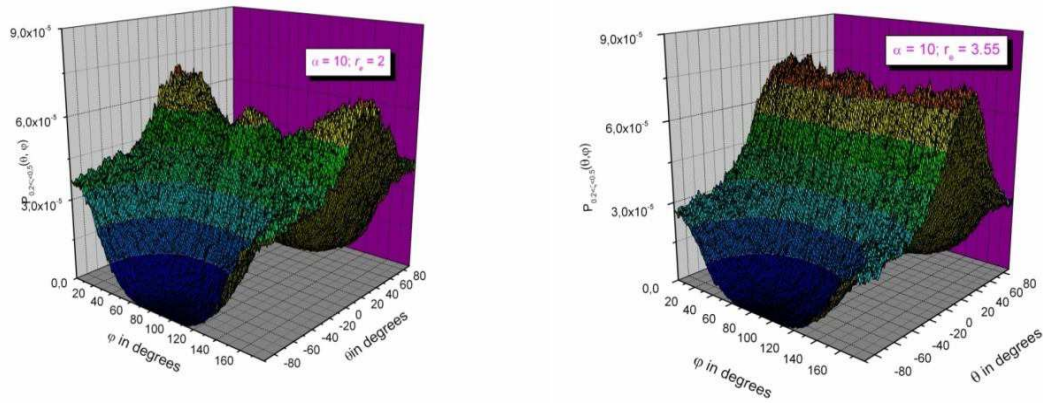
FigIII.13 Simulation results for normalized angular PDF, P (θ, φ), in region II of the depletion layer with Peclet number α = 10; with aspect ratio a): $r_e = 2$; (b): $r_e = 3.55$, presented as 3D Map Surface
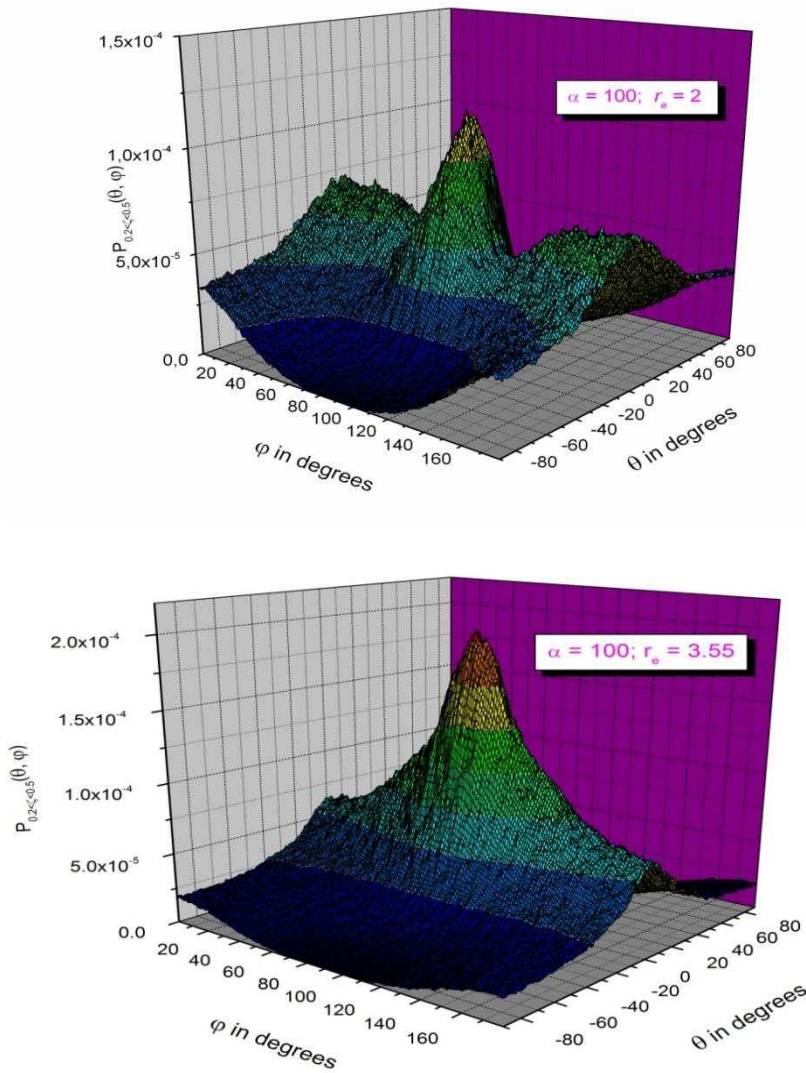
FigIII.14 Simulation results for normalized angular PDF, P (θ, φ), in region II of the depletion layer with Peclet number α = 100; with aspect ratio a): $r_e = 2$; (b): $r_e = 3.55$, presented as 3D Map Surface

3.6 The nematic order tensor S

The nematic phase is characterized by long-range orientation order; i. e. the long axis of the ellipsoidal molecules tends to align along a preferred direction. The locally preferred direction may vary throughout the medium. The geometry and dynamics of the preferred axis, which is defined by a vector n(r), g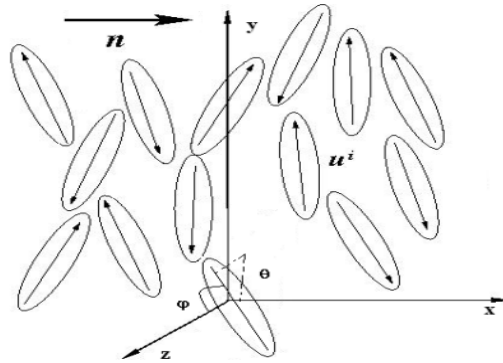iving its local orientation as in FigIII.15, is called a director. The molecules appear to be able to rotate about their long axis, and also there seems to be no preferential arrangement of the two ends of the molecules if they differ.

FigIII.15 Particles orientation in nematic phase; a unit vector $u^{(i)}$ along the axis of ith molecule describes its orientation. The director n shows the average alignment

The molecules are regarded as ellipsoidal rigid particles, such that we can introduce a unit vector $u^{(i)}$ along the axis of ith molecule which describes its orientation. Given the complexity of the colloidal suspension, it is necessary to consider a tensor description of their order which commonly called as the nematic phase order in the solution. A natural order parameter to describe the ordering, is the second rank tensor (Oswald and Pieranski 2005), as follows
.

$$S_{\alpha\beta}(r) = \frac{1}{N} \sum_i \left(u_\alpha^{(i)} u_\beta^{(i)} - \frac{1}{3}\delta_{\alpha\beta} \right) \tag{21}$$

N is the number of ellipsoidal particles in the solution and the indices correspond to Cartesian directions $\alpha, \beta = $ (x, y, z), and $\delta_{\alpha\beta}$ is second rank unit tensor

$$\delta_{\alpha\beta} = \begin{cases} 1 \ if \ \alpha = \ \beta \\ 0 \ if \ \alpha \neq \beta \end{cases}$$

The properties of the order parameter tensor as defined in Eq.21, may be resumed as

1- Since $u_\alpha^{(i)} u_\beta^{(i)} = u_\beta^{(i)} u_\alpha^{(i)}$ and $\delta_{\alpha\beta} = \delta_{\beta\alpha}$, it follows that $S_{\alpha\beta}$ Is a symmetric tensor

$$S_{\alpha\beta} = S_{\beta\alpha}$$

2- $S_{\alpha\beta}$ is traceless:

$$Tr S_{\alpha\beta} = \sum_{\alpha=(x,y,z)} S_{\alpha\alpha} = \frac{1}{N} \sum_{i} \left[\left(u_x^{(i)} \right)^2 + \left(u_y^{(i)} \right)^2 + \left(u_z^{(i)} \right)^2 - \frac{1}{3} 3 \right] = 1 - 1$$

3- The two previous properties reduce the number of independent components for the corresponding 3x3 tensor from 9 to 5.

Transforming Eq.21 to spherical coordinate system

$$u_x = sin\varphi\, cos\theta\ ; u_y = sin\varphi\, sin\theta\ ; u_z = cos\varphi,$$

yields the form

$$S_{\alpha\beta} = \int_{-\pi/2}^{\pi/2} \int_0^\pi sin\,\varphi\, P(\theta,\varphi)\ \left(u_\alpha u_\beta - \frac{1}{3}\delta_{\alpha\beta} \right) d\varphi\, d\theta \qquad (22)$$

As previously, $P(\theta,\varphi)$ is the probability to find the ellipsoidal particles with the orientation given by the angles θ and φ, i.e. the PDF in the 3D-spatial frame . Eqt.22 can hence be presented as

$$S = \int_{\frac{-\pi}{2}}^{\frac{\pi}{2}} \int_0^\pi \begin{pmatrix} sin^2\varphi\, cos^2\theta - \dfrac{1}{3} & sin^2\varphi\, cos\varphi\, sin\theta & sin\varphi\, cos\varphi\, cos\theta \\[2mm] sin^2\varphi\, cos\varphi\, sin\theta & sin^2\varphi\, sin^2\theta - \dfrac{1}{3} & sin\varphi\, cos\varphi\, sin\theta \\[2mm] sin\varphi\, cos\varphi\, cos\theta & sin\varphi\, cos\varphi\, sin\theta & cos^2\varphi - \dfrac{1}{3} \end{pmatrix} sin\varphi\, P(\theta,\varphi) d\varphi\, d\theta$$

Following Eq.21 and Eq.22, the isotropic phase is characterized by S = 0, and he nematic phase by 0 < S < 1. The limit S = 1 corresponds to perfect alignment of all the molecules and, of course, is difficult to realize in practice. S can have a negative value which corresponds to a pancake-like (oblate) molecular distribution, while the positive values of S describe prolate-like distributions. In general, it can be shown that the scalar order parameter S changes in the range from −1/2 to 1 (from perfect oblate to perfect prolate geometry via isotropic phase).

(Hand 1962) introduced another form for the order parameter tensor, with a $Tr\mathsf{S}_{\alpha\beta} = 1$. In spherical coordinates this is expressed as

$$S = \int\limits_{-\frac{\pi}{2}}^{\frac{\pi}{2}} \int\limits_{0}^{\pi} \begin{pmatrix} sin^2\varphi \, cos^2\theta & sin^2\varphi \, cos\varphi \, sin\theta & sin\varphi \, cos\varphi \, cos\theta \\ sin^2\varphi \, cos\varphi \, sin\theta & sin^2\varphi \, sin^2\theta & sin\varphi \, cos\varphi \, sin\theta \\ sin\varphi \, cos\varphi \, cos\theta & sin\varphi \, cos\varphi \, sin\theta & cos^2\varphi \end{pmatrix} sin\varphi \, P(\theta,\varphi) \, d\varphi \, d\theta$$

(23)

This tensor form has been used extensively in the molecular theory for colloidal particles (Doi and Edwards 1978), for fiber-like charged particles (Advani 1987), and in recent research studies (Ausias 2007; Redjeb 2007). This latter Hand form is used henceforth for our purpose and throughout this work, to calculate the nematic order parameter tensor S for the colloidal particles in the bulk liquid and in the depletion layer adjacent to the surface boundaries. Note that the tensor formulation of the nematic order is a generalization of the approach adopted in Chapter 2 for the case of a 2D-spatail frame.

3.6.1 Calculation of the nematic order tensor

For Bulk solution

In this part the order parameter tensor S_{α,r_e} for ellipsoidal particles is calculated for different aspect ratios r_e, and Peclet numbers α. The sense of the indices (r_e, α) on S are evident.

We give next, in matrix form following the Cartesian directions, the numerical results for the calculated S_{α,r_e} in bulk solution for (r_e, α) = (1, 1.02), (100, 1.02), and (1, 2), (100, 2), using the corresponding normalized PDF distributions $P(\theta,\varphi)$ calculated previously in section 3.4

$$S_{1,1.02} \begin{pmatrix} 0.422 & 0 & 0 \\ 0 & 0.409 & 0 \\ 0 & 0 & 0.201 \end{pmatrix} \qquad S_{100,1.02} \begin{pmatrix} 0.429 & 0 & 0 \\ 0 & 0.403 & 0 \\ 0 & 0 & 0.21 \end{pmatrix}$$

$$S_{1,2} \begin{pmatrix} 0.434 & 0 & 0 \\ 0 & 0.403 & 0 \\ 0 & 0 & 0.201 \end{pmatrix} \qquad S_{100,2} \begin{pmatrix} 0.609 & 0 & 0 \\ 0 & 0.243 & 0 \\ 0 & 0 & 0.204 \end{pmatrix}$$

It should be clear from the above that S_{α,r_e} varies with (r_e, α).

The first row of results is for quasi-spherical particles with a small aspect ratio $r_e = 1.02$. for low and high Peclet numbers, $\alpha = 1$ and 100, the results are not significantly modified despite the two orders of magnitude increase in the hydrodynamic flow. It is also noticeable that the preferred alignment in this case is along the X and Y directions in the plane of the flow, as in Fig.III.1, with a weaker component alignment along the Z direction normal to the flow.
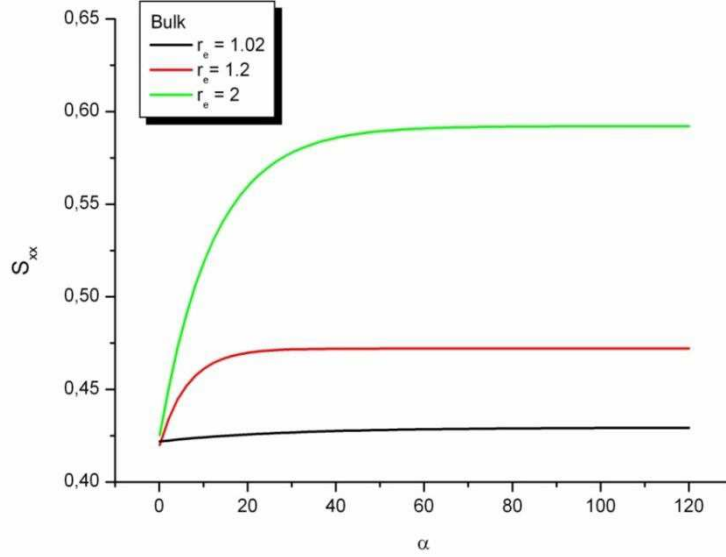
FigIII.16 Nematic order parameter S_{xx} in X-direction as a function of Peclet number a for different ellipsoidal particles in bulk

Increasing the aspect ratio r_e from 1.02
 to 2, under equivalent flow conditions is sufficient to introduce new effects. The favored alignment is visibly in the X direction with weaker component alignments along the Y and Z directions. Increasing the aspect ratio of the ellipsoidal particle gives it distinct and preferential behaviors along X, Y and Z. Indeed in this case it separates its Y behavior from its X behavior. The above results demonstrate that there is no perfect alignment and no isotropic distribution of orientations.

For region II ($0.2 < \zeta \leq 0.5$) in depletion layer

We give in matrix form following the Cartesian directions, the numerical results for the calculated S_{α, r_e} in tensor for ellipsoidal particles in region II ($0.2 < \zeta \leq 0.5$) of the depletion layer for $(r_e, \ \alpha) = (1, 2), (100, 2), \ $ and $ \ (1, 3.55), (100, 3.55),$ using the corresponding normalized PDF distributions $P(\theta, \varphi)$ calculated previously in section 3.5

$$S_{1,2} \begin{pmatrix} 0.39 & 0 & 0 \\ 0 & 0.38 & 0 \\ 0 & 0 & 0.2 \end{pmatrix} \qquad\qquad S_{100,2} \begin{pmatrix} 0.61 & 0 & 0 \\ 0 & 0.26 & 0 \\ 0 & 0 & 0.14 \end{pmatrix}$$

$$S_{1,3.55} \begin{pmatrix} 0.4 & 0 & 0 \\ 0 & 0.35 & 0 \\ 0 & 0 & 0.23 \end{pmatrix} \qquad\qquad S_{100,3.55} \begin{pmatrix} 0.76 & 0 & 0 \\ 0 & 0.21 & 0 \\ 0 & 0 & 0.1 \end{pmatrix}$$

The first row of results is for aspect ratio $r_e = $ 2. for low and high Peclet numbers, $\alpha = 1$ and 100, the results are not significantly modified despite the two orders of magnitude increase in the hydrodynamic flow. It is also noticeable that the preferred alignment in this case is along the X and Y directions in the plane of the flow, with a weaker component alignment along the Z direction normal to the flow. Increasing the aspect ratio r_e from 2 to 3.55, under equivalent flow conditions is sufficient to introduce new effects. The favored alignment is visibly in the X direction with weaker component alignments along the Y and Z directions. Increasing the aspect ratio of the ellipsoidal particle gives it distinct and preferential behaviors along X, Y and Z.
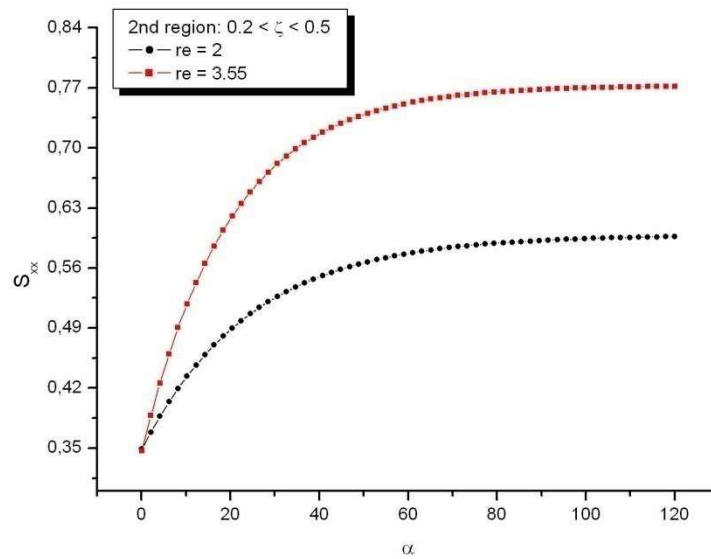
FigIII.17 Nematic order parameter S_{xx} in X-direction as a function of Peclet number a for different ellipsoidal particles in 2nd region of the depletion layer

The results in region II show that as we increase the aspect ratio r_e, the colloidal particles tend to approach the aligned state along the X direction at a greater rate with respect to α, with the simultaneous decrease of order along the Y and Z directions. We interpret this as a

consequence of the novel equilibrium dynamics for the large aspect ratio particles. In region II there is effectively a much wider range of the accessible orientation states on (θ, φ).
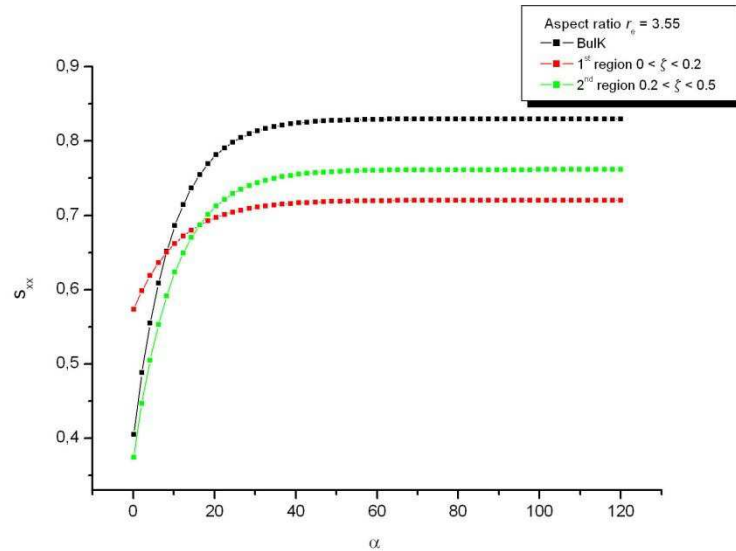
The nematic order parameter S_{xx} along the flow direction as a function of Peclet number α for different ellipsoidal particles in region II of the depletion layer are presented in

FigIII.18 Nematic order parameter S_{xx} in X-direction as a function of Peclet for the bulk and regions I and II of the depletion layer, for a flat surface boundary, for aspect ratio $r_e = 3.55$

FigIII.18 presents our calculated results for the nematic order parameter S_{xx} for the dilute colloidal suspensions of the macromolecular ellipsoidal-like particles with aspect ratio $r_e = 3.55$, along the X-direction, as a function of an increasing Peclet number α from 0.1 to 120. The results illustrate the diverse behavior of the nematic order for the different regions of the solution, namely the bulk, and regions I and II of the depletion layer, over a significant range of the flow hydrodynamics.

In particular the alignment goes to $S_{xx} \sim 0.8$ for $\alpha = 120$ in the bulk solution, which corresponds to a nearly perfect order alignment at $S_{xx} = 1$ is attainable in this region for very high Peclet numbers. Given the nature of the diffusive and random interactions which the particles suffer at the solid surface boundaries, this perfect order is not possible for the colloidal suspensions in the depletion layer. At very high Peclet numbers, however, there is still a significant partial order in the depletion layers, greater in region II than in region I.

The analysis of the results obtained for ellipsoidal particles with a relatively big aspect ratio r_e = 3.55, in regions I and II of the depletion layer FigIII.10 and FigIII.12, explains why we do not attain the same behavior of the nematic order parameter for regions I and II. In region II there is a greater liberty for the ellipsoidal-like particles to move in real space than in region I, which is translated in terms of a lesser order alignment, for small to medium α. Increasing the hydrodynamic flow at relatively larger α brings the colloidal suspension in region II to increasing alignment, whereas in region I there is a limit to such alignment imposed by the random diffusive collisions attained rather rapidly at $\alpha \sim 20$.

3.6 Conclusions

We have developed algorithms and carried out numerical simulations to analyze the dynamics of dilute colloidal suspensions of macromolecular particles in solutions flowing on open channel pore. The pores are modeled in a three-dimensional frame of reference with boundaries. The colloidal particles are subject to hydrodynamic forces, Brownian motion and random collisions at the solid surface boundaries of the pores. The numerical simulations are carried out to calculate in particular the spatial statistical PDF distributions for the spatial the orientations of ellipsoidal particles in colloidal suspensions in a solution under equilibrium dynamics for the bulk liquid and in the depletion layers next to an atomically flat solid surface boundary. The simulations are developed for and open pore channels, and are valid throughout the space of the pores and in the boundary depletion layers, for a wide variety of hydrodynamic flow conditions, at low, intermediate, and high flow, characterised by the rotational Peclet number and for variable aspect ratios characteristic of the ellipsoidal particles under study.

Our simulations yield directly the nematic order parameter for colloidal suspensions in the over its tensorial representation, for a variety of forms of ellipsoidal particles selected to correspond to real polymer particles.

References

Advani, S. (1987). "The Use of Tensors to Describe and Predict Fiber Orientation in Short Fiber Composites." J. Rheol. **31**(8): 751.

Advani, S. G. and C. L. Tucker (1990). "A numerical simulation of short fiber orientation in compression molding." Polymer Composites **11**(3): 164-173.

Ausias, G. (2007). Une rhéologie des suspensions :Applications aux composites à matrices thermoplastiques. Habilitation à Diriger des Recherches, Université de Bretagne-Sud.

Bernard P, B. (2002). "Particles as surfactants—similarities and differences." Current Opinion in Colloid & Interface Science **7**(1-2): 21-41.

Boeder, P. (1932). "Über Strömungsdoppelbrechung." Zeitschrift für Physik A Hadrons and Nuclei **75**(3): 258.

Bretherton, F. P. (1962). "The motion of rigid particles in a shear flow at low Reynolds number." Journal of Fluid Mechanics **14**(02): 284-304.

Champion, J. A., Y. K. Katare, et al. (2007). "Making polymeric micro- and nanoparticles of complex shapes." Proceedings of the National Academy of Sciences **104**(29): 11901-11904.

Doi, M. and S. F. Edwards (1978). "Dynamics of rod-like macromolecules in concentrated solution. Part 1." Journal of the Chemical Society, Faraday Transactions 2: Molecular and Chemical Physics **74**: 560-570.

Férec, J. (2009). "Modeling fiber interactions in semiconcentrated fiber suspensions." J. Rheol. **53**(1): 49.

Folgar, F. and C. L. Tucker (1984). "Orientation Behavior of Fibers in Concentrated Suspensions." Journal of Reinforced Plastics and Composites **3**(2): 98-119.

Fuji, M., H. Fujimori, et al. (1998). "Wettability of Glass-Bead Surface Modified by Trimethylchlorosilane." The Journal of Physical Chemistry B **102**(51): 10498-10504.

Gavze, E. and M. Shapiro (1997). "Particles in a shear flow near a solid wall: Effect of nonsphericity on forces and velocities." International Journal of Multiphase Flow **23**(1): 155-182.

Han, Y., A. Alsayed, et al. (2009). "Quasi-two-dimensional diffusion of single ellipsoids: Aspect ratio and confinement effects." Physical Review E **80**(1): 011403.

Hand, G. L. (1962). "A theory of anisotropic fluids." Journal of Fluid Mechanics **13**(01): 33-46.

Holm, R. and D. Söderberg (2007). "Shear influence on fibre orientation." Rheologica Acta **46**(5): 721-729.

Hsu, R. and P. Ganatos (1994). "Gravitational and zero-drag motion of a spheroid adjacent to an inclined plane at low Reynolds number." Journal of Fluid Mechanics **268**: 267-292.

Jeffery, G. B. (1922). "The Motion of Ellipsoidal Particles Immersed in a Viscous Fluid." Proceedings of the Royal Society of London. Series A **102**(715): 161-179.

Jia, H., G. Zhu, et al. (2003). "Catalytic behaviors of enzymes attached to nanoparticles: the effect of particle mobility." Biotechnology and Bioengineering **84**(4): 406-414.

Khater, A. (1989). "INTENSITY REFLECTION COEFFICIENTS OF ATOMICALLY IRREGULAR SURFACES IN PHONON SCATTERING." Europhys. Letters **2**(7): 539.

Moses, K. B., S. G. Advani, et al. (2001). "Investigation of fiber motion near solid boundaries in simple shear flow." Rheologica Acta **40**(3): 296-306.

Oswald, P. and P. Pieranski (2005). NEMATIC AND CHOLESTERIC LIQUID CRYSTALS. United States of America, CRC Press, Taylor & Francis Group.

Park, J. I., A. Saffari, et al. (2010). "Microfluidic Synthesis of Polymer and Inorganic Particulate Materials." Annual Review of Materials Research **40**(1): 415-443.

Ranganathan, S. and S. G. Advani (1991). Fiber-fiber interactions in homogeneous flows of nondilute suspensions, SOR.

Redjeb, A. (2007). Simulation numérique de l'orientation de fibres en injection de thermoplastique renforcé, École Doctorale 364 : Sciences Fondamentales et Appliquées.

Sokolov, A., I. S. Aranson, et al. (2007). "Concentration Dependence of the Collective Dynamics of Swimming Bacteria." Physical Review Letters **98**(15): 158102.

Trevelyan, B. J. and S. G. Mason (1951). "Particle motions in sheared suspensions. I. Rotations." Journal of Colloid Science **6**(4): 354-367.

Chapter 4

Simulations for the dynamics and nematic order of dilute colloidal suspensions of rod-like particles flowing in 3D space in the bulk and near solid boundaries

Abstract: Algorithms for the dynamics of a special class of molecular particles, namely rigid rod-like particles, for which the aspect ratio is much greater than unity, are developed. The simulations to calculate the *equilibrium* PDF distributions for rod-like particles in suspension in a fluid under hydrodynamic flow are carried out for two types of solid boundaries, the ideal atomically flat and the rough surface boundaries. To accomplish this we investigate in this chapter in particular the influence of the roughness on the choice of the hydrodynamic boundary conditions. The simulation results for the PDF distributions for the spatial positions and the orientations of rod-like particles are calculated. They are calculated over several orders of magnitude of the rotational Peclet number. They demonstrate the importance and significance of modeling in a three-dimensional spatial frame as compared to the simulation results based in the Boeder approach over a two-dimensional spatial frame. In particular we are able to produce a complete topography for the PDF distributions segmented as a hierarchy in the depletion layer, covering a complete range of orientations in 3D spatial frames. The simulations permit to calculate, for the colloidal suspension, the nematic order parameter over its tensorial representation, rod-like particles our results for the nematic order parameter which may be calculated locally inside the space of the depletion layer are innovating and represent a new input as regards these systems.

4.1 Introduction

Interest in the dynamics and average orientations of macromolecules at dilute concentrations in the bulk and near solid surface boundaries of a flowing liquid in 3D, stems from the physical effects that may arise when these solutions flow, with their load of macromolecules, inside channels of mesoscopic dimensions (Storm, Chen et al. 2003). The statistics for the spatial positions of the centers of mass and for the orientations of such macromolecules, under equilibrium dynamics inside the flow, are then of particular interest.

In Chapter 2 we presented the dynamic behavior of dilute colloidal suspensions of macromolecular rod-like particles in confining and open pores with rough surface boundaries modeled by the 2D-spatial frame. In contrast in Chapter 3 we presented the dynamic behavior of suspensions of ellipsoidal-like particles in the bulk solution and in the depletion layer, flowing inside pores modeled in the 3D-spatial frame, with flat surface boundaries. This illustrates the differences for the dynamics of such suspensions between confining channels and unbounded channels between two and one solid surface boundaries.

This chapter deals with the modelling of a limiting case of ellipsoidal-like particles, namely the rod-like particles for which the aspect ratio is much greater than unity. This is treated separately because of its particular interest. The rod-like particles represent a wide class of polymer and naturally existing as the TMV tobacco virus, and may also be produced synthetically for a wide range of technological exploitation, such as the carbon nano-tube.

Our study is focused on the determination of the PDF distributions and the corresponding nematic order for the positions and the orientations of the dilute colloidal suspensions of rod-like particles in the bulk, and near surface boundaries, in the 3D-spatial frame. We have chosen also to calculate, by the available simulation codes, the interactions of these particles with two types of surfaces, namely the ideally flat and the rough surface. This permits to illustrate the difference between the equilibrium dynamics in the depletion layer next to both types of surfaces, and to compare their corresponding distributions.

In section 4.2, we present a general introduction to the problem and to liquid bulk macromolecular dynamics under Brownian and hydrodynamic motion. Section 4.3 presents the developed algorithm for diffusive collisions at the surface boundaries of mesopores systems. Section 4.4 presents simulation results for the spatial and angular distributions under a variety of hydrodynamic and the particles centres of mass positions with respect to the solid surface boundary for rod-like particle, the conclusions are presented in section 4.5.

4.2 Bulk model dynamic for rod-like particles in 3D space

In this chapter, we generalize the algorithm to numerical simulations in a 3D-spatial frame of Cartesian space, with a view to calculate the PDF distributions of rod-like macromolecular particles in dilute colloidal suspensions in the bulk solution and in the vicinity of solid surface pore boundaries. Furthermore, the surfaces are considered for two cases, namely as ideal atomically flat and as rough with a Gaussian profile.

We apply Jeffery's equations (Jeffery 1922) for the ellipsoidal particles chapter 3 to the motion of rigid rod-like cylindrical forms by extending the length L of the macromolecular particles (major axis) in comparison with its diameter d (minor axis), so that the aspect ratio increases greatly $r_e = L/d \gg 1$. It is this version which is used in the present model to calculate the PDF distributions for the macromolecular rigid rod-like particles. Jeffery's differential equations become for $r_e \gg 1$ in the form

$$\left[\frac{d\theta}{dt}\right] = -\gamma' \left(\frac{r_e^2}{r_e^2+1}\right) \sin^2\theta - \gamma'\left(\frac{1}{r_e^2+1}\right)\cos^2\theta \cong -\gamma'\sin^2\theta \qquad (1)$$

$$\left[\frac{d\varphi}{dt}\right] = \frac{\gamma'}{4}\left(\frac{r_e^2-1}{r_e^2+1}\right)\sin 2\varphi \, \sin 2\theta \cong \frac{\gamma'}{4}\sin 2\varphi \, \sin 2\theta \qquad (2)$$

As previously γ' is the shear rate, θ is defined as the angle of the particle with respect to flow direction, φ the vorticity axis. The rod-like particles lie in the plane of shear for $\varphi = \frac{\pi}{2}$. It can be seen that the angular velocity θ' is maximum when the rod-like particles is perpendicular to the flow direction ($\theta = \frac{\pi}{2}$) and minimum when it is aligned along the flow direction($\theta = 0$).

In the simulations using the Jeffery's equations, the hydrodynamic force tends to align the macromolecular rod-like particles in the direction of the shear flow, θ is taken as positive or negative in the trigonometric sense, where $\theta = 0$, parallel to the flow direction, is taken parallel to the boundary walls. To simulate the effects of hydrodynamic effects in a time interval Δt between two successive simulation events labelled s and $s+1$, we compute $\Delta\theta_{hyd}(s+1;s)$, and $\Delta\varphi_{rot}(s+1;s)$, the hydrodynamic rotation about the centre of mass of the particles, using the following algorithm

$$\Delta\theta_{hyd}(s+1;s) = \theta(t_{s+1}) - \theta(t_s) \cong -\gamma'\sin^2\theta \, \Delta t \qquad (3)$$

$$\Delta\varphi_{hyd}(s+1;s) = \varphi(t_{s+1}) - \varphi(t_s) \cong \frac{\gamma'}{4}\sin 2\varphi \, \sin 2\theta \, \Delta t \qquad (4)$$

As above we can eliminate Δt from the algorithm, therefore we get the following equations:

$$\Delta\theta_{hyd} = -\frac{1}{2}\alpha \ sin^2\theta \ \Delta\varphi_{rot}^2 \tag{5}$$

$$\Delta\varphi_{hyd} = \frac{1}{8}\alpha \ (sin \ 2\theta \ sin \ 2\varphi) \ \Delta\varphi_{rot}^2 \tag{6}$$

For the purpose of the present simulations, we typically take $\Delta\varphi_{rot} = 0.003 \ rad$, for a wide range of the Peclet number α. This value for $\Delta\varphi_{rot}$ may however be varied for different experimental conditions and different Peclet numbers.

4.3 Simulation algorithms for pore channels with rough surface boundaries

In this section, we present the model for numerical simulations. The joint PDF distributions, P(θ, φ), are calculated as a function of angular ordinations θ and φ, of the macromolecular rod-like particles and normalized distance of their center of mass ζ measured from a reference plane at the boundary surface.

To develop an appropriate simulation algorithm at the solid boundaries for 3D spatial frames, we use the same coefficients of mechanical restitution, namely *e* and *é*, in Chapter 2, in the same time the same algorithm in Chapter 3 is modified and generalized to adequate the rod-like particles in 3diminsional space.

In this chapter we hence generalize our simulations and corresponding algorithms to investigate the influence of boundary roughness on the fluid flow.

(Panzer, Liu et al. 1992) gave an analytical equation for calculating the effective boundary height h_{eff} for a gently rough surface modeled by small cosine-shaped surface variations, given by h(z) = h_{max}/2 + (h_{max}/2) x cos(qz), where q is the wave number. It is applicable for the analysis of hydrodynamic events in a solution flowing between parallel infinite planes separated by a distance 2D much greater than the roughness measure h_{max}. The corresponding h_{eff} length is found to be:

$$h_{eff} = \frac{h_{max}}{2}\left(1 + k\frac{1-\frac{1}{4}k^2+\frac{19}{64}k^4+\mathcal{O}(k^6)}{1+k^2\left(1-\frac{1}{2}k^2\right)+\mathcal{O}(k^6)}\right) \tag{7}$$

Figure IV.1 (Kunert and Harting 2007). The effective boundary height h_{eff} is found between the deepest valley at h_{min} and the highest peak at h_{max}. For the utilized geometries the average roughness is equal to half the maximum height $R_a = h_{max}/2$

Eqt (7) is valid only for $k = \frac{qh_{max}}{2} \ll 1$, however, for realistic surfaces, k can become substantially larger than 1 causing this theoretical approach to fail.

(Kunert and Harting 2007) showed by a combination of experimental measurements and numerical simulations as regards the above approach, that the position of the effective boundary height is dependent on the shape of the roughness elements, i.e. for strong surface distortions it is between 1.69 and 1.90 times the average height of the roughness $R_a = h_{max}/2$. These authors also simulate the flow over surfaces generated from Atomic Force Micrsocopy (AFM) data of gold-coated glass used in micro-flow experiments by (Vinogradova and Yakubov 2006), and found that the height distribution of such a surface is Gaussian and that a randomly arranged surface with a similar distribution gives the same result for the position of the effective boundary. Later (Harting and Kunert 2008) investigated Gaussian distributed heights with different widths σ, and found that the effective height h_{eff} can be fitted by:

$$h_{eff} = (1 + 3.1\,\sigma)h_{max}/2$$

At this point, we generalize our algorithm and corresponding simulations, and we take h_{eff} as defining a new *reference boundary* for the walls; and we suppose that the liquid is stationary (not moving) for $y < h_{eff}$.

We can hence define a new variable y_{new} to specify the position of the centre of mass of the macromolecular rod-like particles from this reference surface

$$y_{new} = y - h_{eff} \tag{8}$$

and

$$v(y_{new}) = \gamma' y_{new} + \gamma'\Lambda \tag{9}$$

Then we calculate a renormalized shear rate as:

$$R_{new} = \frac{v(y_{new}) - v(y_{new} = 0)}{y_{new} - 0} = \frac{\gamma' y_{new} + \gamma' \Lambda - \gamma' \Lambda}{y_{new}}$$

As may be observed, this leads to an unchanged shear ratio

$$\alpha_{new} = \frac{R_{new}}{D_{rot}} = \frac{\gamma'}{D_{rot}} = \alpha$$

and the Peclet number α remains valid for this rough boundary.

However, the effective width of the pore is modified from $2D$ to $2D - 2h_{eff}$ because of the new boundary conditions over the rough surface boundaries. This is duly taken account of in the numerical simulations, by admitting that the extremity may randomly touch different step levels in the rough surface boundary beyond   .
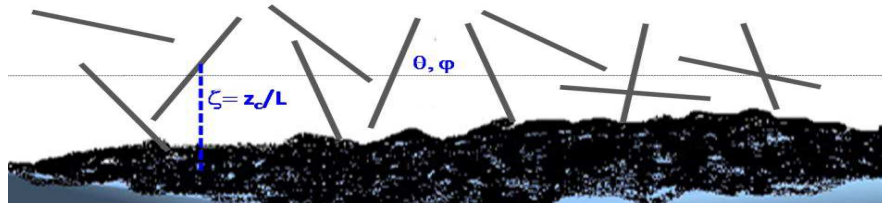

Fig IV.2 Schematic representaion of the rigid-like macromolecular particles in the depeltion layer next to the solid surface boundary of one of the two plates which confine the hydrodynamic flow of the fluid

4.4 Simulation results for pore channels with rough / flat surface boundaries

The simulation results are presented in bulk and for the depletion layer over the interval $0 \leq \zeta = z/L \leq 0.5$ next to the solid surface boundary. The simulations in the depletion layer are made for *atomically flat* boundaries and Gaussian rough surface. $\zeta = 0$ is the reference plane corresponding to the lowest material levels that a particle extremity can touch in diffusive collisions.

### 4.4.1 PDF distribution results for rod-like particles in the bulk solution

FigIV.3a, b and c, present the normalized PDF orientation distributions, P (θ, φ), as a *3D contour fill surface*, over the plane (θ, φ), for rod-like macromolecular particle in the bulk of a flowing solution in the 3D-spatial frames, for different Peclet numbers α, from a relatively low value, as in FigIV.3a, to a medium value in FigIV.3b, and then to a high value FigIV.3c.

The angles θ and φ represent the orientational angle in 3D space for the rod-like particles. Note that we use a color scheme in these figures: **red** corresponds to the highest probability for the PDF distributions, and **black** to the lowest. Note also that the absolute numerical values per color interval may vary from one set of PDF figures to another.

The colloidal rod-like particles in dilute suspensions orient themselves in the bulk of the flowing solution under the influence of two primary forces, the Brownian and the hydrodynamic forces. The hydrodynamic force tends to act on the particle to turn it in the shear flow (θ = 0˚). In general, the simulation results, valid for the open interval

$$\varphi =]\, 0°,\ 180°\, [,$$

Indicate that for low flow conditions, with a typically low Peclet number α = 1, the Brownian effect is dominant for the rod-like particles in comparison with the hydrodynamic motion. For relatively medium and high flow conditions, which correspond to typically medium and high Peclet numbers, α = 10 and 100, the influence of Brownian motion is less important. For the higher Peclet flow the particle orients increasingly in the direction of the flow under the dynamic equilibrium conditions. Moreover, the PDF probability around $\theta = 0$ and $\varphi = \pi/2$ increases with increasing α.
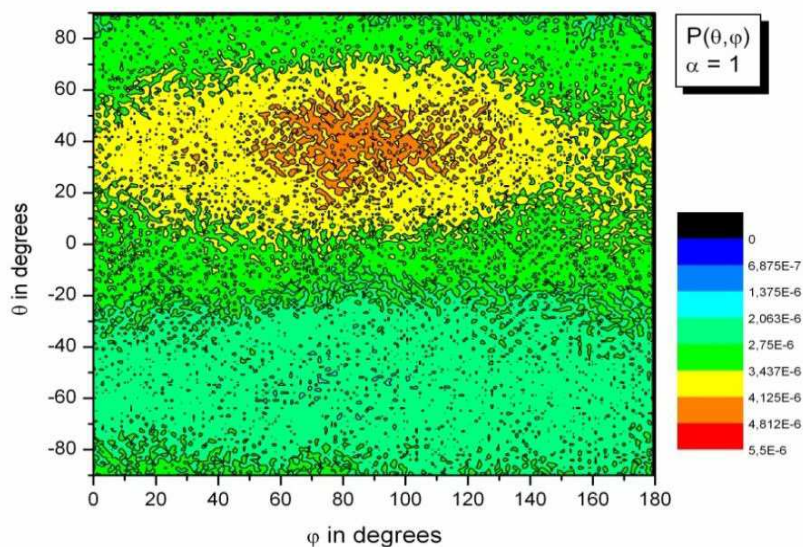
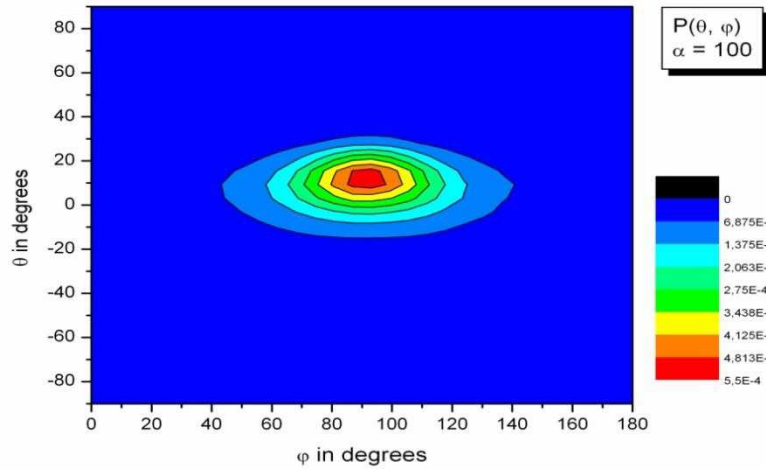FigIV.3a Simulation results for normalized angular PDF, P (θ, φ), in the bulk for Peclet number α = 1
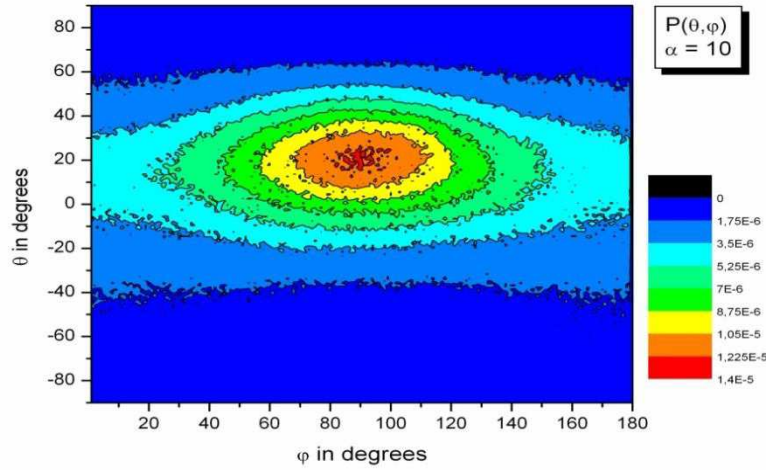
FigIV.3b Simulation results for normalized angular PDF, P (θ, φ), in the bulk for Peclet number α = 10

FigIV.3c Simulation results for normalized angular PDF, P (θ, φ), in the bulk for Peclet number α = 100

The PDF distribution for α = 1, FigIV.3a, shows a broad and symmetrical distribution about the vorticity axes $\varphi = \pi/2$, with appreciable suspension concentration in the orientation solid angle frame { $\theta \approx$ [10°, 50°], $\varphi \approx$ [60°, 120°] }. The existence of this broad distribution in the (θ, φ) plane comes from the Brownian motion. Increasing the hydrodynamic flow to Peclet numbers α = 10, and 100, increases the tendency of the colloidal particles to regroup in significant concentrations, under equilibrium dynamics, in the narrow solid angle frames { $\theta \approx$ [10°, 30°] , $\varphi \approx$ [80°, 100°] } for α = 10, as in FigIV.3b, and in the yet smaller frame { $\theta \approx$ [5°, 10°] , $\varphi \approx$ [85°, 95°] } for α = 100, as in FigIV.3c.

4.4.2 PDF distribution results for rod-like particles in the depletion layer

The simulation results are presented for the depletion layer next to the solid surface boundary, within the interval $0 \leq \zeta = z/L \leq 0.5$. The simulations are performed for two types of solid surface boundaries, namely the atomically flat and the rough on the scale of the particle length, for comparison. Note that the reference surface boundary plane is different for theses two types of surfaces. For the purpose of the simulations, we consider in particular a Gaussian distribution of step heights to model the rough surface.

Our simulation results, based on the Jeffry algorithm applied for the 3D-spatial frame, present novel and significant effects observable in the 3D-spatial frame (Atwi, Khater et al. 2010), beyond those from previous calculations in the 2D-spatial frame (Hijazi and Khater 2001; Hijazi and Khater 2008).

PDF Simulation results in region I of the depletion layer, $(0 < \zeta \leq 0.2)$**, under variable hydrodynamic flow conditions**

FigIV.4 shows the calculated result for the normalized PDF distributions at Peclet number $\alpha = 1$, in the 3D-spatial frame, near an atomically *flat* surface boundary, as a function of the accessible orientation angles θ and φ, in region I of the depletion layer, $(0 < \zeta \leq 0.2)$ where $\zeta = 0$ defines the flat solid surface boundary. In comparison the PDF distributions for a Gaussian *rough* surface are presented in FigIV.5, where $\zeta = 0$ corresponds to h_{eff} in the rough boundary.
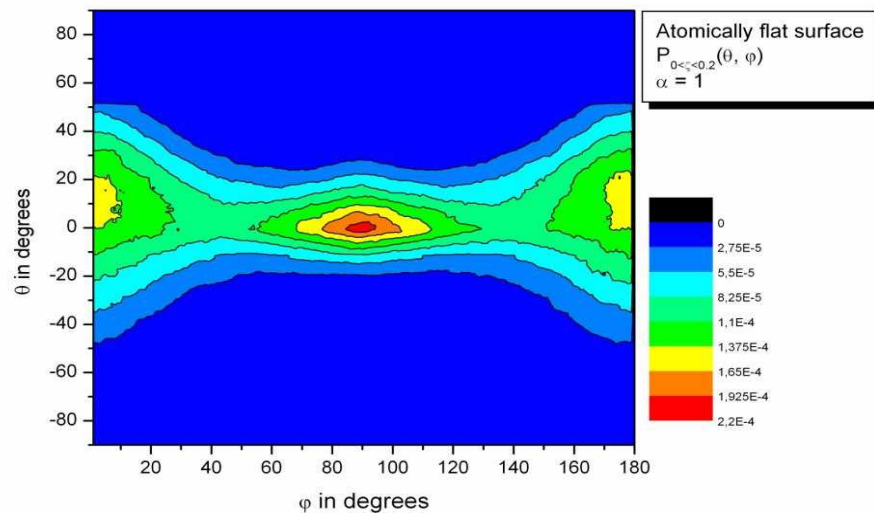
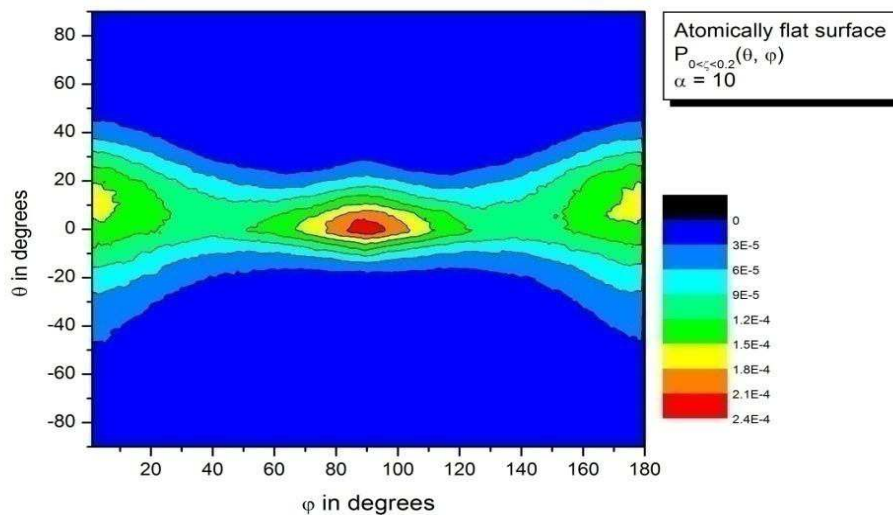FigIV.4 Simulation results for the normalized PDF distributions, P $_{0<\zeta<0.2}$ (θ, φ), at Peclet number $\alpha = 1$, in the depletion layer near an *atomically flat* solid surface boundary, presented as 3D contour fill surface
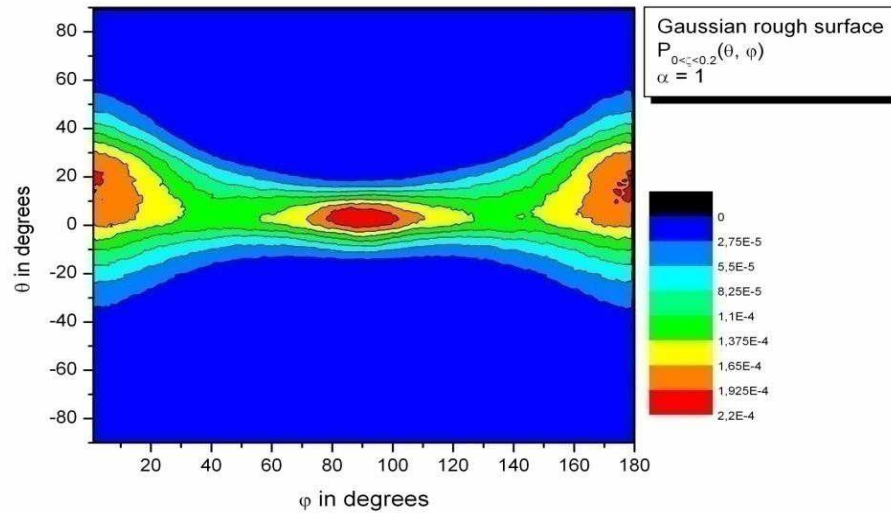
FigIV.5 Simulation results for the normalized PDF distributions, $P_{0<\zeta<0.2}$ (θ, φ), at Peclet number $\alpha = 1$, in the depletion layer near a *Gaussian rough* solid surface boundary.

The calculated normalized PDF distributions of the colloidal suspension in region I, next to the *flat* surface boundary, present significant *peak* probabilities with an absolute value $\sim 2.2 \times 10^{-4}$ (*red*) for the orientation states in the solid angle $\{\theta \approx [-2°, 2°]$, $\varphi \approx [87°, 93°]\}$, as in FigIV.4, while for the *rough* surface boundary the PDF distribution narrows down to the solid angle $\{$ $\theta \approx [-4°, 4°]$, $\varphi \approx [80°, 100°]$ $\}$ with a comparable absolute value $\sim 2.2 \times 10^{-4}$ as in FigIV.5.
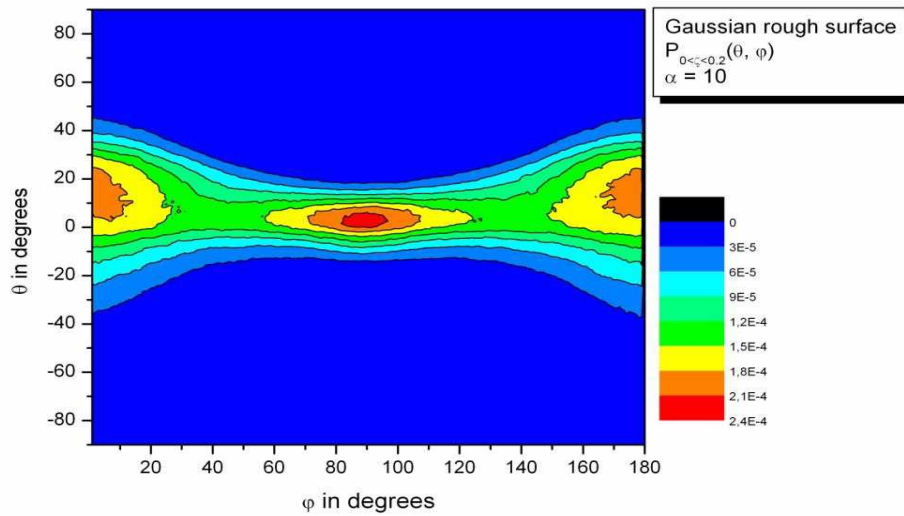

FigIV.6 Simulation results for the normalized PDF distributions, $P_{0<\zeta<0.2}$ (θ, φ), at Peclet number $\alpha = 10$, in the depletion layer near an *atomically flat* solid surface boundary.

FigIV.7 Simulation results for the normalized PDF distributions, P $_{0<\zeta<0.2}$ (θ, φ), at Peclet number α = 10, in the depletion layer near a *Gaussian rough* solid surface boundary.

The effects observed in FigIV.4 and FigIV.5 for α = 1, continue to be observed, for both the flat and the rough surface boundaries, for α = 10 as in FigIV.6 and FigIV.7, and for α = 100 as in FigIV.8 and FigIV.9. However, they clearly show that increasing the Peclet number heightens and increases the PDF distributions of the colloidal particle suspensions in the plane of the shear flow φ = π/2.

FigIV.8 Simulation results for the normalized PDF distributions, P $_{0<\zeta<0.2}$ (θ, φ), at Peclet number α = 100, in the depletion layer near an *atomically flat* solid surface boundary.
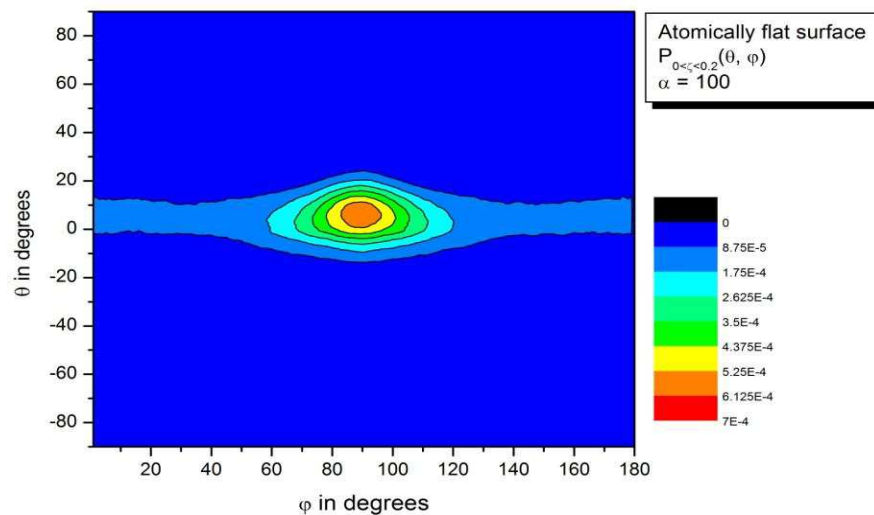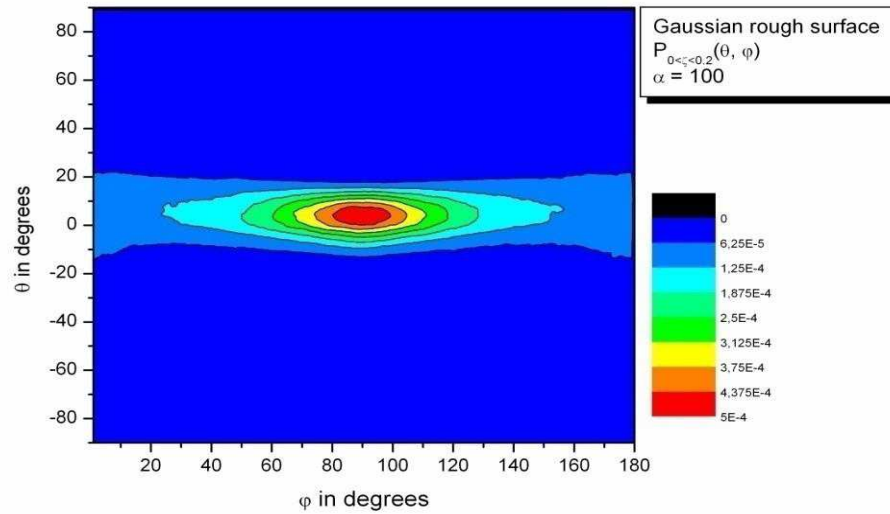
FigIV.9 Simulation results for the normalized PDF distributions, P $_{0<\zeta<0.2}$ (θ, φ), at Peclet number $\alpha = 10$, in the depletion layer near a *Gaussian rough* solid surface boundary.

The roughness of the surface boundary seems to have a *focusing effect* with a heightened and précised probability distribution, compared to the PDF from the flat boundary, for an equal number of particles or of simulation events. Both distributions are broad based indicating that the rod-like particles rotate in a set of closed orbits around the vorticity axis φ. Such orbits are determined by two random forces, the Brownian diffusion movement and the diffusive collisions of the particle extremities at the solid surface boundaries, and from the hydrodynamic shear force, under their equilibrium dynamics.

PDF Simulation results in region II of the depletion layer, $(0.2 < \zeta \leq 0.5)$**, under variable hydrodynamic flow conditions**

This section presents the results for the normalized PDF orientation distributions P (θ, φ) for macromolecular rod-like particles in region II of the depletion layer ($0.2 < \zeta \leq 0.5$). The equilibrium dynamics are treated for two types of surface boundaries, namely the atomically *flat* surface and the Gaussian *rough*, for the medium and high Peclet numbers α in the 3D-spatial frame. We shall see that the normalized PDF distributions in region II are quite different from those in region I.

FigIV.10 and FigIV.11, for respectively flat and rough surface boundaries, present our calculated results for the normalized PDF distributions P (θ, φ) for medium hydrodynamic flow condition $\alpha = 10$. Equally, FigIV.12 and FigIV.13, present similar results for the high flow condition $\alpha = 100$. The simulation results indicate in general that the part of the phase space (θ, φ) available to the particles in region II increases compared to that in region I, due to

110

the wider range of angles accessible to the dynamics of the particles when they move out from region I towards the bulk solution.

In region II, the calculated normalized PDF distributions for the typically medium flow conditions $\alpha = 10$, in the neighbourhood of the atomically *flat* surface boundary, present significant *peak* probabilities with a value $\sim 1 \times 10^{-4}$ (*red*) for the orientation states in the solid angle $\{\theta \approx [10°, 20°], \varphi \approx [80°, 100°]\}$ as in FigIV.10, while in the neighbourhood of the Gaussian *rough* solid surface the PDF distribution narrows down to the solid angle $\{\theta \approx [10°, 20°], \varphi \approx [85°, 95°]\}$ with a greater value $\sim 1.8 \times 10^{-4}$ as FigIV.11.

The results for high flow conditions $\alpha = 100$, show comparable effects as above, regrouping the colloidal suspension at significant *peak* probabilities with a value $\sim 6 \times 10^{-4}$ in the solid angle $\{\theta \approx [7°, 14°], \varphi \approx [85°, 95°]$ in the neighbourhood of the *flat* surface boundary as in FigIV.12, and with a value $\sim 7 \times 10^{-4}$ in the solid angle $\{\theta \approx [5°, 10°], \varphi \approx [87°, 93°]\}$ in the neighbourhood of the Gaussian *rough* solid, as in FigIV.13.
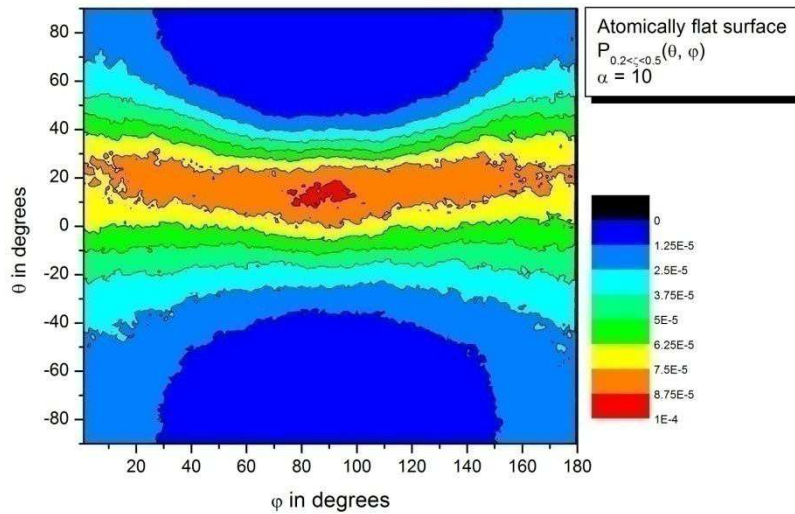
FigIV.10 Simulation results for the normalized PDF distributions, P $_{0.2 < \zeta < 0.5}$ (θ, φ), at Peclet number $\alpha = 10$, in the depletion layer near an *atomically flat* solid surface boundary.

The simulation results for region II indicate that the part of the phase space (θ, φ) available to the rod-like particles in region II is greater than that available for region I. Effectively, there is a much wider range of solid angles in region II accessible for the dynamics of the particles including those available when touching the solid boundary. The major differences for the PDF distributions in regions I and II arise hence primarily due to the reorganization of the contributions of the three principal forces acting on the particles, under equilibrium dynamics, namely Brownian, hydrodynamic and by diffusive collisions at the surface boundary.

Together these forces determine for each region its *characteristic* equilibrium dynamics, and the PDF distributions constitute consequently the signature of such equilibrium dynamics. It is again observed that increasing the flow will accentuate the PDF distributions into smaller solid angle frames in the (θ, φ) plane.
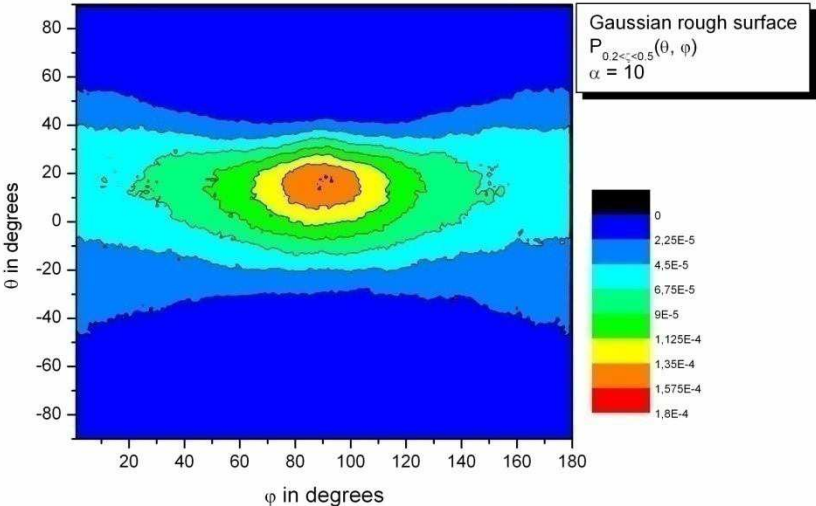
FigIV.11 Simulation results for the normalized PDF distributions, P $_{0.2<\zeta<0.5}$ (θ, φ), at Peclet number $\alpha = 10$, in the depletion layer near a *Gaussian rough* solid surface boundary.

FigIV.12 Simulation results for the normalized PDF distributions, P $_{0.2<\zeta<0.5}$ (θ, φ), at Peclet number $\alpha = 100$, in the depletion layer near an *atomically flat* solid surface boundary.
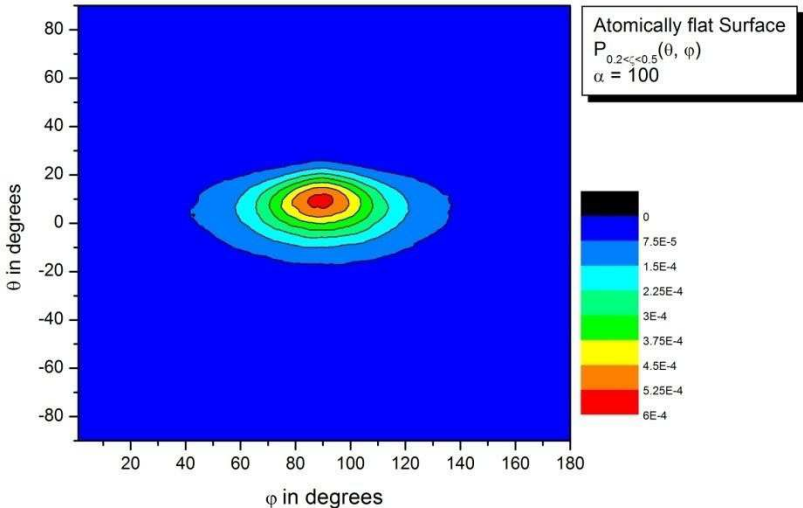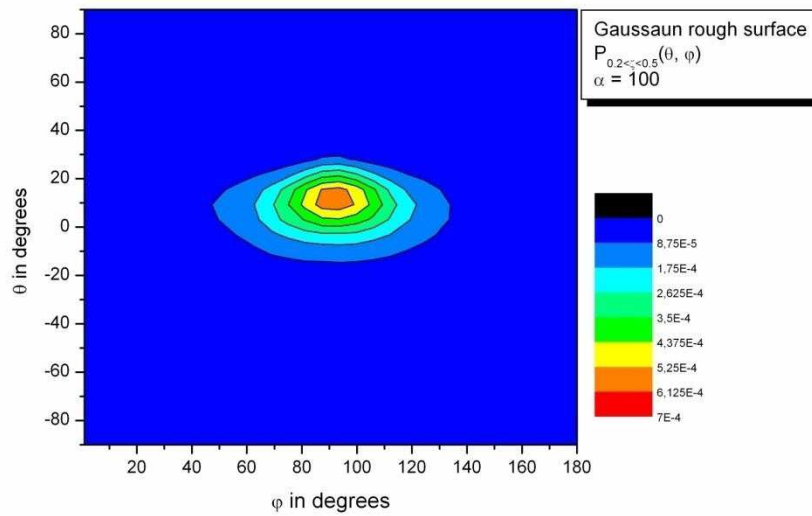
FigIV.13 Simulation results for the normalized PDF distributions, P $_{0.2 < \zeta < 0.5}$ (θ, φ), at Peclet number $\alpha = 100$, in the depletion layer near a *Gaussian rough* solid surface boundary.

4.5 Nematic order parameter S_{xx} for rod-like particles

The order parameter S_{xx} for rod-like particles in the bulk solution and in the two regions I and II of the depletion layer, next to two types of surface boundaries, the atomically *flat* and the Gaussian *rough*, are calculated thanks to our present simulation results and using Eq.23 of Chapter 3. These results are presented in FigIV.14, FigIV.15 and FigIV.16.
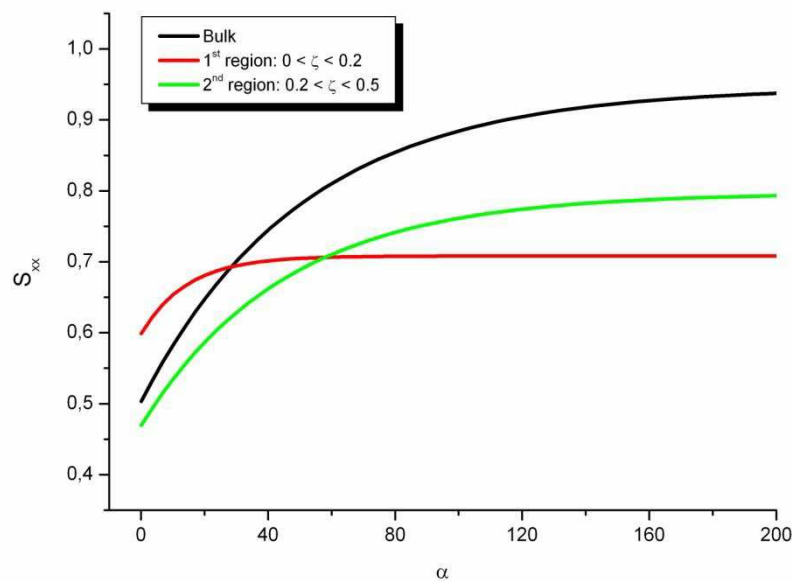
FigIV.14 presents our calculated results for the nematic order parameter S_{xx} for the dilute colloidal suspensions of the macromolecular rod-like particles, along the X-direction, as a function of an increasing Peclet number α from 0.1 to 200. The results illustrate the diverse behavior of the nematic order for the different regions of the solution, namely the bulk, and regions I and II of the depletion layer, over a significant range of the flow hydrodynamics.

In particular the alignment goes to $S_{xx} \sim 0.9$ for $\alpha = 200$ in the bulk solution, which suggests that a perfect order alignment at $S_{xx} = 1$ is attainable in this region for very high Peclet numbers. Given the nature of the diffusive and random interactions which the particles suffer at the solid surface boundaries, whether flat or rough, this perfect order is not attainable for the colloidal suspensions in the depletion layer. At very high Peclet numbers, however, there is still a significant partial order in the depletion layers, greater in region II than in region I.

Although not presented here, the normalized PDF orientation distributions $P(\theta, \varphi)$ for rod-like particles have been calculated for the low Peclet number $\alpha = 1$, in regions I and II of the depletion layer for the two types of surface boundaries, atomically *flat* surface and Gaussian *rough*. Those for a flat surface boundary are comparable to those in FigIII.11 and FigIII.14 for ellipsoidal particles with a relatively big aspect ratio $r_e = 3.55$, in regions I and II of the depletion layer. An analysis of these results explains why we do not attain the same behavior of the nematic order parameter for regions I and II. In region II there is a greater liberty for the rod-like particles to move in real space than in region I, which is translated in terms of a lesser order alignment, for small to medium α. Increasing the hydrodynamic flow at relatively larger α brings the colloidal suspension in region II to increasing alignment, whereas in region I there is a limit to such alignment imposed by the random diffusive collisions attained rather rapidly at $\alpha \sim 20$.

It is also interesting to investigate the influence of the nature of the surface boundary on the behavior of the nematic order parameter for both regions I and II in the depletion layer. The corresponding results for S_{xx} along the direction X of the hydrodynamic flow are presented in FigIV.15 and FigIV.16.

The influence of the nature of the surface boundary on the nematic order parameter S_{xx}; is small on the regions I, while for the region II is the difference is approximately null, in particular for small α.
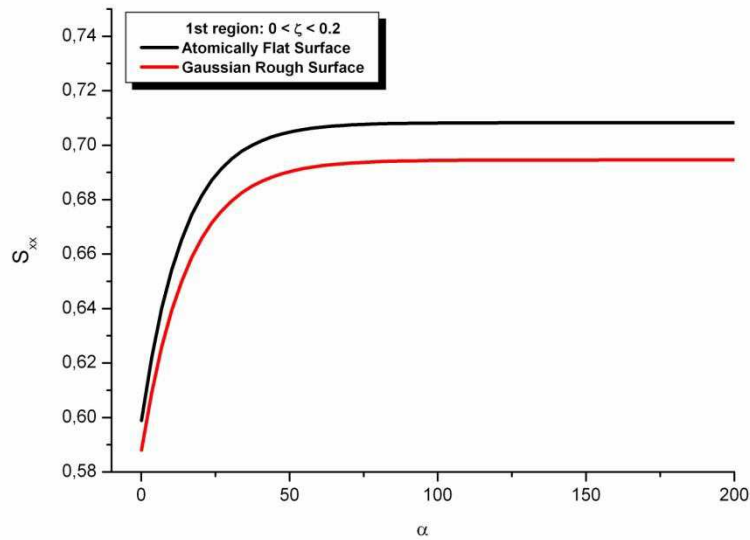
FigIV.15 Nematic order parameter S_{xx} along the direction of the flow X as a function of Peclet number, in region I of the depletion layer, with flat and rough surface boundaries.
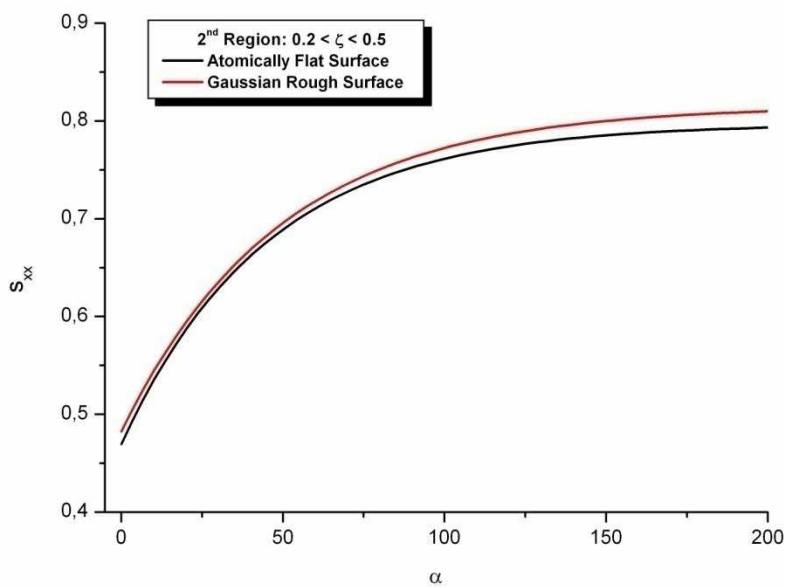
FigIV.16 Nematic order parameter S_{xx} along the direction of the flow X as a function of Peclet number, in region II of the depletion layer, with flat and rough surface boundaries.

It is observed in FigIV.15 that S_{xx} in region I is monotonically greater for a *flat* surface boundary than for a *rough* one. The analysis for the normalized PDF orientation distributions P (θ, φ), for FigIV.4, FigIV.5, FigIV.6, FigIV.7, FigIV.8 and FigIV.9, explain why they attain such a behavior, for example, at high Peclet number $\alpha = 100$, the *peak* probabilities with a

value $\sim 7 \times 10^{-4}$ in the neighbourhood of the *flat* surface boundary is greater than the *peak* probabilities with a value $\sim 5 \times 10^{-4}$ in the neighbourhood of the Gaussian *rough* solid.

In contrary to the result obtains in the region I; the nematic order in region II FigIV.16, is monotonically greater for a *rough* surface boundary than for a *flat* one.

4.6 Conclusions

We have developed algorithms and carried out numerical simulations to analyze the dynamics of dilute colloidal suspensions of a special class of molecular particles, namely rigid rod-like particles, for which the aspect ratio is much greater than unity in solutions flowing on open channel pore. The pores are modeled in a three-dimensional frame of reference with boundaries. The colloidal particles are subject to hydrodynamic forces, Brownian motion and random collisions at the solid surface boundaries of the pores. The numerical simulations are carried out to calculate in particular the spatial statistical PDF distributions for the spatial the orientations of rod-likel particles in colloidal suspensions in a solution under equilibrium dynamics for the bulk liquid and in the depletion layers next two types of solid boundaries, the ideal atomically flat and the rough surface boundaries, to accomplish this we investigated in particular the influence of the roughness on the choice of the hydrodynamic boundary conditions. The simulations are developed for and open pore channels, and are valid throughout the space of the pores and in the boundary depletion layers, for a wide variety of hydrodynamic flow conditions, at low, intermediate, and high flow, characterised by the rotational Peclet number.

Our simulations yield directly the nematic order parameter for colloidal suspensions in the over its tensorial representation, for two types of surface boundaries namely atomically flat sand rough surface boundaries.

References

Atwi, A., A. Khater, et al. (2010). "Three-dimensional Monte Carlo simulations of the dynamics of macromolecular particles in solutions flowing in mesopores." Central European Journal of Chemistry **8**(5): 1009.

Harting, J. and C. Kunert (2008). "Boundary Effects in Microfluidic Setups." John von Neumann Institute for Computing NIC **39**(2): 221.

Hijazi, A. and A. Khater (2001). "Simulations of distribution functions for rod-like macromolecules in linear flow near solid surfaces." Computational Materials Science **20**(2): 213.

Hijazi, A. and A. Khater (2008). "Boëder PDF Brownian simulations for macromolecular rod-like particles near uneven solid surfaces." European Polymer Journal **44**(11): 3409.

Jeffery, G. B. (1922). "The Motion of Ellipsoidal Particles Immersed in a Viscous Fluid." Proceedings of the Royal Society of London. Series A **102**(715): 161-179.

Kunert, C. and J. Harting (2007). "Roughness Induced Boundary Slip in Microchannel Flows." Physical Review Letters **99**(17): 176001.

Panzer, P., M. Liu, et al. (1992). "The effects of boundary curvature on hydrodynamic fluid flow: calculation of slip lengths." International Journal of Modern Physics B (IJMPB) **6**(20): 3251-3278.

Storm, A. J., J. H. Chen, et al. (2003). "Fabrication of solid-state nanopores with single-nanometre precision." Nat Mater **2**(8): 537-540.

Vinogradova, O. I. and G. E. Yakubov (2006). "Surface roughness and hydrodynamic boundary conditions." Physical Review E **73**(4): 045302.

Chapter 5

Modelling adhesion at pore boundaries under diffusive collisions

Abstract: The mechanisms leading to the adhesion of particles of nano sizes in the depletion layer under what would be *non-equilibrium* conditions, due to the conflicting influence of the mechanical diffusive collisions and the attractive Hamaker forces at the boundaries, are of major interest. We have hence investigated in this chapter a theoretical model to calculate the restitution coefficient from basic physical principles. The objective is to quantify the energy balance during the process of a diffusive collision of a nano particle under the influence of the repulsive forces due to the Pauli principle via mechanical bounce on one hand, and the attractive Hamaker forces acting on the nano particle on the other. This is done by developing a model, based on the JKR and Hertz theories, to account for the energy losses during collisions, and for the energy gains due to the Hamaker interactions. Adhesion becomes an outcome if the energy balance permits this. Our theoretical model is developed by proposing a special analytic approach based on the Hamaker potential. We derive from the theoretical analysis a characteristic nonlinear equation for the restitution coefficient, and analyze its properties which determine under given physical conditions the outcome for adhesion or not.

5.1 Introduction

Adhesion science describes how material particles of diverse sizes may adhere on solid boundaries. Adhesion phenomena are important in areas such as chemistry, engineering, and biology. The adhesion phenomenon has been extensively used, even in the prehistoric age, when bitumen and natural resins were used as adhesives for manufacturing weapons and tools, and to repair broken pottery (Eckersley and Rudin 1990), and to make the oldest known paintings which are still adhering on their rock substrate at the Chauvet-Pont-d'Arc cave, in southern France, dated at about 32,000 years ago (Dobler and Holl 1996).

Though daily experience does not directly teach us about adhesion, (the structural design for the oldest cathedrals was based on the assumption that stones do not stick together (Gordon 1978) but are simply held in place by gravity), yet it is obvious that the atoms and molecules, stick together extremely well. At least in the microscopic world almost everything sticks well (Kendall 2001). Nevertheless something hinders the consciousness of universal adhesion in our macroscopic world. A first hint is that clean surfaces in vacuum adhere much better than the same surfaces under typical environmental conditions which render such surfaces dirty or oxygen covered. We now know that almost any surface contamination reduces adhesion. Secondly macroscopic bodies apparently in contact to the human eye, are in fact *not truly touching* over the whole nominal contact area due to their surface roughness (Greenwood 1966). Thus only a small fraction of the contact area is in intimate contact and therefore close enough for molecular interactions (Fuller and Tabor 1975). Further, the bodies will be elastically deformed near those contacts, storing elastic energy (Persson 2002). In summary the adhesion paradox is tributary to two important aspects of molecular contact formation, namely contamination and roughness.

Length scales encountered in adhesion effects cover a wide range from the macroscopic (powder particles, cell adhesion, paint coating of metals...) to the nano scale (molecular...). Adhesion forces between particles and surfaces, i.e. the forces necessary to detach a particle from a surface, is of interest in several industrial applications such as particle filtration (Maynard and Pui 2007), and petroleum production (Aspenes, Dieker et al. 2010). For biological systems such as cells or viruses (Kendall, Kendall et al. 2011), adhesion to surfaces is important for processes like bio-film formation or infection.

In this chapter we are interested in the adhesion of nano-particles and macromolecules. Recent developments on particle adhesion models are well known (Tsai, Pui et al. 1990), (Maugis 1992; Rimai, DeMejo et al. 1992). Additional related articles on particle adhesion

may be found in the books edited by (Mittal 2002, 2003, and 2006), and (King and Gee 2010).

The possible adhesion (stickiness) of metallic and macromolecular nano-particles during a collision with a solid surface depends on the loss of energy of the incident particle owing to the collision. Adhesion should take place if this loss is so great that the particle has not enough kinetic energy left to free itself away from the adhesive forces which act to keep it adhered to the solid surface boundary. The adhesion or non-adhesion may be summarized by a basic relation over the Newtonian restitution coefficient, e determined by

$$K.E_f = e^2 K.E_i$$

$K.E_i$ and $K.E_f$ represent the kinetic energy of the particle before and after collision with the solid surface boundary, so that

Adhesion occurs if $\qquad K.E_f < E_P$

No Adhesion if $\qquad K.E_f > E_P$.

E_P is the energy cost to liberate the particle during its collision rebound from the attractive Hamaker potential V_P binding the particle to solid surface boundary. V_P, which has a strong local character, depends on diverse factors, such as the material nature of the particle and the topography of the surface boundary. This loss of energy depends on a number of factors, in particular the material nature of the particle and the solid surface, the form of the particle, the rough surface topography on the scale of the incident particle, and the Hamaker forces (Israelachvili 2011) that intervene between the particles and the solid surfaces. The energy loss mechanisms include the transfer of the particle incident kinetic energy into other modes such as in rotation, elastic deformation, and heat dissipation to the impacted surface (Sato, Chen et al. 2007).

It is the objective and motivation of this chapter to derive a general relation for the Newtonian restitution coefficient, e, to be able to quantify the possibility of mechanical adhesion of macromolecular and metallic nano particles on the surface boundaries of pores through which the colloidal suspensions are flowing. This would take place under the *non-equilibrium conditions* of the flow, and supplements the known thermodynamic adhesion processes.

Our starting point is the scientific literature which analyzes the contact dynamics of microscopic particles with solid surfaces. In this respect several theories have been advanced to describe the elastic deformation of particles, which have given rise to a family of slightly different expressions for the relations between the applied load force and the contact area or

surface deformation of the particle. These theories were initially developed by Hertz, neglecting the adhesion (Hertz 1882), and subsequently by other groups, in particular (Johnson, Kendall et al. 1971), and (B.V. Derjaguin, Muller et al. 1975). These subsequent works, widely cited as the JKR and DMT theories, will be presented in detail in section 5.2 of the present chapter.

5.2 Theoretical models for surface contact forces

A particle suffers surface forces when sufficiently close to a solid surface. These forces may be electrostatic or mechanical in nature. Electrostatic forces depend on the distribution of electrical charges on the particle and at the surface. Among the many contributions to the interaction between surfaces and particles, however, one type predominates, namely the van der Waals interaction.

A full understanding of the van der Waals forces came with the development of quantum theory, which accounts for the charge fluctuations present in atoms and molecules. Extensive reviews on particle adhesion at solid surface boundaries due to van der Waals forces have been given (Krupp 1967; Visser 1976; Tabor 1977; Bowling 1985). The van der Waals force is the result of three main forces (Lennart 1997), namely the Keesom force (Keesom 1921), the Debye, and the London or dispersion force (London 1937). Since all three vary as r^{-6} where r is the distance between the two bodies, the van der Waals interaction energy can be written (Israelachvili 1991) as

$$U_{VdW}(r) = -\frac{C_2}{r^6} \tag{1}$$

This is an attractive potential, where C_2 is a constant that depends on the properties of the interacting bodies and of those of the intermediate medium (Butt, Graf et al. 2003). At very small distances separating the bodies, repulsive forces based in the quantum Pauli Exclusion Principle, come to dominate. The corresponding potential is usually modeled by the Born Mayer expression

$$U_B(r) = \frac{C_1}{r^{12}} \tag{2}$$

C_1 is a constant. Adding the attractive and repulsive potentials, yields the so called Lennard Jones potential

$$U(r) = \frac{C_1}{r^{12}} - \frac{C_2}{r^6} = 4\varepsilon\left[\left(\frac{z_0}{r}\right)^{12} - \left(\left(\frac{z_0}{r}\right)^6\right)\right] \tag{3}$$

z_0 is the finite distance at which the inter-particle potential is zero, and ε is the depth of the potential well in the equilibrium state, and represents the distance of closest approach when two molecules collide. This equation may also be written in a reduced form (Hirschfelder, Curtiss et al. 1964):

$$U(z) = \frac{C_1}{z^{12}} - \frac{C_2}{z^6} = 4\varepsilon\left[\left(\frac{z_0}{r}\right)^{12} - \left(\left(\frac{z_0}{r}\right)^6\right)\right] = \beta_2 z^{-12} - \beta_1 z^{-6}. \tag{4}$$

The terms represent respectively the repulsive and attractive contributions. $z \equiv r$ in Eq.4 is the distance between the centers of two molecules. The maximum energy of attraction for such two molecules occurs at the separation $z = 2^{\frac{1}{6}} z_0$. The empirical values of z_0 for different materials range from 0.7 to 2 Å. Note that $\beta_1 = 4\varepsilon z_0{}^6$ is called the London- van der Waals constant, $\beta_2 = 4\varepsilon z_0{}^{12}$ represents the repulsive energy, and $\beta_2 = \beta_1 z_0{}^6$.

The molecular potential in Eq.4 is usually used by researchers in the literature to derive expressions for forces acting between two microscopic bodies at small separations between their mass centers. For example, Eq.4 yields the attractive force between two spherical bodies, by integrating the molecular contributions over the spherical forms. (Bradley 1932) and (Hamaker 1937) do this additively. They integrated Eq.4 over all pairs of molecules for two spheres with radii R_1 and R_2, to calculate the resultant van der Waals attractive force in a simple mathematical form as follows

$$F_a = + \frac{A_1 R^*}{6z^2} \tag{5}$$

The $+$ sign represents by convention an attractive force. $A_1 = \pi^2 n_1 n_2 \beta_1$, related to London's constant, is called the Hamaker constant, where n_1 and n_2 are the number densities per unit volume of molecules in spheres 1 and 2 respectively. $R^* = R_1 R_2 / [R_1 + R_2]$ is a parametric radius for the combined system, and z is the minimum separation between their spherical surfaces along a line that joins their centers. If one takes R_2 to infinity, Eq.5 becomes the expression for the attractive force between a sphere of radius R_1 and a plane.

To understand the contact forces between bodies, one has to take into account the elastic deformation due to the contact. This deformation may be due to external forces, but even in absence of external force, the surface forces will lead to a contact deformation. In the following we will shortly review the most common elastic contact models.

5.2.1 Hertz model

(Hertz 1882) described his contact theory between a sphere and a planar surface. The sphere with radius R is assumed smooth and elastic, while the planar surface is assumed ideally flat and rigid. Since the Hertz theory does not take into account surface forces, the radius of the contact area between the particle and the surface is zero in the absence of an external load, and no deformation is observed FigV.1a. This is because Hertz neglects attractive molecular forces between the particle and the surface. When a mechanical force F is applied as a load on the particle, this latter is squeezed against the rigid plane, and deforms consequently, as in FigV.2a. The deformation presents the so called contact radius, a, and the penetration depth δ. Hertz determined the contact radius and the penetration depth as follows:
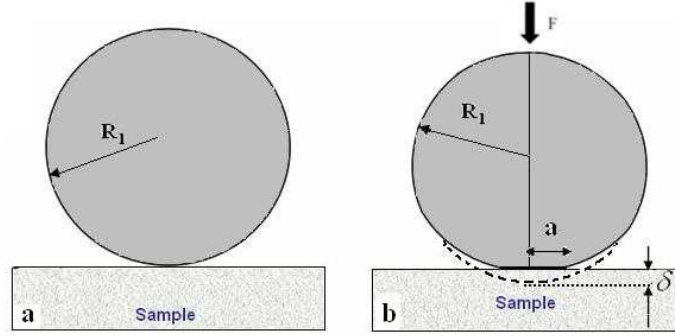
$$a^3 = \frac{R^*F}{K} \tag{6}$$

$$\delta = \frac{a^2}{R^*} = \frac{F}{Ka} \tag{7}$$

In these equations, K is the so-called composite Young's modulus and is given by:

$$\frac{1}{K} = \frac{3}{4}\left(\frac{1-v_1^2}{Y_1} + \frac{1-v_2^2}{Y_2}\right) \tag{8}$$

v_i and Y_i are respectively Poisson's ratio and Young's modulus for the materials i ($i = 1$ or 2), of which the particle and the planar surface are made.

FigV.1An elastic deformation of spherical particle on surface sample following Hertz theory: (a) without force, (b) with force F

Combining Eq.6 and Eq.7, the penetration depth δ may be written as

$$\delta = \frac{a^2}{R^*} = \left[\frac{F}{KR^{*1/2}}\right]^{2/3}$$

In 1971 the Hertz model was extended by Johnson, Kendall and Roberts (JKR) to take the attractive molecular forces between contact bodies into account.

5.2.2 Johnson-Kendall-Roberts (JKR) model

The JKR theory (Johnson, Kendall et al. 1971) were the first to determine a relationship for the contact deformation of an elastic sphere at a rigid surface, taking the attractive molecular forces between the contact surfaces into account. They considered the change in energy that arises from the formation of a contact surface area between the bodies. Molecular interactions outside the contact are neglected, FigV.2.

The JKR contact radius a and the JKR indentation depth δ are given as a function of the externally applied load F for an elastic sphere in contact with a surface (elastic half space) as

$$a = \left(\frac{R^*}{K}\left[F + 3\pi R\gamma + \sqrt{6\pi R\gamma F + (3\pi R\gamma)^2}\right]\right)^{\frac{1}{3}} \tag{9}$$

$$\delta = \frac{a^2}{R} - \sqrt{\frac{2\pi a\gamma}{K}} \tag{10}$$

γ is the effective surface energy of adhesion for both surfaces (Dupré energy of adhesion) (Harkins 1919). In the absence of surface forces ($\gamma = 0$) equations Eq.9 and Eq.10 reduce to the classical equations Eq.6 and Eq.7 from the Hertz model.
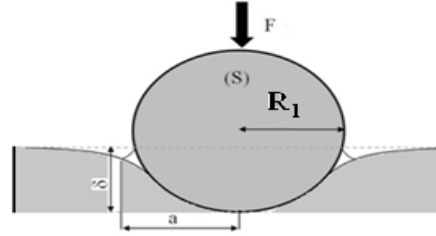
FigV.2: JKR model for a rigid sphere (S) in contact with surface sample.

The adhesion force considered in the JKR theory can be understood as an additional Hertzian force. Under zero load conditions when a particle adheres with zero kinetic energy, a finite contact radius exists and it can be calculated as:

$$a_0{}^3 = \frac{6\pi R^2 \gamma}{K} \tag{11}$$

According to the JKR theory, a finite force called the pull-off force is necessary to separate the two surfaces, and is calculated as:

$$F_{p.o} = \frac{3}{2}\pi R \gamma \tag{12}$$

At the moment of separation a finite contact area persists, and its radius $a_{p.o}$ may be calculated as:

$$a_{p.o} = \frac{a_0}{4^{1/3}} \tag{13}$$

5.2.3 Derjaguin-Muller-Toporov (DMT) Model

The DMT model (Derjaguin, Muller et al. 1975) extends the molecular interactions to the domain of the whole spherical particle, in comparison with the JKR model which limits these interactions to the contact surface. This leads to a larger effective contact area, and modified results for the contact radius and the indentation depth. For a sphere in contact mechanics with a falat surface, we have from DMT:

$$a = \left[\left(\frac{R^*}{K}\right)(F + 2\pi\gamma R^*)\right]^{\frac{1}{3}} \tag{14}$$

$$\delta = \frac{a^2}{R^*} \tag{15}$$

Also, the contact area and the pull-off force are given by the modified expressions:

$$A_R = \pi a^2 = \left[\left(\frac{\pi R^*}{K}\right)(F + 2\pi\gamma R^*)\right]^{\frac{2}{3}} \tag{16}$$

$$F_{p.o}{}^{DMT} = 2\pi R^* \gamma \tag{17}$$

To compare the models described above (Hertz, JKR, DMT) it is useful to introduce normalized parameters. Hence the normalized variables of contact radius $\bar{a}$, force $\bar{F}$ and penetration depth $\bar{\delta}$ become:

$$\bar{a} = a \left(\frac{K}{\pi\gamma R^{*2}}\right)^{1/3}, \bar{F} = \frac{F}{\pi\gamma R^*}, \bar{\delta} = \delta \left(\frac{K^2}{\pi^2 R^* \gamma^2}\right)^{1/3}$$

In Table 1 the assumptions of the three theories with the corresponding normalized equations are presented for quick and easy comparison.

Model	Assumptions	Normalized equations
Hertz	Linear elasticity No attractive surface forces	$\bar{F} = \bar{a}^3$ $\bar{\delta} = \bar{a}^2 = \bar{F}^{2/3}$
JKR	Short-range attractive surface forces acting within the contact area	$\bar{F} = \bar{a}^3 - \bar{a}\sqrt{6\bar{a}}$ $\bar{\delta} = \bar{a}^2 - \frac{2}{3}\sqrt{6\bar{a}}$
DMT	Long-range attractive surface forces acting outside the contact area	$\bar{F} = \bar{a}^3 - 2$ $\bar{\delta} = \bar{a}^2$

Table 1: Model assumptions of the Hertz, JKR and DMT theories at a glance with the corresponding normalized equations.

5.3 Elastic forces and energies for a flattened spherical particle at a surface

(Tsai, Pui et al. 1990) investigated the elastic indentation of the particle in contact mechanics with a flat surface, and derived in their (TPL) mode the modified attractive and repulsive Hamaker potentials for a flattened sphere-surface system. They used this as a starting point for an analysis based on the energy conservation principle and force balance, to obtain analytical expressions that describe the relationship between the deformation elastic flattening and Hamaker adhesion.

We detail and explain the derivation of the attractive force and its corresponding potential energy, F_a, E_a, and of the repulsive force and its corresponding potential energy, F_r, E_r, as obtained (Tsai, Pui et al. 1990), in Annex AIII. They are as follows:

$$F_a = + \frac{A_1 R}{6z^2}\left\{1 + \frac{\delta}{z}\right\} \tag{18a}$$

$$F_r = - \frac{A_2 R}{180z^8}\left\{1 + \frac{4\delta}{z}\right\} \tag{18b}$$

$$E_a = - \frac{A_1 R}{6z}\left\{1 + \frac{\delta}{2z}\right\} \tag{19a}$$

$$E_r = + \frac{A_2 R}{1260z^7}\left\{1 + \frac{7\delta}{2z}\right\} \tag{19b}$$

$A_1 = \pi^2 n_1 n_2 \beta_1$ and $A_2 = \pi^2 n_1 n_2 \beta_2$, are the Hamaker constants for the attraction and repulsion terms. Since $\beta_2 = \beta_1 z_0{}^6$, one can deduce that $A_2 = A_1 z_0{}^6$. In this model (Tsai, Pui et al. 1990) introduced a force constant K_a where $A_2 = K_a A_1 z_0{}^6$, to obtain a force balance; it is shown that without K_a the force balance cannot be otherwise satisfied.

In what follows, we analyze the Tsai et al model, taking a slightly different value for the elastic deformation energy into account, than the one used by these authors.

Consider the energy conservation principle which may be written in general in closed system as:

$$Q + W = \Delta E \tag{20}$$

Q is the heat input to the system, W is the work done on the system, and ΔE is the total energy change of the system. If no heat transfer is required, the work done on the system must be equal to an increase in the total energy of the system. Total energies include elastic energy E_e and potential energy E_p, which cover the Tsai et al terms E_a and E_r. Other contributions to total energies such as gravitational and electrostatic effects are not considered here. It follows that Eq.20 may be rewritten as:

$$W = \Delta E_e + \Delta E_a + \Delta E_r \tag{21a}$$

Considering force balance for an isolated particle in the particle-surface system the Newton's third law can be written as

$$\sum F = F_{ext} + F_a + F_r = 0 \tag{21b}$$

F_{ext}, (assumed to be normal to the surface), represent the external forces applied to the particle, and F_a and F_r are the Tsai et al terms. In the absence of external forces, the sum of attractive and repulsive forces must be zero.

The elastic energy E_e is a necessary component to ensure the application of the energy conservation principle in this model. In the Hertzian contact theory, the contact force can be calculated (Popov 2010) as $\frac{2}{3} K R^{1/2} \delta^{3/2}$. We calculate hence the elastic energy E_e as

$$E_e = \frac{4}{15} K R^{1/2} \delta^{5/2} \tag{22}$$

Tsai et al give a slightly different numerical coefficient, namely $\frac{2}{5} K R^{1/2} \delta^{5/2}$.

Consider the case when a particle is at static equilibrium in contact with the surface; in this case one assumes the total energy E_t to be zero. By substituting Eqs.18a, 18b, 19a, 19b, and 22, into the Eqs.21a and 21b, the energy conservation and force balance at this equilibrium condition become:

$$\frac{A_2 R}{1260 z_0^7}\left\{1 + \frac{7\delta_0}{2z_0}\right\} - \frac{A_1 R}{6z_0}\left\{1 + \frac{\delta_0}{2z_0}\right\} + \frac{4}{15} K R^{1/2} \delta_0^{5/2} = 0 \qquad (23a)$$

$$\frac{A_1 R}{6z_0^2}\left\{1 + \frac{\delta_0}{z_0}\right\} - \frac{A_2 R}{180 z_0^8}\left\{1 + \frac{4\delta_0}{z_0}\right\} = 0 \qquad (23b)$$

The subscript "0" represents the equilibrium condition. By introducing the following constants $K_{2o} = \delta_0/z_0$ as a deformation parameter, we determine a so called adhesion parameter

$$\Pi = \left(\frac{225 R\, A_1^2}{576 z_0^7 K^2}\right)^{1/3}.$$

Our adhesion parameter differs from that $\Pi_{TPL} = \left(\frac{25 R\, A_1^2}{144 z_0^7 K^2}\right)^{1/3}$ given by Tsai et al, such that their ratio is $\Pi/\Pi_{TPL} = 1.3104$. The difference is important because of the sensitivity of the results to the value of this parameter, see FigV.3.

Using the previously defined force constant $K_a = \frac{A_2}{A_1 z_0^6}$, and Eq.23a, the deformation and adhesion parameters may be derived as follows:

$$\frac{A_2 R}{1260 z_0^7}\left\{1 + \frac{7\delta_0}{2z_0}\right\} - \frac{A_1 R}{6z_0}\left\{1 + \frac{\delta_0}{2z_0}\right\} + \frac{4}{15} K R^{1/2} \delta_0^{5/2} = 0$$

$$\Rightarrow \frac{A_1 R}{6z_0}\left[\left\{1 + \frac{1}{2} K_{2o}\right\} - \frac{K_a}{210}\left\{1 + \frac{7}{2} K_{2o}\right\}\right] = \frac{4}{15} K R^{1/2} \delta_0^{5/2}$$

Squaring both sides
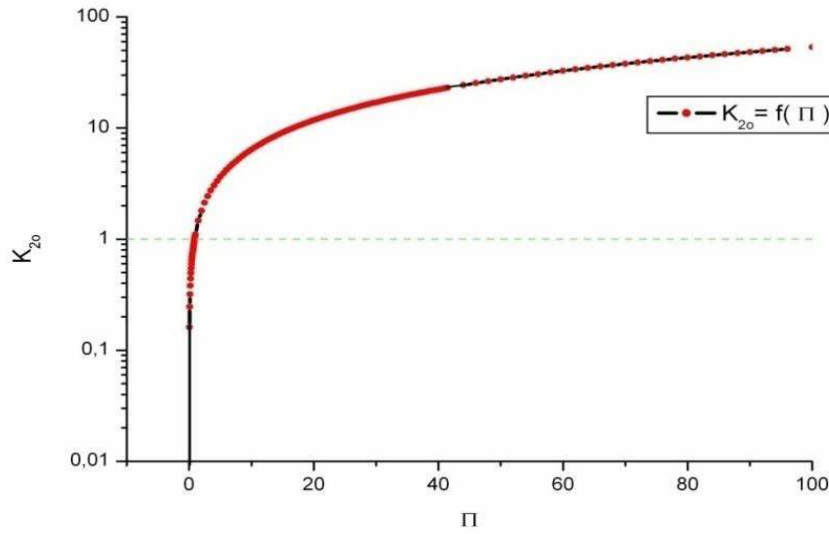
$$\Rightarrow \frac{A_1^2 R^2}{36 z_0^2}\left[\left\{1 + \frac{1}{2} K_{2o}\right\} - \frac{K_a}{210}\left\{1 + \frac{7}{2} K_{2o}\right\}\right]^2 = \left(\frac{4}{15}\right)^2 K^2 R^2 \delta_0^5$$

Multiplying both sides by $\Pi = \frac{576 z_0^7 K^2}{225 R\, A_1^2}$ we obtain:

$$\Rightarrow \frac{16 z_0^5 R}{225}\left[\left\{1 + \frac{1}{2} K_{2o}\right\} - \frac{K_a}{210}\left\{1 + \frac{7}{2} K_{2o}\right\}\right]^2 = \left(\frac{4}{15}\right)^2 \delta_0^5 R \frac{1}{\Pi^3}$$

Dividing by R, and eliminating the denominators we finally we derive the following Tsai et al equation from considerations of the conservation of energy:

$$K_{2o}^5 = \Pi^3 \left[\left\{1 + \frac{1}{2} K_{2o}\right\} - \frac{K_a}{210}\left\{1 + \frac{7}{2} K_{2o}\right\}\right]^2 \qquad (24a)$$

FigV.3 Equilibrium deformation parameter K_{2o} versus adhesion parameter $\prod$

In contrast Eq. 23b derived from the force balance at static equilibrium $z = z_0$, yields:

$$\frac{A_1 R}{6z_0{}^2}\left\{1 + \frac{\delta_0}{z_0}\right\} - \frac{A_2 R}{180z_0{}^8}\left\{1 + \frac{4\delta_0}{z_0}\right\} = 0$$

$$\Longrightarrow \frac{A_1 R}{6z_0{}^2}\{1 + K_{2o}\} - \frac{A_1 K_a R}{180z_0{}^2}\{1 + 4\,K_{2o}\} = 0$$

Dividing both sides by $\frac{A_1 R}{6z_0{}^2}$

$$\Longrightarrow \{1 + K_{2o}\} = \frac{K_a}{30}\{1 + 4\,K_{2o}\} \tag{24b}$$

Putting together Eq.24a and Eq.24b, we finally derive

$$K_{2o}{}^5 = \prod^3 \left[\left\{1 + \frac{1}{2}\,K_{2o}\right\} - \frac{1}{7}\left\{\frac{1 + K_{2o}}{1 + 4\,K_{2o}}\right\}\left\{1 + \frac{7}{2}\,K_{2o}\right\}\right]^2 \tag{24c}$$

For given particle and solid surface materials, this equation yields the required deformation parameters as a function of their elastic properties. This equation is graphically represented in FigV.3. In particular it yields $K_{2o} = \delta_0/z_0$ as a function of the adhesion parameter $\prod$.

5.4 Collision restitution for nano-particles at a solid surface: 1st model

Motivated by the diffusive collisions of macromolecular particles and by nanoparticles in colloidal suspensions flowing inside mesopores, we are interested to analyze in this chapter the detailed mechanical dynamics of these particles during their collisions the solid boundaries of the mesopores.

Consider a spherical nano particle in contact mechanics at static equilibrium with a surface (no external force are applied and total particle energy $E_t = 0$). The *displacement* of the center of mass of the particle under deformation is at $\Delta_0 = z_o - \delta_0$ with respect to an ideal position that corresponds to the undeformed spherical particle form just touching the flat surface. z_o is the equilibrium distance between the flattened particle surface and the plane surface, and δ_0 is the minimum penetration, as in FigV.4a. When a particle comes into the contact with a surface arriving with a specific kinetic energy $E_i \neq 0$, the particle deforms beyond the deformation at static equilibrium. The above *displacement* of the particle center of mass is modified to $\Delta = \Delta_0 - (z_m - \delta_m) = \delta_m - \delta_0 + z_o - z_m$, where $z_m < z_0$ is the new distance between the flattened particle surface and the plane surface, while $\delta_m > \delta_0$ is the maximum penetration at $E_i \neq 0$, as in FigV.4b. We interpret the load in this case as the applied Newtonian force normal to the surface, generated by the changing particle momentum on its inward trajectory, from its initial value position (z_o, δ_0) to the new one (z_m, δ_m).
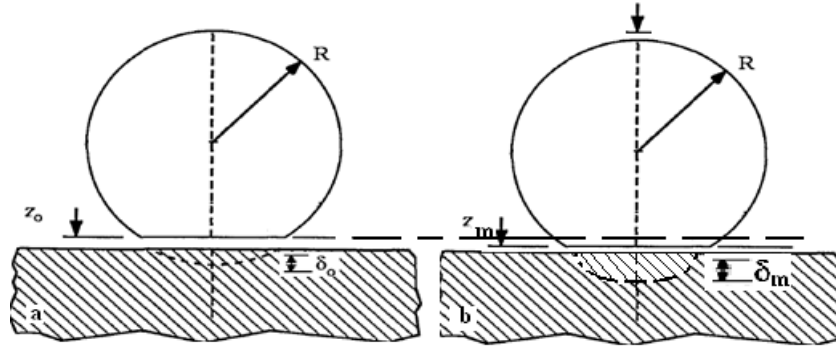
FigV.4: a) Spherical nano-particle initially at equilibrium with a surface. b) Spherical nano-particle with a specific kinetic energy

The load F may hence be written as $F = \frac{\Delta p}{\Delta \tau}$ from the rate of change of the momentum. This gives:

$$F = \frac{p_i - 0}{\Delta \tau} \tag{25}$$

Given the nano scale of distances involved in this analysis, we can approximate $\Delta \tau$ by the relation $\Delta \tau = \frac{\Delta}{v}$, where v is average speed of the particle on its trajectory between (z_o, δ_0) and (z_m, δ_m).

$$\frac{1}{\Delta \tau} = \frac{v}{\Delta} = \frac{v_{i(\text{intial})} - 0_{(\text{final})}}{\delta_m - \delta_0 + z_o - z_m}$$

so that

$$\frac{1}{\Delta \tau} = \frac{1}{m} \frac{m v_i}{\delta_m - \delta_0 + z_o - z_m} = \frac{\frac{2}{2m} m v_i}{\delta_m - \delta_0 + z_o - z_m} = \frac{2\frac{p_i}{2m}}{\Delta} \tag{26}$$

Hence

$$F_i = \frac{p_i}{\Delta \tau} = \frac{2(p_i)^2}{2m} \frac{1}{\delta_m - \delta_0 + z_o - z_m}$$

and

$$F = 2 \frac{[E_i - (E_e(\delta_m) - E_e(\delta_0))]}{\delta_m - \delta_0 + z_0 - z_m} \tag{27}$$

From the JKR Eq.9, we have the contact radius a as a function of the applied loading force:

$$a = \left(\frac{R}{K} \left[F + 3\pi R\gamma + \sqrt{6\pi R\gamma F + (3\pi R\gamma)^2} \right] \right)^{\frac{1}{3}}$$

Therefore

$$\frac{a^3 K}{R} = F + 3\pi R\gamma + \{6\pi R\gamma F + (3\pi R\gamma)^2\}^{1/2} \tag{28}$$

Let $y(a) = \frac{a^3 K}{R}$, and $G = 3\pi R\gamma$ so Eq.28 becomes as:

$$y(a) = F + G + \{2GF + G^2\}^{1/2}$$
$$\Rightarrow F^2 - 2yF + y^2 - 2yG = 0$$

So

$$F = \frac{+2y \pm \sqrt{8yG}}{2}$$

Hence

$$F = \frac{a^3 K}{R} \pm \sqrt{6\pi\gamma a^3 K}$$

Also from Eq.11, $a_0{}^3 = \frac{6\pi R^2 \gamma}{K}$. It follows that:

$$F = \frac{K}{R} \left(a^3 \pm \sqrt{a_0{}^3 a^3} \right) \tag{29}$$

Eq.29 yields two equations, and we must find the unique solution. Since Eq.9 and E.q11, yield $a = a_0$ for $F = 0$, one deduces the physical solution as:

$$F = \frac{K}{R} \left(a^3 - \sqrt{a_0{}^3 a^3} \right) \tag{30}$$

On the other hand according to the Chord theorem (Israelachvili 1991), see also Annex AIII, one can calculate the value of the contact radius a , now function of the incident energy, as:

$$a_m(E_i) = \sqrt{2R\delta_m(E_i) - \delta_m{}^2(E_i)} \cong 2R\delta_m(E_i) \tag{31}$$

By Combining Eq.27 and Eq.30, we get the following expression

$$\frac{K}{R}\left(a_m{}^3 - \sqrt{a_0{}^3 a_m{}^3}\right) = 2\frac{[E_i - (E_e(\delta_m) - E_e(\delta_0))]}{\delta_m - \delta_0 + z_o - z_m} \qquad (32)$$

Hence

$$\frac{K}{R}\left(a_m{}^3 - \sqrt{a_0{}^3 a_m{}^3}\right)(\delta_m - \delta_0 + z_o - z_m) = 2\left(E_i + E_e(\delta_0) - E_e(\delta_m)\right)$$

$$\qquad (33)$$

By using Eq.31 and Eq.33 then we get:

$$\frac{2\left(E_i + \frac{4}{15}KR^{\frac{1}{2}}\delta_0{}^{\frac{5}{2}} - \frac{4}{15}KR^{\frac{1}{2}}\delta_m{}^{\frac{5}{2}}\right)}{(\delta_m - \delta_0 + z_o - z_m)} = \frac{K}{R}\left[\left(2R\delta_m - \delta_m{}^2\right)^{3/2} - \left(a_0{}^3\left(2R\delta_m - \delta_m{}^2\right)^{3/2}\right)^{1/2}\right]$$

$$\qquad (34)$$

To solve the nonlinear Eq.34, for a given incident energy E_i, to yield δ_m as a function of z_m / z_0, it is necessary to know the numerical values for a number of necessary input parameters: $K_{2o} = \delta_0 / z_0$, K, R. This is illustrated in the following example.

Consider a spherical polystyrene particle with radius R = 25 A° incident onto a copper rough surface, for two separate kinetic energies, $E_i = 0.9 \times 10^{-21}$ J and $E_i = 1.8 \times 10^{-21}$ J Cu has the Poisson's ratio $\nu = 0.34$ (Wang and John 1988) and the young modulus $Y = 130 \times 10^9$ Nm^{-2} (Dahneke 1972; Yia, Kima et al. 2005), while for polystyrene, we have the Poisson's ratio $\nu = 0.37$ (Rimai, Demejo et al. 1994) and the young modulus $Y = 3 \times 10^9$ Nm^{-2} (Van Krevelen and Te Nijenhuis 2009). Using Eq.8 the effective system $K = 4.52 \times 10^9$ Nm^{-2}.

The second main subject next is how to deal with the rough surface boundary. For this purpose we introduce an effective Hamaker constant in the depletion layer adjacent to a rough pore surface boundary. A model calculation is given in detail in Annex IV to this end; we calculate for example for the above system of a copper rough surface, water liquid solution in the pore, and incident polystyrene particle the effective system Hamaker constant as $A_{system} = \sqrt{A_{22eff} A_{11}} = 6.012 \times 10^{-20}$ J This value is a necessary input in the generating equation

$$\Pi = \left(\frac{225R\, A_{system}{}^2}{576 z_0{}^7 K^2}\right)^{1/3}$$

A major difficulty at this stage, evident in all the literature on this subject, is the assignment of a credible value for z_0 for a given system. The literature values for z_0 vary in general from 0.2

nm to 0.4 nm which is an important range since z_0 appears to the seventh power in the $\prod$ expression. In the present example we take z_0 = 0.2 nm. Using this value and either FigV.3 or FigV.5, we can calculate δ_0 .
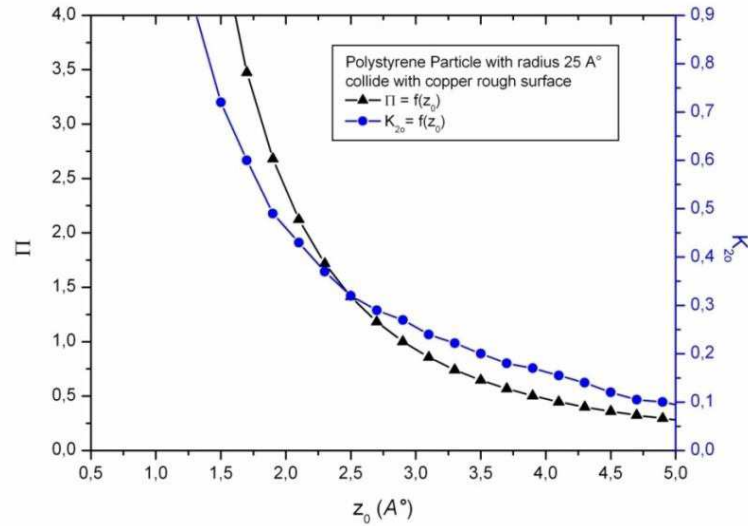
FigV.5 Adhesion and deformation parameter $\prod$ and K_{2o} as function of z_0
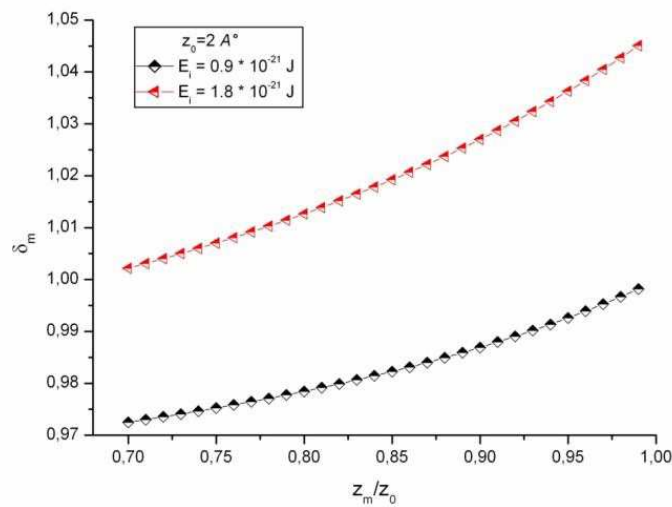
FigV.6 δ_m as a function of z_m / z_0 for z_0 = 2 $A°$, at two different incident kinetic energies

The previous analysis permits us to calculate next the penetration distance δ_m under kinetic conditions, as a function of z_m / z_0, and the numerical results for the above material example are plotted in FigV.6. Unfortunately these results are unphysical, which implies that the model leading to the nonlinear Eq.34 is spurious. It is for this reason that we have adopted a different approach for this problem, which is presented in the following section.

133

5.5 Collision restitution for nano-particles at a solid surface: improved model

As pointed out earlier predicting the so-called sticking efficiency for macromolecular particles is of interest when colloidal suspensions flow inside confining pores. There are two manners for this sticking to take place, via thermodynamic equilibrium exchange, and via mechanical sticking under non-equilibrium conditions. It is the second of these mechanisms which is of interest her. The coefficient of restitution is hence an important parameter for the mechanical sticking mode.

Consider an uncharged particle with kinetic energy $K.E_i$ incident onto a surface as in FigV.7. The potential energy $V_{p,i}$ between the particle and the surface is activated at relatively short separations, and goes to an equilibrium which corresponds to the minimum $V_{p,o}$. On a classical trajectory the particle penetrates into the surface to a *classical turning* point characterized by the potential $V_{p,t}$. The particle is repulsed at this distance in the opposite sense until it reaches a final position with potential energy $V_{p,f}$.
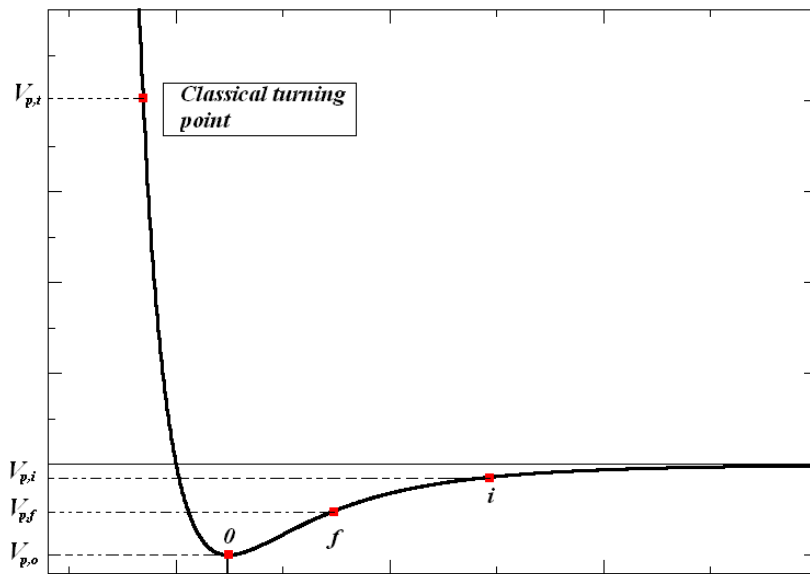
FigV.7 Potential energy versus the separation distance between the particle and surface atoms where $V_{p,o}$, $V_{p,t}$ and $V_{p,f}$ represent respectively the potential energies at equilibrium, classical turning point and final position

Form energy conservation

$$K.E_i = V_{p,t} - V_{p,i} + E_e \tag{35}$$

E_e is the elastic deformation energy. We can write Eq.35 on another form:

$$K.E_i = (V_{p,t} - V_{p,0}) + (V_{p,0} - V_{p,i}) + E_e \tag{36}$$

We consider $(V_{p,0} - V_{p,i})$ in Eq.36 as the surface energy $E_{s,t}$ in contact mechanics (van Beek 2001) on the *way in* for the particle, so that $E_{s,t} = (V_{p,0} - V_{P,i})$. Hence

$$K.E_i = (V_{p,0} - V_{p,i}) + E_{s,t} + E_e \tag{37}$$

Similarly we can define the final kinetic energy $K.E_f$ on the *way out* for the particle (van Beek 2001), as:

$$K.E_f = (V_{p,0} - V_{p,f}) + E_{s,p} + E_e \tag{38}$$

Therefore

$$K.E_i - K.E_f = -V_{P,i} + V_{P,f} + E_{s,t} - E_{s,p} \tag{39}$$

The energy loss $(E_{s,t} - E_{s,p})$ is a complex term which depends on a variety of factors. (Johnson 1976) derives an equation for this as a function of the work adhesion γ, the composite Young's modulus K, and particle radius R, as:

$$E_{s,t} - E_{s,p} = 7.09\left(\frac{R^4\, \gamma^5}{K^2}\right)^{\frac{1}{3}} \tag{40}$$

Here we have 2 cases to consider which depend on the potential energies $V_{p,i}\ and\ V_{p,f}$:

- 1st case:

$$\textbf{If}\ \ \boldsymbol{V_{p,i} = V_{p,f} = V_{p,\infty} = 0}$$

$$K.E_i - K.E_f = E_{s,t} - E_{s,p} \tag{41}$$
$$K.E_f = K.E_i - (E_{s,t} - E_{s,p})$$
$$e^2 K.E_i = K.E_i - (E_{s,t} - E_{s,p})$$

Therefore

$$e^2 = 1 - \frac{E_{s,t} - E_{s,p}}{K.E_i} \tag{42}$$

- 2nd case

$$\textbf{If}\ \ \boldsymbol{V_{p,i} \neq V_{p,f}}$$

In this case the positions of the particle before and after the collision are different. If we suppose that z_i is the initial position of the particle before the collision hence we can get the position of the particle after the collision z_f by:

$$z_f = e\, z_i \tag{43}$$

where e is the unknown restitution coefficient for the collision. We shall make numerical applications for this model later in this section.

To solve for e, we need to express $E_{s,t} - E_{s,p}$ from Eq.40 explicitly. (Fowkes 1968) gives γ in contact surface mechanics for microscopic particles as $\gamma = 2\sqrt{\gamma_1\gamma_2}$, a function of the surface free energies of the two surfaces 1 and 2. We tried and neglected this because it gave spurious results. In contrast (Tabor 1977) developed a theoretical model to calculate γ at the molecular scale for surfaces in contact mechanics, as

$$\gamma = \frac{A}{12\pi z_0^2} \tag{44}$$

Using this last equation we obtain an explicit expression for $E_{s,t} - E_{s,p}$ at the molecular scale, as

$$E_{s,t} - E_{s,p} = 7.09\left[\frac{R^4\left(\frac{A}{12\pi z_0^2}\right)^5}{K^2}\right]^{\frac{1}{3}} \tag{46}$$

5.5.1 Hamaker potential V_p for a cylindrical particle with hemispherical extremities

The interaction Hamaker energy V_P for a cylindrical particle with hemispherical extremities that is parallel to a solid surface is given by (Popov 2010)

$$V_P(\text{Sphere}) = -\frac{A}{6}\frac{R}{Z}$$

A is the Hamaker constant for the interaction, 2R is the diameter of the hemispherical extremities. For a cylindrical particle of the same diameter 2R and of length L near a flat surface, the interaction energy is given by (Mullins, Michaels et al. 1992):

$$V_p(\text{Cylinder}) = -\frac{AL\sqrt{R}}{6\sqrt{2}z^3}$$

This yields Hamaker energy V_P for the cylindrical particle with hemispherical extremities, when entirely parallel to the surface as:
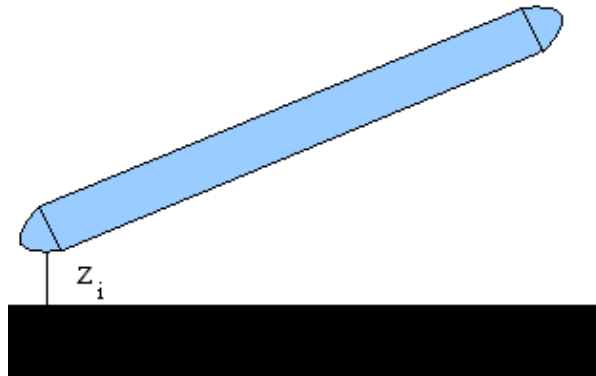
$$V_P(\text{Sphero- Cylindrical}) = V_P(\text{Sphere}) + V_P(\text{Cylinder})$$

$$= -\frac{A}{6}\left[\frac{R}{z} + \frac{L\sqrt{R}}{\sqrt{2z^3}}\right]$$

For such a system at an arbitrary angle θ with respect to the surface, as in FigV.8, the potential can be *approximated* by the following general form

$$V_P = -\frac{A}{12}[\frac{R}{z}\,sin^2\theta + \left(\frac{2R}{z} + \frac{2L\sqrt{R}}{\sqrt{2z^3}}\right)cos^2\theta]$$

z_i is the distance between the nearest point of the surface particle to the surface

FigV.8 Sphero-Cylindrical particle

We calculate $-V_{p,i} + V_{p,f}$, using Eq.43 to replace z_f by z_i, to get

$$-V_{P,i} + V_{P,f} =$$

$$\frac{A}{12}\left[\frac{R}{z_i}\,sin^2\theta + \left(\frac{2R}{z_i} + \frac{2L\sqrt{R}}{\sqrt{2z_i^3}}\right)cos^2\theta\right] - \frac{A}{12}[\frac{R}{ez_i}\,sin^2\theta + \left(\frac{2R}{ez_i} + \frac{2L\sqrt{R}}{\sqrt{2e^3z_i^3}}\right)cos^2\theta]$$

$$= \frac{A}{12}[\frac{R}{z_i}sin^2\theta(1 - e^{-1}) + cos^2\theta\left[\frac{2R}{z_i}(1 - e^{-1}) + \frac{2L\sqrt{R}}{\sqrt{2z_i^3}}(1 - e^{-3/2})\right]$$

$$-V_{P,i} + V_{P,f} = \frac{A}{12z_i}\{sin^2\theta(1 - e^{-1}) + \left[(1 - e^{-1}) + \frac{2L\sqrt{R}}{\sqrt{2z_i^3}}\left(1 - e^{-3/2}\right)\right]cos^2\theta\} \qquad (47)$$

Therefore Eq.39 becomes

$$K.E_i - K.E_f = \frac{A}{12z_i}\left\{sin^2\theta(1 - e^{-1}) + \left[(1 - e^{-1}) + \frac{2L\sqrt{R}}{\sqrt{2z_i^3}}\left(1 - e^{-3/2}\right)\right]cos^2\theta\right\} + E_{s,t}$$

$$- E_{s,p}$$

$$eK.E_i - e^3K.E_i$$

$$= -\frac{A}{12z_i}\left\{sin^2\theta(e - 1) + \left[(e - 1) + \frac{2L\sqrt{R}}{\sqrt{2z_i^3}}\left(\frac{e^2 - \sqrt{e}}{e}\right)\right]cos^2\theta\right\} + e(E_{s,t}$$

$$- E_{s,p})$$

This procedure yields finally the generating function for the restitution coefficient from Eq.39, as

$$e^2(1 - e^2)K.E_i + \frac{A}{12z_i}\left\{e(e - 1) + \left[\frac{2L\sqrt{R}}{\sqrt{2z_i^3}}(e^2 - \sqrt{e})\right]cos^2\theta\right\} = e^2(E_{s,t} - E_{s,p})$$

$$(48a)$$

For the limit value $e = 1$, the energy loss $(E_{s,t} - E_{s,p}) = 0$ (i.e. no loss of energy) which is what should be expected. For the other limit value $e = 0$, the above equation behaves as an identity, which is what should also be expected.

Substituting for $(E_{s,t} - E_{s,p})$, one gets

$$e^2(1 - e^2)K.E_i + \frac{A}{12z_i}\left\{e(e - 1) + \left[\frac{2L\sqrt{R}}{\sqrt{2z_i^3}}(e^2 - \sqrt{e})\right]cos^2\theta\right\} = e^2 \, 7.09\left[\frac{R^4(\frac{A}{12\pi z_0^2})^5}{K^2}\right]^{1/3}$$

$$(48b)$$

Eq.48b may be solved in general for $e \neq 0$, for the collision scattering of a particle, as in FigV.8, with the rough surface boundary.

Consider a specific example of a polystyrene rod-like particle, presenting hemispherical extremities of radius R = 2.5 nm, and an overall length L = 40 nm, with a kinetic energy equal to thermal energy

$$K.E_i = \frac{1}{2}k_B T = 2.07 \times 10^{-21} \, J$$

at room temperature. This choice evokes effectively a random Brownian displacement of a particle in the depletion layer bringing it into collision with a rough copper surface boundary. The energy loss in scattering $(E_{s,t} - E_{s,p}) = 4.203 \times 10^{-21}$ J, is calculated using Eq.46, and the equilibrium position is taken as $z_0 = 0.4$ nm between the hemispherical particle surface at its incoming extremity and the h_{eff} level of the rough surface (see Chapter 4 for a definition of this rough surface level).

Using Eq.48 we solve for e for different z_i and θ. This nonlinear equation has seven roots of which six are complex imaginary, and one is real. We plot the real solutions of e for the above kinetic energy, as a function of the variable initial positions z_i and angles θ in FigV.9. Since Eq.48 is quite complex it is useful to give a best-fit analytical expression for the real roots of e as a function of z_i and variable θ. This is given as follows

$$e = 0.321 - [sin^2\theta/\,15] + 0.708 \times Exp\left[-\frac{z_i}{131.902 - (0.85 \times \theta)}\right] \quad (49)$$
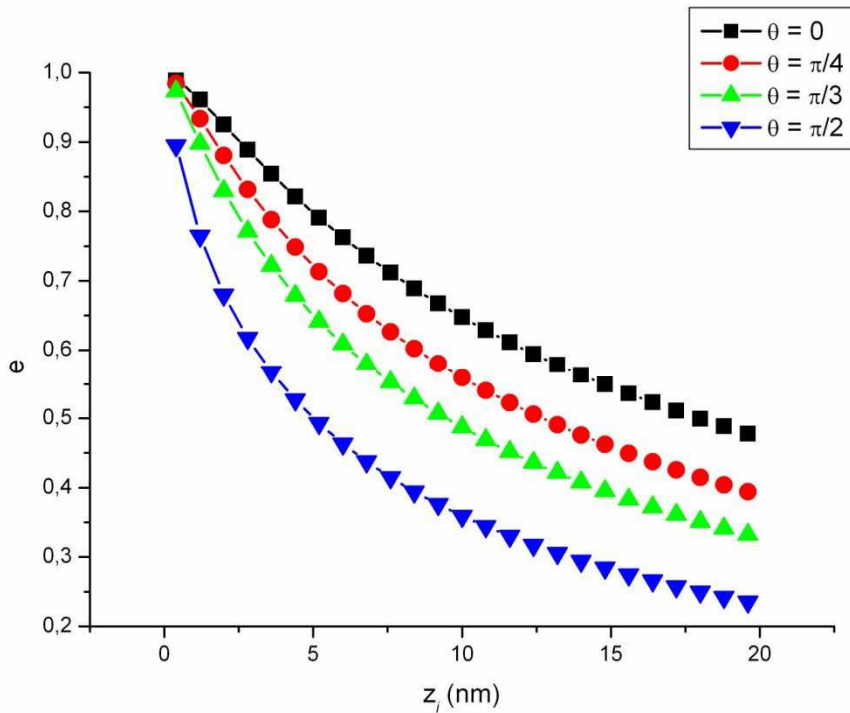

FigV.9 Restitution coefficient e as a function of particle extremity position from the surface, and at different angles of collision

5.5.2 Hamaker potential V_p for shish-kebab and spherical particles

Shish-kebab particles

In this section we simply give the Hamaker potentials for the two types of particles above. Consider macromolecular particles to have a shish-kebab form (Doi and Edwards 1986). This consists in considering the macromolecule as N pearls, or spheres, of equal d = 2R diameters, and N=L/d, where L is the length of this macromolecular from tip to tip as in FigV.10.
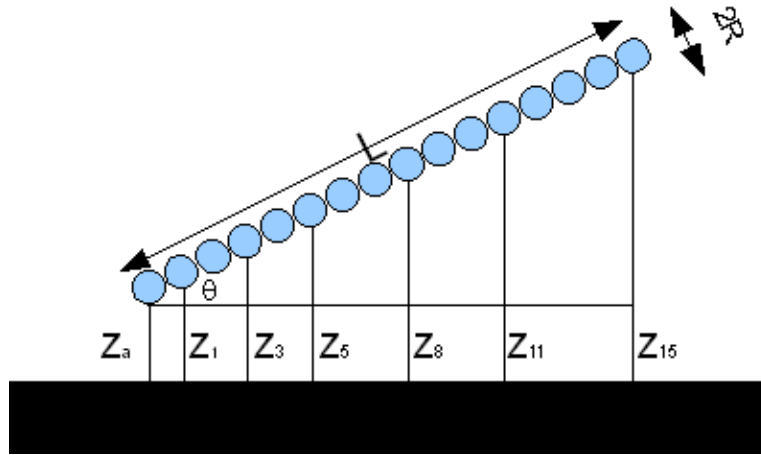
FigV.10 macromolecular rod like particles has a shish-kebab' model

The nearest distances to the plane surface of the different beads may be written successively as

$$z_1 = 2R\,sin\theta + z_i = 1(2R\,sin\theta) + z_i$$
$$z_2 = 2R\,sin\theta + z_1 = 2(2R\,sin\theta) + z_i$$
$$z_3 = 2R\,sin\theta + z_2 = 3(2R\,sin\theta) + z_i$$
$$.$$
$$.$$
$$z_n = 2R\,sin\theta + z_{n-1} = n(2R\,sin\theta) + z_i$$

It follows that the successive Hamaker potentials are

$$V_0 = -\frac{AR}{6}\left[\frac{1}{z_i} + \frac{2R}{z_i + 2R}\right]$$

$$V_1 = -\frac{AR}{6}\left[\frac{1}{z_1} + \frac{2R}{z_1 + 2R}\right] = -\frac{AR}{6}\left[\frac{1}{2Rsin\theta + z_i} + \frac{2R}{2Rsin\theta + z_i 2R}\right]$$

$$V_2 = -\frac{AR}{6}\left[\frac{1}{z_2} + \frac{2R}{z_2 + 2R}\right] = -\frac{AR}{6}\left[\frac{1}{2(2Rsin\theta) + z_i} + \frac{2R}{2(2Rsin\theta) + z_i + 2R}\right]$$

$$.$$
$$.$$

$$V_n = -\frac{AR}{6}\left[\frac{1}{z_{n-1}} + \frac{2R}{z_{n-1} + 2R}\right] = -\frac{AR}{6}\left[\frac{1}{n(2Rsin\theta) + z_i} + \frac{2R}{n(2Rsin\theta) + z_{ia} + 2R}\right]$$

Hence the Hamaker sum for the shish-kebab particle is

$$V_P = -\frac{AR}{6} \sum_{n=0}^{n} \left\{ \frac{1}{n(2R\sin\theta) + z_i} + \frac{2R}{n(2R\sin\theta) + z_i + 2R} \right\}$$

It follows that

$$-V_{p,i} + V_{p,f} =$$
$$-\frac{AR}{6} \sum_{n=0}^{n} \left\{ \frac{-1}{n(2R\sin\theta)+z_i} + \frac{-1}{n(2R\sin\theta)+z_i+2R} + \frac{1}{n(2R\sin\theta)+ez_i} + \frac{1}{n(2R\sin\theta)+ez_i+2R} \right\} \quad (50)$$

This procedure yields finally the generating function for the restitution coefficient from Eq.39, as

$$(1 - e^2)K.E_i +$$
$$\frac{AR}{6} \sum_{n=0}^{n} \left\{ \frac{-1}{n(2R\sin\theta)+z_i} + \frac{-1}{n(2R\sin\theta)+z_i+2R} + \frac{1}{n(2R\sin\theta)+ez_i} + \frac{1}{n(2R\sin\theta)+ez_i+2R} \right\} = (E_{s,t} - E_{s,p})$$
$$(51)$$

Eq.51 may be solved in general for $e \neq 0$, for the collision scattering of this particle form, as in FigV.10, with the rough surface boundary.

Spherical particles

We consider the simplest case when the particle is a sphere, with an attractive Hamaker potential

$$V_P = -\frac{A}{12} \left[\frac{2R}{Z} \right]$$

We take the 1st approximation for the attractive Hamaker potential therefore as

$$V_p \approx -\frac{AR}{6z} = -\frac{B}{z}, \text{ Where } B = \frac{AR}{6}$$
$$V_{P,i} = -\frac{B}{z_i} \text{ and } V_{P,f} = -\frac{B}{z_f} = \frac{B}{ez_i}$$

Hence we get

$$-V_{P,i} + V_{P,f} = +\frac{B}{z_i} - \frac{B}{ez_i} = \frac{B}{z_i}(1 - e^{-1}) = \Phi_i(1 - e^{-1}) \; ; \; \Phi_i = \frac{B}{z_i} \quad (52)$$

Therefore Eq.39 becomes

$$K.E_i - K.E_f = \Phi_i(1 - e^{-1}) + (E_{s,t} - E_{s,p})$$

$$e^3 K.E_i + \left[\Phi_i + (E_{s,t} - E_{s,p}) - K.E_i\right]e - \Phi_i = 0$$

This procedure yields finally the generating function for the restitution coefficient from Eq.39, as

$$e^3 - \frac{[K.E_i - \Phi_i - (E_{s,t} - E_{s,p})]e}{K.E_i} - \frac{\Phi_i}{K.E_i} = 0 \qquad (53a)$$

Eq.53 may be solved in general for $e \neq 0$, for the collision scattering of this particle form, with the rough surface boundary.

5.6 Adhesion sticking algorithms

The possible adhesion (stickiness) of metallic and macromolecular nano-particles during a collision with a solid surface depends on the loss of energy of the incident particle owing to the collision.

If and when the particle comes near the solid surface boundaries, as is the case in particular in region I of the depletion layer, due to hydrodynamic and Brownian events preceding this latest position, the simulation algorithm can be switched on to analyse whether or not the particle is in a position to submit to the consequences of the Hamaker attraction. In this case the program algorithm between the N*th* and the (N+1)*th* events will decide whether or not the particle will collide with the surface boundary, and calculate its restitution coefficient using an equation such as Eq.48 (Eq.49), and consequently whether or not it loses sufficient energy to stick – adhere at the surface.

The adhesion or non-adhesion may be summarized by a basic relation over the Newtonian restitution coefficient e as

$$K.E_f = e^2 K.E_i$$

$K.E_i$ and $K.E_f$ represent the kinetic energy of the particle before and after collision with the solid surface boundary, so that

Adhesion occurs if $\qquad K.E_f < E_P$

No Adhesion if $\qquad K.E_f > E_P$.

Adhesion should take place if the final kinetic energy of the particle is not enough to free it from the adhesive forces which act to keep it at the solid surface boundary. $E_P = |V_P(N)|$ is the energy necessary to liberate the particle during its collision rebound from the attractive Hamaker potential V_P binding the particle to solid surface boundary.

Using this procedure it is possible to chart the probabilities for the adhesion of different forms of particles at surface boundaries in mesopores, and to design an algorithm to calculate by numerical simulations the effective mobility for such particles during their flow inside mesopores under non-equilibrium conditions.

Note that under these conditions the ergodic assumption of equilibrium dynamics ceases to be valid and that an initial colloidal suspension will change its character and in concentration as the flow takes its deeper down the pore.

References

Aspenes, G., L. E. Dieker, et al. (2010). "Adhesion force between cyclopentane hydrates and solid surface materials." Journal of Colloid and Interface Science **343**(2): 529-536.

B.V. Derjaguin, V. M. Muller, et al. (1975). "Effect of contact deformations on the adhesion of particles." Journal of Colloid and Interface Science **53**(2): 314.

Bowling, R. A. (1985). "An Analysis of Particle Adhesion on Semiconductor Surfaces." Journal of The Electrochemical Society **132**(9): 2208-2214.

Bradley, R. S. (1932). "The Cohesive Force between Solid Surfaces and the Surface

Energy of Solids." Philosophical Magazine Series **7** (13): 853-862.

Butt, H.-J., K. Graf, et al. (2003). Physics and Chemistry of Interfaces. Uwe Krieg, Berlin Germany, Wiley-VCH.

Dahneke, B. (1972). "The influence of flattening on the adhesion of particles." Journal of Colloid and Interface Science **40**(1): 1-13.

Derjaguin, B. V., V. M. Muller, et al. (1975). "Effect of contact deformations on the adhesion of particles." Journal of Colloid and Interface Science **53**(2): 314-326.

Dobler, F. and Y. Holl (1996). "Mechanisms of latex film formation." Trend Polym Sci **4**: 145-151.

Doi, M. and S. F. Edwards (1986). "The Theory of Polymer Dynamics.

." Oxford University Press,.

Eckersley, S. T. and A. Rudin (1990). "Mechanism of film formation from polymer latexes." Journal of Coatings Technology **61**(780): 89-100.

Fowkes, F. M. (1968). "Calculation of work of adhesion by pair potential suummation." Journal of Colloid and Interface Science **28**(3-4): 493-505.

Fuller, K. N. G. and D. Tabor (1975). "The effect of surface roughness on the adhesion of elastic solids." Proc. Roy. Soc. London A **345**: 327-342.

Gordon, J. E. (1978). Structures: Or, Why Things Don't Fall Down. Great Britain by Cox & Waman Ltd, Penguin Group.

Greenwood, J. A. (1966). "Constriction resistance and the real area of contact." British Journal of Applied Physics **17**(12): 1621.

Hamaker, H. C. (1937). "The London-van der Waals attraction between spherical particles." Physica **4**(10): 1058-1072.

Harkins, W. D. (1919). "Cohesion, Internal Pressure, Adhesion, Tensile Strength, Tensile Energy, Negative Surface Energy, and Molecular Attraction." Proceedings of the National Academy of Sciences **5**(12): 562-568.

Hertz, H. (1882). "Über die Berührung fester elastischer Körper. ." Journal für die Reine und Angewandte Mathematik **92**: 156.

Hirschfelder, J. O., C. F. Curtiss, et al. (1964). The Molecular Theory of Gases and Liquids. New York John Wiley & Sons.

Israelachvili, J. (1991). Intermolecular and Surface Forces Academic Press, London.

Israelachvili, J. N. (2011). Intermolecular and Surface Forces, Third Edition. San Diego, United States of America, Academic Press Elsevier.

Johnson, K. L. (1976). Adhesion at the contact of solids. North-Holland, Amsterdam.

Johnson, K. L., K. Kendall, et al. (1971). "Surface Energy and the Contact of Elastic Solids." Proceedings of Royal Society **A324**: 301.

Keesom, W. H. (1921). "The cohesion forces in the theory of van der Waals." Phys. Zeit **22**: 129.

Kendall, K. (2001). Molecular Adhesion and Its Applications: The Sticky Universe. New York, Kluwer Academic/Plenum Publishers

Kendall, K., M. Kendall, et al. (2011). Adhesion of Cells, Viruses and Nanoparticles. Dordrecht, Netherlands, Springer.

King, M. and D. Gee (2010). Multiscale Modeling of Particle Interactions: Applications in Biology and Nanotechnology. New Jersey, United States of America, Wiley.

Krupp, H. (1967). "Particle Adhesion: Theory and Experiment " Adv. Colloid Interface Sci **1**: 111-140.

Lennart, B. (1997). "Hamaker constants of inorganic materials." Advances in Colloid and Interface Science **70**(0): 125-169.

London, F. (1937). "The general theory of molecular forces." Transactions of the Faraday Society **33**.

Maugis, D. (1992). "Adhesion of Sphere: The JKR-DMT Transition Using a Dugdale Model." J. Colloid Interface Sci **150**: 243-269.

Maynard, A. and D. Y. H. Pui (2007). Nanotechnology and Occupational Health. Dordrecht, Netherlands, Springer.

Mittal, K. L. (2002, 2003, and 2006). Particle on Surfaces: Detection, Adhesion and Removal, Vol, 7-9. AH Zeist , The Netherlands, VSP.

Mullins, M. E., L. P. Michaels, et al. (1992). "Effect of Geometry on Particle Adhesion." Aerosol Science and Technology **17**(2): 105-118.

Persson, B. N. J. (2002). "Adhesion between Elastic Bodies with Randomly Rough Surfaces." Physical Review Letters **89**(24): 245502.

Popov, V. (2010). Contact Mechanics and Friction: Physical Priciple and Application. Germany, Berlin, Springer.

Rimai, D. S., L. P. Demejo, et al. (1994). "Mechanics of particle adhesion." Journal of Adhesion Science and Technology **8**(11): 1333-1355.

Rimai, D. S., L. P. DeMejo, et al. (1992). "The Effect of Young's Modulus on The Surface-Force-Induced Contact Radius of Spherical Particles on Polystyrene Substrates. ." J. Appl. Phys. **71**: 2253-2258.

Sato, S., D.-R. Chen, et al. (2007). "Molecular Dynamics Study of Nanoparticle Collision with a Surface – Implication to Nanoparticle Filtration." Aerosol and Air Quality Research **7**(3): 278-303.

Tabor, D. (1977). "Surface forces and surface interactions." Journal of Colloid and Interface Science **58**: 2-13.

Tabor, D. (1977). "Surface forces and surface interactions." Journal of Colloid and Interface Science **58**(1): 2-13.

Tsai, C. J., D. Y. H. Pui, et al. (1990). "Capture and Rebound of Small Particles upon Impact with Solid Surfaces." Aerosol Sci. Technol **12**: 497-507.

van Beek, M. C. (2001). Gas-side fouling in heat-recovery boilers. Doctoral degree PHD thesis, Technische Universiteit Eindhoven.

Van Krevelen, D. W. and K. Te Nijenhuis (2009). Properties of Polymers: Their Correlation with Chemical Structure; their Numerical Estimation and Prediction from Additive Group Contributions. Amsterdam, The Netherlands, Elsevier Science; 4 edition.

Visser, J. (1976). "Adhesion of Colloidal Particle." Surface and Colloid Science **(Ed.), Matijevic, E 8**: 3-84.

Wang, H.-C. and W. John (1988). "Dynamic contact charge transfer considering plastic deformation." Journal of Aerosol Science **19**(4): 399-411.

Yia, M.-Y., D.-S. Kima, et al. (2005). "Molecular dynamics (MD) simulation on the collision of a nano-sized particle onto another nano-sized particle adhered on a flat substrate." J. Aerosol Sci **36**: 1427-1443.

Chapter 6

Conclusions and directions for future work

The main scope of this thesis aims at investigating the equilibrium dynamics of biological and macromolecular particles of nano dimensions, in colloidal suspensions in fluids inside pore systems, for a wide range of particle forms, for ideally flat and rough surface pore boundaries on the scale of the particles, and under a realistic range of physical conditions (system temperature, solution viscosity, Peclet number, pore width, particle length, particle form and aspect ratio, …). The simulation results such as for the nematic order parameter may also be compared with experimental data whenever these are available.

In Chapter II, we have developed algorithms and carried out numerical simulations to investigate the dynamics of dilute colloidal suspensions of macromolecular particles in solutions flowing inside a porous system, in this chapter the pores are modeled in a two-dimensional frame of reference with boundaries. The colloidal particles are subject to hydrodynamic forces, Brownian stochastic motion and random collisions at the solid surface boundaries of the pores. The numerical simulations are carried out to calculate in particular the spatial and orientation statistical PDF distributions of the macromolecular rod-like particles in colloidal suspensions in a solution under equilibrium dynamics in a Poiseuille flow inside the pore channels. The results are presented for different widths of pore channels referenced to the size of a rod-like particle and for a wide variety of hydrodynamic flow conditions, at low, intermediate, and high flow, characterised by the rotational Peclet number. Our simulations yield directly the nematic order parameter for colloidal suspensions in the two dimensional frame.

Chapter III has focused on the theoretical and numerical modeling for the dynamics of particle in the bulk and their diffusive collisions at the solid surface boundary in real 3D spatial frames. The considered particles are taken ellipsoidal like macromolecular particles flowing in dilute solution. We developed a theoretical model based in this case on the equations of Jeffrey for the dynamics of solid particles in fluids and the molecular dynamics by mechanical restitution for the diffusive collisions of the particles at the solid boundaries. *Equilibrium* PDF distributions are calculated over several orders of magnitude of the rotational Peclet number, and for variable aspect ratios characteristic of the ellipsoidal particles under study. Results demonstrate the importance and significance of modeling in a three-dimensional spatial frame as compared to the simulation results based in the Boeder

approach over a two-dimensional spatial frame Chapter II. The nematic order parameter over its tensorial representation also calculated for a variety of forms of ellipsoidal particles selected to correspond to real polymer particles.

The special class of molecular particles namely rigid rod-like particles for which the aspect ratio is much greater than unity are considered in Chapter IV. We have developed algorithms and carried out numerical simulations to investigate the dynamics of dilute colloidal suspensions of rod like particles in solutions flowing in bulk and near two types of solid boundaries the ideal atomically flat and the rough surface boundaries, for this reason of the hydrodynamic boundary conditions are considered to investigate in particular the influence of the roughness on the shear flow and on the diffusive collision.

Finally in Chapter V, We investigated for a theoretical model to calculate the restitution coefficient of particles of nano sizes in the depletion layer due to the conflicting influence of the mechanical diffusive collisions and the attractive Hamaker forces at the boundaries, the theoretical analysis for the restitution coefficient determine under given physical conditions the outcome for adhesion or not. For this reason, a theoretical model is developed, based on the JKR and Hertz theories, to account for the energy losses during collisions and for the energy gains due to the Hamaker interactions and we have shown that adhesion becomes an outcome if the energy balance permits this

For all of these problems, numerical simulations have proven a remarkable ally for the modeling the complex effects arising from dynamics of dilute colloidal suspensions of macromolecular particles in solutions flowing inside a porous system (closed or open pores) to the diffusive collisions of the nano particles at the solid surface boundary in 2D spatial frames to a real 3D spatial frame. However: much work remains to be done as we attempt to simulate yet larger and more complex systems.

Several areas like mobility, adhesion and complex fluid dynamics, are yet to be fully understood, and we describe a few of these below.

One of the major perspectives of this work is to use our theoretical model for the adhesion and corresponding mobility under non-equilibrium conditions to produce numerical simulations for the adhesion profiles, for different species of particles flowing in colloidal suspensions through pore networks. Such profiles should lead to technical applications as regards the filtering capacities by pore networks for diverse species of biological and macromolecular particles.

The problems described in this work all involved suspensions that were dilute; in many instances more concentrated suspensions are important (Semi dilute and concentration regime). The modeling of these effects is typically quite difficult, for this reason the numerical simulation in these regimes offer new challenges to count up the large number of the collisions between the particles and the boundary solid surface and between the particles themselves.

Complex physics: The greatest challenge of complex fluid dynamics today may exist in in the description of systems involving multiple physical phenomena, such as electric, thermal, chemical or mechanical phenomena. Such systems arise commonly in micro- and nano-fluidic devices, and also in the case for numerous biophysical systems. The difficulty in tackling these problems is double. On the one hand, a precise understanding of the basic physical phenomena and their coupling is in most cases still absent. On the other hand, the numerical simulation of these phenomena offers new challenges owing to the large number of degrees of freedom and of the highly nonlinear coupling between the various effects.

Annex AI

Brownian motion

Brownian motion is a phenomenon where small colloidal particles suspended in a fluid tend to move in relatively random or stochastic paths. The effect was discovered by Robert Brown in 1827, and is called Brownian motion after him. In 1905, Albert Einstein published a theory to explain Brown's observations, and showed that the so-called Brownian motion becomes more rapid and the colloidal particles move farther in a given time interval, when the temperature of the water is raised, when the viscosity of the fluid is lowered, and when the size of the colloidal particles is reduced

The atoms or molecules that make up a liquid or gas are in continuous thermal motion. This motion causes the molecules to strike the suspended colloidal particles at random. The consequent impacts force a colloidal particle to move in an erratic and random manner through the fluid. This phenomenon gives rise to what is called *translational Brownian diffusion*. The impacts of liquid molecules can also force the suspended particle to rotate. This phenomenon gives rise to what is called *rotational Brownian diffusion*.

The first approach of Einstein's theory is based on an argument of thermodynamic equilibrium. Suppose that x (t) - x (0) = X (t) is the *translation* diffusion distance of a colloidal particle, between an initial time t = 0 and a later time t. The average value at thermodynamics equilibrium of the statistical parameter $< X^2 >$ can be written in Einstein's work as:

$$< X^2 > = 2Dt \qquad (A1.1)$$

Where D is the diffusion coefficient of the colloidal particle, and is given by Einstein's theory as:

$$D = \frac{K_B T}{\varsigma} \qquad (A1.2)$$

In Eq. A1.2, T is absolute temperature, K_B is Boltzmann's constant $=1.38 \ 10^{-23}$ J K^{-1}, and λ is a friction coefficient of the particle in the fluid. To give an example, the friction coefficient λ for a sphere of radius R is given according to Stokes theorem by $\varsigma = 6\pi R \eta$, where η is viscosity of the fluid.

AI.1 Langevin solution for Brownian motion

Consider a single isolated colloidal particle suspended in a liquid, and undergoing random motion caused by its collisions and the surrounding liquid molecules. The colloidal particle has no preferred direction and at any instant it is not possible to predict in what direction it is going to move after such collisions.

We may nevertheless write down the equation of motion of such a particle under the action of two forces: a viscous force f = - ς v, where v is velocity of the particle and ς is the friction coefficient, and a fluctuating random forces $F(t)$ owing to the collisions.
The equation of the motion of the particle is then given by Newton's law

$$\frac{dv}{dt} = -\gamma v + \frac{F(t)}{m} \tag{AI.3}$$

Where $\gamma = \frac{\varsigma}{m}$

$F(t)$ is also called the Langevin force; it represents the unceasing impacts of the molecules of the fluid on the Brownian particles. Eq.AI.3 is called the Langevin equation, (Langevin 1908) It is a stochastic differential equation, and contains a fluctuating term $F(t)$. This term is a stationary random force, since

$$\langle F(t) \rangle = 0 \tag{AI.4a}$$

$$\langle F(t)F(t') \rangle = 2D_v m^2 \delta(t - t') \tag{AI.4b}$$

Putting v = v₀ at time t = 0, the general solution of the Langevin equation may be written formally as follows

$$v(t) = v_0 e^{\frac{-t}{\tau}} + \frac{e^{\frac{-t}{\tau}}}{m} \int_0^t F(t') e^{\frac{-t'}{\tau}} dt' \tag{AI.5}$$

Where $\tau = \frac{1}{\gamma} = \frac{m}{\varsigma}$ is the relaxation time of the velocity auto-correlation function and γ is friction coefficient per unit time.

Eq. AI.5 shows that the particle velocity is a random quantity and that it is a function of time. As the average fluctuating force $F(t)$ is zero, we may readily show that:

$$\langle v(t) \rangle = v_0 e^{\frac{-t}{\tau}} \tag{AI.6}$$

Physically, the colloidal particle will come to equilibrium in the fluid when its average velocity goes to zero after a time t >> τ, where τ is a characteristic diffusion time. Further; we

can define an auto-correlation function, between the instants t and $t + \tau_v$, using the Eq. AI.3 and AI.4.

$$C_v(\tau_v) = \langle V(t)V(t + \tau_v) \rangle \tag{AI.7a}$$

$$C_v(\tau_v) = \langle v_0^2 \rangle e^{\frac{-(2t+\tau_v)}{\tau}} + D_v\tau(e^{\frac{-\tau_v}{\tau}} - e^{\frac{-(2t+\tau_v)}{\tau}}) \tag{AI.4b}$$

Under this condition $(t/\tau \gg 1)$, the previous relation is simplified and take the following form

$$C_v(\tau_v) = \langle V(t)V(t + \tau_v) \rangle \cong D_v\tau e^{\frac{-\tau_v}{\tau}} \tag{AI.8}$$
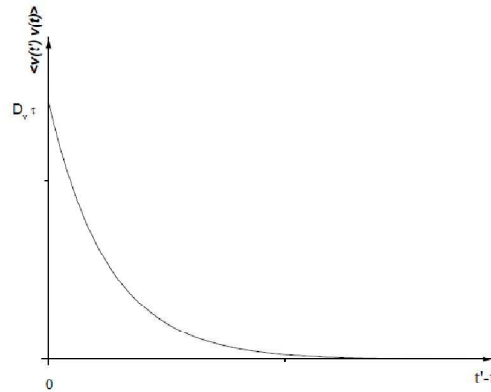
Fig AI.1 velocity auto-correlation function

For $\tau_v = 0$, we find a relation according to the thermal energy

$$\langle v^2(t) \rangle \cong D_v\tau = \frac{D_v}{\gamma} = \frac{K_BT}{m} \tag{AI.9}$$

Then we can deduce the expression of the diffusion coefficient constant in term of , m ,T and Boltzman's constant K_B :

$$D_v = \frac{K_BT}{m}\gamma \tag{AI.10}$$

The position of the particle is a random variable, and it is a function of time; we will calculate the average position in terms of time to obtain the necessary information on the behaviour of the Brownian particles in the fluid.

We Assume that at time t = 0, x_0 = 0; from Eq. AI.5, we conclude that:

$$x(t) = v_0\tau\left(1 - e^{\frac{-t}{\tau}}\right) + \frac{1}{m}\int_0^t dt' \int_0^{t'} F(t'')e^{\frac{-(t'-t'')}{\tau}}dt'' \qquad \text{(AI.11)}$$

The average value of x (t) is $\langle x(t)\rangle$

$$\langle x(t)\rangle = v_0\tau(1 - e^{\frac{-t}{\tau}}) \qquad \text{(AI.12)}$$

Since the auto-correlation function of velocity is difficult to derive, it is preferable to calculate the square displacement,. Putting at instant t = 0, x = x_0, one obtains

$$\langle(x(t) - x_0)^2\rangle = \langle(\int_0^t v(t')\,dt')^2\rangle = \int_0^t dt_1 \int_0^t dt_2 \langle v(t_1)v(t_2)\rangle \qquad \text{(AI.13)}$$

Using the Eq. AI.8 and t $\gg \tau$ we obtain:

$$\langle(x(t) - x_0)^2\rangle \cong \frac{2D_v}{\gamma^2}t = 2D_x t \qquad \text{(AI.14)}$$

With $D_x = \frac{D_v}{\gamma^2}$ is the spatial diffusion coefficient.

AI.2 Translation and Rotational Diffusion Coefficients for Rod-like Particles

For the rod, the translation diffusion, parallel and perpendicular to its axis may be treated separately Fig A1.2; we assign by $D_\parallel$ and $D_\perp$ the diffusion coefficients parallel and normal to the rod. The distances $R_\parallel$ and $R_\perp$, moved by the rod respectively parallel and normal to its symmetry axis, during a short instant $\Delta t = t_2 - t_1$, are then:

$$\langle|R_\perp(t_2 - t_1)|^2\rangle = 2D_\perp\Delta t$$

$$\text{(AI.15)}$$

$$\langle|R_\parallel(t_2 - t_1)|^2\rangle = 2D_\parallel\Delta t$$
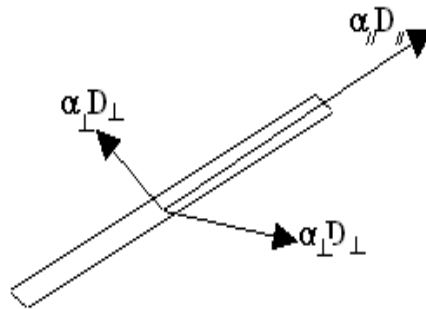

Fig A1-2: $D_{//}$ and $D_\perp$ Translation diffusion of the rod

(Riseman and Kirkwood 1950), have calculated the values of the diffusion coefficients, $D_{//}$, $D\perp$, and D_r from the hydrodynamics and using the model of shish-kebab, and here their results:

$$D_\parallel = \frac{K_B T}{\varrho_\parallel} = \frac{K_B T ln(\frac{L}{d})}{2\pi\eta L}$$

$$D_\perp = \frac{K_B T}{\varrho_\perp} = \frac{K_B T ln(\frac{L}{d})}{4\pi\eta L} \qquad (AI.16)$$

$$D_r = \frac{K_B T}{\varrho_r} = \frac{K_B T ln(\frac{L}{d})}{2\pi\eta L^3}$$

The rod diffuses more readily parallel to its symmetry axis than perpendicular to it, as $D_\parallel = 2D_\perp$ an effective translational diffusion coefficient is defined in the literature as:

$$D_t = \frac{1}{3}(D_\parallel + D_\perp) \qquad (AI.20)$$

(Broersma 1960; Broersma 1960) rewrote the previous inequalities by introducing a correction factor β, taking into account the hydrodynamic behaviour for a smooth cylinder and combining the theoretical and experimental approaches:

$$D_r = \left(\frac{3K_B T}{\pi\eta L^3}\right)(\Omega - \beta)$$
$$\beta = 1.45 - 7.51(\frac{1}{\Omega} - 0.27)^2$$
$$D_t = \left(\frac{K_B T}{3\pi\eta L}\right)(\Omega - \frac{1}{2}(\lambda_\parallel - \lambda_\perp))$$
$$D_\parallel = \left(\frac{K_B T}{2\pi\eta L}\right)(\Omega - \lambda_\parallel) \qquad (AI.21)$$
$$D_\perp = \left(\frac{K_B T}{4\pi\eta L}\right)(\Omega - \lambda_\perp)$$
$$\lambda_\parallel = 1.27 - 7.4(\frac{1}{\Omega} - 0.34)^2$$
$$\lambda_\perp = 0.19 - 4.2(\frac{1}{\Omega} - 0.39)^2$$
$$\Omega = ln(\frac{2L}{d})$$

AI.3 Translation and Rotational Diffusion Coefficients for Ellipsoidal-like Particles

The Brownian diffusion coefficient for a spheroid particle with long axis of length L and two short axes of length R = d/2, translational diffusion is anisotropic and is described by

diffusion coefficients $D_L = \frac{K_B T}{\varsigma_L}$ along the long axis and $D_R = \frac{K_B T}{\varsigma_R}$ along the short axes. The rotationnel diffusion coefficient of the spheroid about its short axes is $D_\theta = \frac{K_B T}{\varsigma_\theta}$. Generally, the drag coefficients ς_L, ς_R and ς_θ depend on the shape and size of the ellipsoid.

Brownian motion of anisotropic particles was first seriously considered by F. Perrin (Perrin 1934; Perrin 1936) who computed these drag coefficients analytically for a spheroid diffusing in three dimensions space. When a ellipsoidal particle with semi-axes (L/2, R, R), moves along one of its principle axes with velocity v, through an unbounded quiescent fluid with viscosity η at low Reynolds number, then the translational and rotational drag coefficients affecting the ellipsoidal are:

$$\varsigma = 6\pi\eta dG \tag{AI.22a}$$

$$\varsigma_\theta = 6\pi\eta V G_\theta \tag{AI.22b}$$

Where V is the volume of the spheroid and G is the geometric factor that renders the ellipsoid different relative to the case of a sphere. The geometric factors for spheroids diffusing in 3D are analytically derived from Perrin's equations (Happel and Brenner 1991)

$$G_L = \frac{8}{3} \frac{1}{\left[\frac{2r_e}{1-r_e^2} + \frac{2r_e^2-1}{(r_e^2-1)^{3/2}} ln\left(\frac{r_e+\sqrt{r_e^2-1}}{r_e-\sqrt{r_e^2-1}}\right)\right]} \tag{AI.23a}$$

$$G_R = \frac{8}{3} \frac{1}{\left[\frac{r_e}{r_e^2-1} + \frac{2r_e^2-3}{(r_e^2-1)^{3/2}} ln\left(r_e+\sqrt{r_e^2-1}\right)\right]} \tag{AI.23b}$$

and (Perrin 1934; Koenig 1975)

$$G_\theta = \frac{2}{3} \frac{r_e^4-1}{\left[\frac{2r_e^2-1}{\sqrt{r_e^2-1}} ln\left(r_e+\sqrt{r_e^2-1}\right)-r_e\right]} \tag{AI.23c}$$

Here $r_e = L/d$ is the ellipsoid aspect ratio. When $r_e = 1$, then $G = G_\theta = 1$ and Eq. AI.22 reduces to the translational and rotational Stokes laws for a sphere. Note also that Eqs. AI.22 and AI.23 are obtained using stick boundary conditions.

Rotational Brownian motion relation in 3D spatial frames

The Brownian forces in the bulk create a diffusive rotational motion of the particles. The Brownian rotation variables between two successive simulation events labelled s and s +1 $\Delta\theta_{rot}(s; s+1)$ and $\Delta\varphi_{rot}(s; s+1)$ can then be simplified in the algorithm to

$$\Delta\varphi_{rot}(s; s+1) = \pm\Delta\varphi_{rot} \tag{AII.1a}$$
$$\Delta\theta_{rot}(s; s+1) = \pm\Delta\theta_{rot} \tag{AII.1b}$$

The notations $\pm\Delta\varphi_{rot}$ and $\pm\Delta\theta_{rot}$ is clock and anticlockwise Brownian rotation. In this procedure the simulation time interval Δt is related to an effective variable for the Brownian rotation diffusion by the following equation.

$$\Delta\varphi_{rot}^2 = 2D_{\varphi\,rot}\,\Delta t \tag{AII.2a}$$
$$\Delta\theta_{rot}^2 = 2D_{\theta\,rot}\,\Delta t \tag{AII.2b}$$

For the small simulation time intervals Δt to be unique, they must satisfy

$$\Delta t = \frac{1}{2D_{\theta\,rot}}\,\Delta\theta_{rot}^2 = \frac{1}{2D_{\varphi\,rot}}\,\Delta\varphi_{rot}^2 \tag{AII.3}$$

This leads to the simulation relationship that

$$\Delta\theta_{rot}^2 = \frac{2D_{\theta\,rot}}{2D_{\varphi\,rot}}\,\Delta\varphi_{rot}^2 \equiv r_{\theta,\varphi}\,\Delta\varphi_{rot}^2 \tag{AII.4}$$

There are two ways to treat $r_{\theta,\varphi}$ in the numerical simulations as follows

$$r_{\theta,\varphi} = \frac{D_{\theta\,rot}}{D_{\varphi\,rot}} = 1 \tag{AII.5a}$$
$$r_{\theta,\varphi} = (\sin\varphi)^{-2} \tag{AII.5b}$$

Eq. AII.5a is based on the assumption of independent and random Brownian simulation events, where the ellipsoidal symmetry cuts the same diffusion coefficient in whatever angular displacement it makes.

Relation between $\Delta\theta_{rot}$ and $\Delta\varphi_{rot}$ in Eq. AII.5b

Consider rod-like particle with length OP = r; the particle orientation is defined by two angles (θ, φ); the spherical angles θ and φ defined in a fixed Cartesian coordinate x, y, z in three dimensional spatial frames Fig AII.1; θ is defined as the angle of the particle with respect to flow direction, φ as the vorticity axis.
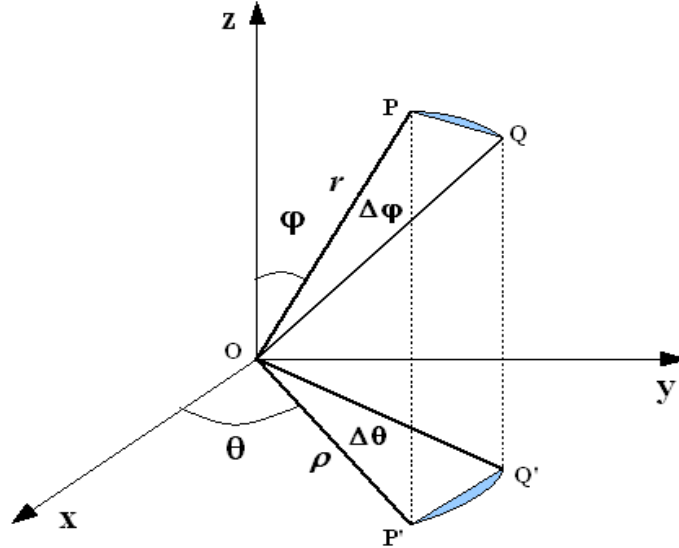

Fig AII.1 Coordinate system for rod-like OP and subject to a simple shear flow in xy plane.

Geometrical study

OP' = ρ is the projection of OP = r in xy plane

$$OP' = \rho = r \sin \varphi \qquad (AII.6)$$

OQ = r corresponds to the rotation of OP by small angle $\Delta\varphi$; $\widehat{POQ} = \Delta\varphi$

OQ' = ρ is the projection of OQ in xy plane, the small angle between OP' and OQ' is $\widehat{P'OQ'} = \Delta\theta$

We have

$$\overline{PQ} = \overline{P'Q'} \qquad (AII.7)$$

For small angle we have

$$\widehat{PQ} = \overline{PQ} \qquad (AII.8)$$

thus

$$\widehat{PQ} = \widehat{P'Q'} \qquad (AII.9)$$

In the same we can calculate $\widehat{PQ}$ and $\widehat{P'Q'}$ as following:

$\widehat{PQ} = r \, \Delta\varphi$, and $\widehat{P'Q'} = \rho\Delta\theta$

Hence

$$\widehat{PQ} = \widehat{P'Q'} = r \, \Delta\varphi = \rho\Delta\theta$$

Using Eq. AII.6

$$r\,\Delta\varphi = r\,sin\Delta\theta$$

Therefore

$$\Delta\varphi = sin\varphi\,\Delta\theta \qquad\qquad (AII.10)$$

On the other hand

$$r_{\theta,\varphi} = \frac{2D_{\theta\,rot}}{2D_{\varphi\,rot}} = \frac{\Delta\theta_{rot}^2}{\Delta\varphi_{rot}^2} = \frac{\Delta\theta_{rot}^2}{(sin\varphi\,\Delta\theta)^2} = \frac{1}{sin\varphi^{\,2}}$$

Therefore Eq. AII.5b is proved

$$r_{\theta,\varphi} = (\sin\varphi)^{-2}$$

Comparison Between the results obtained for different $r_{\theta,\varphi}$

Fig AII.2a and b, and Fig AII.3a will present the angular PDF distributions, P (θ, φ), for ellipsoidal macromolecular; while Fig AII.4a and b will present the angular PDF distributions, P (θ, φ), for rod-like macromolecular particles in 3 dimensional spatial frames in bulk system, at different ratio $r_{\theta,\varphi}$ and at medium Peclet number α = 10; The angles θ and φ represent the orientational angle of the particles in the 3D system, θ is defined as the angle of the particle with respect to flow direction, φ as the vorticity axis, for the ellipsoidal particles we define also the aspect ratio which corresponds to the ratio of the length of the ellipsoid to its width. The maximum probability in these Figs corresponds to the red color which decreases to attain the minimum value (black color).

The PDF distribution in Fig AII.2a and b at medium hydrodynamic flow α = 10, and for small aspect ratio r_e = 1.02, show a uniform distribution of the particles all over the bulk region with no preferred axes of rotation This wide range of distribution comes from the small aspect ratio of the ellipsoidal particle . The ratio $r_{\theta,\varphi}$ between the two figures is not the same which means that the total stochastic Brownian motion of particles is not the same; this gives two kind of Brownian activation. Indeed it's important to mention that the physical distributions for the two figures are the same. Similarly the physical distributions Fig AII.3a and b and Fig AII.4a and b are the same
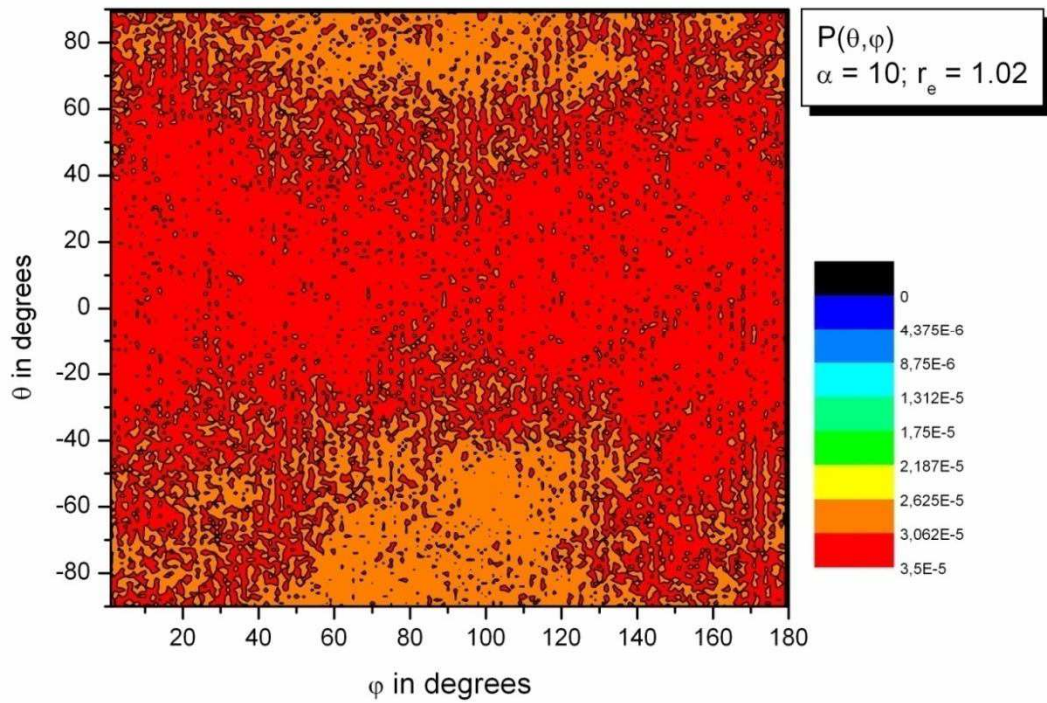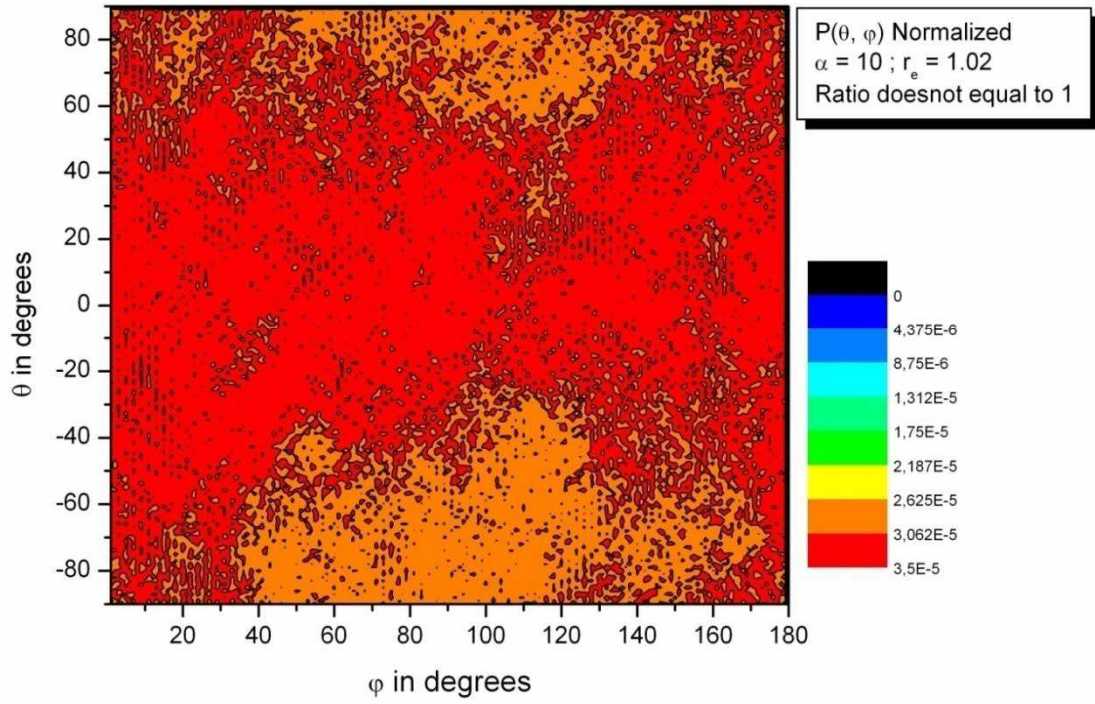
Fig AII.2 Simulation results for normalized angular PDF, P (θ, φ), in the bulk at medium Peclet number α = 10 and at small aspect ratio $r_e = 1.02$ a): $r_{\theta,\varphi} = (\sin\varphi)^{-2}$ (b): $r_{\theta,\varphi} = 1$
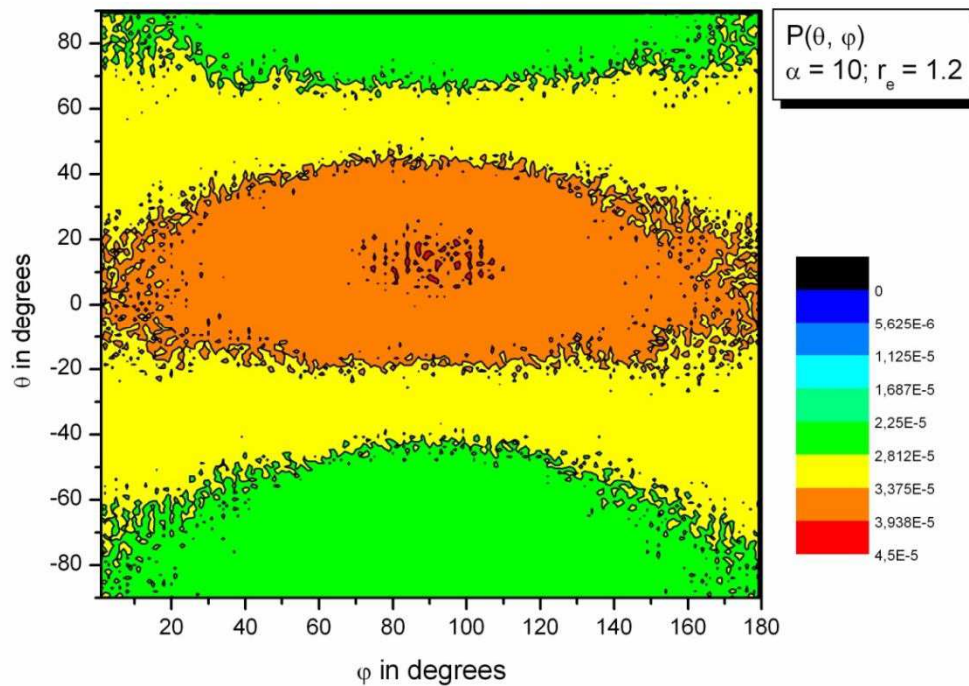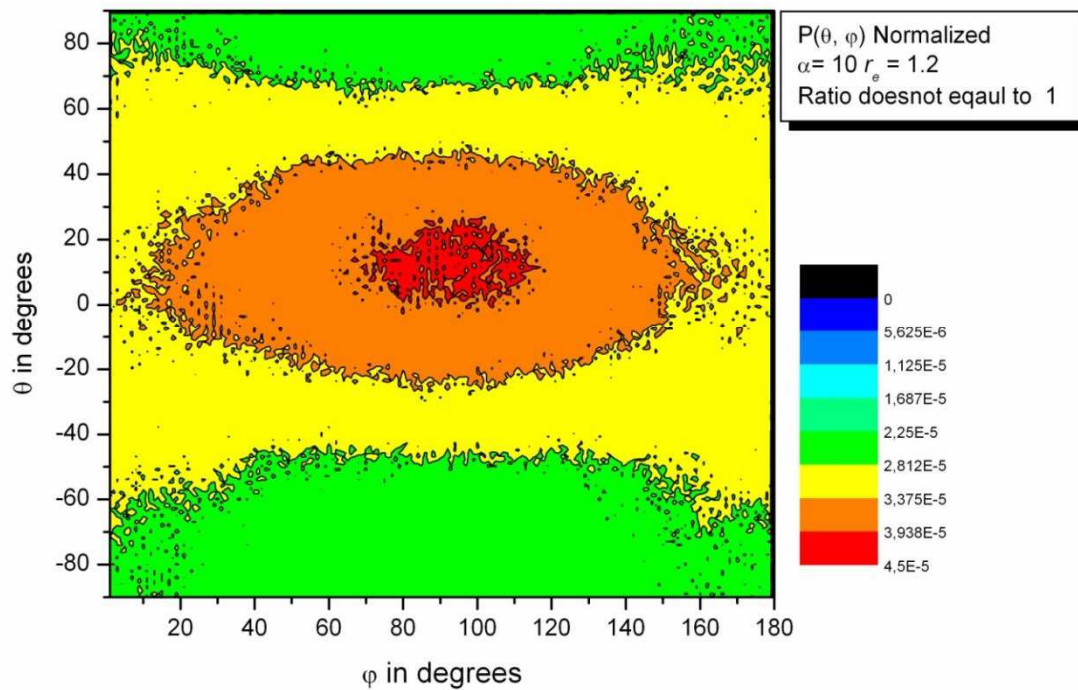
Fig AII.3 Simulation results for normalized angular PDF, P (θ, φ), in the bulk at medium Peclet number α = 10 and at aspect ratio r_e = 1.2 a): $r_{\theta,\varphi}$ = $\left(\sin\varphi\right)^{-2}$ (b): $r_{\theta,\varphi}$ = 1
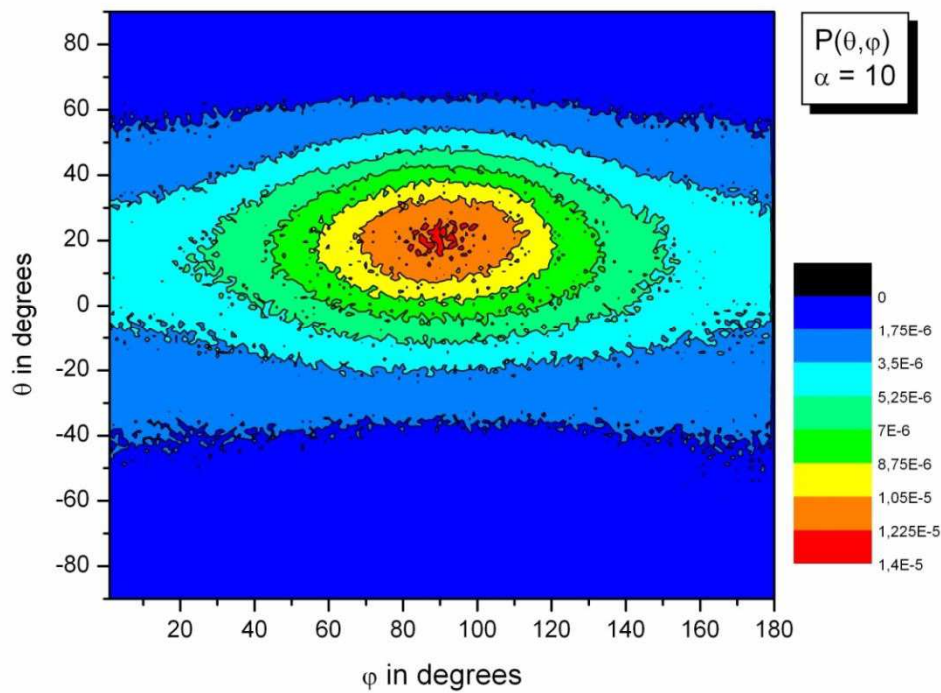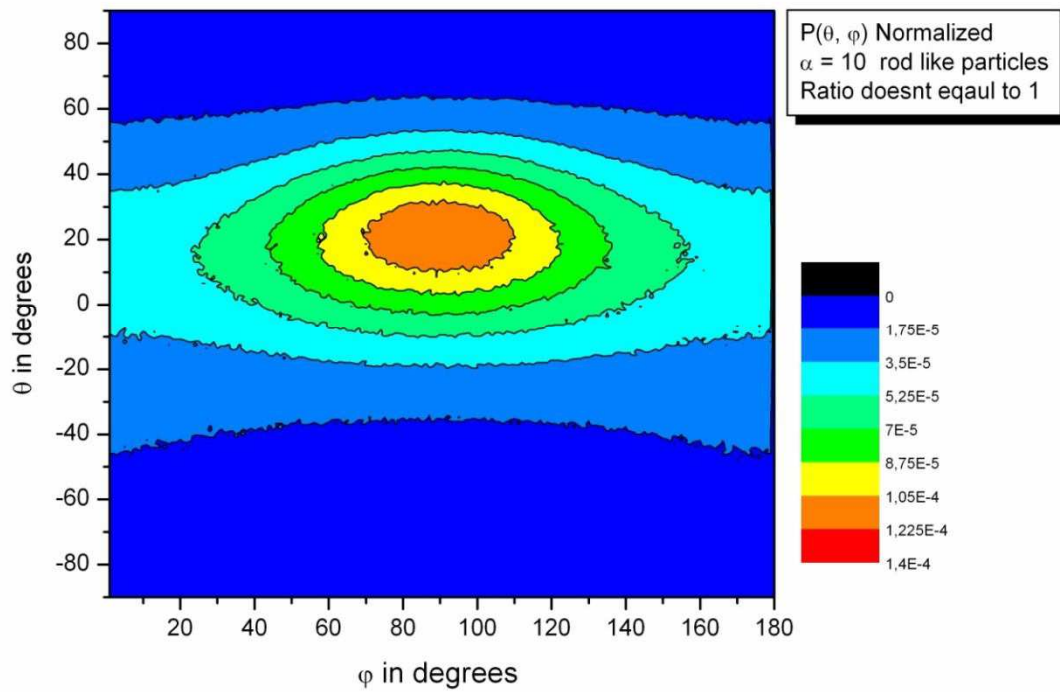
Fig AII.4 Simulation results for normalized angular PDF, P (θ, φ), in the bulk at medium Peclet number $\alpha = 10$ for rod-like particles a): $r_{\theta,\varphi} = (\sin \varphi)^{-2}$ (b): $r_{\theta,\varphi} = 1$

Particles interaction

AIII.1 Tsai derivation for Attractive and Repulsive Forces and Energies for a Flattened Spherical Particle on the Surface (Tsai, Pui et al. 1991)

Both the attractive and repulsive molecular contributions are integrated based on the additive assumption for a flattened sphere on the plane Fig AIII.1. Consider the interaction force between a molecule P in the flattened surface and a molecule in the plane, this interaction can be integrated as follows:

$$F_{P-Plane} = 2\pi(n-1)n_1\lambda \int_c^\infty x_1\,dx_1 \int_0^\infty \frac{y_1}{(x_1^2+y_1^2)^{\frac{(n+1)}{2}}}\,dy_1 = \frac{2\pi n_1\lambda}{(n-3)C^{n-3}} \quad (AIII.1)$$

$n = 7, \lambda = \beta_1$ For attractive force

$n = 13, \lambda = -\beta_2$ For repulsive force

The constant term β_1 is equal $4\varepsilon z_0^6$ and it's called the London- van der Waals constant, and the constant term β_2 is equal $4\varepsilon z_0^{12}$, and represents the repulsive components. β_1 and β_2 are related as $\beta_2 = \beta_1 z_0^6$. Chapter 5
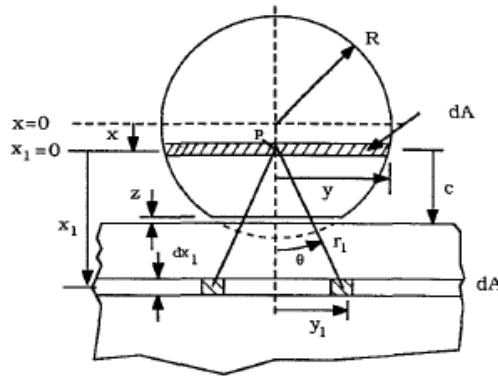

Fig AIII.1

Because of the symmetry $F_{P-Plane}$, of every point in the area dA of the flattened sphere and the plane can be calculated using the same expression. Hence the interaction force between the flattened sphere and the plane can be integrated as:

$$F = \frac{2\pi^2 n_1 n_2 \lambda}{(n-3)} \int_{-R}^{R-\delta} \frac{(R^2-x^2)}{(R'-x)^{n-3}} = \frac{4\pi^2 n_1 n_2 \lambda R}{(n-3)(n-4)(n-5)z^{n-5}}\left\{1 + \frac{(n-5)\delta}{z}\right\} + D \quad \text{(AIII.2)}$$

In the above equations, n_1 and n_2 are the numbers of the molecules in the plane and the flattened sphere respectively $R' = R + z - \delta$, δ represents the amount of deformation and is the relative approach between the particle and surface; the constant D are due to the deformed contact profile. They depend on n value and can be shown to be:

For $n = 7$

$$D = -\frac{\pi^2 n_1 n_2 \lambda R}{6z^2}\frac{\delta}{z}\left\{\frac{1}{\left(1-2\frac{z}{\delta}\right)^5}\right\}\left[1 - 12\frac{z}{\delta} + 72\left(\frac{z}{\delta}\right)^2 + \cdots\right] \quad \text{(AIII.3a)}$$

For $n = 13$

$$D = -\frac{\pi^2 n_1 n_2 \lambda R}{180z^8}\frac{4\delta}{z}\left\{\frac{1}{\left(1-2\frac{z}{\delta}\right)^{11}}\right\}\left[1 - \frac{45}{2}\frac{z}{\delta} + \frac{1620}{7}\left(\frac{z}{\delta}\right)^2 + \cdots\right] \quad \text{(AIII.3b)}$$

By adding the constant D into Eq. AIII.2 and neglecting high order terms, the attractive force $F_a(n = 7)$ and repulsive force $F_r(n = 13)$ can be written as:

$$F_a = + \frac{A_1 R}{6z^2}\left\{1 + \frac{\delta}{z}\right\} \quad \text{(AIII.4a)}$$

$$F_r = -\frac{A_2 R}{180z^8}\left\{1 + \frac{4\delta}{z}\right\} \quad \text{(AIII.4b)}$$

Where $A_1 = \pi^2 n_1 n_2 \beta_1$ and $A_2 = \pi^2 n_1 n_2 \beta_2$, are the Hamaker constant for attraction and repulsion respectively. If the concept of molecular- molecular interaction is used, it can be shown $A_2 = A_1 z_0^6$ (Tsai, Pui et al. 1991) found that a force constant K_a must be added such that $A_2 = K_a A_1 z_0^6$, Without this force constant, force balance cannot be otherwise satisfied.

The attractive (E_a) and repulsive (E_r) interaction energies can be obtained in the same way as follows

$$E_a = -\frac{A_1 R}{6z}\left\{1 + \frac{\delta}{2z}\right\} \quad \text{(AIII.5a)}$$

$$E_r = +\frac{A_2 R}{1260z^7}\left\{1 + \frac{7\delta}{2z}\right\} \quad \text{(AIII.5b)}$$

AIII.2 Interaction Potentials between Macroscopic Bodies

In this section we shall relate the pair potentials between small molecules to those between molecules and surfaces, and between large particles of different geometries.

AIII.2.1 Molecule-Surface Interaction

Let us assume that the pair potential between two atoms or small molecules is purely attractive and of the form $w(r) = -\frac{C}{r^n}$. Then, with the further assumption of additives, the net interaction energy of a molecule and the planar surface of a solid made up of like molecules (AIII.2) will be the sum of its interactions with all the molecules in the body. For molecules in a circular ring of cross-sectional area *dxdz* and radius x, the ring volume is *2πxdxdz*, and the number of molecules in the ring will be *2ρxdxdz*, where *ρ* is the number density of molecules in the solid. The net interaction energy for a molecule at a distance D away from the surface will therefore be:

$$W(D) = -2\pi C\rho \int_{z=D}^{Z=\infty} dz \int_{x=0}^{x=\infty} \frac{Xdx}{(z^2+x^2)^{n/2}} = -\frac{2\pi C\rho}{(n-2)} \int_{D}^{\infty} \frac{dz}{z^{n-2}}$$

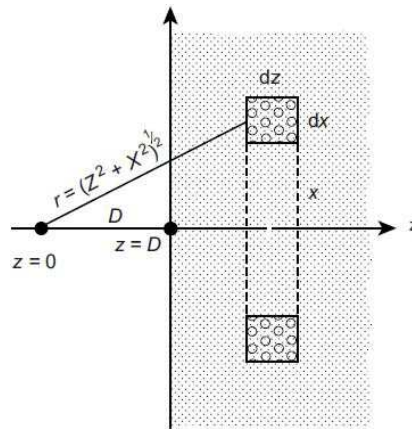$$W(D) = -2\pi C\rho/(n-2)(n-3)D^{n-3} \text{ For n} > 3 \qquad (AIII.6)$$

Fig AIII.2 Methods of summing (integrating) the interaction energies between molecules in condensed phases to Molecule near a flat surface or "wall

For n = 6 (van der Waals forces) becomes

$$W(D) = -\pi C\rho/6D^3 \qquad (AIII.7)$$

The corresponding force, $F(D) = -\frac{dw(D)}{dD} = -\frac{\pi C\rho}{2D^4}$, could, of course, have been derived in a similar way by summing (integrating) all the pair forces resolved along the z-axis.

AIII.2.2 Sphere-Surface and Sphere-Sphere Interaction

We can now calculate the interaction energy of a large sphere of radius R and a flat surface (Fig AIII.3). From the chord theorem, for the circle: $x^2 = (2R - z)z$; The volume of a thin circular section of area πx^2 and thickness dz is therefore $\pi x^2 dz = \pi(2R - z)z\, dz$, so that the number of molecules contained within this section is $\pi \rho\,(2R - z)z\,dz$; where ρ is the number density of molecules in the sphere. Since all these molecules are at a distance $(D+z)$ from the planar surface, the net interaction energy is, using Eq. AIII.6
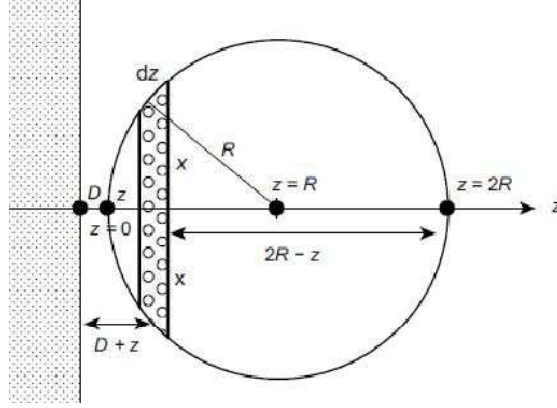

Fig AIII.3 Methods of summing the interaction energies between spherical particle near a wall (R » D)

$$W(D) = \frac{2\pi^2 C \rho^2}{(n-2)(n-3)} \int_{z=0}^{z=2R} \frac{(2R-z)z\,dz}{(D+z)^{n-3}} \tag{AIII.8}$$

For $D \ll R$ only the small values of z $(z \sim D)$ contribute to the integral, and we obtain

$$W(D) = \frac{2\pi^2 C \rho^2}{(n-2)(n-3)} \int_{z=0}^{z=2R} \frac{2Rz\,dz}{(D+z)^{n-3}} = \frac{4\pi^2 C \rho^2 R}{(n-2)(n-3)(n-4)(n-5)D^{n-5}} \tag{AIII.9}$$

For n = 6 (van der Waals forces) becomes

$$W(D) = -\pi C \rho^2 / 6D \tag{AIII.10}$$

Note that the interaction energy is proportional to the radius of the sphere and that it decays as 1/D, very much slower than the $1/r^6$ dependence of the intermolecular pair interaction.
For D » R, we may replace (D + z) in the denominator of Eq. AIII.8 by D, and we then obtain

$$W(D) = \frac{2\pi^2 C \rho^2}{(n-2)(n-3)} \int_0^{2R} \frac{(2R-z)z\,dz}{(D+z)^{n-3}} = \frac{2\pi^2 C \rho(4\pi R^3 \rho/3)}{(n-2)(n-3)D^{n-3}} \tag{AIII.11}$$

Since $(4\pi R^3 \rho/3)$ is simply the number of molecules in the sphere, the preceding is essentially the same as Eq. AIII.6 for the interaction of a molecule (or small sphere) with a surface.

AIII.3 chord theorem

Two rigid macroscopic spheres of radius R are in adhesive contact as in Fig AIII.4, the effective contact area can be calculated by what called chord theorem.
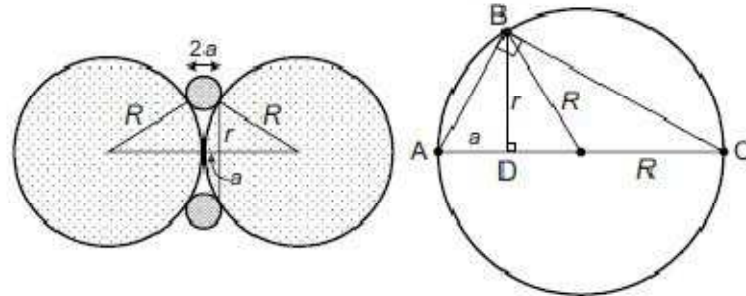
Referring to Fig AIII.4 (left), we need to determine the area that excludes solvent molecules, of radius a, between the surfaces. That is, we need to determine πr^2 in terms of R and a. From the geometric construction of Fig AIII.4 (right) we apply Pythagoras's theorem:

$$AC^2 = AB^2 + BC^2 = AD^2 + BD^2 + DC^2$$

Thus:

$$4R^2 = a^2 + 2r^2 + (2R - a)^2$$

This simplifies to

$$r^2 = (2R - a)a \approx 2Ra \ \ for \ R \gg a \tag{AIII.12}$$

Effective Hamaker constant at a rough surface boundary

The most notable research work for developing rough surface boundaries is the study of (Greenwood and Williamson 1966) (GW). GW is a statistically based approach. The GW theory makes the following assumptions: i) all asperities in contact were spherical with the same radius of curvature, ii) asperity heights follow a Gaussian distribution, and iii) there is no interaction between contacting asperities. (Fuller and Tabor 1975) made use of the statistical framework developed by GW and used it to create an adhesive solution for JKR contact types. The two rough surface contact theories mentioned above and of course many others (Maugis 1992; Kim, McMeeking et al. 1998; Morrow, Lovell et al. 2003) are based upon conventional statistical parameters such as standard deviation of asperity heights, slope and radius of curvature. In this work we will solve the problem of an effective Hamaker constant for the rough surface boundary of a pore with a liquid solution that fills it, by extending the GW analysis.
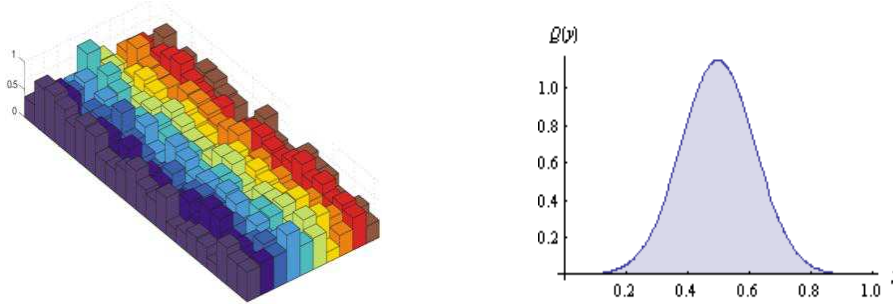

Fig AIV.1 Gaussian rough surface, (a) Topography and (b) height distribution

Consider a Gaussian rough surface Fig AIV.1 a with statistical distribution $Q(y)$, as in Fig AIV.1 b, over terrace heights y with a given mean μ and standard deviation σ. Further, we consider, the maximum height of surface profile roughness to be $y = h_{max} = 1$ *unit* and other *characteristic statistical parameters* for the terrace height distributions,($h_{max}=1$ *unit* , $h_{avgrage}=$ 0.5 unit $h_{min}=0.0$ *unit)*. The Gaussian function can be written in the following form:

$$Q(y) = \frac{1}{\sqrt{2\pi\sigma^2}} e^{-\frac{(y-\mu)^2}{2\sigma^2}}$$
(AIV.1)

Now we take a square sample of the Gaussian rough surface presented in Fig AIV.1, with N*N boxes and each box has its own height. The length and width of this sample is $L = 9\sigma$ as in Fig AIV.2.
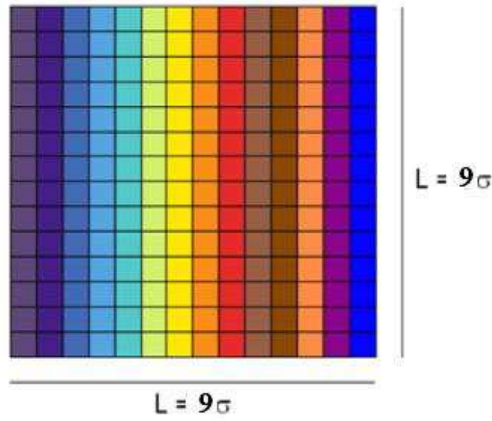
Fig AIV.2 N*N Square Gaussian Rough Surface Sample

Consider now 1 row element from this sample with length $L = 9\sigma$, this row consists of N = 100 small boxes each box has length and width b Therefore:

$$L = Nb \Rightarrow b = \frac{L}{N} = \frac{9\sigma}{100} = 0.09\sigma$$

Each box has specific height h by using Eq. AIV.1 with $\mu = 0.5$ and $\sigma = 0.12$, we get typically the following results:

20 boxes $0.4375 < h < 0.5$; 20 boxes $0.5 < h < 0.5625$

15 boxes $0.375 < h < 0.4375$; 15 boxes $0.5625 < h < 0.625$

8 boxes $0.3125 < h < 0.375$; 8 boxes $0.625 < h < 0.6875$

4 boxes $0.25 < h < 0.3125$; 4 boxes $0.6875 < h < 0.75$

1 box $0.1875 < h < 0.25$; 1 box $0.75 < h < 0.8125$

1 box $0.125 < h < 0.1875$; 1 box $0.8125 < h < 0.875$

1 box $0.0625 < h < 0.125$; 1 box $0.875 < h < 0.9375$

From the above information we can calculate the volume governed by this roughness of one row element by multiplying the height by the area of each box

$$V_{ele} = 40.90625 \times b^2$$
$$V_{ele} = 40.90625 \times (0.09 \times 0.12)^2$$
$$\Rightarrow V_{ele} = 4.77 \times 10^{-3} unit\ volume$$
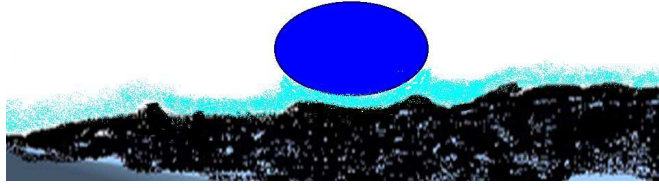$$\Rightarrow V_{sur} = V_{ele} \times 100 = 0.477\ unit\ volume$$

Fig AIV.3 polystyrene particle with radius R in water medium collide with a copper rough surface.

On the other hand the total volume of the surface with same height all over the surface

$$V_{tot} = 1\ unit\ volume$$

Consider a particle with radius R in fluid medium collides with a Gaussian rough surface Fig AIV.3. We assume that the liquid solution inside the pore fills up the region between the occupies the empty space of the rough surface, equivalent to $0.523 \times V_{tot}$, and the material roughness of the surface has a volume $0.477 \times V_{tot}$.

These results permit to calculate an effective Hamaker constant, by combining the appropriate configurations of the Hamaker constants of the particle, the solution as an intermediate medium, and the solid surface (Israelachvili 1972; Israelachvili 2011), in the depletion layer above the rough surface.

Taking the following Hamaker constants for the considered system with water as the liquid solution in the pores (Israelachvili 2011),

$$A_{poly} = A_{11} = 6.5 \times 10^{-20}\ J$$
$$A_{H_2o} = A_{22} = 3.7 \times 10^{-20}\ J$$
$$A_{Cu} = A_{33} = 7.6 \times 10^{-20}\ J$$

the Hamaker constant for the copper rough surface with water is:

$$A_{22eff} = 0.477A_{33} + 0.5237A_{22} = 5.56 \times 10^{-20}\ J$$

Hence the effective system Hamaker constant for copper rough surface, water liquid solution and incident polystyrene particle is:

$$A = A_{tot} = \sqrt{A_{22eff}A_{11}} = 6.012 \times 10^{-20}\ J$$

References

Broersma, S. (1960). "Rotational Diffusion Constant of a Cylindrical Particle." The Journal of Chemical Physics **32**(6): 1626-1631.

Broersma, S. (1960). "Viscous Force Constant for a Closed Cylinder." The Journal of Chemical Physics **32**(6): 1632-1635.

Fuller, K. N. G. and D. Tabor (1975). "The effect of surface roughness on the adhesion of elastic solids." Proc. Roy. Soc. London A **345**: 327-342.

Greenwood, J. A. and J. B. P. Williamson (1966). "Contact of Nominally Flat Surfaces." Proceedings of the Royal Society of London. Series A. Mathematical and Physical Sciences **295**(1442): 300-319.

Happel, J. and H. Brenner (1991). Low Reynolds Number Hydrodynamics: with special applications to particulate media (Mechanics of Fluids and Transport Processes). The Netherlands Kluwer, Dordrecht.

Israelachvili, J. N. (1972). "The Calculation of Van Der Waals Dispersion Forces between Macroscopic Bodies." Proceedings of the Royal Society of London. A. Mathematical and Physical Sciences **331**(1584): 39-55.

Israelachvili, J. N. (2011). Intermolecular and Surface Forces, Third Edition. San Diego, United States of America, Academic Press Elsevier.

Kim, K. S., R. M. McMeeking, et al. (1998). "Adhesion, slip, cohesive zones and energy fluxes for elastic spheres in contact." Journal of the Mechanics and Physics of Solids **46**(2): 243-266.

Koenig, S. H. (1975). "Brownian motion of an ellipsoid. A correction to Perrin's results." Biopolymers **14**(11): 2421-2423.

Langevin, P. (1908). "Sur la Théorie du Mouvement Brownien (On the Theory of Brownian Motion)." Comptes Rendus de l'Académie des Sciences Paris **146**: 530-533.

Maugis, D. (1992). "Adhesion of spheres: The JKR-DMT transition using a dugdale model." Journal of Colloid and Interface Science **150**(1): 243-269.

Morrow, C., M. Lovell, et al. (2003). "A JKR–DMT transition solution for adhesive rough surface contact." Journal of Physics D: Applied Physics **36**(5): 534.

Perrin, F. (1934). "Mouvement Brownien d'un elliposoide; I: Dispersion dielectrique pour des molecules ellipsoidales." J. Phys. Radium **5**: 497.

Perrin, F. (1936). "Mouvement Brownien d'un elliposoide;II: Rotation libre et depolarisation des molecules escences. Translation et diffusion de molecules ellipsoidales." J. Phys. Radium **7**: 1-11.

Riseman, J. and J. G. Kirkwood (1950). "The Intrinsic Viscosity, Translational and Rotatory Diffusion Constants of Rod-Like Macromolecules in Solution." The Journal of Chemical Physics **18**(4): 512-516.

Tsai, C.-J., D. Y. H. Pui, et al. (1991). "Elastic Flattening and Particle Adhesion." Aerosol Science and Technology **15**(4): 239-255.

Abstract: The purpose of this thesis is to develop a comprehensive model analysis in a three-dimensional spatial frame for the dynamics of molecular particles in dilute colloidal suspensions in solutions flowing inside pores of variable width, subject to hydrodynamic forces, Brownian motion and diffusive collisions at the rough pore boundaries, by using numerical simulations. The approach by simulations is necessary because it is extremely complex to use analytical tools at present to deal with the problem of diffusive collisions of the particles at the solid pore boundaries. The algorithms which we have developed and the corresponding simulations are sufficiently general and refined to be directly applied to the study of the dynamics of a wide variety of polymer and biological particles in dilute solutions under diverse physical and applicable hydrodynamic conditions inside pores.

Moreover, the mechanisms leading to the adhesion of particles of nano sizes under what would be *non-equilibrium* conditions, due to the conflicting influence of the mechanical diffusive collisions and the attractive Hamaker forces at the boundaries, are of major interest. We have hence investigated a theoretical model to calculate the restitution coefficient from basic physical principles. The objective is to quantify the energy balance during the process of a diffusive collision of a nano particle under the influence of the repulsive forces on one hand, and the attractive Hamaker forces acting on the nano particle on the other. This is done by developing a model, based on the JKR and Hertz theories, to account for the energy losses during collisions, and for the energy gains due to the Hamaker interactions. Adhesion becomes an outcome if the energy balance permits this. Our theoretical model is developed by proposing a special analytic approach based on the Hamaker potential. We derive from the theoretical analysis a characteristic nonlinear equation for the restitution coefficient, and analyze its properties which determine under given physical conditions the outcome for adhesion or not.

Résumé : Les objectifs de cette thèse visent le développement d'un traitement inédit dans un repère spatiale tridimensionnel, pour le problème de la dynamique de collisions diffusives d'objets macromoléculaires en solution en écoulement hydrodynamique à l'intérieur des pores de largeur variable, soumis aux forces hydrodynamiques, du mouvement brownien et des collisions diffusifs aux parois des pores, en utilisant la modélisation théorique et les simulations numériques. L'approche par simulation numérique est nécessaire car il est extrêmement complexe d'utiliser des outils analytiques à présent pour traiter le problème de ces collisions diffusives aux parois solides. Les algorithmes que nous avons développés et les simulations correspondantes sont suffisamment généraux et avancés pour être directement appliquée à l'étude de la dynamique d'une grande variété de polymère et des particules biologiques dans des solutions diluées sous diverses conditions physiques et hydrodynamiques à l'intérieur des pores.

Par ailleurs, les mécanismes conduisant à l'adhésion de nano particules et de particules macromoléculaires sous conditions de non-équilibre, en raison de l'influence contradictoire des collisions mécaniques diffusifs et les forces attractives de Hamaker aux parois solides, sont d'un intérêt majeur. Nous avons donc développé un modèle théorique pour calculer le coefficient de restitution. L'objectif est de quantifier le bilan énergétique pendant le processus de collision diffusive de ces particules aux parois, sous l'influence des forces de répulsion d'une part et les forces attractives de Hamaker. Cela se fait par l'élaboration d'un modèle, basé sur le JKR et les théories d'Hertz, pour tenir compte des pertes d'énergie lors des collisions et des gains d'énergie en raison des interactions Hamaker. L'adhésion arrive si le bilan énergétique le permet. Notre modèle théorique est développé en proposant une approche particulière basée sur le potentiel Hamaker. Nous démontrons ce bilan par le biais d'une équation caractéristique non linéaire pour le coefficient de restitution, et analysons ses propriétés qui déterminent l'adhésion ou non pour diverses conditions physiques initiales.